THESE DE DOCTORAT

Présentée à

L'UNIVERSITE DE LILLE

Ecole Doctoral Régionale Sciences Pour l'Ingénieur Lille Nord-de-France

Université de Lille

Pour obtenir le grade de

DOCTEUR EN SCIENCES

Dans la spécialité :

Micro-nanosystèmes et capteurs

par

Min LI

PREPARATION OF COMPOSITE MATERIALS FOR

HIGH-PERFORMANCE SUPERCAPACITORS

PRÉPARATION DE MATÉRIAUX COMPOSITES POUR

SUPERCONDENSATEURS À HAUTES PERFORMANCES

Directeur de thèse :
Dr. Rabah BOUKHERROUB
Co-directeur de thèse :
Prof. Sabine SZUNERITS

Soutenue le 16 Juillet 2020 devant le jury composé de :

Prof. Saïd Sadki	Rapporteur	Université Grenoble Alpes
Prof. Christine Taviot-Gueho	Rapporteur	Université Clermond Auvergne
Prof. Sorin Melinte	Président	Université Catholique de Louvain
Dr. Christophe Lethien	Examinateur	Université de Lille

ABSTRACT

Supercapacitors, as energy storage devices, have drawn great attention in our daily life to bridge the gap between batteries and capacitors. Therefore, the preparation of high-performance material electrodes for supercapacitors plays a vital role in the future technological developments. In this context, layered double hydroxides (LDHs) and $Ni(OH)_2$ have been recognized as promising electrodes for supercapacitors, owing to their fast redox reaction and battery-type behavior.

The **Chapter 1** of my PhD work gives a brief historic overview, principles and mechanism of energy storage, electrode materials of supercapacitors and the corresponding characterization methods.

In **Chapter 2**, after a brief introduction on LDHs and their investigation as electrode materials in supercapacitors, we summarize our results obtained on Ni-based LDHs as electrodes for supercapacitors. Firstly, NiFe LDHs on Ni foam (NF) coated with reduced graphene oxide (NiFe LDHs/rGO/NF) was prepared by electrochemical deposition method. NiFe LDHs/rGO/NF achieved enhanced specific capacity (585 C g^{-1} at a current density of 5 A g^{-1}). Additionally, a flexible asymmetric supercapacitor was assembled using NiFe LDHs/rGO/NF as the cathode and mesoporous carbon (MC) coated on NF as the anode. The supercapacitor exhibited an energy density of 17.71 Wh kg^{-1} at a power density of 348.49 W kg^{-1}. Secondly, NiAl LDHs coated on carbon spheres (CS) supported by Ni foam (NiAl LDHs@CS/NF) electrodes were synthesized by a facile hydrothermal method. The performance of the prepared materials as binder-

free electrodes in supercapacitors was assessed. The NiAl LDHs@CS/NF electrode achieved the largest areal capacity (1042 mC cm^{-2}), as compared to the areal capacity values attained by NiFe LDHs@CS/NF (705.8 mC cm^{-2}) and NiCr LDHs@CS/NF (814.9 mC cm^{-2}) at 1 mA cm^{-2}. Therefore, a hybrid supercapacitor device comprising NiAl LDHs@CS/NF as the positive electrode and N-doped reduced graphene/NF as the negative electrode was assembled, which attained an energy density of 43 μWh cm^{-2} at a power density of 0.805 mW cm^{-2}. The hybrid supercapacitor was successfully applied to operate a windmill device continuously for 32 s. Finally, NiMnCr LDHs-carbon spheres modified Ni foam (NiMnCr LDHs@CS/NF) nanocomposite was prepared using a two-step hydrothermal process and exhibited a high specific capacity of 569 C g^{-1} at 3 A g^{-1} with good reversibility and stability. Furthermore, a hybrid supercapacitor was fabricated using NiMnCr LDHs@CS/NF as the positive electrode and FeOOH coated on NF (FeOOH/NF) as the negative electrode. The energy storage device reached an energy density of 48 Wh kg^{-1} at a power density of 402.7 W kg^{-1}.

In **Chapter 3**, Ni(OH)$_2$@CuO@Cu foam binder-free electrodes were fabricated by a two-step process at room temperature with various deposition times (30, 50, 90, 150 and 200s). Among all the samples, Ni(OH)$_2$@CuO@Cu-150 exhibited the largest areal capacity of 7063 mC cm^{-2} at 20 mA cm^{-2}, and was therefore chosen as the positive electrode in a hybrid supercapacitor. Using N-doped reduced graphene oxide on nickel foam (N-rGO/NF) as the negative electrode, a hybrid supercapacitor was assembled. It displayed good flexibility, cycling stability and high areal energy density of 130.4 μWh

cm^{-2} at a power density of 1.6 mW cm^{-2}.

In conclusion, all the results obtained in this thesis imply the promising potential application of Ni-based hydroxide composites as energy storage devices and provide valuable highlights to the exploration of new composite materials for supercapacitor electrodes in future works (**Chapter 4**).

RÉSUMÉ

Les supercondensateurs, en tant que dispositifs de stockage d'énergie, ont attiré une grande attention dans notre vie quotidienne pour combler l'écart entre les batteries et les condensateurs. Par conséquent, la préparation d'électrodes en matériaux composites à hautes performances pour les supercondensateurs joue un rôle vital dans leurs futurs développements technologiques. Dans ce contexte, les hydroxydes doubles lamellaires (HDL) et $Ni(OH)_2$ ont été reconnus comme des électrodes prometteuses pour les supercondensateurs en raison de leurs réactions redox rapides et de leur comportement de type batterie.

Le **chapitre 1** donne un bref aperçu historique ainsi que les principes et le mécanisme de stockage d'énergie, les matériaux d'électrode des supercondensateurs, et les méthodes de caractérisation correspondantes.

Le **chapitre 2**, après un bref rappel sur la synthèse et l'utilisation de matériaux à base d'HDL comme électrodes de supercondensateurs, on décrit la préparation d'HDL à base de Ni comme électrodes pour les supercondensateurs. Premièrement, des HDLs à base de NiFe sur mousse de Ni (NF) recouverte d'oxyde de graphène réduit (LDF NiFe/rGO/NF) ont été préparées par une méthode de dépôt électrochimique. L'électrode NiFe HDL/rGO/NF présente une capacité spécifique de 585 C g^{-1} à une densité de courant de 5 A g^{-1}. De plus, un supercondensateur asymétrique flexible a été assemblé en utilisant NiFe HDL/rGO/NF comme cathode et du carbone mésoporeux (MC) déposé sur NF comme anode. Le supercondensateur présente une densité

d'énergie de 17.71 Wh kg^{-1} et une densité de puissance de 348.49 W kg^{-1}. Dans la deuxième partie de ce chapitre, nous décrivons la synthèse hydrothermale d'HDLs à base de NiAl enrobées sur des sphères de carbone (CS) supportées par des électrodes en mousse de Ni (NiAl DHL@CS/NF). La performance des matériaux préparés en tant qu'électrodes sans liant dans des supercondensateurs a été évaluée. Le matériau d'électrode NiAl DHL@CS/NF présente une capacité surfacique de 1042 mC cm^{-2} à 1 mA cm^{-2}, beaucoup plus élevée comparée aux valeurs de capacités surfaciques de NiFe HDL@CS/NF (705.8 mC cm^{-2}) et de NiCr LDHs@CS/NF (814.9 mC cm^{-2}) à 1 mA cm^{-2}. Par conséquent, un supercondensateur hybride comprenant NiAl HDL@CS/NF comme électrode positive et du graphène réduit dopé à l'azote (N-rGO)/NF comme électrode négative a été assemblé. Le dispositif présente une densité d'énergie de 43 μWh cm^{-2} à une densité de puissance de 0.805 mW cm^{-2}, et a été appliqué pour faire fonctionner un appareil éolien en continu pendant 32 s. Enfin, un matériau composite à base de NiMnCr sur un substrat de mousse de nickel recouvert de sphères de carbone (NiMnCr HDL@CS/NF) a été préparée en utilisant un processus hydrothermal en deux étapes. Le nanocomposite ainsi obtenu a été investigué comme électrode dans un supercondensateur et présente une capacité spécifique de 569 C g^{-1} à 3 A g^{-1} avec une bonne stabilité. De plus, un supercondensateur hybride a été fabriqué en utilisant NiMnCr HDL@CS/NF comme électrode positive et FeOOH déposé sur NF (FeOOH/NF) comme électrode négative. Le dispositif présente une densité d'énergie de 48 Wh kg^{-1} à une densité de puissance de 402.7 W kg^{-1}.

Dans le **chapitre 3**, des électrodes sans liant Ni(OH)$_2$@CuO sur une mousse de cuivre ont été synthétisées par un processus en deux étapes à température ambiante. Nous avons étudié l'effet du temps de dépôt (30, 50, 90, 150 et 200 s) sur le comportement électrochimique des électrodes obtenues. Parmi tous les échantillons, Ni(OH)$_2$@CuO@Cu-150 présente la plus grande capacité surfacique de 7063 mC cm^{-2} à 20 mA cm^{-2}, et a donc été choisi comme électrode positive dans un supercondensateur hybride. En utilisant de l'oxyde de graphène réduit dopé à l'azote sur de la mousse de nickel (N-rGO/NF) comme électrode négative, un supercondensateur hybride a été assemblé. Il présente une bonne flexibilité, une stabilité cyclique et une densité d'énergie surfacique élevée de 130.4 µWh cm^{-2} à une densité de puissance de 1.6 mW cm^{-2}.

Une conclusion générale rappelle les principaux résultats obtenus dans ce travail de thèse sur l'application de composites d'hydroxydes doubles lamellaires à base de Ni en tant qu'électrodes dans des dispositifs de stockage d'énergie, et présente quelques perspectives envisageables à la lumière de ces travaux (**chapitre 4**).

Mots-clés: Hydroxydes doubles lamellaires, Hydroxyde de nickel, procédé hydrothermal, dépôt électrochimique, supercondensateur, dispositifs de stockage d'énergie

ACKNOWLEDGEMENTS

the help with SEM imaging. Also, many thanks to Abir Swaidan, Chengnan Li, Elizaveta Sviridova, Liuqing Pang, Yuan Zhang, Yuanyuan Miao, Jing Zhang, Léa Rosselle, Anna Voronova, Vladyslav Mishyn, Madjid Ifires, Adel Khane...It's my pleasure to work with all of you!

I also want to thank my friends here, Ningkui Wang, Ce Zheng, Siyuan Wang, Hong Pan, Shuie Sun, Wenting Zhu, Yue Shi, Lei Shi, Longfei Liao…for their friendship.

I would like to say thank you to my best friends Guoxi Luo, Mengyu Yang and Xueyan Wang in China for their big support.

Specially, I want to thank the China Scholarship Council (CSC) for supporting me to study in France.

Finally, I would like to thank my parents, brother and sister. Thank you very much for your unrequited dedication for no return. Thank you very much for supporting me to pursue my dream.

TABLE OF CONTENTS

GENERAL INTRODUCTION

Supercapacitors (SCs), as energy storage devices, have drawn great attention in our daily life to bridge the gap between batteries and capacitors owing to their advantages like enhanced power density, being almost maintenance-free, experiencing no memory effect, safe, short charge/discharge time, and low cost.

Typically, SCs can generally be classified into three different types including electric double-layer capacitors (EDLCs), pseudocapacitors, and asymmetric supercapacitors (ASCs). The charge of an EDLC is physically stored by reversible electrostatic charge adsorption at the electrode-electrolyte interface, which is the simplest and most commercially available supercapacitor. Different from the EDLC, the key to store energy in pseudocapacitors is rapid reversible faradaic redox reactions at the surface or near surface of the electrode materials. In addition to EDLCs and pseudocapacitors, there is another configuration, called asymmetric supercapacitors (ASs). According to the type of the electrodes, hybrid supercapacitors and capacitive asymmetric supercapacitors are applied to distinguish the difference. It is generally accepted that a "hybrid supercapacitor" is composed by two electrodes with two different charge-storage mechanisms: one capacitive and one battery-type (Faradaic), whereas a capacitive asymmetric supercapacitor contains two capacitive electrodes of different materials.

In the last few years, to obtain high-performance supercapacitors, numerous

electrode materials have been explored. Typically, carbon-based materials are the most widely used materials for EDLC electrodes and transition metal hydroxides/oxides like manganese dioxide (MnO_2), nickel oxide (NiO), titanium dioxide (TiO_2), layered double hydroxides (LDHs) and conducting polymers such as polypyrrole, polythiophene, etc are promising electrode materials for pseudocapacitors. Among all the materials, Ni-based hydroxides have drawn great attention and interest in the field of supercapacitors. $Ni(OH)_2$ with large theoretical specific capacitance (2082 F g^{-1}) has been extensively investigated for supercapacitors. Besides, Ni-based layered double hydroxides (LDHs), due to their well-defined and high redox activity, wide tunability of the types of metal cations and environmentally friendly nature, were also greatly explored for supercapacitor applications.

In the first part of my work, I have investigated the influence of different metal ions (Fe, Al, Mn, Cr) on the performance of Ni-based LDH electrode materials. In this context, NiFe, NiAl, NiMnCr LDH materials were coated on reduced graphene oxide (rGO)- or carbon spheres (CS)-modified nickel foam (NF) to produce NiFe LDHs/rGO/NF, NiAl LDHs@CS/NF and NiMnCr LDHs@CS/NF composites. The prepared electrode materials displayed improved specific/areal capacity than that of the same composites without carbon-based (reduced graphene oxide or carbon spheres) materials. NiFe LDHs/rGO/NF achieved a specific capacity of 585 C g^{-1} at 5 A g^{-1}, which is higher than that of NiFe LDHs/NF (530 C g^{-1} at 5 A g^{-1}). NiAl LDHs@CS/NF electrode material attained an areal capacity of 1042.2 mC cm^{-2} at 1 mA cm^{-2}, which

greater than that of NiAl LDHs/NF (851.9 mC cm^{-2} at 1 mA cm^{-2}). NiMnCr LDHs@CS/NF composite exhibited a much larger specific capacity of 569 C g^{-1} at 3 A g^{-1}, as compared to 173.2 C g^{-1} at 3 A g^{-1} recorded for NiMnCr LDHs/NF.

In the second part of my thesis work, Ni(OH)$_2$@CuO@Cu foam binder-free electrodes were fabricated by a two-step process at room temperature with different deposition times. Ni(OH)$_2$@CuO@Cu-150 exhibited large areal capacity of 7063 mC cm^{-2} at 20 mA cm^{-2}, and was therefore chosen as the positive electrode in a hybrid supercapacitor. Using N-doped reduced graphene oxide on nickel foam (N-rGO/NF) as the negative electrode, a hybrid supercapacitor was assembled. It displayed good flexibility, cycling stability and high areal energy density of 130.4 μWh.cm^{-2} at a power density of 1.6 mW.cm^{-2}.

Furthermore, a hybrid supercapacitor device was assembled based on as-prepared NiFe LDHs/rGO/NF as the positive electrode and mesoporous carbon (MC)/NF as the negative electrode, exhibiting an energy density of 17.71 Wh kg^{-1} and a power density of 348.49 W kg^{-1}. Besides, a hybrid supercapacitor device comprising NiAl LDHs@CS/NF as the positive electrode and N-doped reduced graphene/NF as the negative electrode attained an energy density of 43 μWh cm^{-2} at a power density of 0.805 mW cm^{-2}. Finally, a hybrid supercapacitor was assembled using NiMnCr LDHs@CS/NF as the positive electrode and FeOOH coated on NF (FeOOH/NF) as the negative electrode, reaching an energy density of 48 Wh kg^{-1} at a power density of 402.7 W kg^{-1}.

CHAPTER 1

Introduction

Faced with a series of problems such as the ever-increasing exhaustion of fossil fuels, environmental pollution and global warming, people have realized the importance to develop green, pollution-free and sustainable energy supplies throughout the world [1-4]. Natural energies including wind energy, solar energy, water energy and so on are being explored. As a consequence, it is urgent to develop effective energy storage and conversion devices to make the best use of these energies [5-8]. Therefore, various energy-storage devices such as batteries, supercapacitors (SCs), fuel cells are being extensively investigated.
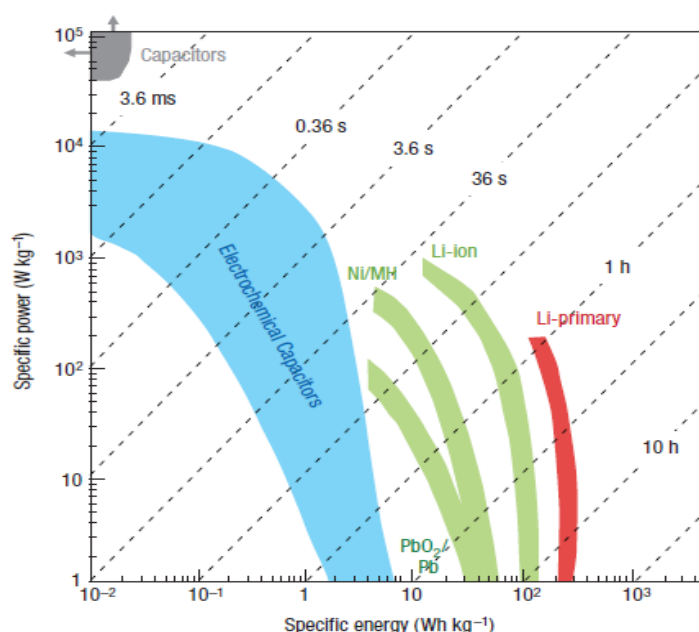
Figure 1.1: Ragone plot illustrating the performances of specific power *vs.* specific energy for different electrical energy-storage technologies. Times shown in the plot

are the discharge time, obtained by dividing the energy density by the power density

[9].

As a bridge for energy-power difference between a traditional capacitor (having high power) and fuel cells/batteries (having high energy storage) illustrated in **Figure 1.1**, SCs have drawn wide attention, owing to their advantages like enhanced power density, being almost maintenance-free, experiencing no memory effect, safe, short charge/discharge time, and low cost [10-13].

On the one hand, SCs can be applied to offer high power density for electric and hybrid vehicles required for short-term acceleration along with recuperation of energy during braking (**Figure 1.2**). On the other hand, SCs can also be utilized as power supplies for portable devices like mobile phones, notebook computers, digital cameras etc. -being small, lightweight and flexible (**Figure 1.2**).
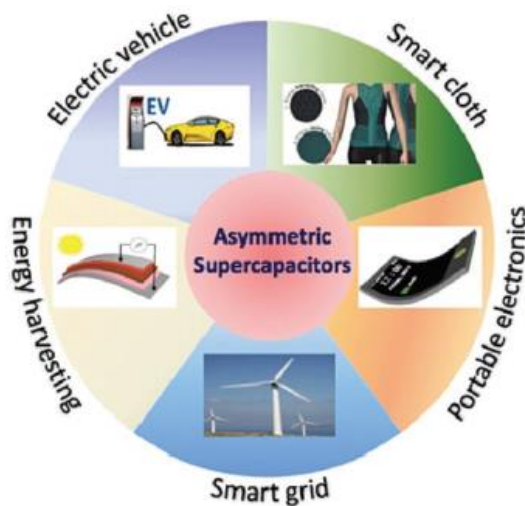
Figure 1.2: Some application areas of asymmetric supercapacitor devices [14].

Compared with SCs, batteries with higher energy density have been widely utilized

and commercialized; however, batteries tend to generate heat and dendrites when running at high power, which can lead to serious safety issues [15]. In contrast, supercapacitors can safely provide high power and fast charging, and have good cycle stability, which can replace batteries in some applications [16, 17]. Recently, Tesla announced that a combination of batteries and SCs will be applied to provide power to its new electric car, offering a promising potential application of SCs in the future.

1.1 Brief Historic Overview

Capacitor technology was pioneered thanks to the invention of the Leyden Jar (1745-1746), which was made of glass containers with metal foil [18]. The metal foil served as the electrode, and the jar was used as the dielectric. During the charging process of the above device, the positive (+ ve) charge accumulated on one electrode and the negative (-ve) charge accumulated on the other electrode. When metal wires are used to connect these two charges, a discharge process occurs.
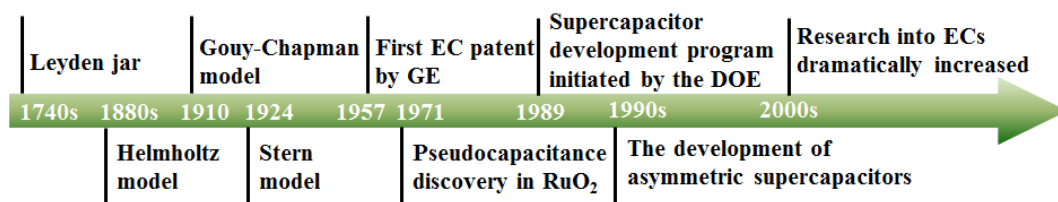
Figure 1.3: Historic timeline for the development of supercapacitors.

However, people were not familiar to the concept of storing static electricity until the electric double layer model was first proposed by the German physicist Helmholtz in the 19th century (**Figure 1.3**). He pointed out that due to static electricity at the

interface between the electrode and the electrolyte, two closely charged layers with equal amounts of opposite charges will be formed and the distance is about the diameter of an atom. After that, Gouy, Chapman and Stern further developed the Gouy-Chapman model and Stern model on the basis of the Helmholtz model.

In 1957, a patent for the first supercapacitor (Electric Double Layer Capacitor-EDLC) was granted to Becker, which used activated carbon as the electrode plate [19]. In EDLC, the charge storage occurs statically (non-Faradaic), that is, no charge transfer occurs between the electrode and the electrolyte (this makes it highly reversible and highly stable). After Becker, Sohio, based in Cleveland, Ohio, also utilized high-area carbon material for double-layer capacitors in a nonaqueous solvent electrolyte containing a dissolved tetraalkylammonium salt, achieving a higher operating voltage (3.4~4.0 V), owing to the greater decomposition voltage of the non-aqueous electrolyte as compared to aqueous electrolyte. Consequently, they can accommodate higher charge densities and provide greater specific energy storage since the storable energy increases with the square of the voltage attainable on charge.

In order to increase the specific capacitance of SC, in 1971, Trasatti *et al*. discovered a new type of electrochemical capacitor based on RuO_2 film which involved the Faraday process, called pseudocapacitor [20]. The discovery of pseudocapacitors opened a new approach to enhance the charge storage capacity of electrochemical capacitors. During 1975~1980, B. E. Conway has extensively studied RuO_2 pseudocapacitors.

In 1989, the U.S. Department of Energy (DOE) supported a long-term research, aiming to develop supercapacitors with high energy density for electric drivetrains, which is a part of its Electric and Hybrid Vehicle Program. After that, Maxwell Technologies. Inc., the world's leading supercapacitor manufacturing company, signed a contract with the DOE to develop high-performance supercapacitors, further working with batteries or fuel cells in electric or hybrid vehicles to collect braking energy and release electrical energy to accelerate driving. Since then, supercapacitor companies from around the world, such as Nesscap (Korea), ELTON (Russia), Nippon Chemicon (Japan) and CAP-XX (Australia), have been developing and delivering different types of supercapacitors such as EDLCs, pseudocapacitors, and asymmetric supercapacitors for different applications.

Since 2000, with the growing demand for high-power, high-reliability and safe energy storage equipment, the research related to supercapacitors has continued to increase significantly. At the same time, the rapid development of nanoscience and advanced characterization technologies promoted the development of EDLC and pseudocapacitor systems, which obviously need further research based on the charge storage mechanism.

1.2 Principles and Charge Storage Mechanisms

A supercapacitor (SC) consists of two electrodes, electrically isolated by a separator in the electrolyte, as is illustrated in **Figure 1.4**. The electrode material is a carrier for the SC to store charges, so the choice of electrode materials directly determines the

performance of the supercapacitor. It is necessary to investigate the working mechanism of different electrode materials.
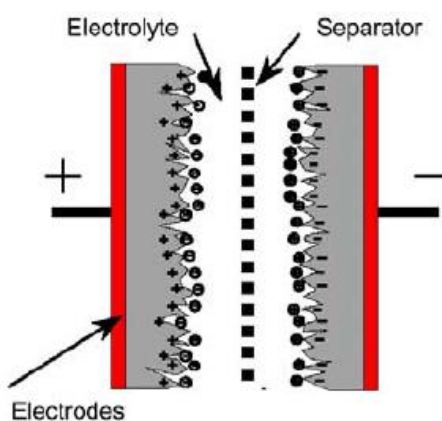
Figure 1.4: Schematic diagram of a supercapacitor structure [21].

Typically, SCs can generally be classified into three different types including electric double-layer capacitors (EDLCs), pseudocapacitors, and asymmetric supercapacitors (ASCs) (**Figure 1.5**) [22-25].
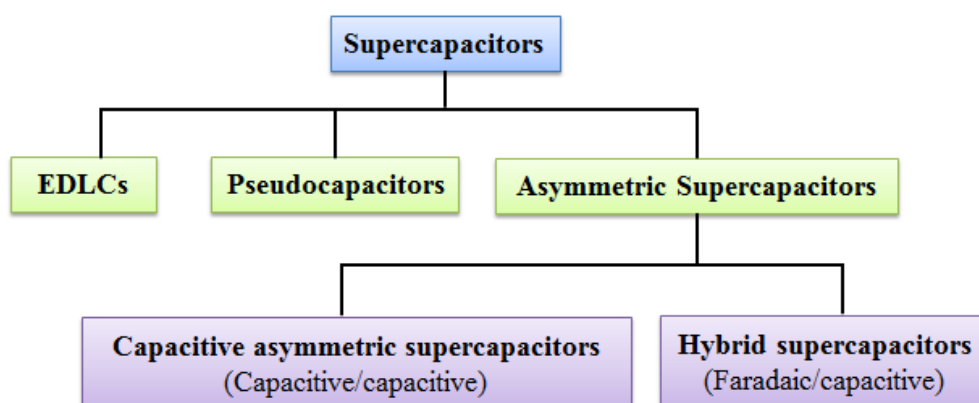
Figure 1.5: Classification of supercapacitors.

Generally, ASCs are classified into two types, namely, capacitive asymmetric

supercapacitors with two capacitive electrodes and hybrid supercapacitors (HSCs) in which one electrode stores charge by a battery-type Faradaic process, while the other electrode stores charge based on a capacitive mechanism [26]. To better understand their energy storage mechanism, they are discussed separately.

1.2.1 Electric Double Layer Capacitors (EDLCs)

This capacitance mechanism is similar to a typical mechanism of dielectric capacitors; however, a supercapacitor can store more energy on the basis of EDL principle, owing to the large interfacial area of the electrodes. The charge of an EDLC is physically stored by reversible electrostatic charge adsorption at the electrode-electrolyte interface, as depicted in **Figure 1.6**, which is the simplest and most commercially available supercapacitor [24, 27-29].
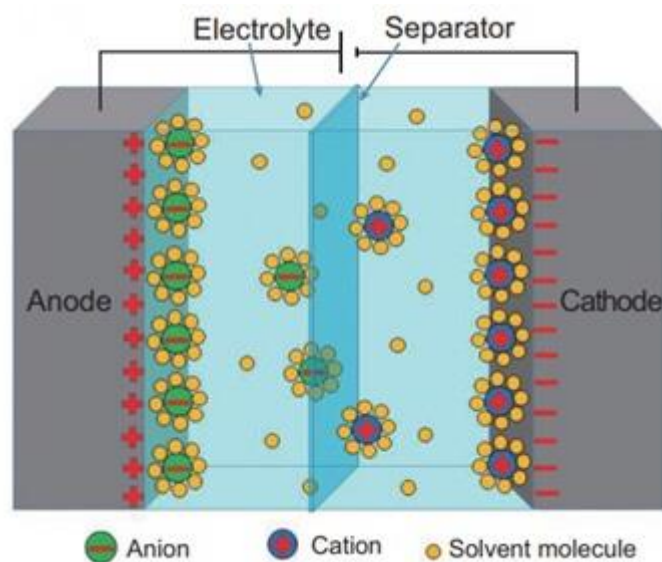
Figure 1.6: The scheme of an electrical double layer capacitor (EDLC) [30].

In EDLC, the capacitance arises due to true capacitance effect that the charge

storage takes place directly across the double layer of the electrode material without any charge transfer across the interface. According to the physical electrostatic process, the formation and relaxation of the electric double layer occur in a very short time range, on the order of 10^{-8} s, which is less than that of the redox reaction of the pseudocapacitor ($10^{-2} \sim 10^{-4}$ s). The electric double layer can immediately respond to potential changes, because there is no Faraday reaction during the charging/discharging process of EDLC.

The capacitance of an EDLC electrode can be generally estimated according to **Equation 1.1**:

$$C = \frac{\varepsilon_r \varepsilon_0 \times A}{d} \quad \text{(Eq. 1.1)}$$

Where ε_r is the relative permittivity related to the liquid electrolyte used, ε_0 is the permittivity of vacuum, A is the effective surface area of the electrode material which is accessible to the electrolyte ions, and d is the effective charge separation distance between the electrical double layer, i.e., the Debye length.

At the same time, according to **Equation 1.1**, the high effective surface area plays a vital role for the capacitance of an EDLC. Therefore, carbon-based materials with high specific surface areas were widespread investigated for EDLCs electrodes, such as activated carbons [31, 32], carbon aerogels [33-35], carbon nanotubes [27, 36, 37] and graphene [38-40]. Theoretically, a carbon-based electrode with high specific surface area ($1000 \sim 3000$ m^2 g^{-1}) can achieve an areal capacitance of $10 \sim 21$ μF cm^{-2} [41-43], corresponding to a specific capacitances of $300 \sim 550$ F g^{-1} [44]. However, the

specific surface area of the electrode materials cannot be fully available experimentally, that is why the specific capacitance of pure carbon-based EDLCs practically achieved has generally been limited to about 100~250 F g^{-1} [27, 45, 46] and the energy density lies in the range of 3~10 Wh kg^{-1} [47].

1.2.2 Pseudocapacitors

Different from the EDLC, the key to store energy in pseudocapacitors is rapid reversible faradaic redox reactions in the surface or near surface of the electrode materials [48-50]. This process involves a valence state change, which can deliver higher energy density and capacitance than EDLCs. The pseudocapacitance (C) is acquired by the derivative of charge acceptance (ΔQ) and changing potential (ΔV) displayed in **Equation 1.2**:

$$C = \frac{d(\Delta Q)}{d(\Delta V)} \quad \text{(Eq. 1.2)}$$

Transition metal oxides/hydroxides and conductive polymers are greatly applied as pseudocapacitive electrode materials [51-53]. Based on various materials, the faradaic mechanisms can typically be classified into three types, as shown in **Figure 1.7** [54]: (a) underpotential deposition, (b) redox pseudocapacitance, and (c) intercalation pseudocapacitance.

(a) Underpotential deposition occurs when the metal ion forms an adsorbed monolayer on the surface of another metal substrate that is much higher than its redox potential. However, pseudocapacitive materials normally work in aqueous electrolytes, limiting

their widespread application.

(b) Redox pseudocapacitance is based on redox reactions generated at the surface or near-surface of electrode materials with ions from the electrolyte. Usually, in the redox process, cations in the electrolyte are electrochemically adsorbed on the surface oxidized species along with fast and reversible electron transfer across the interface between the electrode and the electrolyte, which can be described by **Equation 1.3**:

$$Ox + zB^+ + ze^- \leftrightarrow RedB_z \quad \text{(Eq. 1.3)}$$
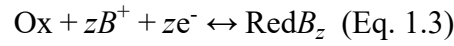
where B^+ is the surface-absorbed electrolyte cation (H^+, K^+, Na^+, ...) and z is the number of transferred electrons. The reactions depend upon the interface between the electrode and electrolyte. Therefore, the porosity and surface area of the electrode materials are of relevance to obtain high specific capacitance values.
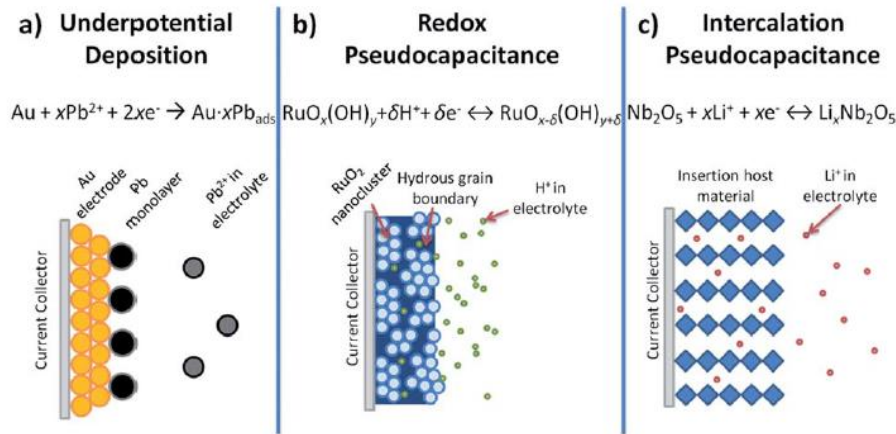
Figure 1.7: Different types of reversible redox mechanisms that give rise to pseudocapacitance: (a) underpotential deposition, (b) redox pseudocapacitance, and (c) intercalation pseudocapacitance [54].

(c) Intercalation pseudocapacitance occurs when electrolyte ions intercalate into the interlayers of a pseudocapacitive material, accompanied by a faradaic charge-transfer without involving crystallographic phase change. The electrode materials must have a crystal structure, with high interlayer distance among lattice planes, to allow the diffusion of ions into interlayers. The reactions can be illustrated by **Equation 1.4**:

$$MA_y + x\text{Li}^+ + xe^- \leftrightarrow \text{Li}_xMA_y \quad \text{(Eq. 1.4)}$$
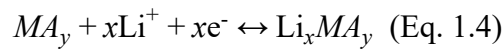
where MA_y is the layer-lattice intercalation host material (e.g., Nb_2O_5 [55, 56]) and x is the number of transferred electrons. It is obvious that the metal valence must change to keep electric neutrality during the intercalation process.

1.2.3 Asymmetric Supercapacitors (Capacitive Asymmetric Supercapacitors *vs.* Hybrid Supercapacitors)

In addition to EDLCs and pseudocapacitors, there exists a special configuration, called asymmetric supercapacitors. They are energy storage devices, which consist of two different electrodes, separator and electrolyte. According to the type of the electrode, hybrid supercapacitors and capacitive asymmetric supercapacitors are applied to distinguish the difference. It is generally accepted that a "hybrid supercapacitor" is composed by two electrodes with two different charge-storage mechanisms: one capacitive and one battery-type Faradaic [44, 57-59], whereas a capacitive asymmetric supercapacitor contains two capacitive electrodes of different materials [28, 60-63].

It is universally acknowledged that it is an effective method to construct hybrid supercapacitors to enhance the energy density [64, 65]. In a hybrid supercapacitor, the capacitive electrode typically acts as the negative electrode to supply high power density, and the battery-type pseudocapacitive component works as the positive electrode to impart high energy density [66, 67]. Moreover, devices consisting of a Faradaic electrode (such as $Ni(OH)_2$ or Co_3O_4) and a carbon electrode represent a typical type of hybrid supercapacitor device. This combination leads to higher working potential and yields higher capacitance value, which is two to three times higher than that of conventional capacitors as well as EDLC and pseudocapacitors.

For a hybrid supercapacitor, to acquire an optimal performance, a charge balance Q_+ (charges stored in the positive electrode) = Q_- (charges stored in the negative electrode) between the two electrodes is necessary.

The charge stored (Q) is determined following the **Equation 1.5**:

$$Q = C \times m \quad \text{(Eq. 1.5)}$$

Where C (C g^{-1}) is the specific capacity and m (g) is the mass of active material. So that the mass balancing follows the **Equation 1.6**:

$$\frac{m_+}{m_-} = \frac{C_-}{C_+} \quad \text{(Eq. 1.6)}$$

Where m_+ and m_- are the mass of positive and negative electrode materials, respectively, C_+ and C_- are the specific capacity of the positive and negative electrodes, respectively.

1.3 Electrode materials for supercapacitors

In the last few years, to obtain high-performance supercapacitors, numerous electrode materials have been explored. Typically, carbon-based materials are the most widely used materials for EDLC electrodes. The unique stability of carbon in various electrolyte solutions under a wide range of potentials and temperatures enables the utilization of conductive carbon materials (e.g., activated carbon, porous carbon, carbon nanotubes, graphene and carbon quantum dots) for various electrochemical systems and devices [68-70]. Besides, to further improve the performance, carbon-based electrodes doped with heteroatom such as N, P and B atoms were also investigated [33, 34, 71, 72].

Owing to the reversible faradaic redox reactions on the surface or near surface of the electrode materials, the pseudocapacitance (C) is 10~100 times larger than that achieved in EDLC [73]. As a result, pseudocapacitor electrode materials have attracted widespread attention. Generally, transition metal hydroxides/oxides like manganese dioxide (MnO_2) [74, 75], nickel oxide (NiO) [11, 76, 77], titanium dioxide (TiO_2) [78, 79], layered double hydroxides (LDHs) [80-82] and conducting polymers such as polypyrrole [83-85], polythiophene [86, 87], etc are promising electrode materials for pseudocapacitors.

In the thesis, we will focus on typical carbon-based materials and transition metal oxides/ hydroxides as examples to discuss electrode materials.

1.3.1 Carbon-based materials

Carbon-based materials are attractive for electrochemical applications since carbon is the sixth most abundant element in the Earth's crust and hence its massive use is cost effective. Herein, a few representative carbon-based materials are discussed as follows.

1.3.1.1 Activated carbon (AC)

AC is a carbon material with well-developed pores formed by disorderly arrangement of graphite-like crystallites, which has the advantages of large specific surface area, abundant pores and simple preparation process, making it the earliest carbon electrode material used in supercapacitor electrodes [88-90]. At present, the common types of activated carbon mainly include: activated carbon powder, activated carbon cloth, activated carbon fibers, etc. [91-93]. The electric double layer capacitance of activated carbon in organic electrolytes can reach 100-120 F g^{-1}; this value can exceed 300 F g^{-1} in aqueous electrolytes [9].

In 2015, Li *et al*. prepared nitrogen-doped activated carbons (NACs) (**Figure 1.8**), utilizing agricultural waste (corncob) as a precursor [64]. Doping with nitrogen helps to increase the specific capacitance of AC materials effectively.
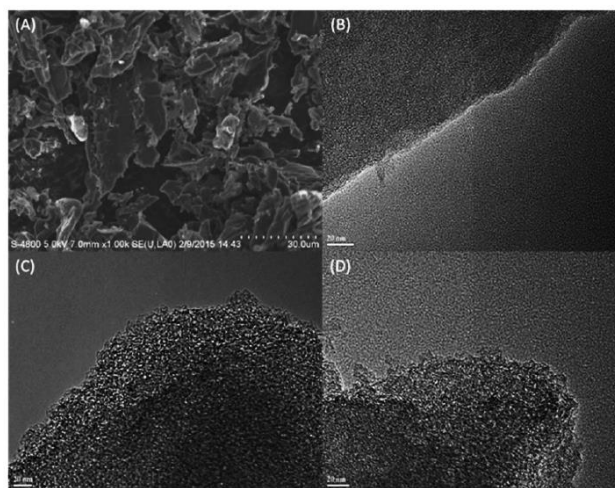
Figure 1.8: (a) SEM image of NAC-400, TEM images of (b) NAC-0, (c) NAC-400, and (d) NAC-600 [64].

The obtained NACs had a narrow micro- to meso-pore distribution and showed a high specific surface area of up to 2859 m^2 g^{-1} with a moderate N content of up to 4 wt%. The NACs delivered a high specific capacity of up to 129 mA h g^{-1} (185 F g^{-1}) in an organic electrolyte at a current density of 0.4 A g^{-1}, as well as an excellent rate capability and much improved cycling stability.

1.3.1.2 Carbon nanotubes (CNTs)

Since the first report that showed a promising high power density (8 kW kg^{-1}), there has been increasing interest in CNTs as supercapacitor electrodes [94]. CNTs are formed by wrapping graphene sheets with carbon atoms that are covalently bonded with each other through sp^2 hybridization. Depending on the number of layers of graphene sheets, they are categorized as single-walled CNTs (SWCNTs) or multi-walled CNTs (MWCNTs). CNTs can be of great interest to design composite electrodes for supercapacitors, since they have a unique internal structure, excellent physical and

chemical stability, low gravimetric density and excellent electronic conductivity [95-97].

In 2010, Najafabadi *et al*. prepared supercapacitor electrodes solely from the purest as-grown single-walled carbon nanotubes (SWNTs) available to achieve the full potential of CNT electrodes (**Figure 1.9**). They have well-defined structures with high surface area, consist of only carbon with no surface functional groups, are conductive and as one-dimensional fibers transformable into electrode sheets without any binders. By fabricating electrodes from SWNTs with high carbon purity (99.98%), exclusive SWNT selectivity (> 99%), negligible carbonaceous impurity (< 2% amorphous carbon), and near-ideal specific surface area (1300 m^2 g^{-1}), they achieved device operation at a higher voltage (4 V), while maintaining durable full charge–discharge cyclability, with an energy density of 94 Wh kg^{-1} (47 Wh L^{-1}) and a power density of 210 kW kg^{-1} (105 kW L^{-1}) far exceeding those of AC both gravimetrically (33 Wh kg^{-1}, 60 kW kg^{-1}) and volumetrically (19.8 Wh L^{-1} , 36 kW L^{-1}).
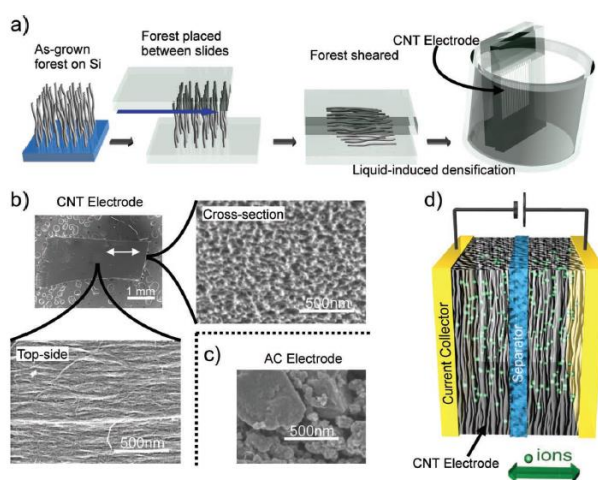
Figure 1.9: (a, b, c, d) Electrode fabrication and characterization [98]. (a) SWNT

electrode fabrication. (b) SEM image of SWNT electrode showing ordered pore structure and alignment. (c) SEM image of AC depicting random pore structure. (d) Typical cell assembly.

1.3.1.3 Graphene

Graphene is a new type of two-dimensional planar carbon nanomaterial composed of carbon atoms with hexagonal honeycomb lattice [99, 100]. Generally, graphene could be divided into single-layer graphene, double-layer graphene and multi-layer graphene, according to the number of the graphene layers. In single-layer graphene, carbon atoms are bonded to surrounding carbon atoms through sp^2 hybridization, with a C-C bond length of ~ 0.142 nm [101, 102]. The three σ bonds in the crystal lattice are connected to each other to form a structure similar to a benzene ring. Therefore, the graphene structure is very stable, and the atoms are very flexible. The π bond pair in the direction perpendicular to the crystal plane promotes the conduction of charge in graphene, and the electron mobility at room temperature is as high as 1.5×10^4 cm^2/(V s), conferring an excellent electrical conductivity. Furthermore, graphene also has excellent thermal conductivity and mechanical properties. These excellent physical, mechanical and chemical properties, especially the high conductivity of graphene, as well as the high specific surface area and rapid ion migration channel, have made graphene-based materials widely investigated in the field of supercapacitors [103-105]. Perfect graphene has an ideal two-dimensional structure with a theoretical specific surface area of up to 2.6×10^2 m^2 g^{-1}; the theoretical specific capacitance of single-layer

graphene is ~21 μF cm^{-2}, and the corresponding mass specific capacitance is ~550 F g^{-1} [99, 106]. At present, there have been many studies on the application of graphene in supercapacitors, and the specific capacitance of graphene supercapacitors reported is about 200 F g^{-1} [40, 106].

In 2008, Ruoff *et al*. reported the application of graphene in supercapacitors for the first time (**Figure 1.10**) [107]. The as-obtained chemically modified graphene (CMG) was made of 1-atom thick sheets of carbon, and their performance was demonstrated in a supercapacitor cell (**Figure 1.10d**). The measured conductivity of these CMG materials (~2 × 10^2 S/m) closely approaches that of pristine graphite, the surface area of the CMG agglomerate is 705 m^2 g^{-1}, and calculated specific capacitances were 135 and 99 F g^{-1} in aqueous and organic electrolytes, respectively. Furthermore, in 2011, Ruoff *et al*. synthesized a porous microwave exfoliated graphene oxide (MEGO) and thermally exfoliated graphene oxide (TEGO) using a simple activation with KOH to achieve specific surface area values up to 3100 m^2 g^{-1}, exhibiting a specific capacitance of 166 F g^{-1} at a current density of 5.7 A g^{-1} [108].
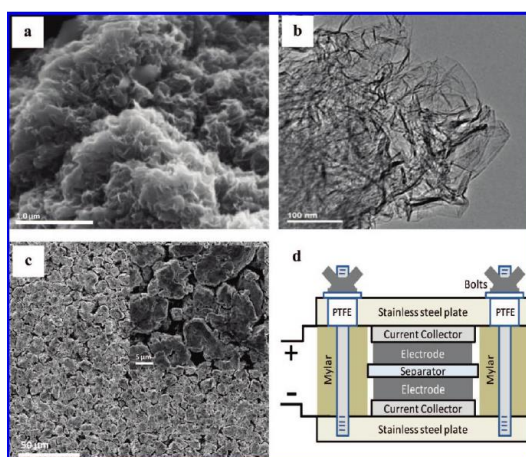
Figure 1.10: (a) SEM image of CMG particle surface, (b) TEM image showing individual graphene sheets extending from CMG particle surface, (c) low and high (inset) magnification SEM images of CMG particles electrode surface, and (d) schematic of test cell assembly [107].

1.3.2   Transition metal oxides/hydroxides (TMOs/TMHOs)

Compared with carbon-based materials, TMOs/TMHOs possess higher specific capacity due to the multiple oxidation states [109, 110]. Early investigations on electrode materials have concentrated on noble TMOs, such as RuO_2 and IrO_2. RuO_2 with three oxidation states within 1.4 V displays a large specific capacitance of 2000 F g^{-1} [111, 112]. However, the exceedingly high cost and environmentally poisonous nature of TMOs limit their practical applications. Hence, cheap and high-performance TMOs/TMHOs, such as MnO_2, NiO, Co_3O_4, CuO, Fe_3O_4, $Ni(OH)_2$ and FeOOH, have been extensively studied as electrode materials for SCs [12, 113-118]. Here, we will discuss some commonly used transition metal oxide electrode materials only.

1.3.2.1 Manganese dioxide (MnO_2)

Manganese is the 12th most abundant element in the Earth's crust, and MnO_2 has drawn extensive interest as electrode for supercapacitors due to its low cost, high natural abundance, high theoretical specific capacitance (~1370 F g^{-1}), rich polymorphisms (**Figure 1.11**), and environmental benignity [119-122].

The energy storage process of MnO_2 is mainly achieved by the III/IV oxidation state change at or near the surface. The reaction mechanism equation is as follows (**Equation**

1.7):

$$MnO_2 + C^+ + e^- \leftrightarrow MnOOC \quad (Eq. 1.7)$$
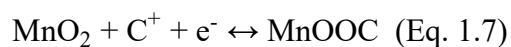
where C represents electrolyte cations such as H^+, K^+, Na^+ and Li^+.
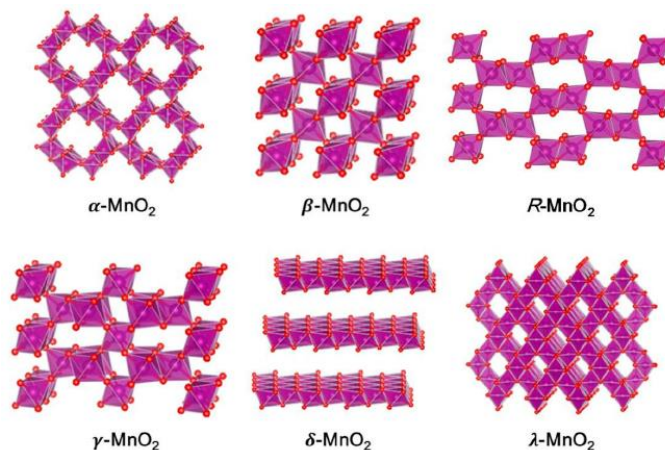
Figure 1.11: Crystal structures of MnO_2 polymorphs (Mn: magenta and O: red) [123]. (1) α-MnO_2 (2 × 2 tunnel or hollandite), (2) β-MnO_2 (1 × 1 tunnel or pyrolusite), (3) R-MnO_2 (2 × 1 tunnel or Ramsdellite), (4) γ-MnO_2 (mix of 2 × 1 and 1 × 1 tunnels or nsutite), (5) δ-MnO_2 (layered or birnessite), and (6) λ-MnO_2 (3-dimensional pores or spinel).

In 1999, Lee and Goodenough first applied amorphous $MnO_2 \cdot nH_2O$ as an electrode for supercapacitors and tested the performance in a mild KCl aqueous electrolyte. They obtained a specific capacitance of about 200 F g^{-1} at 2 mA cm^2 [124]. After that, to improve the specific capacitance of SCs, research works focused on MnO_2-based electrodes with different morphologies, hierarchical porous structures, large pore volumes and high specific surface areas. In 2010, Lu *et al*. synthesized MnO_2 nanotube

and nanowire arrays *via* an electrochemical deposition technique using porous alumina templates [125]. Benefiting from the nanotubular architecture, which provides much shorter diffusion paths for both cations and electrons, the MnO_2 nanotube array electrode achieved a larger specific capacitance of 320 F g^{-1} than that of MnO_2 nanowire array electrode (101 F g^{-1}) at a scan rate of 20 mV s^{-1}. In 2013, Thomas *et al*. prepared highly ordered MnO_2 nanopillars for supercapacitors by a facile method called spin-on nanoprint (SNAP), revealing a specific capacitance of 603 F g^{-1} at a current density of 10 A g^{-1} [126]. In 2018, Zhang *et al*. assembled β-MnO_2/birnessite core-shell structure with β-MnO_2 as the core and highly aligned "birnessite-type" MnO_2 thin sheets as the shell for SCs [119]. The highly aligned birnessite-type MnO_2 thin sheets are parallel to each other with open pores that are readily accessible to electrolyte ions, and obtained a specific capacitance of 657 F g^{-1} at a current density of 0.25 A g^{-1} based on the weight of parallel birnessite.

Additionally, to address the conductivity problem of MnO_2-based electrodes, an effective approach consists of combining MnO_2 with highly conductive materials such as porous metal substrates [127], conducting polymers [128, 129] and carbon-based materials [130-132].

1.3.2.2 Cobalt oxides (Co_3O_4)

Due to the ultrahigh theoretical specific capacitance (3560 F g^{-1}) [133] and a variety of structures and morphologies (nanoparticles [134], nanowires [115, 135], nanorods [136], nanosheets [137] and porous nanostructures [138]), Co_3O_4 has been diffusely

investigated as a candidate for supercapacitor electrodes and it is considered to be a potential candidate for state-of-the-art RuO_2 [135]. The reason behind choosing Co_3O_4 as a promising candidate for pseudocapacitors over most promising hydrous RuO_2 is its low cost, and can provide a variety of oxidation states for efficient redox charge transfer [111, 139].

Usually, the supercapacitive reactions of Co_3O_4 can be described by **Equations 1.8** and **1.9**:

$$Co_3O_4 + OH^- + H_2O \leftrightarrow 3CoOOH + e^- \quad (Eq. \ 1.8)$$

$$CoOOH + OH^- \leftrightarrow CoO_2 + H_2O + e^- \quad (Eq. \ 1.9)$$
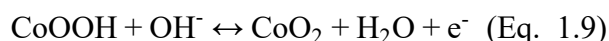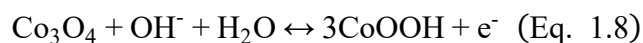
Based on this energy storage mechanism, Chen *et al.* successfully synthesized Co_3O_4 nanotubes (**Figure 1.12**) by chemically depositing cobalt hydroxide in anodic aluminum oxide (AAO) templates and subsequent thermal annealing at 500 °C [140]. The electrochemical behavior of the Co_3O_4 nanotubes electrode was investigated in 6 M KOH solution and displayed a specific capacitance of 574 F g^{-1} at a current density of $0.1Ag^{-1}$. In 2011, Tu *et al.* prepared self-supported hollow Co_3O_4 nanowire arrays by a facile hydrothermal synthesis method and further assessed its electrochemical properties in 1 M KOH [141]. The self-supported hollow Co_3O_4 nanowire arrays exhibited superior supercapacitor performance with high specific capacitance values (599 F g^{-1} at 2 A g^{-1} and 439 F g^{-1} at 40 A g^{-1}) as well as excellent cycling life, making them suitable for high-rate supercapacitor application.
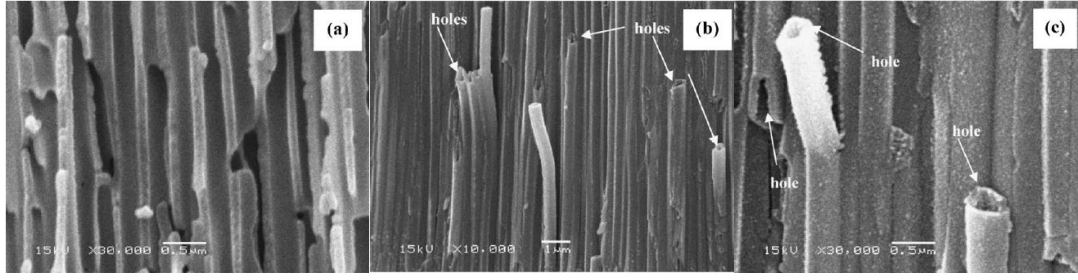
Figure 1.12: SEM images of vacant AAO template (a), as-prepared Co_3O_4 nanotubes embedded in an AAO template (b and c).

1.3.2.3 Nickel hydroxide (Ni(OH)$_2$)

Among various pseudocapacitive materials, $Ni(OH)_2$ is cost-effective, stable in alkaline electrolytes and is available in various morphologies with high theoretical specific capacitance (2082 F g^{-1}), making it an attractive candidate for high performance supercapacitors [142-144]. Typically, it has a hexagonal layered structure with two polymorphs, α- and β-$Ni(OH)_2$ [145].
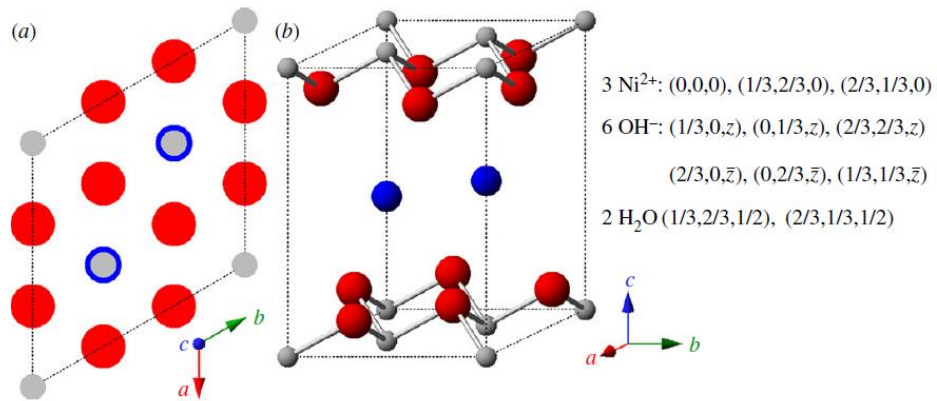
Figure 1.13: The idealized crystal structure of α-Ni(OH)$_2$ represented by (a) unit cell projection and (b) ball-and-stick unit cell for x =0.67 (actual value varies, 0.41$\leqslant$x$\leqslant$ 0.7). Small (grey) spheres, Ni^{2+}; large (red) spheres, OH^-; medium size (blue) spheres, H_2O [146].

The α-form is isostructural with hydrotalcite (HT)-like compounds and consists of a stacking of positively charged Ni(OH)$_{2-x}$ layers, with intercalated anions (e.g., carbonate, nitrate, etc.) and water molecules in the interlayer space (~7 Å) to restore charge neutrality (**Figure 1.13**), whereas the β-form possesses a brucitelike (Mg(OH)$_2$) structure and does not contain any intercalated species with an interlayer distance of ~4.6 Å (**Figure 1.14**) [146, 147]. It is generally accepted that α-nickel hydroxide will exhibit superior electrochemical properties compared to the β-form. However, the α-nickel hydroxide is a metastable phase and is difficult to synthesize, because it changes rapidly to the β-form during synthesis or upon storage in a strong alkaline solution [147].
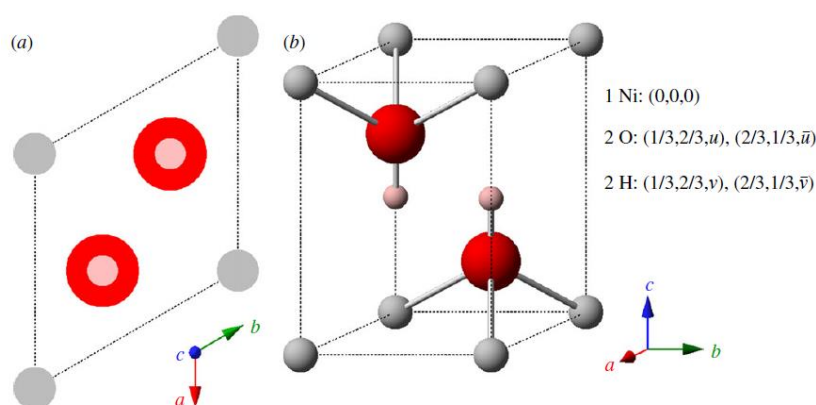
Figure 1.14: The crystal structure of β-Ni(OH)$_2$ represented by (a) unit cell projection and (b) ball-and-stick unit cell (u=0.24 and v =0.47; or u=0.2221 and v =0.4275). Medium size (grey) spheres, Ni^{2+}; large (red) spheres, O^{2-}; small (pink) spheres, H^{+} [146].

For Ni(OH)$_2$ electrode material, it is well-accepted that the Faradaic reactions will proceed according to the following reaction (**Equation 1.10**):

$$Ni(OH)_2 + OH^- \leftrightarrow NiOOH + H_2O + e^- \quad (Eq. \ 1.10)$$

In 2013, Xiao *et al.* fabricated coral-like nanoporous β-Ni(OH)$_2$ nanobars by a facile and template-free coprecipitation approach [148]. The as-made β-Ni(OH)$_2$ electrode delivered a specific capacitance of 1780 F g^{-1} at a current density of 1.0 A g^{-1} in 6 M KOH solution. In 2017, Pocrifka *et al.* obtained cabbage-like α-Ni(OH)$_2$ with a good long-term cycling stability for supercapacitor, exhibiting a maximum specific capacitance of 1903 F g^{-1} at a current density of 1 mA cm^{-2} [149]. All the results indicate that Ni(OH)$_2$ is a promising electrode material for supercapacitor applications.

1.3.2.4 Layered double hydroxides (LDHs)

Generally, as shown in **Figure 1.15**, LDHs or hydrotalcite-like compounds can be represented by $M^{2+}_{1-x}M^{3+}_x(OH)_2(A^{n-})_{x/n} \cdot mH_2O$, where M^{2+} and M^{3+} correspond to the bivalent (Ni^{2+}, Co^{2+}, Cu^{2+}, Mg^{2+}, Mn^{2+}) and trivalent (Fe^{3+}, Al^{3+}, Co^{3+}, V^{3+}, Cr^{3+}) metal cations, respectively, A^{n-} represents the interlayer anion (CO_3^{2-}, NO_3^-, OH^-), $x = M^{3+}/(M^{2+} + M^{3+})$ is the surface charge and is generally in the range of 0.2~0.33 [4, 150-152]. Each hydroxyl group in the LDH layers is oriented toward the interlayer region and may be hydrogen bonded to the interlayer anions and water molecules. Besides, interlayer bonding in LDHs is relatively weak, exhibiting excellent expanding properties.

LDHs have evoked great attention on the basis of their well-defined and high redox activity, wide tunability of the types of metal cations and environmentally friendly

nature. They have been employed in several processes such as oxygen evolution reaction [153, 154], hydrogen evolution reaction [155], corrosion protection [156], hot coal gas desulfurization [157], supercapacitors [16, 158, 159] and so on.
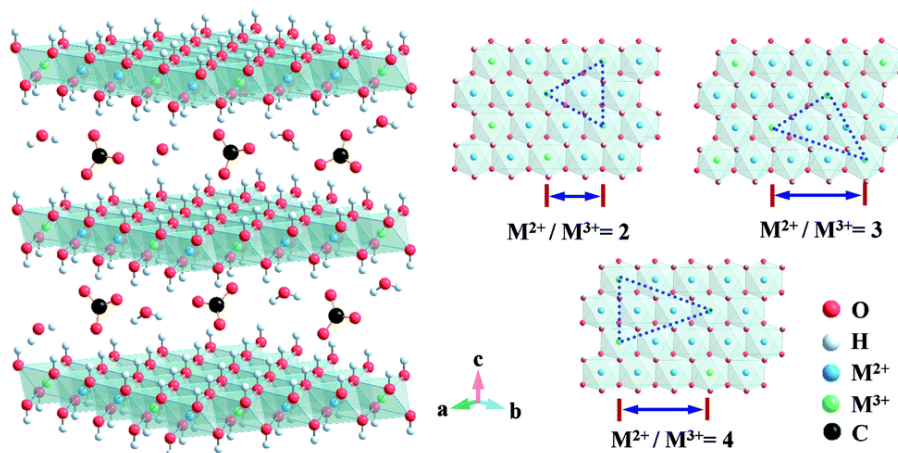
Figure 1.15: The idealized structure of carbonate-intercalated LDHs with different M^{2+}/M^{3+} molar ratios showing the metal hydroxide octahedral stacked along the crystallographic c-axis, as well as water and anions present in the interlayer region [160].

In 2014, Leroux *et al*. revealed a monometallic $Co^{II} Co^{III}–CO_3$ LDH by converting a β-Co(OH)$_2$ brucite type structure through a topochemical oxidative reaction (TOR) under air [16]. The electrochemical behavior was investigated in 0.1 M KOH aqueous electrolyte and the largest specific capacitance was determined to be as high as 1490 F g^{-1} at a current density of 0.5 A g^{-1}. In 2013, Lokhande *et al*. prepared nanostructured porous $Co_{1-x}Ni_x$ LDHs thin films on stainless steel substrate and studied their structure, morphology, surface wettability and electrochemical performance [161]. As shown in **Figure 1.16**, the $Co_{1-x}Ni_x$ LDHs thin films possess different morphologies for different

Ni proportions. The maximal specific capacitance of $Co_{1-x}Ni_x$ LDHs electrode was ~1213 F g^{-1} for a composition $Co_{0.66}Ni_{0.34}$ LDH in 2 M KOH electrolyte at a scan rate of 5 mV s^{-1}.
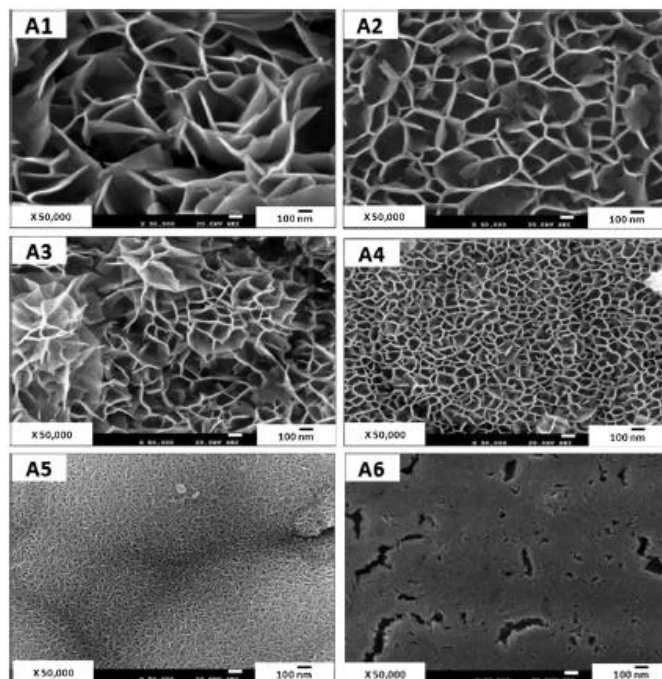
Figure 1.16: SEM micrographs of $Co_{1-x}Ni_x$ LDHs thin films: A1 (1.0:0.0), A2 (0.75:0.25), A3 (0.6:0.4), A4 (0.5:0.5), A5 (0.25:0.75) and A6 (0.0:1.0) at ×50000 magnification [161].

1.4 Synthesis approach of electrode materials

The method of synthesis of electrode materials plays an important role in controlling the structures and properties of the materials. Some synthesis methods are described here briefly:

1.4.1 Chemical vapor deposition (CVD)

CVD is a well-established vacuum deposition technique used to produce high

quality, high-performance, solid materials. In typical CVD, the substrate is exposed to one or more volatile precursors, which react and/or decompose on the substrate surface to produce the desired deposit. Frequently, volatile by-products are also produced, which are removed by gas flow through the reaction chamber.

Many electrode materials such as silicon (dioxide [162], carbide [163], nitride [164] and oxynitride [165]), carbon (nanotubes [166], diamond [167] and graphene [168]), fluorocarbons [169] and titanium nitride [170] are widely used CVD method.

1.4.2 Electropolymerization/Electrodeposition

Electrodeposition is a well-known conventional surface modification method to produce *in situ* metallic coatings by the action of an electric current on a conductive material immersed in a solution containing a salt of the metal to be deposited.
At present, electrodeposition is emerging as an accepted versatile technique involving simple processing conditions for the preparation of nanomaterials with no toxic chemicals in the process. Generally, conductive polymers such as polyaniline (PANI), poly (3, 4-ethylenedioxythiophene) (PEDOT), polypyrrole (PPy), etc. are synthesized by this approach [171-174].

1.4.3 Hydrothermal/solvothermal methods

Hydrothermal method can be defined as a method of synthesis of single crystals that depends on the solubility of minerals in hot water under high pressure. The crystal growth is performed in an apparatus consisting of a steel pressure vessel called an autoclave, in which a precursor is supplied along with water. The difference between

41

hydrothermal and solvothermal methods is that in the hydrothermal method the solution is aqueous (water), while in solvothermal method the solution is non-aqueous (solvent other than water) under relatively higher temperatures. It is universally acknowledged that hydrothermal method is a facile low-temperature sintering process and is simple to implement and scale up, which is extensively utilized for synthesis of electrode materials [175-177].

1.4.4   Co-precipitation method

Co-precipitation is the carrying down by a precipitate of substances normally soluble under the conditions employed and is a facile and convenient approach to prepare large-scale powder samples. Typically, co-precipitation reactions involve the simultaneous formation of nucleation, growth, coarsening and/or agglomeration processes. For precipitation to occur, the concentration of a solute should be greater than the solubility limit, and the temperature should be high enough to quickly separate into a precipitate. As a consequence, due to the rapid precipitation rate, it is difficult to adjust the morphology of the prepared sample.

1.5   Electrochemical measurements for electrode materials

1.5.1   Supercapacitors metrics of electrode materials

- Capacitance (C, F) quantifies the amount of charge stored within a specific potential window for a known weight (or area or volume) of a capacitive electrode. High specific capacitance is the key requirement for high charge storage or high energy density electrode.

- Capacity is the charge-storage amount for a battery-like electrode based on a Faradaic reaction, in Coulombs (C), or mAh.

- Rate capability is the charge storage/energy density capacity at high applied current density compared to the value at low applied current density. High rate capability value is an important requirement for high-rate applications and for fast charge of supercapacitors.

- Energy density (E) is the amount of energy that can be stored per mass (Wh kg^{-1}), per area (Wh cm^{-2}) or per volume (Wh cm^{-3}).

- Power density (P) is the charge/discharge rate, which describes how fast the same amount of energy can be absorbed or delivered for a given time, which is directly related to rate capability.

- Cycling stability is charge capacitance/capacity degradation for a given number of fully charge-discharge cycles. High cycling stability is an important factor for the practical application of supercapacitors.

These metrics are totally determined by the properties of electrode/electrolyte interface. The surface morphology, architecture, porosity, conductivity, ionic diffusion and redox activity of electrode materials play a significant role on the performance of a supercapacitor.

1.5.2   Electrochemical measurements for electrode materials

Typically, electrochemical measurements are conducted in a classical three-electrode configuration or two-electrode system. To perform an investigation on the

performance of active materials, the three-electrode system is commonly utilized, including the active materials as the working electrode, a reference electrode and a counter electrode. For asymmetric supercapacitor devices, two-electrode system is practical and widely employed to investigate the electrochemical performance. Both of them contain cyclic voltammetry (CV)，galvanostatic charge-discharge (GCD) and electrochemical impedance spectroscopy (EIS) tests, which are the most commonly used techniques to evaluate the electrochemical properties of SCs. The above test modes can measure three basic parameters: voltage, current and time, and then can derive other performance indicators, such as operating voltage, specific/areal capacitance/capacity, equivalent series resistance, and subsequent energy density and power density.

1.5.2.1 Cyclic voltammetry (CV)

CV is one of the most commonly used methods to study the electrochemical performance of electrode materials. The principle is to record the corresponding current change by controlling the change of the electrode potential at a constant rate.

The resulting *I-V* curve can provide useful information on the electrode reaction process, such as the reversibility of the electrode reaction, and the performance of hydrogen evolution and oxygen evolution, which is an effective and basic electrochemical technique to identify the capacitive behavior of SC electrode materials, which is introduced in detail with galvanostatic charge-discharge (GCD) together.

1.5.2.2 Galvanostatic Charge-Discharge (GCD)

GCD is an important method to study the electrochemical performance of electrode materials. A consecutive charging/discharging of the working electrode is performed at a constant current density with or without a dwelling period (a time period between charging and discharging while the peak voltage V_0 remains constant). From the GCD curves, we can obtain the charge and discharge time and potential window. Consequently, the specific capacitance/capacity (C) of the active material can be calculated using the charge-discharge curve according to **Equation 1.11**, and the charge-discharge test at different current densities can be used to study the rate performance of electrode materials.

$$C\,(\text{capacitance}) = \frac{I\,\Delta t}{m\,\Delta V} \quad (\text{Eq. } 1.11.1)$$

$$C\,(\text{capacity}) = \frac{I\,\Delta t}{m} \quad (\text{Eq. } 1.11.2)$$

where I is the applied current, Δt is the discharge time, m is the mass loading of SC electrodes and ΔV is the potential window.

Additionally, the cycling stability of electrode materials in this thesis was performed by the charge and discharge tests at different cycles.

For an asymmetric supercapacitor, the energy density (E) and power density (P) are important indicators to study their practical application value. According to the calculated specific capacitance/capacity, the E and P of the device can be further

calculated. The formula used to determine respectively E and P are:

$$E = \frac{1}{2} C \Delta V^2 = \frac{Q \Delta V}{2} \quad \text{(Eq. 1.12)}$$

$$P = \frac{E}{\Delta t} \quad \text{(Eq. 1.13)}$$

Importantly, the CV and GCD (**Figure 1.17**) provide convenient means to categorize the mode of charge storage for an electrode material. For EDLCs and redox pseudocapacitors, the CV curves typically exhibit a rectangular shape, which usually show a potential-independent current (capacitive feature) (**Figure 1.17a, b**). The corresponding GCD curves show a linear relationship between V and t (**Figure 1.17c**). However, the CV curves of batteries ordinarily show prominent and widely separated redox peaks involved in charge storage (**Figure 1.17g, h**), and V versus t for the discharge is profoundly nonlinear and characterized by plateaus of nearly constant potential, corresponding to the potentials at which the Faradaic reduction or oxidation of the metal centers is occurring (**Figure 1.17i**). An intermediate behavior between these two extremes signifies the presence of pseudocapacitance (**Figure 1.17d-f**).
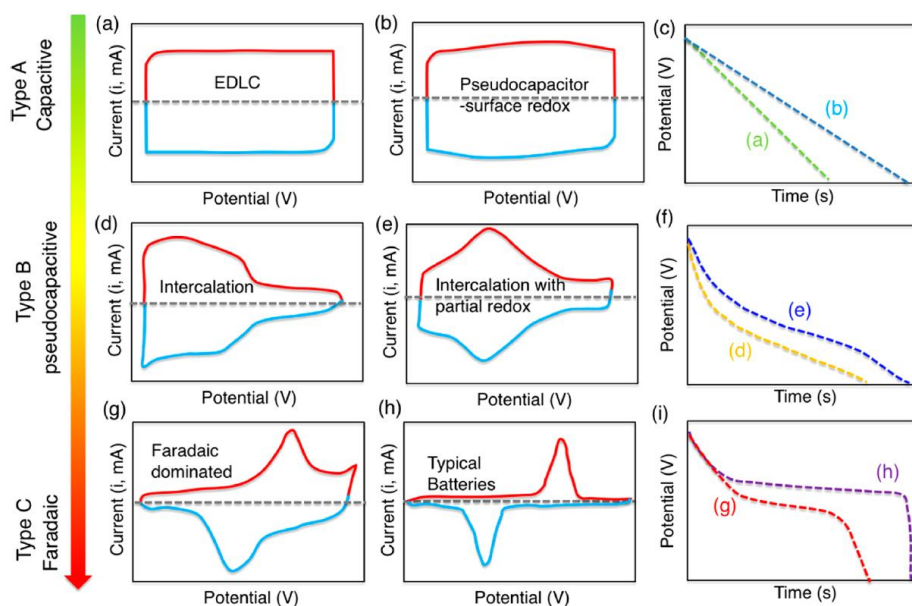
Figure 1.17: (a, b, d, e, g, h) Schematic cyclic voltammograms and (c, f, i) the corresponding galvanostatic discharge curves for various kinds of energy-storage materials. A pseudocapacitive material will generally have the electrochemical characteristics of one, or a combination, of the following categories: (b) surface redox materials (e.g., MnO_2 in neutral, aqueous media), (d) intercalation-type materials (e.g., lithium insertion in Nb_2O_5 in organic electrolytes), or (e) intercalation-type materials showing broad, but electrochemically reversible redox peaks (e.g., Ti_3C_2 in acidic, aqueous electrolytes). Electrochemical responses in (g~i) correspond to battery-like materials [178].

For pseudocapacitors, the electrodes with CV containing intense, clearly separated oxidative and reductive peaks (**Figure 1.17g, h**), or constant-current charge/discharge curves with obvious plateaus (**Figure 1.17i**), were categorized as battery-type electrodes. For strictly battery-type Faradaic reactions, ion intercalation is limited by solid-state ion diffusion processes and the peak current (i) response of a battery-type

47

electrode is proportional to the square root of the scan rate ($i \sim v^{1/2}$), whereas a capacitor-type material with capacitive feature will show linear current response dependency on the scan rate ($i \sim v$). Therefore, the CV curve can also be used to determine the capacitive and diffusion-controlled (battery-type Faradaic reactions) contributions (**Figure 1.18**). The instantaneous current at a certain potential can be expressed as **Equation 1.10:**

$$i\,(V) = k_1 v + k_2 v^{1/2} \quad \text{(Eq. 1.14)}$$

where $k_1 v$ is the surface-controlled current and $k_2 v^{1/2}$ is the diffusion-controlled current. The coefficients k_1 and k_2 can be obtained through the linear fitting of voltammetric currents at each potential. It leads to the calculation of $k_1 v$ and $k_2 v^{1/2}$, which, therefore, allows for the separation of capacitive and diffusion currents.
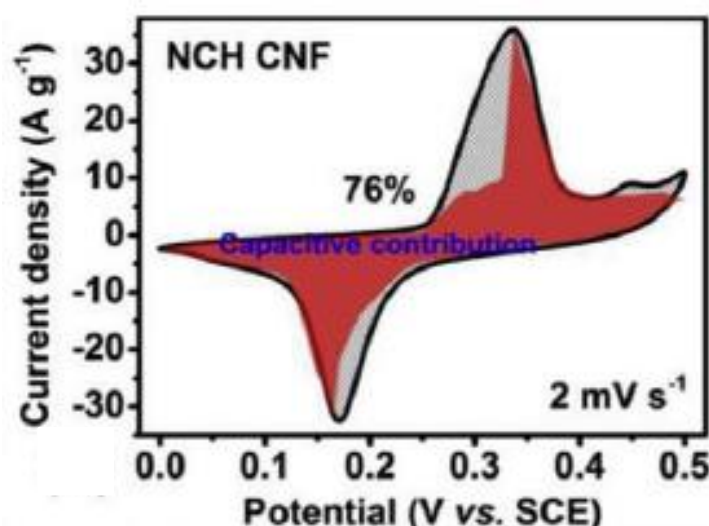
Figure 1.18: Capacitive (red) and diffusion-controlled (grey) contributions to charge storage of Ni(OH)$_2$ nanosheets/NiCo$_2$O$_4$/carbon nanofiber (NCH CNF) at 2 mV s^{-1}

[179].

In addition to GCD, CV also provides a method of calculating the capacitance/capacity. The integral area of the CV curve is proportional to the capacitance/capacity contribution of the material according to **Equation 1.15**, so it can be used to roughly compare the specific capacitance of electrode materials.

$$C \text{ (capacitance)} = \frac{1}{2mv\Delta V} \int_{V_1}^{V_2} I(V)\, dV \quad \text{(Eq. 1.15.1)}$$

$$C \text{ (capacity)} = \frac{1}{2mv} \int_{V_1}^{V_2} I(V)\, dV \quad \text{(Eq. 1.15.2)}$$

where m is the mass loading of SC electrodes, v is the scan rate, V_1 and V_2 are respectively the low- and high-end potentials, and $I(A)$ is the current.

1.5.2.3 Electrochemical Impedance Spectroscopy (EIS)

EIS can be used to analyze the charge transfer and material transport of electrode materials at the electrode/electrolyte interface and the electrode reaction kinetics. **Figure 1.20** displays a typical EIS and the corresponding equivalent circuit [180].

49
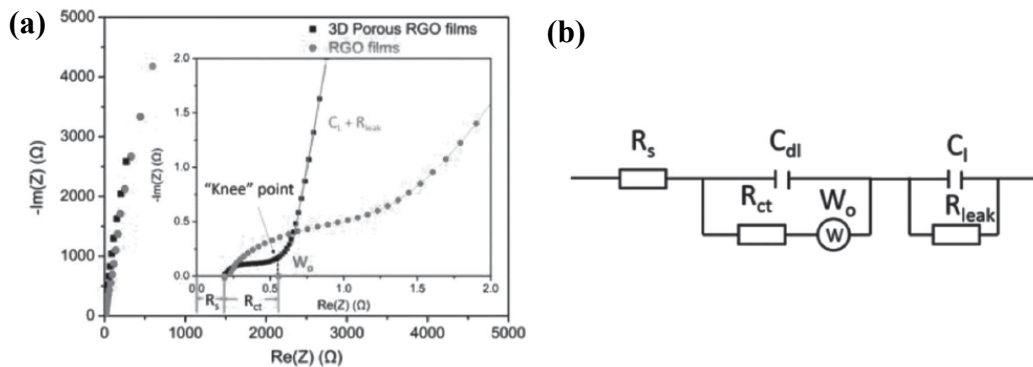
Figure 1.20: (a) Electrochemical impedance spectroscopy data. (b) A Randles

equivalent circuit. The equivalent circuit used to fit the Nyquist spectra [180].

Typically, the Nyquist plots (**Figure 1.20a**) reveal the typical depressed semicircle

in high-to-medium frequency region related to the charge transfer, and a straight line in

low-frequency region arising from ion diffusion in the electrode material. According to

the simulated equivalent circuit, the internal resistance of the solution, the charge

transfer resistance, the electric double layer capacitance of the electrode and the

diffusion mass transfer process can be estimated. The EIS conditions measured in this

thesis are an open circuit voltage, an amplitude of 5 m V, and a frequency range of 0.01

Hz-100 k Hz.

1.6   Objectives and outline of the thesis

The primary purpose of this thesis is to explore new possibilities and synthesize

high-performance electrode materials *via* low-cost facile method for supercapacitors.

New composites will be explored to take advantage of different materials. Therefore,

this thesis includes four chapters describing the various materials proposed and their

characterization and measurements. More detailed information will be introduced in

each chapter.

In **chapter 1**, a brief historic overview, basic background, principles and mechanism

of energy storage, electrode materials of supercapacitors and the corresponding

characterization methods were discussed, revealing a deep insight into the foundation

of supercapacitors.

In **Chapter 2**, NiFe LDHs on Ni foam coated with reduced graphene oxide (NiFe LDHs/rGO/NF) was prepared by electrochemical deposition method. The effect of different Ni/Fe ratio on the performance of the composites was explored. Combining with mesoporous carbon (MC) coated on NF as the negative electrode, a hybrid supercapacitor device was constructed and fully characterized. Moreover, NiAl layered double hydroxides coated on carbon spheres (CS) supported by Ni foam (NiAl LDHs@CS/NF) nanocomposite was synthesized *via* a facile hydrothermal method. The performance of the prepared materials as binder-free electrodes in supercapacitors was assessed. Moreover, a hybrid supercapacitor device comprising NiAl LDHs@CS/NF as the positive electrode and N-doped reduced graphene/NF as the negative electrode was successfully fabricated. Furthermore, taking advantage of plentiful oxidation states of Cr, composite of NiMnCr LDHs-carbon spheres modified Ni foam (NiMnCr LDHs@CS/NF) was obtained by a two-step hydrothermal process. Furthermore, a hybrid supercapacitor was assembled using NiMnCr LDHs@CS/NF as the positive electrode and FeOOH coated on NF (FeOOH/NF) as the negative electrode. The hybrid supercapacitor was applied to power a home-designed windmill device and to light up a yellow LED and a red LED in parallel, indicating its potential application as an energy storage device.

In **Chapter 3**, we fabricated $Ni(OH)_2$@CuO@Cu foam binder-free electrodes by a two-step process at room temperature with various deposition times (30, 50, 90, 150

and 200s). Among all the samples, Ni(OH)$_2$@CuO@Cu-150 exhibited the largest areal capacity of 7063 mC cm^{-2} at 20 mA cm^{-2} which was chosen as the positive electrode in a hybrid supercapacitor. Combing with N-doped reduced graphene oxide on nickel foam (N-rGO/NF) as the negative electrode, a hybrid supercapacitor was assembled and displayed good flexibility, cycling stability and high areal energy density of 130.4 μWh cm^{-2} at a power density of 1.6 mW cm^{-2}.

In conclusion, all of the findings in this thesis imply the promising potential application of Ni-based hydroxides composites for supercapacitors as energy storage devices and provide valuable highlights to the exploration of new composite materials for supercapacitor electrodes in future works (**Chapter 4**).

1.7 References

[1] X. Xiong, G. Waller, D. Ding, D. Chen, B. Rainwater, B. Zhao, Z. Wang, M. Liu, Controlled synthesis of $NiCo_2S_4$ nanostructured arrays on carbon fiber paper for high-performance pseudocapacitors, Nano Energy, 16 (2015) 71-80.

[2] N. Choudhary, C. Li, H.S. Chung, J. Moore, J. Thomas, Y. Jung, High-Performance One-Body Core/Shell Nanowire Supercapacitor Enabled by Conformal Growth of Capacitive 2D WS_2 Layers, ACS Nano, 10 (2016) 10726-10735.

[3] D. Du, X. Wu, S. Li, Y. Zhang, W. Xing, L. Li, Q. Xue, P. Bai, Z. Yan, Remarkable supercapacitor performance of petal-like LDHs vertically grown on graphene/polypyrrole nanoflakes, Journal of Materials Chemistry A, 5 (2017) 8964-8971.

[4] B. Wang, G.R. Williams, Z. Chang, M. Jiang, J. Liu, X. Lei, X. Sun, Hierarchical NiAl layered double hydroxide/multiwalled carbon nanotube/nickel foam electrodes with excellent pseudocapacitive properties, ACS Applied Materials & Interfaces, 6 (2014) 16304-16311.

[5] H. Pan, Y.-S. Hu, L. Chen, Room-temperature stationary sodium-ion batteries for large-scale electric energy storage, Energy & Environmental Science, 6 (2013) 2338.

[6] K.W. Wee, S.S. Choi, D.M. Vilathgamuwa, Design of a Least-Cost Battery-Supercapacitor Energy Storage System for Realizing Dispatchable Wind Power, IEEE Transactions on Sustainable Energy, 4 (2013) 786-796.

[7] A. Afzal, F.A. Abuilaiwi, A. Habib, M. Awais, S.B. Waje, M.A. Atieh,

Polypyrrole/carbon nanotube supercapacitors: Technological advances and challenges, Journal of Power Sources, 352 (2017) 174-186.

[8] J. Wang, Z. Wen, Y. Zi, P. Zhou, J. Lin, H. Guo, Y. Xu, Z.L. Wang, All-Plastic-Materials Based Self-Charging Power System Composed of Triboelectric Nanogenerators and Supercapacitors, Advanced Functional Materials, 26 (2016) 1070-1076.

[9] P. Simon, Y. Gogotsi, Materials for electrochemical capacitors, Nature Materials, 7 (2008) 845-854.

[10] M. Liang, M. Zhao, H. Wang, J. Shen, X. Song, Enhanced cycling stability of hierarchical $NiCo_2S_4$@$Ni(OH)_2$@PPy core–shell nanotube arrays for aqueous asymmetric supercapacitors, Journal of Materials Chemistry A, 6 (2018) 2482-2493.

[11] S.I. Kim, J.S. Lee, H.J. Ahn, H.K. Song, J.H. Jang, Facile route to an efficient NiO supercapacitor with a three-dimensional nanonetwork morphology, ACS Applied Materials & Interfaces, 5 (2013) 1596-1603.

[12] J. Liu, M. Zheng, X. Shi, H. Zeng, H. Xia, Amorphous FeOOH Quantum Dots Assembled Mesoporous Film Anchored on Graphene Nanosheets with Superior Electrochemical Performance for Supercapacitors, Advanced Functional Materials, 26 (2016) 919-930.

[13] Y.L. Liu, C. Yan, G.G. Wang, H.Y. Zhang, L.Y. Dang, B.W. Wu, Z.Q. Lin, X.S. An, J.C. Han, Achieving Ultrahigh Capacity with Self-Assembled $Ni(OH)_2$ Nanosheet-Decorated Hierarchical Flower-like $MnCo_2O_{4.5}$ Nanoneedles as Advanced Electrodes

of Battery-Supercapacitor Hybrid Devices, ACS Applied Materials & Interfaces, 11 (2019) 9984-9993.

[14] N. Choudhary, C. Li, J. Moore, N. Nagaiah, L. Zhai, Y. Jung, J. Thomas, Asymmetric Supercapacitor Electrodes and Devices, Advanced Materials, 29 (2017) 1605336.

[15] Y. Wu, W. Wang, J. Ming, M. Li, L. Xie, X. He, J. Wang, S. Liang, Y. Wu, An Exploration of New Energy Storage System: High Energy Density, High Safety, and Fast Charging Lithium Ion Battery, Advanced Functional Materials, 29 (2019) 1805978.

[16] P. Vialat, C. Mousty, C. Taviot-Gueho, G. Renaudin, H. Martinez, J.C. Dupin, E. Elkaim, F. Leroux, High-Performing Monometallic Cobalt Layered Double Hydroxide Supercapacitor with Defined Local Structure, Advanced Functional Materials, 24 (2014) 4831-4842.

[17] J. Zhao, J. Chen, S. Xu, M. Shao, Q. Zhang, F. Wei, J. Ma, M. Wei, D.G. Evans, X. Duan, Hierarchical NiMn Layered Double Hydroxide/Carbon Nanotubes Architecture with Superb Energy Density for Flexible Supercapacitors, Advanced Functional Materials, 24 (2014) 2938-2946.

[18] D.A.J. Rand, A journey on the electrochemical road to sustainability, Journal of Solid State Electrochemistry, 15 (2011) 1579-1622.

[19] I. Jiya, N. Gurusinghe, R. Gouws, Electrical Circuit Modelling of Double Layer Capacitors for Power Electronics and Energy Storage Applications: A Review, Electronics, 7 (2018) 268.

[20] K. Kuratani, H. Tanaka, T. Takeuchi, N. Takeichi, T. Kiyobayashi, N. Kuriyama, Binderless fabrication of amorphous RuO_2 electrode for electrochemical capacitor using spark plasma sintering technique, Journal of Power Sources, 191 (2009) 684-687.

[21] S. Wasterlain, A. Guven, H. Gualous, J. Fauvarque, R. Gallay, Hybrid power source with batteries and supercapacitor for vehicle applications, ESSCAP2006, (2006).

[22] D. Feng, T. Lei, M.R. Lukatskaya, J. Park, Z. Huang, M. Lee, L. Shaw, S. Chen, A.A. Yakovenko, A. Kulkarni, J. Xiao, K. Fredrickson, J.B. Tok, X. Zou, Y. Cui, Z. Bao, Robust and conductive two-dimensional metal−organic frameworks with exceptionally high volumetric and areal capacitance, Nature Energy, 3 (2018) 30-36.

[23] M.R. Lukatskaya, S. Kota, Z. Lin, M.Q. Zhao, N. Shpigel, M.D. Levi, J. Halim, P. L. Taberna, M.W. Barsoum, P. Simon, Y. Gogotsi, Ultra-high-rate pseudocapacitive energy storage in two-dimensional transition metal carbides, Nature Energy, 2 (2017) 17105.

[24] C. Xia, Z. Lin, Y. Zhou, C. Zhao, H. Liang, P. Rozier, Z. Wang, H.N. Alshareef, Large Intercalation Pseudocapacitance in 2D VO_2 (B): Breaking through the Kinetic Barrier, Advanced Materials, 30 (2018) e1803594.

[25] X. Mu, D. Wang, F. Du, G. Chen, C. Wang, Y. Wei, Y. Gogotsi, Y. Gao, Y. Dall'Agnese, Revealing the Pseudo-Intercalation Charge Storage Mechanism of MXenes in Acidic Electrolyte, Advanced Functional Materials, 29 (2019) 1902953.

[26] Y. Shao, M.F. El-Kady, J. Sun, Y. Li, Q. Zhang, M. Zhu, H. Wang, B. Dunn, R.B. Kaner, Design and Mechanisms of Asymmetric Supercapacitors, Chemical Reviews,

118 (2018) 9233-9280.

[27] Z. Niu, Y. Zhang, Y. Zhang, X. Lu, J. Liu, Enhanced electrochemical performance of three-dimensional graphene/carbon nanotube composite for supercapacitor application, Journal of Alloys and Compounds, 820 (2020) 153114.

[28] M. Serrapede, A. Rafique, M. Fontana, A. Zine, P. Rivolo, S. Bianco, L. Chetibi, E. Tresso, A. Lamberti, Fiber-shaped asymmetric supercapacitor exploiting rGO/Fe_2O_3 aerogel and electrodeposited MnO_x nanosheets on carbon fibers, Carbon, 144 (2019) 91-100.

[29] X. Lu, C. Shen, Z. Zhang, E. Barrios, L. Zhai, Core-Shell Composite Fibers for High-Performance Flexible Supercapacitor Electrodes, ACS Applied Materials & Interfaces, 10 (2018) 4041-4049.

[30] X. Chen, R. Paul, L. Dai, Carbon-based supercapacitors for efficient energy storage, National Science Review, 4 (2013) 453-489.

[31] J. Xu, X. Wang, X. Zhou, N. Yuan, S. Ge, J. Ding, Activated carbon coated CNT core-shell nanocomposite for supercapacitor electrode with excellent rate performance at low temperature, Electrochimica Acta, 301 (2019) 478-486.

[32] A. Volperts, G. Dobele, A. Zhurinsh, D. Vervikishko, E. Shkolnikov, J. Ozolinsh, Wood-based activated carbons for supercapacitor electrodes with a sulfuric acid electrolyte, Carbon, 124 (2017) 729.

[33] J. Zhang, G. Chen, Q. Zhang, F. Kang, B. You, Self-Assembly Synthesis of N-Doped Carbon Aerogels for Supercapacitor and Electrocatalytic Oxygen Reduction,

ACS Applied Materials & Interfaces, 7 (2015) 12760-12766.

[34] J. Guo, D. Wu, T. Wang, Y. Ma, P-doped hierarchical porous carbon aerogels derived from phenolic resins for high performance supercapacitor, Applied Surface Science, 475 (2019) 56-66.

[35] P. Hao, Z. Zhao, J. Tian, H. Li, Y. Sang, G. Yu, H. Cai, H. Liu, C.P. Wong, A. Umar, Hierarchical porous carbon aerogel derived from bagasse for high performance supercapacitor electrode, Nanoscale, 6 (2014) 12120-12129.

[36] L. Song, X. Cao, L. Li, Q. Wang, H. Ye, L. Gu, C. Mao, J. Song, S. Zhang, H. Niu, General Method for Large-Area Films of Carbon Nanomaterials and Application of a Self-Assembled Carbon Nanotube Film as a High-Performance Electrode Material for an All-Solid-State Supercapacitor, Advanced Functional Materials, 27 (2017) 1700474.

[37] S. Hussain, R. Amade, E. Jover, E. Bertran, Nitrogen plasma functionalization of carbon nanotubes for supercapacitor applications, Journal of Materials Science, 48 (2013) 7620-7628.

[38] M.P. Down, C.E. Banks, Freestanding Three-Dimensional Graphene Macroporous Supercapacitor, ACS Applied Energy Materials, 1 (2018) 891-899.

[39] Y. Shabangoli, M.S. Rahmanifar, M.F. El-Kady, A. Noori, M.F. Mousavi, R.B. Kaner, Thionine Functionalized 3D Graphene Aerogel: Combining Simplicity and Efficiency in Fabrication of a Metal-Free Redox Supercapacitor, Advanced Energy Materials, 8 (2018) 1802869.

[40] X.N. Tang, C.Z. Liu, X.R. Chen, Y.Q. Deng, X.H. Chen, J.J. Shao, Q.H. Yang,

Graphene aerogel derived by purification-free graphite oxide for high performance supercapacitor electrodes, Carbon, 146 (2019) 147-154.

[41] M.D. Stoller, C.W. Magnuson, Y. Zhu, S. Murali, J.W. Suk, R. Piner, R.S. Ruoff, Interfacial capacitance of single layer graphene, Energy & Environmental Science, 4 (2011) 4685.

[42] J. Zhu, A.S. Childress, M. Karakaya, S. Dandeliya, A. Srivastava, Y. Lin, A.M. Rao, R. Podila, Defect-Engineered Graphene for High-Energy- and High-Power-Density Supercapacitor Devices, Advanced Materials, 28 (2016) 7185-7192.

[43] A.G. Pandolfo, A.F. Hollenkamp, Carbon properties and their role in supercapacitors, Journal of Power Sources, 157 (2006) 11-27.

[44] T. Kshetri, D.T. Tran, D.C. Nguyen, N.H. Kim, K.T. Lau, J.H. Lee, Ternary graphene-carbon nanofibers-carbon nanotubes structure for hybrid supercapacitor, Chemical Engineering Journal, 380 (2020) 122543.

[45] T. Liu, C. Zhu, T. Kou, M.A. Worsley, F. Qian, C. Condes, E.B. Duoss, C.M. Spadaccini, Y. Li, Ion Intercalation Induced Capacitance Improvement for Graphene-Based Supercapacitor Electrodes, ChemNanoMat, 2 (2016) 635-641.

[46] D. Yang, C. Bock, Laser reduced graphene for supercapacitor applications, Journal of Power Sources, 337 (2017) 73-81.

[47] C. Zhu, T. Liu, F. Qian, T.Y. Han, E.B. Duoss, J.D. Kuntz, C.M. Spadaccini, M.A. Worsley, Y. Li, Supercapacitors Based on Three-Dimensional Hierarchical Graphene Aerogels with Periodic Macropores, Nano Letters, 16 (2016) 3448-3456.

[48] W. Huang, A. Zhang, X. Li, J. Tian, L. Yue, L. Cui, R. Zheng, D. Wei, J. Liu, Multilayer NiMn layered double hydroxide nanosheets covered porous Co3O4 nanowire arrays with hierarchical structure for high-performance supercapacitors, Journal of Power Sources, 440 (2019) 227123.

[49] C. Zhao, R. Wang, Y. Zhang, L. Chen, T. Li, X. Deng, P. Zhang, X. Lu, Electrostatic force-driven anchoring of $Ni(OH)_2$ nanocrystallites on single-layer MoS2 for high-performance asymmetric hybrid supercapacitors, Electrochimica Acta, 320 (2019) 134591.

[50] J. Huang, T. Lei, X. Wei, X. Liu, T. Liu, D. Cao, J. Yin, G. Wang, Effect of Al-doped β-$Ni(OH)_2$ nanosheets on electrochemical behaviors for high performance supercapacitor application, Journal of Power Sources, 232 (2013) 370-375.

[51] J. Qiu, Z. Bai, E. Dai, S. Liu, Y. Liu, NiO/Co_3O_4 nanoheterostructure derived from nickelocene filled ZIF-67 for supercapacitors, Journal of Alloys and Compounds, 763 (2018) 966-974.

[52] S.N.J. Syed Zainol Abidin, M.S. Mamat, S.A. Rasyid, Z. Zainal, Y. Sulaiman, Electropolymerization of poly(3,4-ethylenedioxythiophene) onto polyvinyl alcohol-graphene quantum dot-cobalt oxide nanofiber composite for high-performance supercapacitor, Electrochimica Acta, 261 (2018) 548-556.

[53] H. Luo, B. Wang, T. Liu, F. Jin, R. Liu, C. Xu, C. Wang, K. Ji, Y. Zhou, D. Wang, S. Dou, Hierarchical design of hollow Co-Ni LDH nanocages strung by MnO_2 nanowire with enhanced pseudocapacitive properties, Energy Storage Materials, 19 (2019) 370-

378.

[54] V. Augustyn, P. Simon, B. Dunn, Pseudocapacitive oxide materials for high-rate electrochemical energy storage, Energy & Environmental Science, 7 (2014) 1597.

[55] S. Zhang, J. Wu, J. Wang, W. Qiao, D. Long, L. Ling, Constructing T-Nb_2O_5@Carbon hollow core-shell nanostructures for high-rate hybrid supercapacitor, Journal of Power Sources, 396 (2018) 88-94.

[56] J. Zhai, Y. Wu, X. Zhao, Q. Yang, Facile preparation of flower-like hierarchical Nb_2O_5 microspheres self-assembled by nanorod for high-power anodes in advanced hybrid supercapacitor, Journal of Alloys and Compounds, 715 (2017) 275-283.

[57] K.V. Sankar, S.C. Lee, Y. Seo, C. Ray, S. Liu, A. Kundu, S.C. Jun, Binder-free cobalt phosphate one-dimensional nanograsses as ultrahigh-performance cathode material for hybrid supercapacitor applications, Journal of Power Sources, 373 (2018) 211-219.

[58] Q. Qin, D. Ou, C. Ye, L. Chen, B. Lan, J. Yan, Y. Wu, Systematic study on hybrid supercapacitor of Ni-Co layered double hydroxide//activated carbons, Electrochimica Acta, 305 (2019) 403-415.

[59] L. Chen, L. Chen, W. Zhai, D. Li, Y. Lin, S. Guo, J. Feng, L. Zhang, L. Song, P. Si, L. Ci, Tunable synthesis of $LixMnO_2$ nanowires for aqueous Li-ion hybrid supercapacitor with high rate capability and ultra-long cycle life, Journal of Power Sources, 413 (2019) 302-309.

[60] Z. Yu, M. McInnis, J. Calderon, S. Seal, L. Zhai, J. Thomas, Functionalized

graphene aerogel composites for high-performance asymmetric supercapacitors, Nano Energy, 11 (2015) 611-620.

[61] T.M. Masikhwa, M.J. Madito, A. Bello, J.K. Dangbegnon, N. Manyala, High performance asymmetric supercapacitor based on molybdenum disulphide/graphene foam and activated carbon from expanded graphite, Journal of Colloid and Interface Science, 488 (2017) 155-165.

[62] F. Su, M. Miao, Asymmetric carbon nanotube-MnO_2 two-ply yarn supercapacitors for wearable electronics, Nanotechnology, 25 (2014) 135401.

[63] J. Zhang, J. Jiang, H. Li, X.S. Zhao, A high-performance asymmetric supercapacitor fabricated with graphene-based electrodes, Energy & Environmental Science, 4 (2011) 4009.

[64] B. Li, F. Dai, Q. Xiao, L. Yang, J. Shen, C. Zhang, M. Cai, Nitrogen-doped activated carbon for a high energy hybrid supercapacitor, Energy & Environmental Science, 9 (2016) 102-106.

[65] R. Genc, M.O. Alas, E. Harputlu, S. Repp, N. Kremer, M. Castellano, S.G. Colak, K. Ocakoglu, E. Erdem, High-Capacitance Hybrid Supercapacitor Based on Multi-Colored Fluorescent Carbon-Dots, Scientific Reports, 7 (2017) 11222.

[66] R. Yi, S. Chen, J. Song, M.L. Gordin, A. Manivannan, D. Wang, High-Performance Hybrid Supercapacitor Enabled by a High-Rate Si-based Anode, Advanced Functional Materials, 24 (2014) 7433-7439.

[67] G. Yu, X. Xie, L. Pan, Z. Bao, Y. Cui, Hybrid nanostructured materials for high-

performance electrochemical capacitors, Nano Energy, 2 (2013) 213-234.

[68] L. Zhang, Y. Jiang, L. Wang, C. Zhang, S. Liu, Hierarchical porous carbon nanofibers as binder-free electrode for high-performance supercapacitor, Electrochimica Acta, 196 (2016) 189-196.

[69] D.N. Futaba, K. Hata, T. Yamada, T. Hiraoka, Y. Hayamizu, Y. Kakudate, O. Tanaike, H. Hatori, M. Yumura, S. Iijima, Shape-engineerable and highly densely packed single-walled carbon nanotubes and their application as super-capacitor electrodes, Nature Materials, 5 (2006) 987-994.

[70] G. Chen, S. Wu, L. Hui, Y. Zhao, J. Ye, Z. Tan, W. Zeng, Z. Tao, L. Yang, Y. Zhu, Assembling carbon quantum dots to a layered carbon for high-density supercapacitor electrodes, Scientific Reports, 6 (2016) 19028.

[71] N.M. Latiff, C.C. Mayorga-Martinez, L. Wang, Z. Sofer, A.C. Fisher, M. Pumera, Microwave irradiated N- and B,Cl-doped graphene: Oxidation method has strong influence on capacitive behavior, Applied Materials Today, 9 (2017) 204-211.

[72] K. Kakaei, E. Alidoust, G. Ghadimi, Synthesis of N- doped graphene nanosheets and its composite with urea choline chloride ionic liquid as a novel electrode for supercapacitor, Journal of Alloys and Compounds, 735 (2018) 1799-1806.

[73] B.K. Kim, S. Sy, A. Yu, J. Zhang, Electrochemical Supercapacitors for Energy Storage and Conversion, Handbook of Clean Energy Systems, (2015) 1-25.

[74] Q.J. Le, T. Wang, D.N.H. Tran, F. Dong, Y.X. Zhang, D. Losic, Morphology-controlled MnO_2 modified silicon diatoms for high-performance asymmetric

supercapacitors, Journal of Materials Chemistry A, 5 (2017) 10856-10865.

[75] F. Li, Y.X. Zhang, M. Huang, Y. Xing, L.L. Zhang, Rational Design of Porous MnO_2 Tubular Arrays via Facile and Templated Method for High Performance Supercapacitors, Electrochimica Acta, 154 (2015) 329-337.

[76] H. Xiao, F. Qu, X. Wu, Ultrathin NiO nanoflakes electrode materials for supercapacitors, Applied Surface Science, 360 (2016) 8-13.

[77] Q. Chen, J. Li, C. Liao, G. Hu, Y. Fu, O.K. Asare, S. Shi, Z. Liu, L. Zhou, L. Mai, Ni foam supported NiO nanosheets as high-performance free-standing electrodes for hybrid supercapacitors and Ni–Zn batteries, Journal of Materials Chemistry A, 6 (2018) 19488-19494.

[78] S.S. Raut, G.P. Patil, P.G. Chavan, B.R. Sankapal, Vertically aligned TiO_2 nanotubes: Highly stable electrochemical supercapacitor, Journal of Electroanalytical Chemistry, 780 (2016) 197-200.

[79] J.V. Patil, S.S. Mali, J.S. Shaikh, T.S. Bhat, C.K. Hong, J.H. Kim, P.S. Patil, Hydrothermally grown 3D hierarchical TiO_2 based on electrochemically anodized 1D TiO2 nanostructure for supercapacitor, Applied Physics A, 124 (2018) 592.

[80] X. Wang, A. Sumboja, M. Lin, J. Yan, P.S. Lee, Enhancing electrochemical reaction sites in nickel-cobalt layered double hydroxides on zinc tin oxide nanowires: a hybrid material for an asymmetric supercapacitor device, Nanoscale, 4 (2012) 7266-7272.

[81] L. Lv, K. Xu, C. Wang, H. Wan, Y. Ruan, J. Liu, R. Zou, L. Miao, K. Ostrikov, Y.

Lan, J. Jiang, Intercalation of Glucose in NiMn-Layered Double Hydroxide Nanosheets: an Effective Path Way towards Battery-type Electrodes with Enhanced Performance, Electrochimica Acta, 216 (2016) 35-43.

[82] G. Nagaraju, G.S. Raju, Y.H. Ko, J.S. Yu, Hierarchical Ni-Co layered double hydroxide nanosheets entrapped on conductive textile fibers: a cost-effective and flexible electrode for high-performance pseudocapacitors, Nanoscale, 8 (2016) 812-825.

[83] Y. Zhu, K. Shi, I. Zhitomirsky, Polypyrrole coated carbon nanotubes for supercapacitor devices with enhanced electrochemical performance, Journal of Power Sources, 268 (2014) 233-239.

[84] B. Yue, C. Wang, X. Ding, G.G. Wallace, Electrochemically synthesized stretchable polypyrrole/fabric electrodes for supercapacitor, Electrochimica Acta, 113 (2013) 17-22.

[85] D. Aradilla, D. Gaboriau, G. Bidan, P. Gentile, M. Boniface, D. Dubal, P. Gómez-Romero, J. Wimberg, T.J.S. Schubert, S. Sadki, An innovative 3-D nanoforest heterostructure made of polypyrrole coated silicon nanotrees for new high performance hybrid micro-supercapacitors, Journal of Materials Chemistry A, 3 (2015) 13978-13985.

[86] R.B. Ambade, S.B. Ambade, N.K. Shrestha, R.R. Salunkhe, W. Lee, S.S. Bagde, J.H. Kim, F.J. Stadler, Y. Yamauchi, S.-H. Lee, Controlled growth of polythiophene nanofibers in TiO_2 nanotube arrays for supercapacitor applications, Journal of Materials Chemistry A, 5 (2017) 172-180.

[87] Y. Li, M. Zhou, Y. Wang, Q. Pan, Q. Gong, Z. Xia, Y. Li, Remarkably enhanced

performances of novel polythiophene-grafting-graphene oxide composite via long alkoxy linkage for supercapacitor application, Carbon, 147 (2019) 519-531.

[88] V. Subramanian, C. Luo, A.M. Stephan, K.S. Nahm, S. Thomas, B. Wei, Supercapacitors from Activated Carbon Derived from Banana Fibers, The Journal of Physical Chemistry C, 111 (2007) 7527-7531.

[89] M. Zhi, F. Yang, F. Meng, M. Li, A. Manivannan, N. Wu, Effects of Pore Structure on Performance of An Activated-Carbon Supercapacitor Electrode Recycled from Scrap Waste Tires, ACS Sustainable Chemistry & Engineering, 2 (2014) 1592-1598.

[90] G. Wang, H. Wang, X. Lu, Y. Ling, M. Yu, T. Zhai, Y. Tong, Y. Li, Solid-state supercapacitor based on activated carbon cloths exhibits excellent rate capability, Advanced Materials, 26 (2014) 2676-2682, 2615.

[91] S. Hu, S. Zhang, N. Pan, Y.-L. Hsieh, High energy density supercapacitors from lignin derived submicron activated carbon fibers in aqueous electrolytes, Journal of Power Sources, 270 (2014) 106-112.

[92] Z. Wang, Y. Han, Y. Zeng, Y. Qie, Y. Wang, D. Zheng, X. Lu, Y. Tong, Activated carbon fiber paper with exceptional capacitive performance as a robust electrode for supercapacitors, Journal of Materials Chemistry A, 4 (2016) 5828-5833.

[93] S. Jiang, T. Shi, X. Zhan, H. Long, S. Xi, H. Hu, Z. Tang, High-performance all-solid-state flexible supercapacitors based on two-step activated carbon cloth, Journal of Power Sources, 272 (2014) 16-23.

[94] C. Niu, E.K. Sichel, R. Hoch, D. Moy, H. Tennent, High power electrochemical

capacitors based on carbon nanotube electrodes, Applied Physics Letters, 70 (1997) 1480-1482.

[95] M.M.J. Treacy, T.W. Ebbesen, J.M. Gibson, Exceptionally high Young's modulus observed for individual carbon nanotubes, Nature, 381 (1996) 678-680.

[96] T.W. Ebbesen, H.J. Lezec, H. Hiura, J.W. Bennett, H.F. Ghaemi, T. Thio, Electrical conductivity of individual carbon nanotubes, Nature, 382 (1996) 54-56.

[97] J. Zhang, Y. Wang, J. Zang, G. Xin, Y. Yuan, X. Qu, Electrophoretic deposition of MnO_2-coated carbon nanotubes on a graphite sheet as a flexible electrode for supercapacitors, Carbon, 50 (2012) 5196-5202.

[98] A. Izadi-Najafabadi, S. Yasuda, K. Kobashi, T. Yamada, D.N. Futaba, H. Hatori, M. Yumura, S. Iijima, K. Hata, Extracting the full potential of single-walled carbon nanotubes as durable supercapacitor electrodes operable at 4 V with high power and energy density, Advanced Materials, 22 (2010) E235-241.

[99] C. Liu, Z. Yu, D. Neff, A. Zhamu, B.Z. Jang, Graphene-Based Supercapacitor with an Ultrahigh Energy Density, Nano Letters, 10 (2010) 4863-4868.

[100] Y.B. Tan, J.M. Lee, Graphene for supercapacitor applications, Journal of Materials Chemistry A, 1 (2013) 14814.

[101] J. Wang, F. Ma, M. Sun, Graphene, hexagonal boron nitride, and their heterostructures: properties and applications, RSC Advances, 7 (2017) 16801-16822.

[102] R.H. Bradley, P. Pendleton, Structure, Chemistry and Energy of Carbon Surfaces, Adsorption Science & Technology, 31 (2013) 113-133.

[103] J.J. Yoo, K. Balakrishnan, J. Huang, V. Meunier, B.G. Sumpter, A. Srivastava, M. Conway, A.L. Reddy, J. Yu, R. Vajtai, P.M. Ajayan, Ultrathin planar graphene supercapacitors, Nano Letters, 11 (2011) 1423-1427.

[104] M.F. El-Kady, R.B. Kaner, Scalable fabrication of high-power graphene micro-supercapacitors for flexible and on-chip energy storage, Nature Communications, 4 (2013) 1475.

[105] F. Ouhib, A. Aqil, J.M. Thomassin, C. Malherbe, B. Gilbert, T. Svaldo-Lanero, A.S. Duwez, F. Deschamps, N. Job, A. Vlad, S. Melinte, C. Jérôme, C. Detrembleur, A facile and fast electrochemical route to produce functional few-layer graphene sheets for lithium battery anode application, Journal of Materials Chemistry A, 2 (2014) 15298-15302.

[106] F. Zhang, J. Tang, N. Shinya, L.C. Qin, Hybrid graphene electrodes for supercapacitors of high energy density, Chemical Physics Letters, 584 (2013) 124-129.

[107] M.D. Stoller, S. Park, Y. Zhu, J. An, R.S. Ruoff, Graphene-based ultracapacitors, Nano Letters, 8 (2008) 3498-3502.

[108] Y. Zhu, S. Murali, M.D. Stoller, K.J. Ganesh, W. Cai, P.J. Ferreira, A. Pirkle, R.M. Wallace, K.A. Cychosz, M. Thommes, D. Su, E.A. Stach, R.S. Ruoff, Carbon-based supercapacitors produced by activation of graphene, Science, 332 (2011) 1537-1541.

[109] H. Qiu, S. An, X. Sun, H. Yang, Y. Zhang, W. He, MWCNTs-GONRs/Co_3O_4@$Ni(OH)_2$ core-shell array structure with a high performance electrode for supercapacitor, Chemical Engineering Journal, 380 (2020) 122490.

[110] P. Wang, H. Zhou, C. Meng, Z. Wang, K. Akhtar, A. Yuan, Cyanometallic framework-derived hierarchical Co_3O_4-NiO/graphene foam as high-performance binder-free electrodes for supercapacitors, Chemical Engineering Journal, 369 (2019) 57-63.

[111] Z.S. Wu, D.W. Wang, W. Ren, J. Zhao, G. Zhou, F. Li, H.M. Cheng, Anchoring Hydrous RuO_2 on Graphene Sheets for High-Performance Electrochemical Capacitors, Advanced Functional Materials, 20 (2010) 3595-3602.

[112] J. Jiang, Y. Li, J. Liu, X. Huang, C. Yuan, X.W. Lou, Recent advances in metal oxide-based electrode architecture design for electrochemical energy storage, Advanced Materials, 24 (2012) 5166-5180.

[113] Y. Zhang, W.W. Guo, T.X. Zheng, Y.X. Zhang, X. Fan, Engineering hierarchical Diatom@CuO@MnO_2 hybrid for high performance supercapacitor, Applied Surface Science, 427 (2018) 1158-1165.

[114] Z.Q. Wen, M. Li, F. Li, S.J. Zhu, X.Y. Liu, Y.X. Zhang, T. Kumeria, D. Losic, Y. Gao, W. Zhang, S.X. He, Morphology-controlled MnO_2-graphene oxide-diatomaceous earth 3-dimensional (3D) composites for high-performance supercapacitors, Dalton Transactions, 45 (2016) 936-942.

[115] L. An, L. Yu, Y. Cao, W. Li, K. Xu, T. Ji, R. Zou, J. Hu, Hierarchical architectures of Co_3O_4 ultrafine nanowires grown on Co_3O_4 nanowires with fascinating electrochemical performance, New Journal of Chemistry, 40 (2016) 377-384.

[116] S.E. Moosavifard, M.F. El-Kady, M.S. Rahmanifar, R.B. Kaner, M.F. Mousavi,

Designing 3D highly ordered nanoporous CuO electrodes for high-performance asymmetric supercapacitors, ACS Applied Materials & Interfaces, 7 (2015) 4851-4860.

[117] Q. Wang, L. Jiao, H. Du, Y. Wang, H. Yuan, Fe_3O_4 nanoparticles grown on graphene as advanced electrode materials for supercapacitors, Journal of Power Sources, 245 (2014) 101-106.

[118] H. Fan, R. Niu, J. Duan, W. Liu, W. Shen, Fe_3O_4@Carbon Nanosheets for All-Solid-State Supercapacitor Electrodes, ACS Applied Materials & Interfaces, 8 (2016) 19475-19483.

[119] S. Zhu, L. Li, J. Liu, H. Wang, T. Wang, Y. Zhang, L. Zhang, R.S. Ruoff, F. Dong, Structural Directed Growth of Ultrathin Parallel Birnessite on beta-MnO_2 for High-Performance Asymmetric Supercapacitors, ACS Nano, 12 (2018) 1033-1042.

[120] Y. He, W. Chen, X. Li, Z. Zhang, J. Fu, C. Zhao, E. Xie, Freestanding Three-Dimensional Graphene/MnO_2 Composite Networks As Ultralight and Flexible Supercapacitor Electrodes, ACS Nano, 7 (2013) 174-182.

[121] R.A. Davoglio, G. Cabello, J.F. Marco, S.R. Biaggio, Synthesis and characterization of α-MnO_2 nanoneedles for electrochemical supercapacitors, Electrochimica Acta, 261 (2018) 428-435.

[122] E. Eustache, C. Douard, A. Demortière, V. De Andrade, M. Brachet, J. Le Bideau, T. Brousse, C. Lethien, High Areal Energy 3D-Interdigitated Micro-Supercapacitors in Aqueous and Ionic Liquid Electrolytes, Advanced Materials Technologies, 2 (2017) 1700126.

[123] J. Shin, J.K. Seo, R. Yaylian, A. Huang, Y.S. Meng, A review on mechanistic understanding of MnO_2 in aqueous electrolyte for electrical energy storage systems, International Materials Reviews, (2019) 1-32.

[124] H.Y. Lee, J.B. Goodenough, Supercapacitor Behavior with KCl Electrolyte, Journal of Solid State Chemistry, 144 (1999) 220-223.

[125] H. Xia, J. Feng, H. Wang, M.O. Lai, L. Lu, MnO_2 nanotube and nanowire arrays by electrochemical deposition for supercapacitors, Journal of Power Sources, 195 (2010) 4410-4413.

[126] Z. Yu, B. Duong, D. Abbitt, J. Thomas, Highly ordered MnO_2 nanopillars for enhanced supercapacitor performance, Advanced Materials, 25 (2013) 3302-3306.

[127] K. Xiao, J.W. Li, G.F. Chen, Z.Q. Liu, N. Li, Y.Z. Su, Amorphous MnO_2 supported on 3D-Ni nanodendrites for large areal capacitance supercapacitors, Electrochimica Acta, 149 (2014) 341-348.

[128] P. Lv, Y.Y. Feng, Y. Li, W. Feng, Carbon fabric-aligned carbon nanotube/MnO_2/conducting polymers ternary composite electrodes with high utilization and mass loading of MnO_2 for super-capacitors, Journal of Power Sources, 220 (2012) 160-168.

[129] A. Bahloul, B. Nessark, E. Briot, H. Groult, A. Mauger, K. Zaghib, C.M. Julien, Polypyrrole-covered MnO_2 as electrode material for supercapacitor, Journal of Power Sources, 240 (2013) 267-272.

[130] Q. Cheng, J. Tang, J. Ma, H. Zhang, N. Shinya, L.C. Qin, Graphene and

nanostructured MnO$_2$ composite electrodes for supercapacitors, Carbon, 49 (2011) 2917-2925.

[131] Z. Fan, J. Yan, T. Wei, L. Zhi, G. Ning, T. Li, F. Wei, Asymmetric Supercapacitors Based on Graphene/MnO$_2$ and Activated Carbon Nanofiber Electrodes with High Power and Energy Density, Advanced Functional Materials, 21 (2011) 2366-2375.

[132] T. Brousse, P.L. Taberna, O. Crosnier, R. Dugas, P. Guillemet, Y. Scudeller, Y. Zhou, F. Favier, D. Bélanger, P. Simon, Long-term cycling behavior of asymmetric activated carbon/MnO$_2$ aqueous electrochemical supercapacitor, Journal of Power Sources, 173 (2007) 633-641.

[133] W. Wang, Y. Liu, M. Wang, G. Ren, S. Wu, J. Shen, Facilely prepared oxidized carbon Fiber@Co$_3$O$_4$@RGO as negative electrode for a novel asymmetric supercapacitor with high areal energy and power density, Applied Surface Science, 450 (2018) 66-76.

[134] Q. Liao, N. Li, S. Jin, G. Yang, C. Wang, All-Solid-State Symmetric Supercapacitor Based on Co$_3$O$_4$ Nanoparticles on Vertically Aligned Graphene, ACS Nano, 9 (2015) 5310-5317.

[135] Y. Wang, T. Zhou, K. Jiang, P. Da, Z. Peng, J. Tang, B. Kong, W.B. Cai, Z. Yang, G. Zheng, Reduced Mesoporous Co$_3$O$_4$ Nanowires as Efficient Water Oxidation Electrocatalysts and Supercapacitor Electrodes, Advanced Energy Materials, 4 (2014) 1400696.

[136] T. Meng, Q.Q. Xu, Z.H. Wang, Y.T. Li, Z.M. Gao, X.Y. Xing, T.Z. Ren, Co$_3$O$_4$

Nanorods with Self-assembled Nanoparticles in Queue for Supercapacitor, Electrochimica Acta, 180 (2015) 104-111.

[137] K. Qiu, Y. Lu, J. Cheng, H. Yan, X. Hou, D. Zhang, M. Lu, X. Liu, Y. Luo, Ultrathin mesoporous Co_3O_4 nanosheets on Ni foam for high-performance supercapacitors, Electrochimica Acta, 157 (2015) 62-68.

[138] K. Deori, S.K. Ujjain, R.K. Sharma, S. Deka, Morphology controlled synthesis of nanoporous Co_3O_4 nanostructures and their charge storage characteristics in supercapacitors, ACS Applied Materials & Interfaces, 5 (2013) 10665-10672.

[139] C. Feng, J. Zhang, Y. He, C. Zhong, W. Hu, L. Liu, Y. Deng, Sub-3 nm Co_3O_4 Nanofilms with Enhanced Supercapacitor Properties, ACS Nano, 9 (2015) 1730-1739.

[140] J. Xu, L. Gao, J. Cao, W. Wang, Z. Chen, Preparation and electrochemical capacitance of cobalt oxide (Co_3O_4) nanotubes as supercapacitor material, Electrochimica Acta, 56 (2010) 732-736.

[141] X.H. Xia, J.P. Tu, Y.J. Mai, X.L. Wang, C.D. Gu, X.B. Zhao, Self-supported hydrothermal synthesized hollow Co_3O_4 nanowire arrays with high supercapacitor capacitance, Journal of Materials Chemistry, 21 (2011) 9319.

[142] X. Xiong, D. Ding, D. Chen, G. Waller, Y. Bu, Z. Wang, M. Liu, Three-dimensional ultrathin $Ni(OH)_2$ nanosheets grown on nickel foam for high-performance supercapacitors, Nano Energy, 11 (2015) 154-161.

[143] S. Wen, K. Qin, P. Liu, N. Zhao, C. Shi, L. Ma, E. Liu, Ultrafine $Ni(OH)_2$ nanoneedles on N-doped 3D rivet graphene film for high-performance asymmetric

supercapacitor, Journal of Alloys and Compounds, 783 (2019) 625-632.

[144] J. Yan, W. Sun, T. Wei, Q. Zhang, Z. Fan, F. Wei, Fabrication and electrochemical performances of hierarchical porous $Ni(OH)_2$ nanoflakes anchored on graphene sheets, Journal of Materials Chemistry, 22 (2012) 11494.

[145] H. Bode, K. Dehmelt, J. Witte, Zur kenntnis der nickelhydroxidelektrode-I.Über das nickel (II)-hydroxidhydrat, Electrochimica Acta, 11 (1966) 1079-1087.

[146] D.S. Hall, D.J. Lockwood, C. Bock, B.R. MacDougall, Nickel hydroxides and related materials: a review of their structures, synthesis and properties, Proceedings. Mathematical, Physical, and Engineering Sciences, 471 (2015) 20140792.

[147] P. Jeevanandam, Y. Koltypin, A. Gedanken, Synthesis of Nanosized α-Nickel Hydroxide by a Sonochemical Method, Nano Letters, 1 (2001) 263-266.

[148] J. Li, F. Luo, X. Tian, Y. Lei, H. Yuan, D. Xiao, A facile approach to synthesis coral-like nanoporous $β-Ni(OH)_2$ and its supercapacitor application, Journal of Power Sources, 243 (2013) 721-727.

[149] L. Aguilera, Y. Leyet, R. Peña-Garcia, E. Padrón-Hernández, R.R. Passos, L.A. Pocrifka, Cabbage-like $α-Ni(OH)_2$ with a good long-term cycling stability and high electrochemical performances for supercapacitor applications, Chemical Physics Letters, 677 (2017) 75-79.

[150] J. Yu, Q. Wang, D. O'Hare, L. Sun, Preparation of Two Dimensional Layered Double Hydroxide Nanosheets and Their Applications, Chemical Society Reviews, 46 (2017) 5950-5974.

[151] X. Ma, X. Li, A.D. Jagadale, X. Hao, A. Abudula, G. Guan, Fabrication of Cu(OH)$_2$@NiFe-layered double hydroxide catalyst array for electrochemical water splitting, International Journal of Hydrogen Energy, 41 (2016) 14553-14561.

[152] S. Wu, K.S. Hui, K.N. Hui, K.H. Kim, Electrostatic-Induced Assembly of Graphene-Encapsulated Carbon@Nickel-Aluminum Layered Double Hydroxide Core-Shell Spheres Hybrid Structure for High-Energy and High-Power-Density Asymmetric Supercapacitor, ACS Applied Materials & Interfaces, 9 (2017) 1395-1406.

[153] K. Fan, H. Chen, Y. Ji, H. Huang, P.M. Claesson, Q. Daniel, B. Philippe, H. Rensmo, F. Li, Y. Luo, L. Sun, Nickel-vanadium monolayer double hydroxide for efficient electrochemical water oxidation, Nature Communications, 7 (2016) 11981.

[154] Y. Zheng, J. Qiao, J. Yuan, J. Shen, A.-j. Wang, P. Gong, X. Weng, L. Niu, Three-dimensional NiCu layered double hydroxide nanosheets array on carbon cloth for enhanced oxygen evolution, Electrochimica Acta, 282 (2018) 735-742.

[155] J. Zhao, L. Cai, H. Li, X. Shi, X. Zheng, Stabilizing Silicon Photocathodes by Solution-Deposited Ni-Fe Layered Double Hydroxide for Efficient Hydrogen Evolution in Alkaline Media, ACS Energy Letters, 2 (2017) 1939-1946.

[156] G. Zhang, L. Wu, A. Tang, X.B. Chen, Y. Ma, Y. Long, P. Peng, X. Ding, H. Pan, F. Pan, Growth Behavior of MgAl-Layered Double Hydroxide Films by Conversion of Anodic Films on Magnesium Alloy AZ31 and Their Corrosion Protection, Applied Surface Science, 456 (2018) 419-429.

[157] M. Wu, B. Chang, T. T. Lim, W. D. Oh, J. Lei, J. Mi, High-Sulfur Capacity and

Regenerable Zn-Based Sorbents Derived from Layered Double Hydroxide for Hot Coal Gas Desulfurization, Journal of Hazardous Materials, 360 (2018) 391-401.

[158] G. Luo, K. S. Teh, Y. Xia, Z. Li, Y. Luo, L. Zhao, Z. Jiang, Construction of NiCo$_2$O$_4$@NiFe LDHs Core/Shell Nanowires Array on Carbon Cloth for Flexible, High-Performance Pseudocapacitor Electrodes, Journal of Alloys and Compounds, 767 (2018) 1126-1132.

[159] S. Yu, Y. Zhang, G. Lou, Y. Wu, X. Zhu, H. Chen, Z. Shen, S. Fu, B. Bao, L. Wu, Synthesis of NiMn-LDH Nanosheet@Ni$_3$S$_2$ Nanorod Hybrid Structures for Supercapacitor Electrode Materials with Ultrahigh Specific Capacitance, Scientific Reports, 8 (2018) 5246.

[160] G. Fan, F. Li, D.G. Evans, X. Duan, Catalytic applications of layered double hydroxides: recent advances and perspectives, Chemical Society Reviews, 43 (2014) 7040-7066.

[161] S.B. Kulkarni, A.D. Jagadale, V.S. Kumbhar, R.N. Bulakhe, S.S. Joshi, C.D. Lokhande, Potentiodynamic deposition of composition influenced Co$_{1-x}$Ni$_x$ LDHs thin film electrode for redox supercapacitors, International Journal of Hydrogen Energy, 38 (2013) 4046-4053.

[162] K. Teshima, Y. Inoue, H. Sugimura, O. Takai, Room-temperature deposition of high-purity silicon oxide films by RF plasma-enhanced CVD, Surface and Coatings Technology, 146-147 (2001) 451-456.

[163] C.R. Stoldt, C. Carraro, W.R. Ashurst, D. Gao, R.T. Howe, R. Maboudian, A low-

temperature CVD process for silicon carbide MEMS, Sensors and Actuators A: Physical, 97-98 (2002) 410-415.

[164] A. Kshirsagar, P. Nyaupane, D. Bodas, S.P. Duttagupta, S.A. Gangal, Deposition and characterization of low temperature silicon nitride films deposited by inductively coupled plasma CVD, Applied Surface Science, 257 (2011) 5052-5058.

[165] B. Rangarajan, A.Y. Kovalgin, K. Worhoff, J. Schmitz, Low-temperature deposition of high-quality silicon oxynitride films for CMOS-integrated optics, Optics Letters, 38 (2013) 941-943.

[166] H. Qian, A. Bismarck, E.S. Greenhalgh, M.S.P. Shaffer, Synthesis and characterisation of carbon nanotubes grown on silica fibres by injection CVD, Carbon, 48 (2010) 277-286.

[167] A. Kromka, O. Babchenko, T. Izak, K. Hruska, B. Rezek, Linear antenna microwave plasma CVD deposition of diamond films over large areas, Vacuum, 86 (2012) 776-779.

[168] M. Wang, S.K. Jang, W.J. Jang, M. Kim, S.Y. Park, S.W. Kim, S.J. Kahng, J.Y. Choi, R.S. Ruoff, Y.J. Song, S. Lee, A platform for large-scale graphene electronics-- CVD growth of single-layer graphene on CVD-grown hexagonal boron nitride, Advanced Materials, 25 (2013) 2746-2752.

[169] J. Wang, X. Song, R. li, J. Shen, G. Yang, H. Huang, Fluorocarbon thin film with superhydrophobic property prepared by pyrolysis of hexafluoropropylene oxide, Applied Surface Science, 258 (2012) 9782-9785.

[170] S. Tang, S. Gao, S. Wang, J. Wang, Q. Zhu, Y. Chen, X. Li, Characterization of CVD TiN coating at different deposition temperatures and its application in hydrocarbon pyrolysis, Surface and Coatings Technology, 258 (2014) 1060-1067.

[171] Y. He, X. Wang, H. Huang, P. Zhang, B. Chen, Z. Guo, In-situ electropolymerization of porous conducting polyaniline fibrous network for solid-state supercapacitor, Applied Surface Science, 469 (2019) 446-455.

[172] H.P. Cong, X.C. Ren, P. Wang, S.H. Yu, Flexible graphene–polyaniline composite paper for high-performance supercapacitor, Energy & Environmental Science, 6 (2013) 1185.

[173] N.H. Nabilah Azman, H.N. Lim, Y. Sulaiman, Effect of electropolymerization potential on the preparation of PEDOT/graphene oxide hybrid material for supercapacitor application, Electrochimica Acta, 188 (2016) 785-792.

[174] K. Shu, C. Wang, C. Zhao, Y. Ge, G.G. Wallace, A Free-standing Graphene-Polypyrrole Hybrid Paper via Electropolymerization with an Enhanced Areal Capacitance, Electrochimica Acta, 212 (2016) 561-571.

[175] Y. Tian, Y. Ruan, J. Zhang, Z. Yang, J. Jiang, C. Wang, Controllable growth of NiSe nanorod arrays via one-pot hydrothermal method for high areal-capacitance supercapacitors, Electrochimica Acta, 250 (2017) 327-334.

[176] A.J.C. Mary, A.C. Bose, Hydrothermal synthesis of Mn-doped $ZnCo_2O_4$ electrode material for high-performance supercapacitor, Applied Surface Science, 425 (2017) 201-211.

[177] A. Mohammadi, N. Arsalani, A.G. Tabrizi, S.E. Moosavifard, Z. Naqshbandi, L.S. Ghadimi, Engineering rGO-CNT wrapped Co_3S_4 nanocomposites for high-performance asymmetric supercapacitors, Chemical Engineering Journal, 334 (2018) 66-80.

[178] Y. Gogotsi, R.M. Penner, Energy Storage in Nanomaterials-Capacitive, Pseudocapacitive, or Battery-like?, ACS Nano, 12 (2018) 2081-2083.

[179] L. Xu, L. Zhang, B. Cheng, J. Yu, Rationally designed hierarchical $NiCo_2O_4$–C@$Ni(OH)_2$ core-shell nanofibers for high performance supercapacitors, Carbon, 152 (2019) 652-660.

[180] Y. Shao, M.F. El-Kady, C.W. Lin, G. Zhu, K.L. Marsh, J.Y. Hwang, Q. Zhang, Y. Li, H. Wang, R.B. Kaner, 3D Freeze-Casting of Cellular Graphene Films for Ultrahigh-Power-Density Supercapacitors, Advanced Materials, 28 (2016) 6719-6726.

CHAPTER 2

Layered Double Hydroxides (LDHs) for Hybrid Supercapacitors

2.1 Introduction

Layered Double Hydroxides (LDHs), also known as hydrotalcite-like compounds, are cationic 2D metal hydroxides intercalated with anions. The schematic structure of LDHs is illustrated in **Figure 2.1**, and their general formula can be expressed as $M^{2+}_{1-x}M^{3+}_{x}(OH)_2(A^{m-})_{x/m} \cdot nH_2O$, in which M^{2+} and M^{3+} correspond to the bivalent (Ni^{2+}, Co^{2+}, Cu^{2+}, Mg^{2+}, Mn^{2+}) and trivalent (Fe^{3+}, Al^{3+}, Co^{3+}, V^{3+}, Cr^{3+}) metal cations, respectively, A^{m-} represents the interlayer anion (CO_3^{2-}, NO_3^-, OH^-), $x = M^{3+}/(M^{2+} + M^{3+})$ is the surface charge and is generally in the range of 0.2~0.33, and n is the number of crystal water molecules [1, 2].
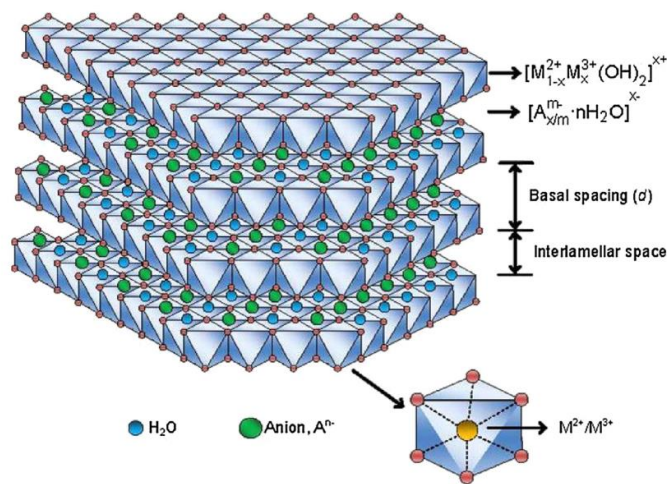

Figure 2.1: Schematic illustration of LDH structures [3].

From the structure above, we can see that positive charges are generated by partially replacing M^{2+} ions with M^{3+} ions in the hydroxide body layer, which can be balanced by anions located in the interlayer space of LDH. The hydrogen bonded water molecules occupy any free space between the layers. $[M(OH)_6]$ octahedra are formed by M ions octahedrally surrounded by hydroxyl groups, in which metal cations occupy the center of the octahedral edge with hydroxide ions at the vertices. More than two types of metal cations can be incorporated into the host layers to compound a single material [4, 5].

There are many approaches to prepare LDHs for various applications, and some representative examples are described below.

2.1.1   Synthesis methods and applications of LDHs

There are several common processing techniques that have been developed to synthesize LDHs such as hydrothermal/solvothermal, electrodeposition, co-precipitation and so on.

2.1.1.1   Hydrothermal/solvothermal synthesis

Hydrothermal and solvothermal techniques are the most widely used methods to obtain well-crystallized transition metal oxides, inorganic-organic hybrid materials and other ternary systems [6]. During the hydrothermal process, the reactants are heated in pressurized aqueous media to obtain LDHs with improved crystalline structure, whereas the reactants are heated in non-aqueous (solvent other than water) under

relatively higher temperatures during the solvothermal synthesis.

Herein, we summarize some common LDHs-based hybrids using hydrothermal/solvothermal synthesis processes and the corresponding applications (**Table 2.1**).

Table 2.1. Representative LDH-based materials with hydrothermal/solvothermal synthesis methods and their applications.

Materials	Synthesis method	Applications	Ref.
Ni-Co LDH	Hydrothermal (180 $^\circ$C, 24 h)	Supercapacitors	[7]
NiFe-LDH nanolates	Hydrothermal (120 $^\circ$C, 12 h)	Oxygen evolution reaction	[8]
rGO/NiAl-LDH	Hydrothermal (120 $^\circ$C, 24 h)	Adsorbents (uranium (VI))	[9]
NiCo-LDH/Co$_9$S$_8$ hybrid	Hydrothermal (120 $^\circ$C, 2 h)	Supercapacitors/ Hydrogen evolution reaction	[10]
NiV LDH	Hydrothermal (120 $^\circ$C, 12 h)	Supercapacitors	[11]
CoAl-LDH/NF	Hydrothermal (120 $^\circ$C, 6 h)	Supercapacitors	[12]
Mg-Al LDH	Hydrothermal (200 $^\circ$C, 20 h)	Adsorbents (methyl orange)	[13]
Fe-Cu-LDH/biochar	Hydrothermal (90 $^\circ$C, 24 h)	Catalysts	[14]
Zn/Al LDHs	Hydrothermal (75 $^\circ$C, 24 h)	/	[15]
NiCoAl LDH/CNT	Solvothermal	NiZn battery	[16]

	(120 °C, 12 h+180 °C, 8 h)		
Ni-Fe LDH/graphene	Solvothermal (150 °C, 48 h)	Reducing fire hazard	[17]
Li/Al LDHs	Solvothermal (150 °C, 12 h)	Supercapacitors/Lithium ion batteries	[18]

2.1.1.2   Electrodeposition

Electrodeposition is a time-saving and convenient method to synthesize LDHs. Typically, the electrodeposition experiments are normally performed in a three-electrode electrochemical configuration in an electrolytic cell to control and monitor the deposition experiments. The electrolytic cell is composed of electrolyte, working electrode (substrate), counter and reference electrodes. It is assumed that the electrode/electrolyte interface is inert in this cell, and redox reaction in the cell is driven by external voltage/current, which is controlled by a potentiostat.

Generally, electrodeposition was developed using nitrate or sulfate solutions containing appropriate metal ions. The deposition can be achieved by reducing nitrate or sulfate ions to generate hydroxide ions that elevate the local pH on the working electrode, resulting in the precipitation of the corresponding LDHs:

$$NO_3^- + H_2O + 2e^- \rightarrow NO_2^- + 2OH^-$$

$$SO_4^{2-} + H_2O + 2e^- \rightarrow SO_3^{2-} + 2OH^-$$
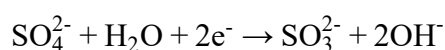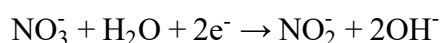
Herein, we summarize some common LDHs-based hybrids prepared using electrodeposition process and the corresponding applications (**Table 2.2**).

Table 2.2. Representative LDH-based materials obtained through electrodeposition method and their applications.

Materials	Conditions	Applications	Ref.
CuO@CoFe LDH	-1 V *vs.* SCE, 0-200 s	micro-supercapacitor	[19]
ZnO@CoNi-LDH	-1 V *vs.* Ag/AgCl, 30-300 s	Photoelectrochemical water splitting	[20]
Co/Al-LDH films	-0.9 V *vs.* SCE, 5-60 s	Supercapacitors	[21]
Au@ErGO@ECoNi LDH	-1 V *vs.* Ag/AgCl, 120 s	Supercapacitors	[22]
NiFeAl-LDHs	-1 V *vs.* SCE, 300 s	Oxygen evolution reaction	[23]
Zn/Al LDH film	-0.9 V, 40-120 s	Sensors	[24]
ZnCo-LDH	-1 V *vs.* Ag/AgCl, 50-180 s	Oxygen evolution reaction	[25]

2.1.1.3 Co-precipitation method

Co-precipitation is the most common method for the preparation of LDHs, in which inorganic salts are placed in an alkaline medium at constant or increasing pH. The morphology and particle size distribution of the materials can be tuned by controlling the evaporation rate or varying the pH. **Table 2.3** summarizes some common LDHs-based hybrids synthesized by co-precipitation and their corresponding applications (**Table 2.3**).

Table 2.3. Representative LDH-based materials prepared by co-precipitation method and their applications.

Materials	Conditions	Applications	Ref.
NiMn-LDH/CNT	Room temperature, 12 h	Supercapacitors	[26]

Mg$_2$Al LDH	Room temperature, 24 h	Adsorbents (Pb(II))	[27]
CoMn-LDH/carbon fibers	Room temperature, 24 h	Supercapacitors	[28]
CoAl-LDH/grapnene	95 °C, 48 h	Supercapacitors	[29]
MgAl-LDH films	/	Corrosion protection	[30]
RGO/NiAl LDH	95 °C, 6 h	Flame retardant materials	[31]
Zn-Ti LDHs	130 °C, 48 h	Photocatalysis	[32]
Ni-Mn LDH/rGO Co-Mn LDH/rGO	Room temperature, 2 h	Supercapacitors	[33]
Fe-Al LDHs	65 °C, 15, 30, 60, 90 min	Adsorbents (bromate)	[34]
Mg-Al LDHs	40 °C, 2 h	CO$_2$ capture	[35]

2.1.1.4 Other methods

There are some other common methods to prepare LDHs such as templating methods and urea synthesis. For example, Liu *et al*. used a metal-organic framework as a sacrificial templating precursor to derive CoMn LDHs from different manganese solutions [36]. Jaiswal *et al*. synthesized CoBi layered double hydroxides (LDHs) *via* urea hydrolysis method, in which the use of urea instead of NaOH as a precipitating agent is obviously advantageous because during the precipitation reaction, lower degree of super-saturation is achieved. Hydrolysis of urea proceeds in two steps:

Step 1 (rate determining step):

$$CO(NH_2)_2 \rightarrow NH_4CNO \text{ (ammonium cyanate)}$$

Step 2 (hydrolysis of ammonium cyanate):

$$NH_4CNO + 2H_2O \rightarrow 2NH_4^+ + CO_3^{2-}$$
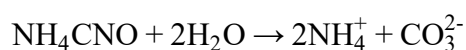
The pH of about 9 is achieved during step 2, which is suitable for precipitating out a large number of metal hydroxides. The compounds having a high charge density are difficult to produce with other methods, but can be synthesized by urea method easily

2.1.2 Applications of LDHs in supercapacitors

Benefiting from their unique structural and compositional merits such as layered structure, high redox activity, tunable composition, environmentally friendly nature and the flexibility of incorporating mixed valence transition metal ions into the LDH structure in different compositions, LDHs have drawn extensive research attention in the field of supercapacitors. As electrode materials, LDHs with a lamellar structure provide a large specific surface area, a high number of active sites, and a shortened diffusion distance that is beneficial to ions to transfer from the electrolyte to the surface of the active material quickly due to the ultrathin thickness of the nanosheets. Besides, tunable metal cation compositions in the LDH host layers, such as Ni^{2+}, Co^{2+}, or Mn^{2+} enable multiple redox states to greatly improve the capacitive performance. From the view of composition of LDHs, we divided them into Ni-based LDHs, Co-based LDHs and others.

2.1.2.1 Ni-based LDHs

Due to the plentiful oxidation states, Ni, as a transition metal element, was universally applied as electrode material. Typically, the reaction of Ni-based LDHs in alkaline electrolyte can be described using **Equation 2.1**:

$$\text{Ni(OH)}_2 + \text{OH}^- \leftrightarrows \text{NiOOH} + \text{H}_2\text{O} + \text{e}^- \qquad \text{(Eq. 2.1)}$$

In this work, some common Ni-LDHs-based hybrids and their electrochemical supercapacitor performance are summarized in **Table 2.4**.

Table 2.4. Representative Ni-based LDHs materials and their electrochemical supercapacitor performance.
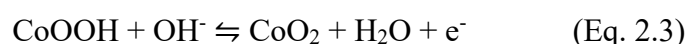
Materials	Specific capacity	Cycle stability	Electrolyte	Ref.
Ni-V LDH/carbon cloth	1226 C g^{-1} / 1 A g^{-1}	75% (2000 cycles)	2 M KOH	[37]
Ni/Al LDH/graphene	286 C cm^{-3} / 1 mA cm^{-2}	88.1% (1000 cycles)	6 M KOH	[38]
NiMn-LDH/Ni foam (NF)	680 C g^{-1} / 2.5 A g^{-1}	92.8% (3000 cycles)	1 M KOH	[39]
NiCo$_2$O$_4$@NiFe LDHs	464 C g^{-1} / 1 A g^{-1}	79% (1000 cycles)	2 M KOH	[40]
Ni-Zn-Fe LDH	653.5 C g^{-1} / 5 mV s^{-1}	95% (1000 cycles)	6 M KOH	[41]
rGO@NiMn-LDH@NF	932.8 C g^{-1} / 1 A g^{-1}	95% (5000 cycles)	3 M KOH	[42]
NiCo LDH/NF	1341 C g^{-1} / 3 A g^{-1}	/	1 M KOH	[7]
rGO@ZIF-67@NiCoAl-LDHs	2291.6 F g^{-1} / 1 A g^{-1}	92% (2000 cycles)	1 M KOH	[43]
NiO@NiMn-LDH/NF	468.5 C g^{-1} / 0.5 A g^{-1}	91% (1000 cycles)	3 M KOH	[44]
NiAl-LDH	631.2 C g^{-1} / 1 A g^{-1}	93.75% (10000 cycles)	6 M KOH	[45]
Ni-Fe LDH/graphene	538.2 C g^{-1} / 1 A g^{-1}	80% (2000 cycles)	6 M KOH	[46]

hybrid aerogel				
fgC$_3$N$_4$-rGO/NiAl LDH	595 C g^{-1} / 1 A g^{-1}	90% (3000 cycles)	6 M KOH	[47]
NiTi-LDH films	10.37 F cm^{-2} / 5 mA cm^{-2}	86% (1000 cycles)	1 M KOH	[48]

From **Table 2.4**, we can see that as battery-like pseudocapacitive electrodes, Ni-based LDHs exhibit a great specific capacity. For example, Liu *et al*. prepared 2D hierarchical NiO/NiMn-LDH nanosheet arrays for supercapacitors with a high specific capacitance of 468.5 C g^{-1} at 0.5 A g^{-1} [44]. Bandyopadhyay *et al*. synthesized graphitic carbon nitride modified graphene/Ni-Al LDH (fgC$_3$N$_4$-rGO/NiAl LDH) for supercapacitors, generating a specific capacity value of 595 C g^{-1} at 1 A g^{-1} [47]. All of these results reveal the potential application of Ni-based LDHs electrode materials.

2.1.2.2   Co-based LDHs

Besides Ni-based LDHs, Co-based LDHs also received extensive attention as electrode candidates for supercapacitors due to plentiful oxidation states of Co. The reactions for Co-based LDHs in alkaline electrolyte can be illustrated by **Equations 2.2** and **2.3**:

$$Co(OH)_2 + OH^- \leftrightharpoons CoOOH + H_2O + e^- \quad \text{(Eq. 2.2)}$$

$$CoOOH + OH^- \leftrightharpoons CoO_2 + H_2O + e^- \quad \text{(Eq. 2.3)}$$

Some representative Co-LDHs-based hybrids and their electrochemical supercapacitor performance are summarized in **Table 2.5**.

Table 2.5. Representative Co-based LDHs materials and their electrochemical

supercapacitor performance.

Materials	Specific capacity	Cycle stability	Electrolyte	Ref.
GO@CoAl LDH	604 C g^{-1} at 1 A g^{-1}	95% (5000 cycles)	6 M KOH	[49]
CoCr-LDHs	182.5 C g^{-1} at 0.5 A g^{-1}	80% (1000 cycles)	1 M KOH	[50]
CoMn LDH/NF	915.85 C g^{-1} at 1 A g^{-1}	93.2% (3000 cycles)	1 M LiOH	[51]
CoAlNi LDH	669.8 C g^{-1} at 1 A g^{-1}	82.2% (3000 cycles)	1 M KOH	[52]
Co$_3$O$_4$@CoNi-LDH/NF	1338.45 C g^{-1} at 0.5 A g^{-1}	67.7% (10000 cycles)	2 M KOH	[53]
CoFe-LDH/multi-layer graphene	353 C g^{-1} at 1 A g^{-1}	36.8% (5000 cycles)	2 M KOH	[54]
CoMn-LDH	582.07 mC cm^{-2} at 2 mA cm^{-2}	77% (5000 cycles)	1 M KOH	[36]
Co^{II}Co^{III}–CO$_3$ LDH	150.75 C g^{-1} at 1 A g^{-1}	85% (300 cycles)	0.1 M KOH	[55]
NiCo$_2$O$_4$@Co-Fe LDH/NF	623 C g^{-1} at 1 A g^{-1}	/	2 M KOH	[56]
MnCo LDH	229.95 C g^{-1} at 2 A g^{-1}	91.6% (2000 cycles)	2 M KOH	[57]
Co-LDH/graphene	76.4 F cm^{-3} at 2 A g^{-1}	90.4% (10000 cycles)	1 M KOH	[58]
Zn-Co LDH	270 mA h g^{-1} at 1 A g^{-1}	97% (1000 cycles)	1 M KOH	[59]
Zn$_1$Co$_2$-LDH@rGO/NF	1071 C g^{-1} at 1 A g^{-1}	90.9% (6000 cycles)	2 M KOH	[60]
Mg-Co-Al-LDH	247.85 C g^{-1} at 1 A g^{-1}	86.32% (10000	1 M KOH	[61]

Materials				
		cycles)		

2.1.2.3 Other materials

There are also many LDHs consisting of other transition metal ions besides Ni and Co ions, which are investigated as electrodes for supercapacitors. Some representative examples and their electrochemical supercapacitor performance are summarized in **Table 2.6**.

Table 2.6. Representative LDHs electrodes without Ni and Co ions and their electrochemical supercapacitor performance.

Materials	Spercific Capacity	Cycle stability	Electrolyte	Ref.
RGO@MgAl LDH	1067.2 C g^{-1} at 1 A g^{-1}	87% (10000 cycles)	1 M KOH	[62]
Ni-foam@Cu-Al LDH/g-C$_3$N$_4$	415.9 C g^{-1} at 0.4 A g^{-1}	92.71% (5000 cycles)	6 M KOH	[63]
CuAl-LDH/CoWO$_4$	337.5 C g^{-1} at 5 A g^{-1}	95.1% (5000 cycles)	2 M LiOH	[64]

In this thesis, we focused on the preparation of Ni-based LDHs electrode materials. First of all, NiFe LDHs deposited on reduced graphene oxide (rGO) supported by nickel foam (NF) skeleton (NiFe LDHs/rGO/NF) was prepared by electrodeposition method. In the second part of this chapter, we describe the synthesis of NiAl LDHs, NiFe LDHs and NiCr LDHs on carbon spheres coated on NF skeleton by hydrothermal method. In the third section of this chapter, a ternary NiMnCr LDHs-carbon spheres modified Ni

foam (NiMnCr LDHs@CS/NF) nanocomposite was prepared using a hydrothermal process. All the synthesized materials were characterized using various techniques to establish their morphology, structure and chemical composition. As positive electrode candidates for hybrid supercapacitors, their electrochemical performances were further investigated.

2.2 NiFe Layered Double Hydroxides

Herein, we prepared new 3D composite materials by combining NiFe LDHs and nickel foam (NiFe LDHs/NF) *via* a facile and eco-friendly electrochemical method. Fe^{3+} was employed in the LDH composites, because compared to most metals such as cobalt and aluminum, iron is much cheaper and more abundant. In order to further improve the conductivity of the composite, NF was electrochemically coated with reduced graphene oxide (rGO) prior to NiFe LDHs electrodeposition to produce NiFe LDHs/rGO/NF composite material. The electrochemical properties of the obtained materials were investigated using cyclic voltammetry (CV), galvanostatic charge/discharge (GCD) curves and impedance spectroscopy measurements. Moreover, using the as-prepared battery-like electrode as a positive electrode, a flexible hybrid supercapacitor device was constructed with mesoporous carbon (MC) coated on NF as a negative electrode. All the details will be discussed in the following sections.

2.2.1 Experimental section

2.2.1.1 Preparation of graphene oxide (GO)

Graphene oxide (GO) was synthesized by the improved Hummers' method [65]. Typically, to a mixture of graphite flakes (1 g) and $KMnO_4$ (6 g) was added a 9:1 (volume) mixture of concentrated H_2SO_4/H_3PO_4 (40:13.3 mL) and allowed to react at about 50 °C under continuous stirring for 12 h. The reaction was cooled to room temperature, followed by adding ice (~100 mL) and 1 mL of 30% H_2O_2. Then, the mixture was centrifuged at 4500 rpm for 40 min, washed successively with 200 mL of

30% HCl, 200 mL of water, and 200 mL of ethanol. Finally, the obtained precipitate was vacuum-dried at room temperature.

2.2.1.2 Preparation of NiFe LDHs/NF

NiFe LDHs were electrochemically deposited onto the surface of nickel foam (NF) using different molar ratios: 5:0, 4:1, 3:2, 1:1, 2:3, 1:4, 0:5 of $Ni(NO_3)_2 \cdot 6H_2O$ and $Fe(NO_3)_3 \cdot 9H_2O$; the overall molar concentration was 50 mM. Nickel foam (NF) acts as the working electrode; the counter and the reference electrodes are platinum foil and saturated calomel electrode (SCE), respectively. Typically, the potentiostatic deposition was performed at -1.2V *vs.* SCE for 10 s to form NiFe LDHs/NF. Different NiFe LDHs/NF electrodes were successfully prepared and samples with different $Ni(NO_3)_2 \cdot 6H_2O$ and $Fe(NO_3)_3 \cdot 9H_2O$ molar ratios of 5:0, 4:1, 3:2, 1:1, 2:3, 1:4, 0:5 were named as S_0, S_1, S_2, S_3, S_4, S_5, S_6, respectively. All the synthesized samples were washed with water and ethanol, and further dried at 60 °C for 6 h.

2.2.1.3 Preparation of reduced graphene oxide coated nickel foam (rGO/NF)

To improve the conductivity of the electrode, reduced graphene oxide (rGO) was first coated on NF by the electrodeposition method. Typically, 0.1 M $LiClO_4$ aqueous solution containing 1.5 mg mL^{-1} of graphene oxide (GO) was used as the electrolyte for graphene electrodeposition to obtain rGO/NF. The deposition of reduced graphene oxide (rGO) was carried out by a potentiostatic method at a constant potential of -1.2 V *vs.* SCE for 600 s. Then, the resulting black sample was washed with water for several

times.

2.2.1.4   Preparation of NiFe LDHs/rGO/NF

A two-step electrodeposition process was used to synthesize NiFe LDHs/rGO/NF

nanocomposite. First, rGO/NF was prepared using the same method mentioned above,

followed by NiFe LDH electrodeposition using $Ni(NO_3)_2 \cdot 6H_2O$ and $Fe(NO_3)_3 \cdot 9H_2O$ at

a molar ratio of 1:4 under constant potential of -1.2 V *vs.* SCE for 10 s to produce NiFe

LDHs/rGO/NF, represented by S_7. Additionally, S_8 and S_9 were also prepared using

different deposition times of 20 s and 30 s, respectively.
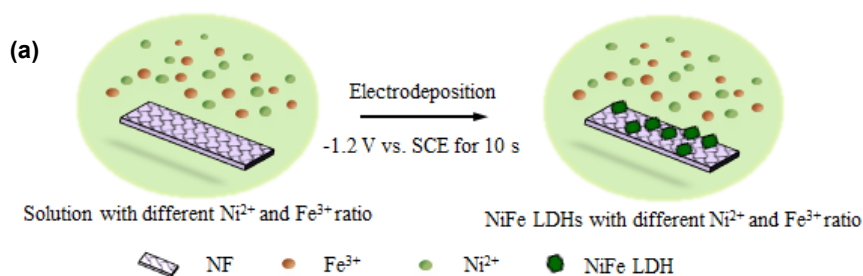
2.2.1.5 Fabrication of an asymmetric supercapacitor

A hybrid supercapacitor device was assembled using the as-prepared NiFe

LDHs/rGO/NF (S_7, 1 cm×1 cm) as the positive electrode and mesoporous carbon

(MC)/NF as the negative electrode, with the separator consisting of a filter paper soaked

into 2 M KOH solution for 30 min.

To acquire the optimal performance of the hybrid supercapacitor, a charge balance

Q_+ (charges stored in the positive electrode) = Q_- (charges stored in the negative

electrode) between the two electrodes is conducted according to **Equation 1.6**. The

optimal mass ratio is ~0.04, but it is difficult to control the accurate mass of MC when

mixing and pressing MC powder with auxiliary materials such as carbon black or binder

onto the Ni foam. Therefore, the mass loadings of NiFe LDHs/rGO/NF and MC on Ni

foam are 0.8 and 10.1 mg, respectively, which corresponds to a mass ratio of 0.08 in

our work.

Electrochemical characterization was performed in a 2-electrode system.

2.2.2 Results and discussion

The procedures for the preparation of NiFe LDHs/NF and NiFe LDHs/rGO/NF are schematically illustrated in **Figure 2.1**. NiFe LDHs/NF and NiFe LDHs/rGO/NF composites were successfully prepared through electrodeposition method. For NiFe LDHs/NF, different molar ratios of $Ni(NO_3)_2 \cdot 6H_2O$ and $Fe(NO_3)_3 \cdot 9H_2O$ (5:0, 4:1, 3:2, 1:1, 2:3, 1:4, 0:5) were investigated during the electrochemical deposition onto the surface of NF to achieve the best performance. Similarly, for the synthesis NiFe LDHs/rGO/NF composite (**Figure 2.1b**), graphene oxide (GO) was first electrochemically reduced into rGO under a constant potential of -1.2 V *vs.* SCE for 600 s, followed by uniform deposition of NiFe LDHs onto rGO/NF using a 4:1 molar ratio of $Ni(NO_3)_2 \cdot 6H_2O$ and $Fe(NO_3)_3 \cdot 9H_2O$. This ratio gave the best electrochemical performance in NiFe LDHs/ NF composite (**Figure 2.1a**). The prepared nanocomposite electrode materials were characterized using various techniques.
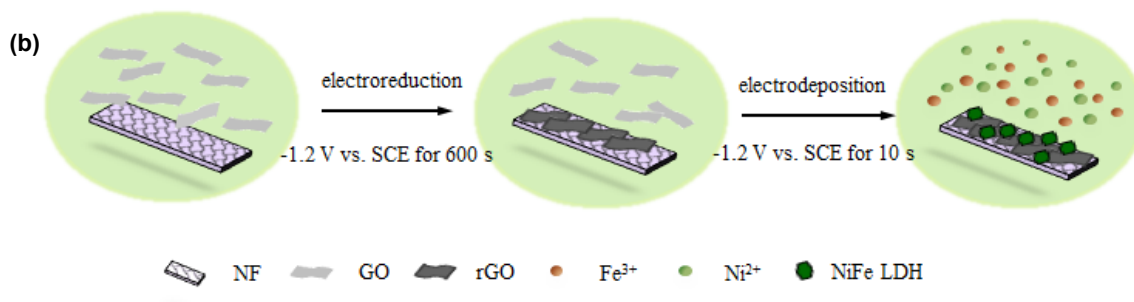

95

(b)

electroreduction
-1.2 V vs. SCE for 600 s

electrodeposition
-1.2 V vs. SCE for 10 s

NF   GO   rGO Fe^{3+} Ni^{2+} NiFe LDH

Figure 2.1: Synthesis of (a) NiFe LDHs/NF and (b) NiFe LDHs/rGO/NF using the electrochemical deposition.

The SEM images indicate that NiFe LDHs/NF, obtained at different precursor ratios, have similar morphologies (**Figure 2.2**). In the absence of Fe^{3+}, the as-obtained $Ni(OH)_2$ consists of a monolayer of nanosheets. With the increase of Fe^{3+} concentration, NiFe LDHs loading on the NF becomes denser, most likely due to partial replacement of Ni^{2+} by Fe^{3+}, which can restrain the self-aggregation of double hydroxide layers by electrostatic interaction and lead to an expansion in the dimension along layer stacking direction, yielding a high dispersion of Ni unit and denser nanosheets of the samples [66]. In particular, when the molar ratio of Ni and Fe precursors is 1:4 (**Fig. 2.2f**), intertwined caterpillar-like NiFe LDHs bridges on NF appear, consisting of lots of nanosheets, which could act as a reservoir for the electrolyte and shorten the ion transport distance. Additionally, the interconnected skeletons ensure more superficial electroactive species and preferential electrolyte ion transport. As illustrated in **Figure 2.2g**, $Fe(OH)_3$ (NiFe LDHs without Ni precursor) morphology corresponds also to an interlaced bridge; however, its structure is more tight and there are no decorated nanosheet branches. For the NiFe LDH/rGO/NF, rGO was successfully deposited on

the NF, with NiFe LDHs coating (**Fig. 2.2h**). The participation of rGO could further

facilitate the electron transport and provide a better charge transfer kinetics and an
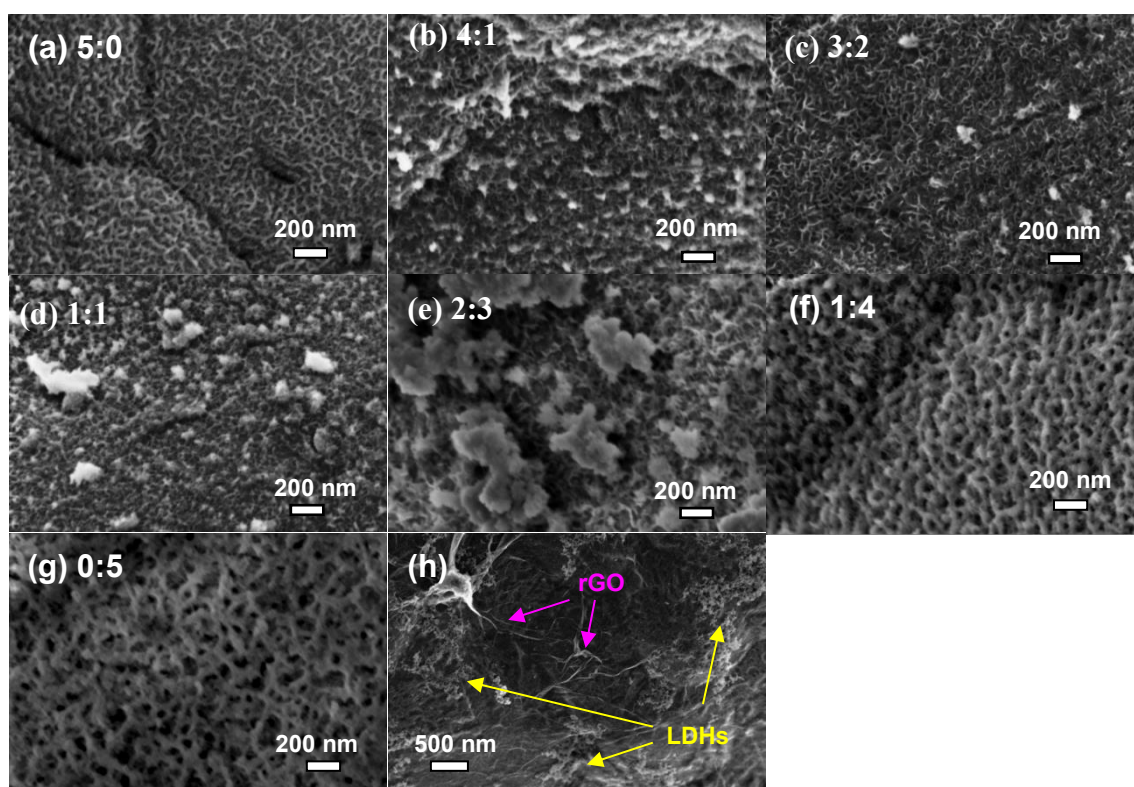
enhanced electrochemical capacity [67].

Figure 2.2: SEM images of the samples deposited using $Ni(NO_3)_2 \cdot 6H_2O$ and

$Fe(NO_3)_3 \cdot 9H_2O$ molar ratios of 5:0 (S_0) (a), 4:1 (S_1) (b), 3:2 (S_2) (c), 1:1 (S_3) (d) , 2:3

(S_4) (e) and 1:4 (S_5) (f) and 0:5 S_6 (g). (h) SEM image of NiFe LDHs/rGO/NF (S_7)

obtained through electrodeposition using $Ni(NO_3)_2 \cdot 6H_2O$ and $Fe(NO_3)_3 \cdot 9H_2O$ at a

molar ratio of 1:4 under constant potential of -1.2 V *vs.* SCE for 10 s.

X-ray photoelectron spectroscopy (XPS) survey scan confirmed the existence of

both Ni_{2p} and Fe_{2p} elements in NiFe LDHs/NF (S_5) (**Figure 2.3a**) and NiFe

LDHs/rGO/NF (S_7) (**Figure 2.4a**) along with O_{1s} and C_{1s}. The elemental compositions of the samples are displayed in **Table 2.7**.

Table 2.7: Elemental composition of the samples.

Elements (at%) Composites	Ni_{2p}	Fe_{2p}	C_{1s}	O_{1s}
NiFe LDHs/NF (S_5)	12.9	4.0	39.1	44
NiFe LDHs/rGO/NF (S_7)	9.4	3.2	47.1	40.3

In NiFe LDHs/NF, the Ni_{2p} high resolution XPS spectrum (12.9 at%) shows two peaks located at binding energies of 855.3 and 872.9 eV due to $Ni_{2p3/2}$ and $Ni_{2p1/2}$ of $Ni(OH)_2$, respectively, along with two satellite peaks (**Figure 2.3b**), while the Ni_{2p} in NiFe LDHs/rGO/NF (9.4 at%) is deconvoluted in two bands at 856.6 and 874.4 eV with a slight shift resulting from the interaction between NiFe LDHs and rGO [68, 69]. The high-resolution Fe_{2p} spectrum reflects that Fe species are mostly in their Fe^{3+} oxidation state (**Figure 2.3c and 2.4c**), with two prominent peaks at 711.5 ($Fe_{2p3/2}$) and 724.8 eV ($Fe_{2p1/2}$) along with two satellite peaks (716.3 and 732.9 eV) for NiFe LDHs/NF (4.0 at%), and 712.5 eV ($Fe_{2p3/2}$) and 725.2 eV ($Fe_{2p1/2}$) along with two satellite peaks (718.6 and 733.9 eV) for NiFe LDHs/rGO/NF (3.2 at%) [70-72].
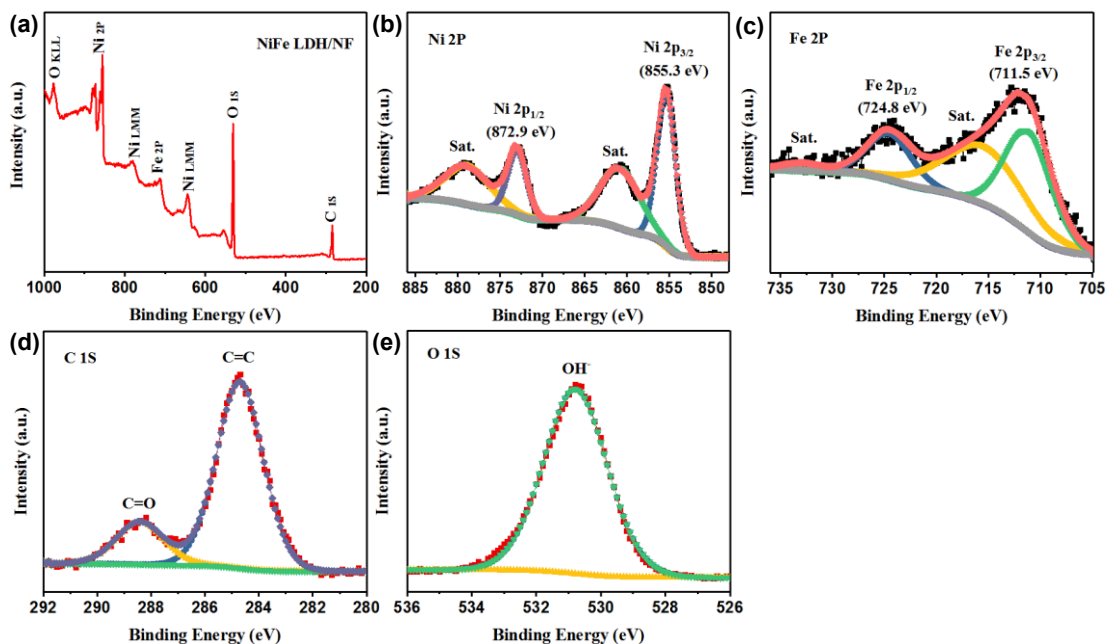
Figure 2.3: XPS survey spectrum (a) and high-resolution spectra of (b) Ni_{2p}, (c) Fe_{2p}, (d) C_{1s} and (e) O_{1s} of NiFe LDHs/NF.

The presence of C_{1s} in NiFe LDHs/NF originates most likely from surface contamination during sample handling. The C_{1s} high-resolution spectrum (**Figure 2.3d**) of NiFe LDH/NF displays two types of carbons: C=C (284.7 eV) and C=O (288.5 eV), while the C_{1s} core level spectrum of NiFe LDHs/rGO/NF can be curve-fitted with three components: C=C (284.7 eV), C-O (285.6 eV) and C=O (288.5 eV) (**Fig. 2.4d**). At the same time, the C content in NiFe LDHs/NF is lower than that in NiFe LDHs/rGO/NF (**Table 2.7**), which further confirms that the rGO was deposited on the surface of NF in NiFe LDHs/rGO/NF and the functional groups of GO were partially removed upon electrochemical reduction [73-75]. The O_{1s} spectrum (**Figure 2.3e** and **2.4e**) is fitted with a single peak ascribed to -OH groups, further confirming that Ni and Fe are in the

form of $Ni(OH)_2$ and $Fe(OH)_3$, respectively [72].
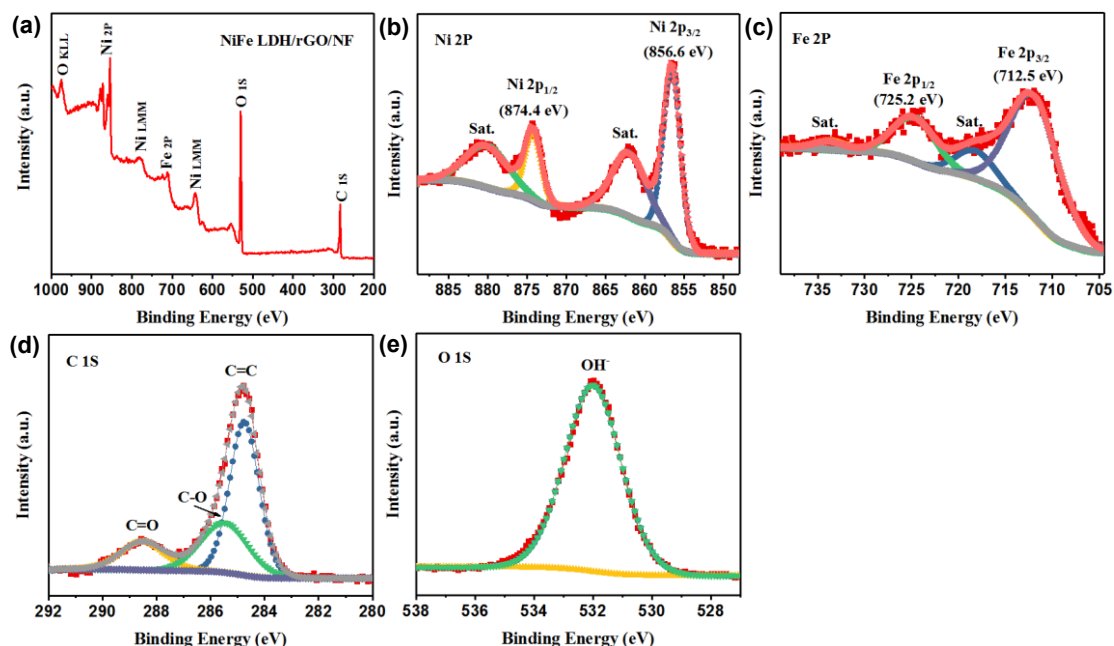

Figure 2.4: XPS analysis of NiFe LDH/rGO/NF: (a) Survey spectrum, and high

resolution spectra of (b) Ni_{2p}, (c) Fe_{2p}, (d) C_{1s} and (e) O_{1s}.

Raman spectroscopy is a valuable tool for analysis of carbon-based materials.

Figure 2.5 depicts the Raman spectrum of rGO/NF composite. It comprises two peaks

at 1353 and 1596 cm^{-1} due to the D- and G-bands of rGO, respectively. The presence

of these characteristic graphitic bands confirms the successful electrodeposition of rGO

on the Ni foam. The Raman spectrum of NiFe LDH/rGO/NF reveals the characteristic

D-band (1355 cm^{-1}) and G-band (1603 cm^{-1}) of rGO along with new peaks at 328, 478,

567 and 691 cm^{-1} due to the vibration modes of NiFe LDH [40, 76, 77]. Interestingly,

the D- and G-bands of rGO in NiFe LDH/rGO/NF are redshifted, suggesting a strong

interaction between rGO and NiFe LDH/NF. Normally, the intensity of the D band

represents the amount of disordered carbon in as-synthesized materials, while the intensity of G band corresponds to the amount of sp^2 hybridization or the degree of graphitization. In order to determine the ratio of disordered and ordered content in rGO sheets, I_D/I_G values of rGO/NF and NiFe LDH/rGO/NF are determined to be 0.86 and 1.06, respectively, suggesting a significant increase of defect density in NiFe LDH/rGO/NF owing to the interaction between rGO and NiFe LDHs, further proving the successful synthesis of NiFe LDH/rGO/NF composite [78, 79].
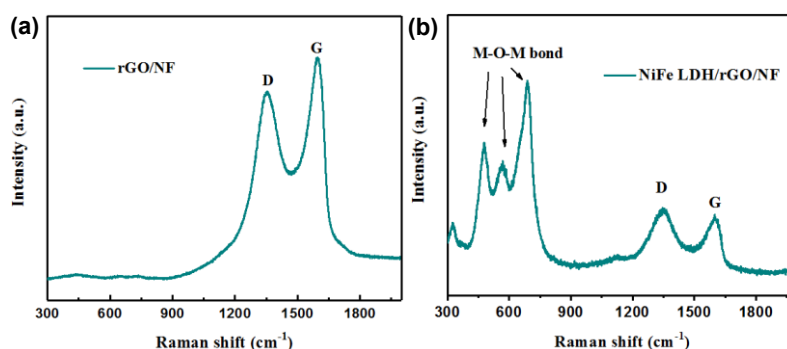

Figure 2.5: Raman spectra of (a) rGO/NF and (b) NiFe LDH/rGO/NF.

The electrochemical properties of the samples were assessed in a classical three-electrode configuration in 2 M KOH aqueous electrolyte by means of CV, GCD and EIS tests. The as-synthesized samples were employed as the working electrode. A platinum foil and a saturated calomel electrode (SCE) acted as the counter and reference electrodes, respectively.

Figure 2.6a depicts the CV curves of NiFe LDHs/NF in the potential range from 0 to +0.5 V at a scan rate of 50 mV s^{-1}. All the samples exhibited redox peaks due to Ni (II)/Ni(III) in the hydroxide sheets of NiFe LDHs, indicating that the capacitance

characteristics are mainly due to Faradaic pseudocapacitance corresponding to the electrochemical reaction shown in **Equation 2.1**.

The CV curves in **Figure 2.6b** indicate that the peak current of NiFe LDH 1:4 (S_5) electrode increases with insignificant change in the curve shape, and the peak potential shifts as the scan rate increases, which originated from the increased internal resistance under higher scan rates. From **Figure 2.6c**, we can see that NiFe LDH 1:4 (S_5) has the best performance with the longest discharge time. According to equation (2), the specific capacity of NiFe LDH 1:4 (S_5) is determined to be 530 C g^{-1} at a current density of 5 A g^{-1}. It is worth noting that NiFe LDH 0:5 (S_6) possesses a relatively higher specific capacity than NiFe LDH 3:2 **(S_2)**, NiFe LDH 1:1 **(S_3)** and NiFe LDH 2:3 **(S_4)**, most likely due to the unique 3D bridge structure, as shown in **Figure 2.3g**.

The calculated specific capacity values of the electrodes from the galvanostatic charge-discharge (GCD) curves at different current densities according to **Equation 1.11.2** are displayed in **Figure 2.6d** and **Table 2.8**, confirming the good performance for all the samples. Among all the samples, NiFe LDH 1:4 (S_5) displays the larger specific capacity values, which were determined to be 500, 480, 460 and 420 C g^{-1} at the current densities of 10, 15, 20 and 30 A g^{-1}, respectively.
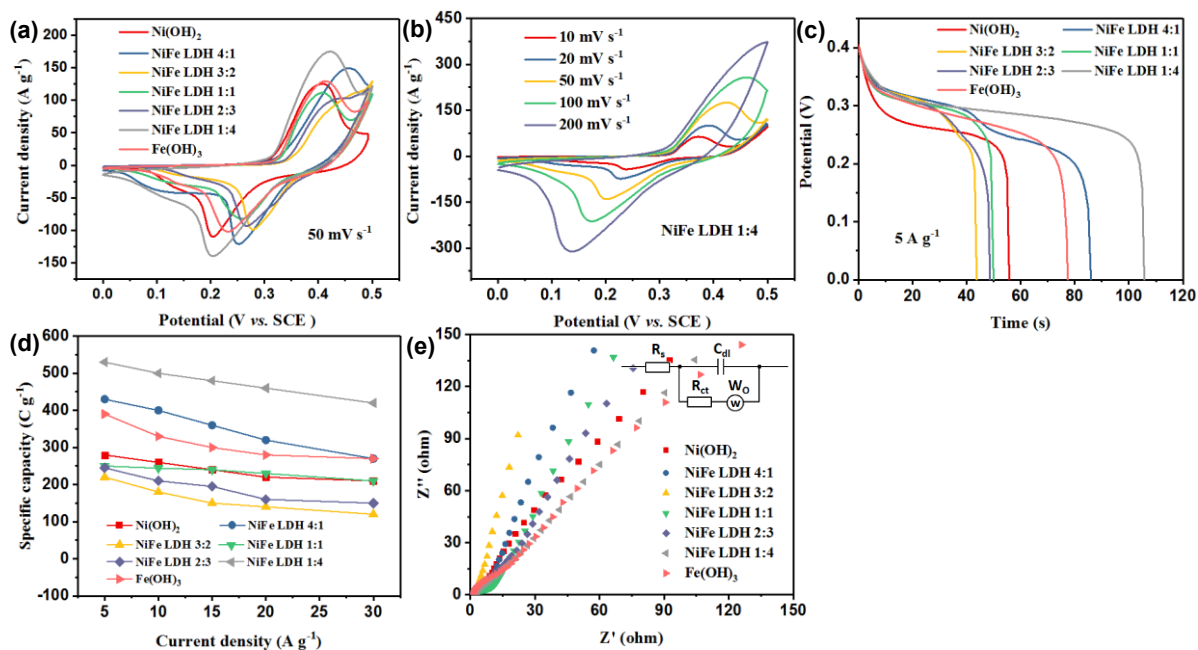
Figure 2.6: Electrochemical characteristics of the electrodes upon immersion in 2 M KOH aqueous solution. (a) CV curves recorded at a scan rate of 50 mV s^{-1}. (b) CV curves of NiFe LDH 1:4 recorded at various scan rates. (c) Galvanostatic discharge curves acquired at a current density of 5 A g^{-1}. (d) Specific capacity at different current densities. (e) Electrochemical impedance spectra recorded at open circuit potential in the frequency range from 0.01 Hz to 100 kHz.

Table 2.8. Specific capacity (C g^{-1}) of the electrodes.

Current density (A g^{-1}) / Samples	5	10	15	20	30
Ni(OH)$_2$ (S$_0$)	280	260	240	220	210
NiFe LDH 4:1 (S$_1$)	430	400	360	320	270
NiFe LDH 3:2 (S$_2$)	220	180	150	140	120
NiFe LDH 1:1 (S$_3$)	250	244	240	230	210

NiFe LDH 2:3 (S4)	245	210	195	160	150
NiFe LDH 1:4 (S5)	530	500	480	460	420
Fe(OH)3 (S6)	390	330	300	280	270

EIS measurements, performed in the frequency range from 100 kHz to 0.01 Hz in 2 M aqueous KOH electrolyte (**Figure 2.6e**), revealed that the Nyquist plots are similar in shape and comprise a small semicircle at high frequency region and a slope line (Warburg curve) in the low frequency region. The inset in **Figure 2.6e** presents the equivalent circuit for impedance analysis based on characterization by the software of ZSimDemo3.30d, where R_s is the internal resistance of an electrode material, electrolyte resistance and contact resistance between the active material and substrate, R_{ct} is the charge-transfer resistance, C_{dl} is the double-layer capacitance, W_o is the Warburg element. All the values are summarized in **Table 2.9**, in which all samples show small R_s and R_{ct}, indicating a good conductivity.

Table 2.9 Resistance values (ohm cm^{-2}) of the electrodes.

Samples	R_s	R_{ct}
Ni(OH)2 (S0)	1.03	25.46
NiFe LDH 4:1 (S1)	1.02	24.68
NiFe LDH 3:2 (S2)	1.50	31.25
NiFe LDH 1:1 (S3)	1.50	15.97
NiFe LDH 2:3 (S4)	1.10	25.09
NiFe LDH 1:4 (S5)	1.91	24.23
Fe(OH)3 (S6)	1.04	24.98

Due to unique characteristics, such as large specific surface area, high electrical conductivity and chemical stability, graphene has been widely employed in supercapacitors. In order to improve the performance of the electrodes, NiFe LDHs/rGO/NF (S$_7$) was prepared using a two-step electrodeposition according to the process in **Figure 2.1b**. At the same time, the electrochemical properties of the samples were assessed using cyclic voltammetry. Compared with NiFe LDH 1:4 **(S$_5$)**, NiFe LDHs/rGO/NF 20 s (S$_8$) and NiFe LDHs/rGO/NF 30 s (S$_9$), NiFe LDHs/rGO/NF (S$_7$) possessed larger currents density with obviously a pair of characteristic redox peaks in the CV, as shown in **Figure 2.7** and **Figure 2.8a**.
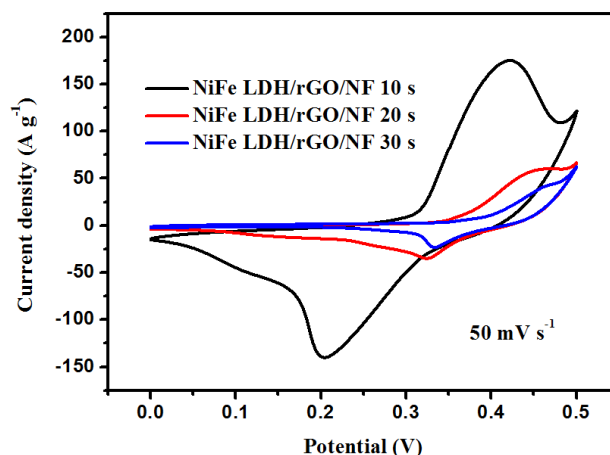

Figure 2.7: CV curves of NiFe LDHs/rGO/NF 10 s (S$_7$), NiFe LDHs/rGO/NF 20 s (S$_8$) and NiFe LDHs/rGO/NF 20 s (S$_9$) measured at a scan rate of 50 mV s^{-1}.

At different scan rates, we could observe the changes of anodic and cathodic peaks towards more positive and negative directions, respectively, originating from the increased internal resistance under higher scan rates (**Figure 2.8b**). Furthermore, as

seen in **Figure 2.8c** and **d**, NiFe LDHs/rGO/NF (S_7) exhibits a better performance and

its specific capacity increased to 585 C g^{-1} at a current density of 5 A g^{-1}. **Figure 2.8d**

indicates that both NiFe LDHs/NF and NiFe LDHs/rGO/NF possess good rate

capability. When the current density is increased from 5 to 30 A g^{-1}, about 79% of the

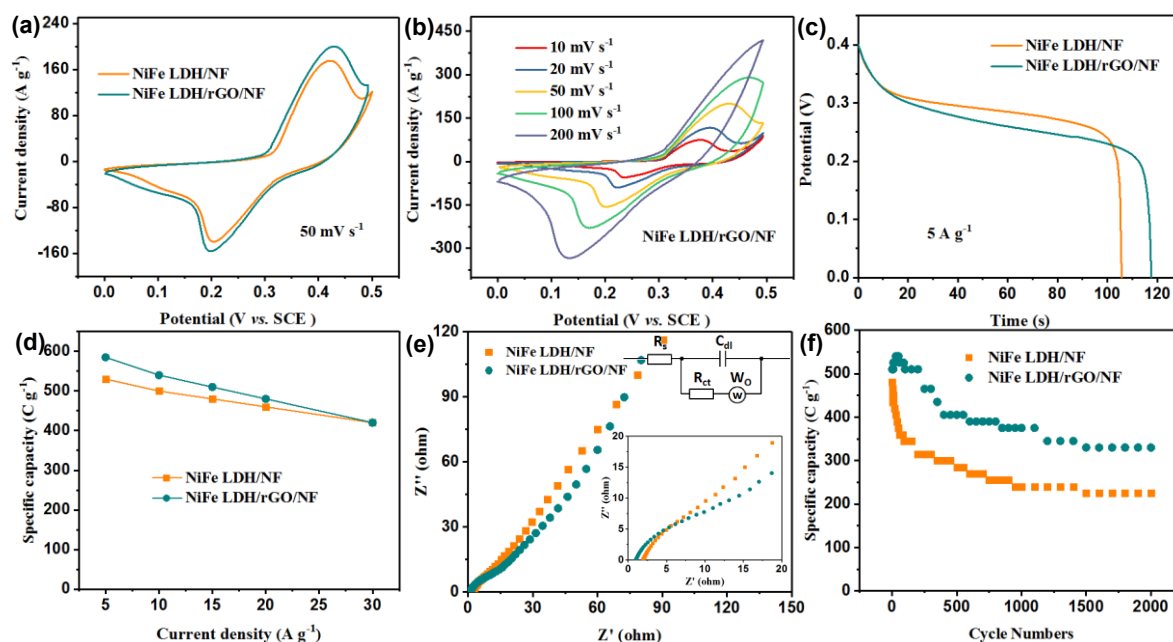initial capacity of NiFe LDHs/NF is retained while 72% capacity is maintained for NiFe

LDHs/rGO/NF.

Figure 2.8: Electrochemical performance of the electrodes in 2 M KOH aqueous

solution. (a) CV curves recorded at a scan rate of 50 mV s^{-1}. (b) CV curves of NiFe

LDH/rGO/NF at various scan rates. (c) Galvanostatic discharge curves at a current

density of 5 A g^{-1}. (d) Specific capacity at different current densities. (e)

Electrochemical impedance spectra recorded at open circuit potential in the frequency

range from 0.01 Hz to 100 kHz. (f) Cycling performance at a constant current density

of 15 A g^{-1}.

The electrochemical impedance spectra are shown in **Figure 2.8e**. And it can be clearly seen that NiFe LDHs/rGO/NF (S$_7$) has a smaller R_s (1.07 ohm cm^{-2}) (a combination of the contact resistance of the active materials with the substrate and the test cell to the apparatus, the ionic resistance of the electrolyte, the intrinsic resistance of electrodes) and also a lower R_{ct} (13.48 ohm cm^{-2}). It might be that rGO provides easy electron-transfer access and more Fe^{3+} ions enhanced the electrical conductivity of Ni(OH)$_2$ [71]. Finally, the prepared electrodes are subjected to an extended charge–discharge cycling at 15 A g^{-1} and the result is depicted in **Figure 2.8f**. After 2,000 cycles, 47% and 64.7% of the original capacitance are retained for NiFe LDH/NF and NiFe LDHs/rGO/NF electrodes, respectively.

Figure 2.9a displays the CV curve of mesoporous carbon (MC) measured at a scan rate of 100 mV s^{-1}, indicating a wide negative working voltage from -1 ~ 0 V. **Figure 2.9b** schematically illustrates the hybrid supercapacitor device, in which the as-obtained NiFe LDH/rGO/NF works as the positive electrode and the mesoporous carbon as the negative electrode, packed between two PET films. Electrochemical characterization was further performed in a two-electrode system. As illustrated in **Figure 2.9c**, the flexible NiFe LDH/rGO/NF//MC hybrid supercapacitor possesses a large cell voltage window (up to 1.6 V), which is attributed to the great voltage window of MC (**Figure 2.9a**); the CVs display similar shapes, indicating an excellent capacitive performance. **Figure 2.9d** shows the CV curves of the hybrid supercapacitor obtained at different scan rates in the cell voltage window between 0 and 1.5 V, exhibiting an

excellent capacitive behavior. As we can see from **Figure 2.9f**, the initial specific

capacity values were 91.1, 50.3, 27.8, 25 and 24.5 C g^{-1} at different current densities of

respectively 0.5, 0.8, 1, 2 and 3 A g^{-1}, corresponding to the discharging curves shown

in **Figure 2.9e**. At the same time, the equivalent circuit for impedance analysis of the

symmetric supercapacitor is illustrated in **Figure 2.9g**, in which R_s is the internal

resistance, R_{ct} is the charge-transfer resistance, C_{dl} is the double-layer capacitance, W_o

is the Warburg element, C_l is the low-frequency mass capacitance. We can also see that

the Nyquist plot exhibits a semicircle associated with the charge transfer resistance at

the high-frequency range and shows a sloping line at the low-frequency region. From

the inset in **Figure 2.9g**, the R_s and R_{ct} values are estimated to be about 12.3 and 19.4

ohm cm^{-2}, respectively.

To completely evaluate the electrochemical performance of the as-fabricated hybrid

supercapacitor, the Ragone plot, according to **Equations 1.12** and **1.13**, is generated in

Figure 2.9h and **Table 2.10**. The results demonstrate that the hybrid supercapacitor

device can reach an energy density of 17.71 Wh kg^{-1} at a power density of 348.49 W

kg^{-1}. This energy density value is greater than those recorded for CoMn-LDH//AC

hybrid supercapacitor [80], PPy/rGO//NCs hybrid supercapacitor [81], MnO$_2$//P-GA

asymmetric supercapacitor [82], MnO$_2$//AC asymmetric supercapacitor [83], Ni-Co

oxide//AC hybrid supercapacitor [84], Cu$_2$O/CuO/Co$_3$O$_4$//AG hybrid supercapacitor

[85] and MnFe$_2$O$_4$//LiMn$_2$O$_4$ hybrid supercapacitor [86].
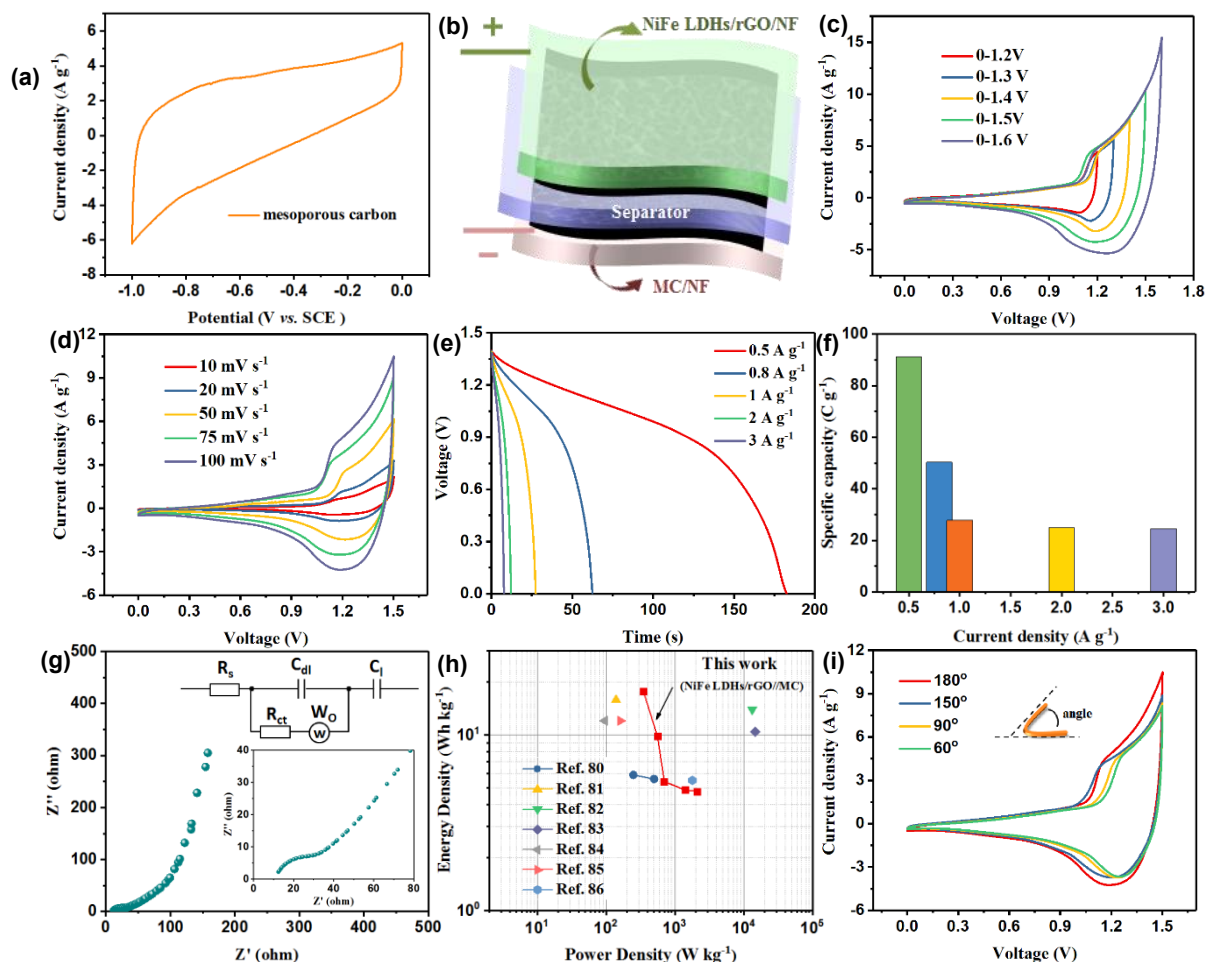
Figure 2.9: (a) CV curve of mesoporous carbon measured at a scan rate of 100 mV s^{-1}.

(b) Schematic diagram of the packed hybrid supercapacitor device. (c) CV curves

performed at different cell voltage windows at 100 mV s^{-1}. (d) CV curves obtained at

different scan rates between 0 and 1.5 V. (e) Galvanostatic discharge curves at different

current densities. (f) Specific capacity recorded at different current densities. (g) EIS

curves acquired in the frequency range of 0.01 Hz and 100 kHz. (h) Ragone plots related

to the energy and power densities of the hybrid supercapacitor. (i) CV curves at 100

mV s^{-1} bending the different angles.

Table 2.10 Comparison of energy densities (Wh kg^{-1}) and power densities (W kg^{-1}) of

different supercapacitor devices.

Device	Energy density (Wh kg^{-1})	Power density (W kg^{-1})
CoMn-LDH//AC	5.9	250
PPy/rGO//NCs	15.8	140
MnO$_2$//P-GA	13.9	13300
MnO$_2$//AC	10.4	14700
Ni-Co oxide//AC	12	95.2
Cu$_2$O/CuO/Co$_3$O$_4$//AG	12	162
MnFe$_2$O$_4$//LiMn$_2$O$_4$	5.5	1800
This work	17.71	348.49

Furthermore, the mechanical properties and flexibility of the hybrid supercapacitor device were assessed (**Figure 2.9i**). There is no obvious change in the CV curves at different bending angles, indicating a satisfactory flexible performance of the hybrid supercapacitor.

2.3 NiAl, NiCr and NiFe Layered Double Hydroxides

Herein, we prepared NiFe, NiCr and NiAl LDHs through a one-step hydrothermal technique and studied the influence of the Fe, Cr and Al in Ni-based LDHs on their electrochemical properties. The same LDHs were further coated on carbon spheres (CS) supported on NF using a facile two-step hydrothermal process to produce NiAl LDHs@CS/NF, NiFe LDHs@CS/NF and NiCr LDHs@CS/NF composites.

Furthermore, a hybrid supercapacitor was assembled using N-doped reduced graphene oxide (N-rGO) as the negative electrode and Ni-based LDHs as the positive electrode.

2.3.1   Experimental section

2.3.1.1   Synthesis of nitrogen-doped reduced graphene oxide (N-rGO)

N-rGO was prepared through graphene oxide (GO) hydrothermal reduction in presence of hydrazine monohydrate ($NH_2NH_2 \cdot H_2O$). Typically, 100 mg of GO were dispersed in 50 mL of Milli-Q water and sonicated for 2 h to form a GO suspension (2 mg mL^{-1}), followed by the addition of 0.5 M hydrazine monohydrate. The resulting mixture was poured into a 100 mL Teflon-lined autoclave and heated at 160 ^{o}C for 3 h. The solution was cooled to room temperature, and the resulting N-rGO was aged in Milli-Q water for 72 h by changing the water every 24 h. Finally, the product was collected by the freezing-dry method for 72 h.

2.3.1.2   Synthesis of carbon spheres on nickel foam (CS/NF)

Carbon spheres coated on nickel foam (CS/NF) nanocomposite was prepared *via* a

simple one-step hydrothermal method [87]. In a typical procedure, 6 g of glucose were dissolved in Milli-Q (MQ) water (35 mL) under continuous stirring to form a homogeneous solution. Then, a piece of nickel foam (3 cm×2 cm×0.5 cm) was placed in the homogeneous solution and transferred into a 50 mL Teflon-lined stainless-steel autoclave for hydrothermal reaction at 190 ℃ for 4 h. After being cooled naturally to room temperature, the nickel foam decorated with carbon spheres (CS/NF) was washed with water and ethanol for several times, and dried at 60 ℃ for 24 h.

2.3.1.3 Preparation of NiCr LDHs/NF, NiFe LDHs/NF and NiAl LDHs/NF

Typically, a homogeneous solution of $Ni(NO_3)_2 \cdot 6H_2O$ (87 mg), $Cr(NO_3)_3 \cdot 9H_2O$ (120 mg), and $CO(NH_2)_2$ (180 mg) in MQ water (35 mL) was prepared through magnetic stirring. NF was dipped into the solution, and the mixture was transferred into an autoclave (50 mL) and heated for 12 h at 120 ℃. The resulting NiCr LDHs/NF was rinsed copiously with water, ethanol, and dried in an oven for 24 h at 60 ℃.

$Al(NO_3)_3 \cdot 9H_2O$ (113 mg) and $Fe(NO_3)_3 \cdot 9H_2O$ (121 mg) were used to replace $Cr(NO_3)_3 \cdot 9H_2O$ (120 mg) for the synthesis of NiAl LDHs/NF and NiFe LDHs/NF, respectively.

2.3.1.4 Preparation of NiCr LDHs@CS/NF, NiFe LDHs@CS/NF and NiAl LDHs@CS/NF

Typically, a mixture of $Ni(NO_3)_2 \cdot 4H_2O$ (87 mg), $Cr(NO_3)_3 \cdot 9H_2O$ (120 mg) and $CO(NH_2)_2$ (180 mg) in 30 mL MQ water was stirred till formation of a homogeneous

solution. The CS/NF was dipped in the above solution, and the mixture was transferred into an autoclave (50 mL) and heated for 12 h at 120 °C. The resulting NiCr LDHs@CS/NF was rinsed copiously with water, ethanol, and dried for 24 h at 60 °C.

Al(NO$_3$)$_3$·9H$_2$O (113 mg) and Fe(NO$_3$)$_3$·9H$_2$O (121 mg) were used to replace Cr(NO$_3$)$_3$·9H$_2$O (120 mg) for the synthesis of NiFe LDHs@CS/NF and NiAl LDHs@CS/NF, respectively.

2.3.1.5 Assembly of a hybrid supercapacitor cell and device

A hybrid supercapacitor cell was assembled in 2M KOH aqueous solution. The NiAl LDHs@CS/NF sample was applied as the positive electrode. The negative electrode (N-rGO/NF) consisted of N-rGO and polyvinylidene difluoride (PVDF) in a mass proportion of 8:2 coated on NF.

To acquire the optimal performance of the hybrid supercapacitor, a charge balance Q_+ (charges stored in the positive electrode) = Q_- (charges stored in the negative electrode) between the two electrodes is necessary so that the area balancing follows the **Equation 1.6.** The optimal area ratio is ~0.2. Taking the real area into consideration, the areas of the positive and negative electrodes were chosen as 1 cm×1 cm and 1.5 cm×1.5 cm, respectively, and the real area ratio is ~0.4 in this work.

To test the mechanical properties and flexibility, a hybrid supercapacitor device was further fabricated using NiAl LDHs@CS/NF (1 cm×1 cm) as the positive electrode, N-rGO/NF (1.5 cm×1.5 cm) as the negative electrode, and a filter paper (immersed into 2 M KOH aqueous solution overnight) as the separator.

Electrochemical characterization was performed in a 2-electrode system.

2.3.2 Results and discussion

The overall capacity of a hybrid supercapacitor is related to the capacity of the positive and negative electrodes, according to **Equation 2.4**:

$$\frac{1}{C_T} = \frac{1}{C_p} + \frac{1}{C_n} \quad \text{(Eq. 2.4)}$$

where C_T is the total capacity of the hybrid supercapacitor, C_p is the capacity of the positive electrode and C_n is the capacity of the negative electrode.

Herein, N-doped reduced graphene oxide coated nickel foam (N-rGO/NF) was first synthesized through hydrothermal reduction of GO in presence of hydrazine monohydrate reducing and doping agent, and applied as a negative electrode with the aim to widen the potential window of a hybrid supercapacitor. The morphology of N-rGO was assessed by scanning electron microscopy (SEM), **Figure 2.10a**. A porous skeleton consisting of overlapped N-rGO nanosheets could be observed; this morphology is favorable for electrolyte diffusion. **Figure 2.10b** depicts the Raman spectrum of N-rGO and shows the typical D and G bands respectively at 1357 and 1586 cm^{-1}.
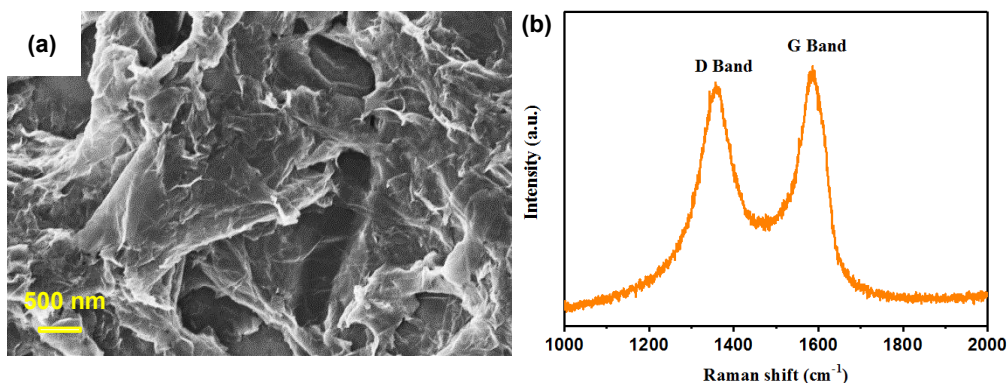
Figure 2.10: (a) SEM image, and (b) Raman spectrum of N-rGO.

XPS analysis was used to assess the elemental composition of N-rGO. The existence of N element with an atomic content of ~3.2 at% proves the successful nitrogen doping of rGO (**Figure 2.11a**). The spectrum comprises also contributions due to O and C elements with 6 at% and 90.8 at%, respectively. **Figure 2.11b** displays the core level spectrum of the C_{1s}, which can be curve-fitted with four obvious peaks at 284.8, 285.3, 286.9 and 288.9 eV related respectively to the C-C, C-N, C-O, C=O groups. **Figure 2.11c** reveals the presence of several components at 399.3, 400.6, 402.5 and 407.3 eV in the core level spectrum of the N_{1s} assigned respectively to pyridinic-N, pyrrolic-N, graphitic-N, and oxidized N peaks; the presence of pyridinic-N and pyrrolic-N could potentially enhance electrolyte diffusion and charge transfer in the carbon matrix [75]. The core level spectrum of the O_{1s} comprises several components ascribed to O=C-OH (531.4 eV), C-OH (533.3 eV) and chemisorbed oxygen (535.5 eV), respectively (**Figure 2.11d**) [88].
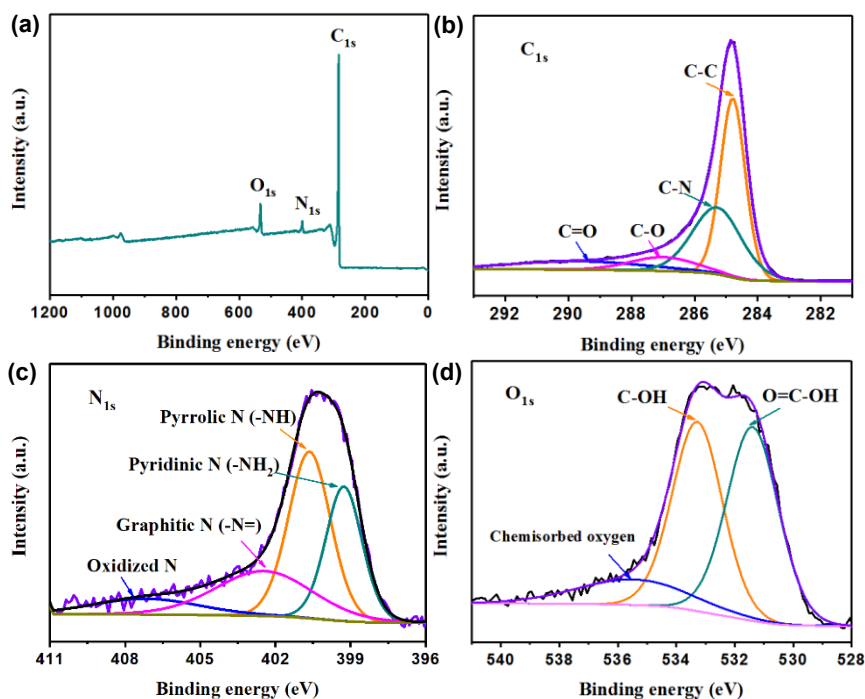
Figure 2.11: XPS analysis of N-rGO: (a) Survey spectrum and core level spectra of the (b) C_{1s}, (c) N_{1s} and (d) O_{1s}.

As previously stated, the N-rGO was meant to be applied as a negative electrode of a hybrid supercapacitor, so its electrochemical performance was further investigated in a classical 3-electrode cell containing using 2 M KOH aqueous electrolyte.

Figure 2.12a depicts the galvanostatic charge-discharge (GCD) plots from -1 to +0.4 V of N-rGO/NF electrode at various current densities (1 to 5 mA cm^{-2}), and the corresponding areal capacity values were calculated according to **Equation 1.11.2**. Areal capacity values of 249.1, 185.3, 163.1, 148.3 and 136.2 mC cm^{-2} were determined respectively at 1, 2, 3, 4 and 5 mA cm^{-2} (**Figure 2.12b**). Furthermore, to get more information on the electrochemical processes at different time constants, impedance spectroscopy (EIS) analysis was performed. The Nyquist plot (**Figure 2.12c**) reveals

the typical depressed semicircle (high-to-medium frequency region) and a straight line (low-frequency region) arising from ion diffusion in the electrode material. The equivalent circuit is presented in the inset (R_s is the internal resistance, R_{ct} is the charge-transfer resistance, Q is the pseudocapacitance, W_o is the ion transport resistance, C_l is the limit capacitance, and R_l is the limit resistance). The R_s and R_{ct} values were determined to be respectively ~0.78 and ~29.78 ohm cm^{-2}, indicating a good conductivity of N-rGO/NF. All the measurements suggest that N-rGO could be a potential negative electrode material.
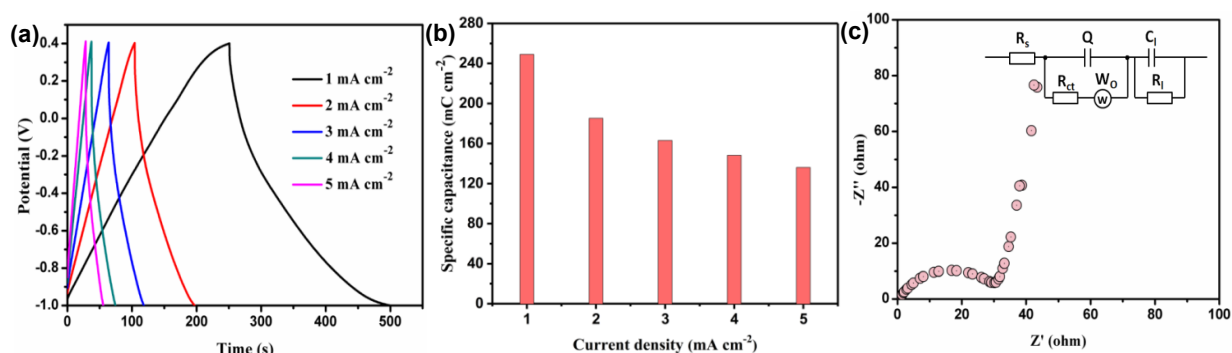

Figure 2.12: The electrochemical behavior of N-rGO in 2 M KOH aqueous solution. (a) GCD plots at various current densities. (b) Areal capacity values at various current densities. (c) EIS acquired at open circuit potential in the frequency range of 0.01 Hz to 100 kHz.

The crystallinity of NiFe LDHs/NF, NiFe LDHs@CS/NF, NiCr LDHs/NF, NiCr LDHs@CS/NF, NiAl LDHs/NF and NiAl LDHs@CS/NF was examined by X-ray diffraction (XRD). As seen in **Figure 2.13** and **2.14**, under the same growth conditions, NiAl LDHs showed obviously better crystallinity than NiFe LDHs and NiCr LDHs.
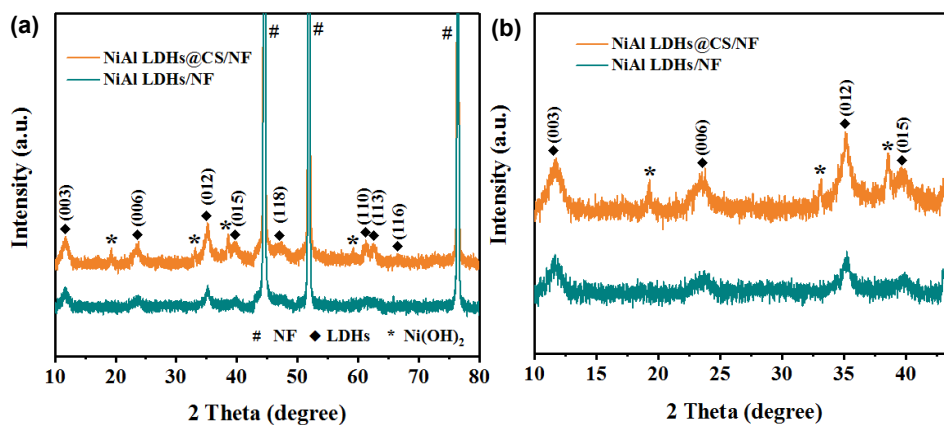
Figure 2.13: (a) XRD patterns of NiAl LDHs/NF and NiAl LDHs@CS/NF, (b) magnified pattern in the 10–44° range.

The XRD pattern of NiAl LDHs presents typical (003), (006), (012), (015), (118), (110), (113) and (116) planes for LDHs, appearing at 11.7°, 23.6°, 35.1°, 39.7°, 47.3°, 61.2°, 62.6° and 66.5°, respectively (JCPDS No. 15-0087) [45]. Moreover, there are four small peaks of Ni(OH)$_2$ located at 19.3°, 33.1°, 38.5° and 59.4° ascribed to the (001), (110), (101) and (110) planes (JCPDS No. 14-0117). Due to the existence of the NF skeleton, the peaks of LDHs exhibit relatively weak intensity so that the magnified XRD pattern in the range of 10–44° was provided in **Figure 2.13b** for more details. However, for NiFe LDHs@CS/NF and NiCr LDHs@CS/NF samples, no obvious peaks of LDHs were observed owing to the poor crystallinity (**Figure 2.14**).
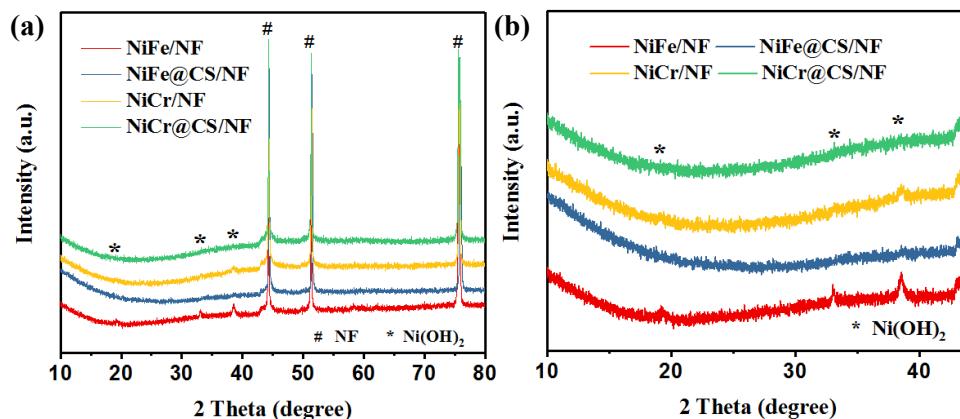
Figure 2.14: (a) XRD patterns of NiFe LDHs/NF, NiFe LDHs@CS/NF, NiCr LDHs/NF and NiCr LDHs@CS/NF, (b) magnified pattern in the 10–44° range.

Furthermore, the microstructures of the LDH samples were assessed by scanning electron microscopy (**Figure 2.15**), and showed totally different shapes for the different trivalent elements. **Figure 2.15a, b** and **g, h** display the SEM images of NiFe LDHs/NF and NiFe LDHs@CS/NF. Interestingly, NiFe LDHs/NF consisted of wool-like nanowires intertwined with each other (**Figure 2.15a, b**), whereas NiFe LDHs@CS/NF was composed of abundant nanosheets evenly attached to the surface of the carbon spheres (**Figure 2.15g, h**).

From **Figure 2.16**, we can see that a carbon spheres (CS, ~400 nm in diameter) layer with a smooth surface was formed on the NF, suggesting the good polymerization of glucose during the hydrothermal process. After the growth of NiFe LDHs, all the CSs exhibit pompom-like morphology. Notably, the big difference of the morphology between NiFe LDHs/NF and NiFe LDHs@CS/NF might be ascribed to the existence of CS, which leads to differences in crystal growth direction and rate.
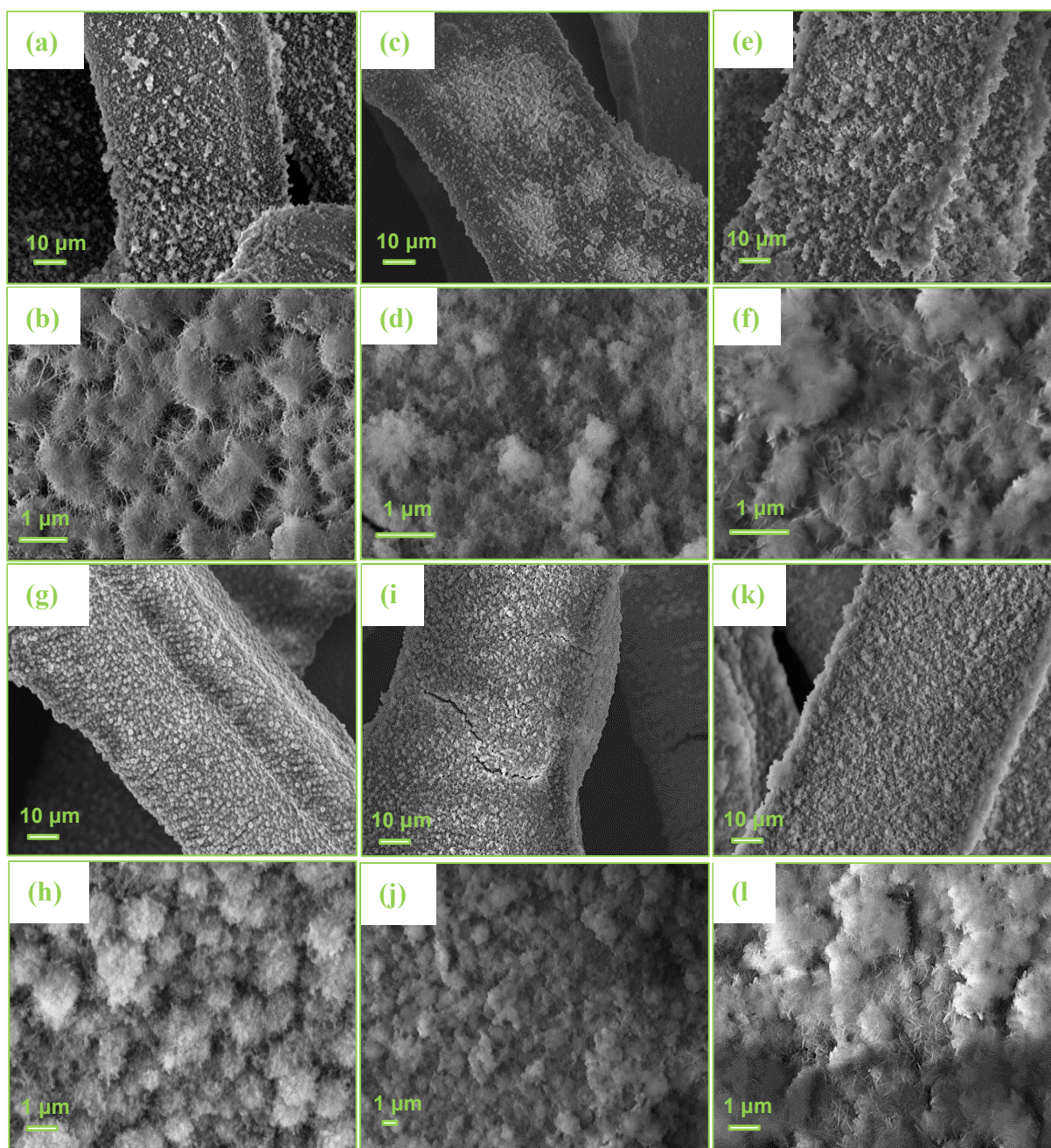
Figure 2.15: SEM images of (a, b) NiFe LDHs/NF, (c, d) NiCr LDHs/NF and (e, f)

NiAl LDHs/NF, (g, h) NiFe LDHs@CS/NF, (i, j) NiCr LDHs@CS /NF and (k, l)

NiAl LDHs@CS/NF.

However, there is no apparent difference between NiAl LDHs/NF (**Figure 2.15e,**

f) and NiAl LDHs@CS/NF (**Figure 2.15k, l**), where a dense intertwined nanosheets

layer was coated on NF and CS/NF, respectively. Apparently, NiAl LDHs nanosheets grew larger than NiFe LDHs on CS/NF, in which the CSs on NF were completely covered by the NiAl LDHs nanosheets in NiAl LDHs@CS/NF, signifying that NiAl LDHs had faster growth rate under the same conditions, consistent with the XRD results. A thin layer of NiCr LDHs nanosheets was spread on the NF and CS/NF, forming NiCr LDH/NF (**Figure 2.15c, d**) and NiCr LDHs@CS/NF (**Figure 2.15i, j**), respectively.
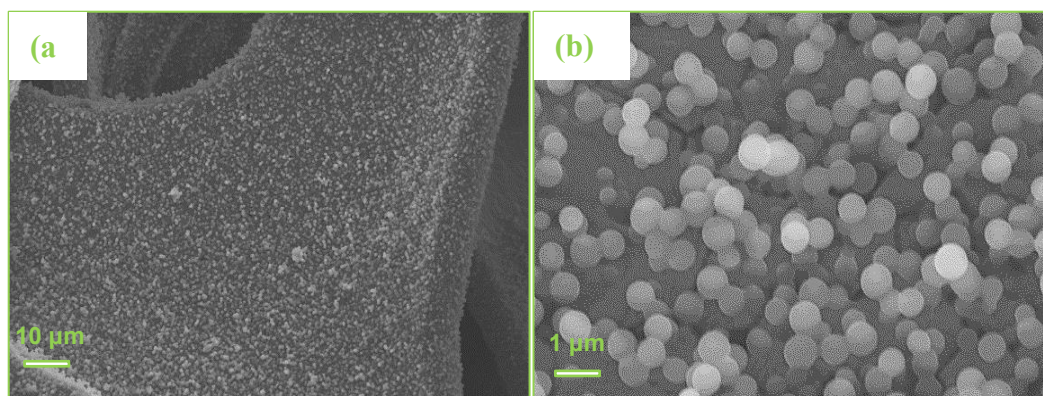

Figure 2.16: SEM images of CS/NF at different magnifications.

To further understand the chemical composition of the sample, XPS analysis was carried out on NiAl LDHs/NF, NiFe LDHs@CS/NF, NiCr LDHs@CS/NF and NiAl LDHs@CS/NF. From the XPS survey spectra in **Figure 2.17a** and **Figure 2.18a-c**, we can see that all the spectra consist of C_{1s}, O_{1s} and Ni_{2p} elements, and the difference is the incorporated metal. The elemental compositions of the samples are displayed in **Table 2.11**.
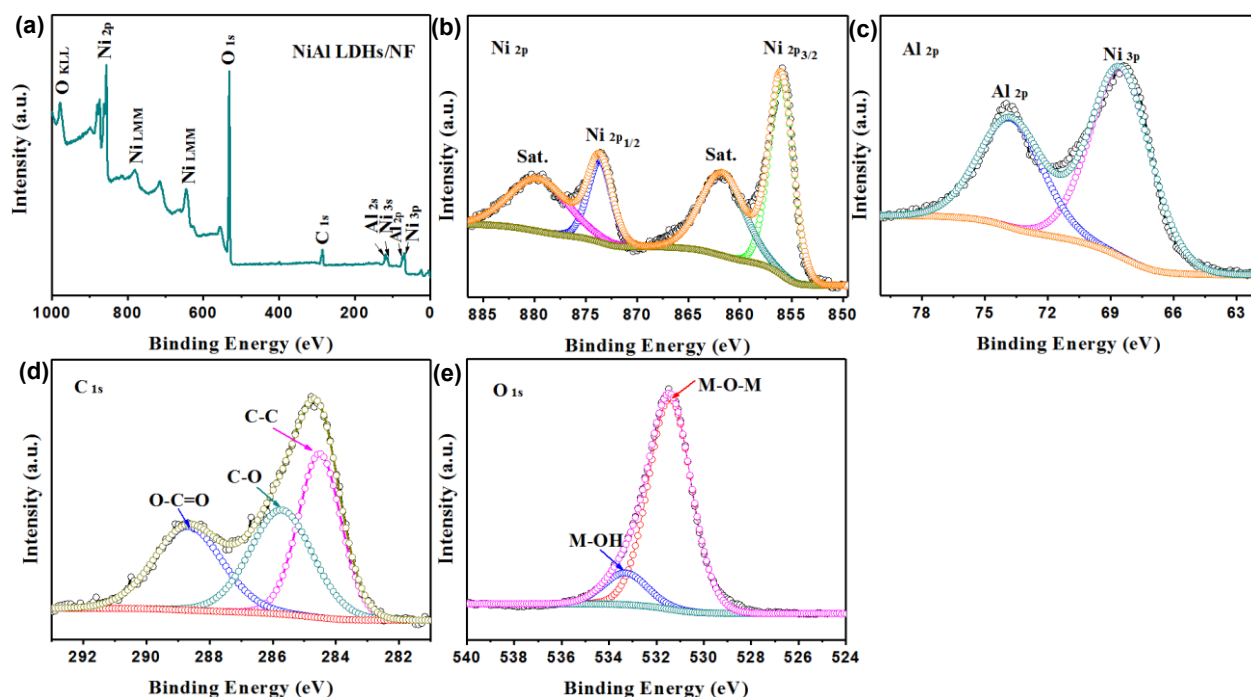
Figure 2.17: XPS analysis. (a) Survey spectrum, and high-resolution spectra of (b) Ni$_{2p}$, (c) Al$_{2p}$, (d) C$_{1s}$ and (e) O$_{1s}$ of NiAl LDHs/NF.

Table 2.11. Elemental composition of the different samples.

Elements (at%) / Composites	Ni$_{2p}$	Fe$_{2p}$/Cr$_{2p}$/Al$_{2p}$	C$_{1s}$	O$_{1s}$
NiFe LDHs@CS/NF	13.7	8.4	27.4	50.5
NiCr LDHs@CS/NF	8.5	31.1	22.4	38.0
NiAl LDHs/NF	8.2	37.8	14.5	39.4
NiAl LDHs@CS/NF	9.7	35.3	16.4	38.6

Figure 2.17b and **Figure 2.18c1** present the high -resolution spectrum of Ni$_{2p}$ in NiAl LDHs/NF (8.2 at%) and NiAl LDHs@CS/NF (9.7 at%). Two main peaks at 855.9 and 873.5 eV in NiAl LDHs/NF and 855.7 and 873.4 eV in NiAl LDHs@CS/NF corresponding to Ni$_{2p3/2}$ and Ni$_{2p1/2}$, respectively, and two satellite peaks (861.9 and 880

eV, 861.5 and 879.5 eV) were observed. The strong interaction between LDHs and CS caused a small shift of the binding energy of Al_{2p} and Ni_{2p}.

Figure 2.18a1 displays the core level spectrum of Ni_{2p} (13.7 at%) in NiFe LDHs@CS/NF, where two peaks at 855.7 and 873.4 eV ascribed respectively to $Ni_{2p3/2}$ and $Ni_{2p1/2}$ along with two satellite peaks at 861.1 and 879.6 eV were observed, suggesting that Ni is in +2 oxidation state [89]. For NiFe LDHs@CS/NF, there is also Fe_{2p} element in the spectrum (8.4 at%). The core level spectrum of Fe_{2p} is depicted in **Figure 2.18a2**, showing two main peaks at 711.4 and 725.1 eV which correspond respectively to $Fe_{2p3/2}$ and $Fe_{2p1/2}$, and two satellite peaks at 716.5 and 732.9 eV, indicating the Fe^{3+} oxidation state in NiFe LDH nanosheets [90].

For NiCr LDHs@CS/NF, there is also Ni_{2p} element (11.6 at%) and the high-resolution spectrum in **Figure 2.18b1** also comprised two peaks located at 856.1 and 873.7 eV due respectively to $Ni_{2p3/2}$ and $Ni_{2p1/2}$, and two satellite peaks at 861.5 and 879.8 eV, proving the existence of Ni^{2+} as well. At the same time, Cr_{2p} element accounts for 5.9 at%, and its core level spectrum can be deconvoluted with two components at 587.3 and 577.7 eV assigned respectively to $Cr_{2p1/2}$ and $Cr_{2p3/2}$, indicating that Cr is trivalent (**Figure 2.18b2**) [4].

Figure 2.17c depicts the high resolution spectrum of Al_{2p} (37.8 at%) in NiAl LDHs/NF at 73.9 eV, ascribed to the presence of Al^{3+} ions, which partly overlapped with Ni 3p peak at 68.7 eV [91]. For NiAl LDHs@CS/NF, the proportion of Al_{2p} is 35.3 at% and its high-resolution spectrum (**Figure 2.18c2**) can be also seen at 73.6 eV
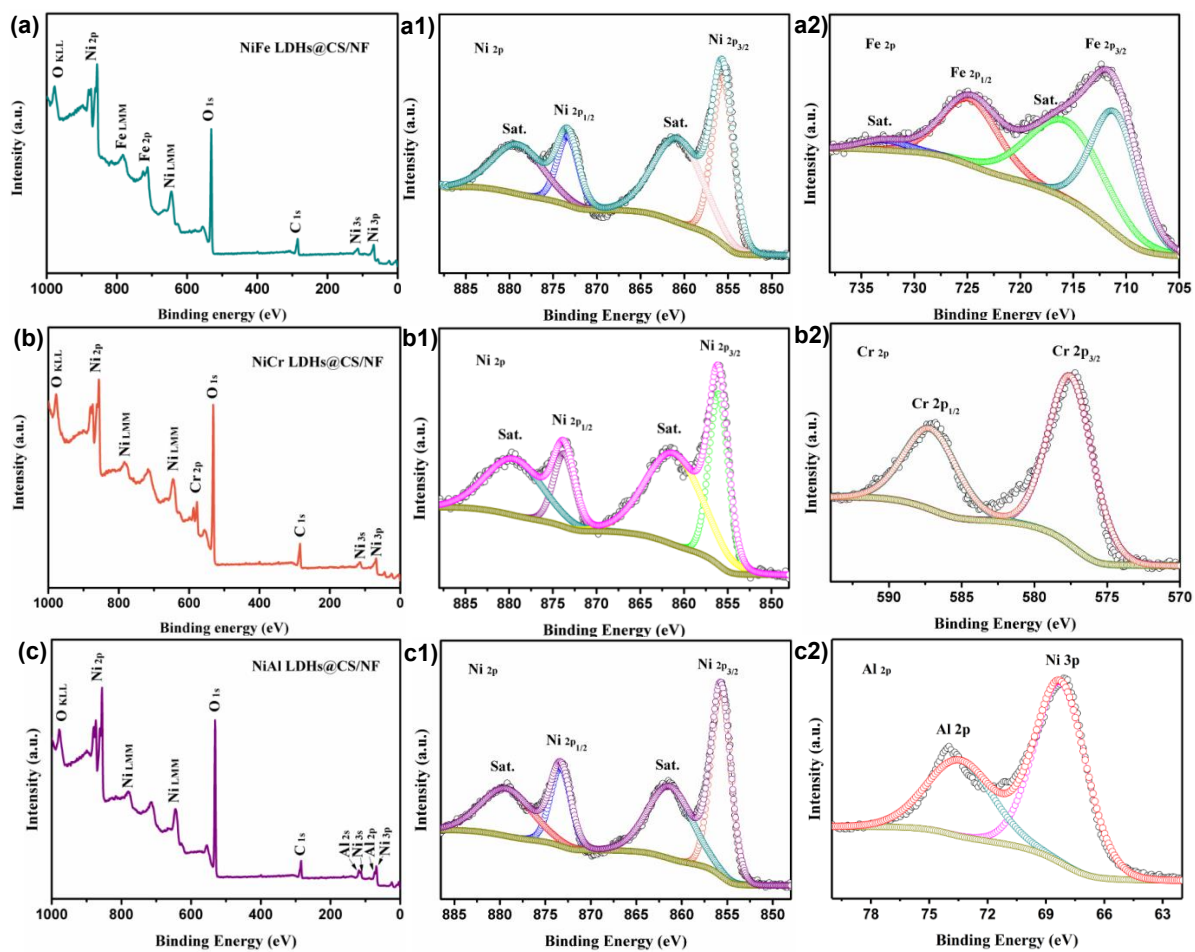
and partly overlapped with Ni_{3p} peak at 68.4 eV.

Figure 2.18: XPS analysis: (a) Survey and core level spectra of (a1) Ni_{2p} and (a2)

Fe_{2p} of NiFe LDHs@CS/NF. (b) Survey and core level spectra of (b1) Ni_{2p} and (b2)

Cr_{2p} of NiCr LDHs@CS/NF. (c) Survey and core level spectra of (c1) Ni_{2p} and (c2)
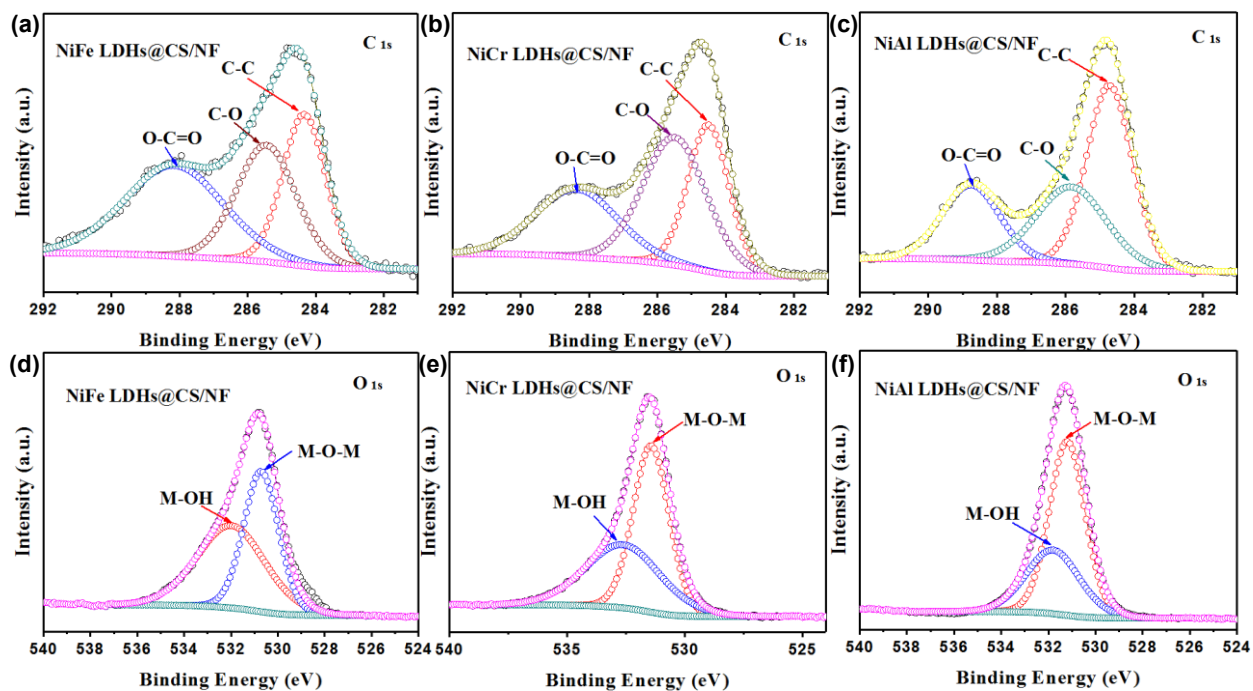
Al_{2p} of NiAl LDHs@CS/NF.

Figure 2.19: High resolution spectra of the C_{1s} of (a) NiFe LDHs@CS/NF, (b) NiCr LDHs@CS/NF, (c) NiAl LDHs@CS/NF. High-resolution spectra of the O_{1s} of (d) NiFe LDHs@CS/NF, (e) NiCr LDHs@CS/NF, (f) NiAl LDHs@CS/NF.

Figure 2.17d, **2.19a,b, c** display the core level spectra of the C_{1s} of NiAl LDHs/NF, NiFe LDHs@CS/NF, NiCr LDHs@CS/NF and NiAl LDHs@CS/NF, which account for 14.5 at%, 27.4 at%, 22.4 at% and 16.4 at% (**Table 2.10**), respectively, and all of them show typical peaks of C-C (~284.5 eV), C-O (~285.9 eV) and O-C=O (~288.8 eV). Compared to NiAl LDHs/NF, the percentage of C element increased slightly in NiAl LDHs@CS/NF and proves the existence of CS. However, the difference of carbon content is relatively low, because of the thicker NiAl LDH (thicker than the sampling depth of XPS). This was also the reason why the recorded carbon content was lower than that of NiFe LDHs@CS/NF and NiCr LDHs@CS/NF. **Figure 2.17e**, **2.19d**, **e** and

f exhibit the O_{1s} high-resolution spectra of NiAl LDHs/NF, NiFe LDHs@CS/NF, NiCr LDHs@CS/NF and NiAl LDHs@CS/NF. All of them comprise two peaks ascribed to M-O-M (~531.2 eV) and M-OH (~531.9 eV) bonds [92]. All the results indicate the successful formation of LDHs.

The electrochemical behavior of all samples was evaluated in a classical 3-electrode cell in KOH (2 M) aqueous solution in which the as-obtained samples (1 cm×1 cm) were applied as the working electrode, a platinum foil and Hg/HgO electrodes acted as the counter and reference electrodes, respectively. From **Figure 2.20a**, we can see obvious redox active peaks in all the CV plots in the 0 ~ 0.7 V potential range, corresponding to the redox process shown in **Equation 2.1**.

$$Ni(OH)_2 + OH^- \leftrightharpoons NiOOH + H_2O + e^-$$
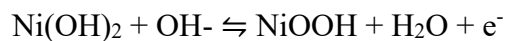
In comparison with the CV plots of $Ni(OH)_2$/NF and $Ni(OH)_2$@CS/NF (**Figure 2.21a**), the redox peaks separation became more important after LDH formation, which could be due to the synergistic effects of Ni with Fe, Cr, and Al elements. Even with the assistance of carbon spheres (CS), $Ni(OH)_2$@CS/NF displays poor electrochemical performance (**Figure 2.21b** and **c**) with an areal capacity of 74.2 mC cm^{-2} at 1 mA cm^{-2}, which is slightly higher than that of $Ni(OH)_2$/NF (70.6 mC cm^{-2} at 1 mA cm^{-2}).

Upon incorporation of Fe, Cr and Al elements, the Ni-based LDHs composites showed improved performance (**Figure 2.20b**). Among all the samples, NiAl LDHs@CS/NF possessed the longest discharge time, signifying the largest areal

capacity. According to **Equation 1.11.2**, the areal capacity values of NiAl LDHs@CS/NF were determined as 1042.2, 870.2, 787.3, 722.9 and 669 mC cm^{-2} at respectively 1, 2, 3, 4 and 5 mA cm^{-2}, indicating good rate performance. About 65-80% of areal capacity was maintained even at 5 mA cm^{-2} (**Figure 2.20c and d**). The areal capacity values of all composites are summarized in **Table 2.12**, where one could observe that the NiAl LDHs/NF exhibited the best performance with areal capacity values of 851.9, 771.4, 714.6, 665.3 and 618.6 mC cm^{-2} at respectively 1, 2, 3, 4 and 5 mA cm^{-2}.
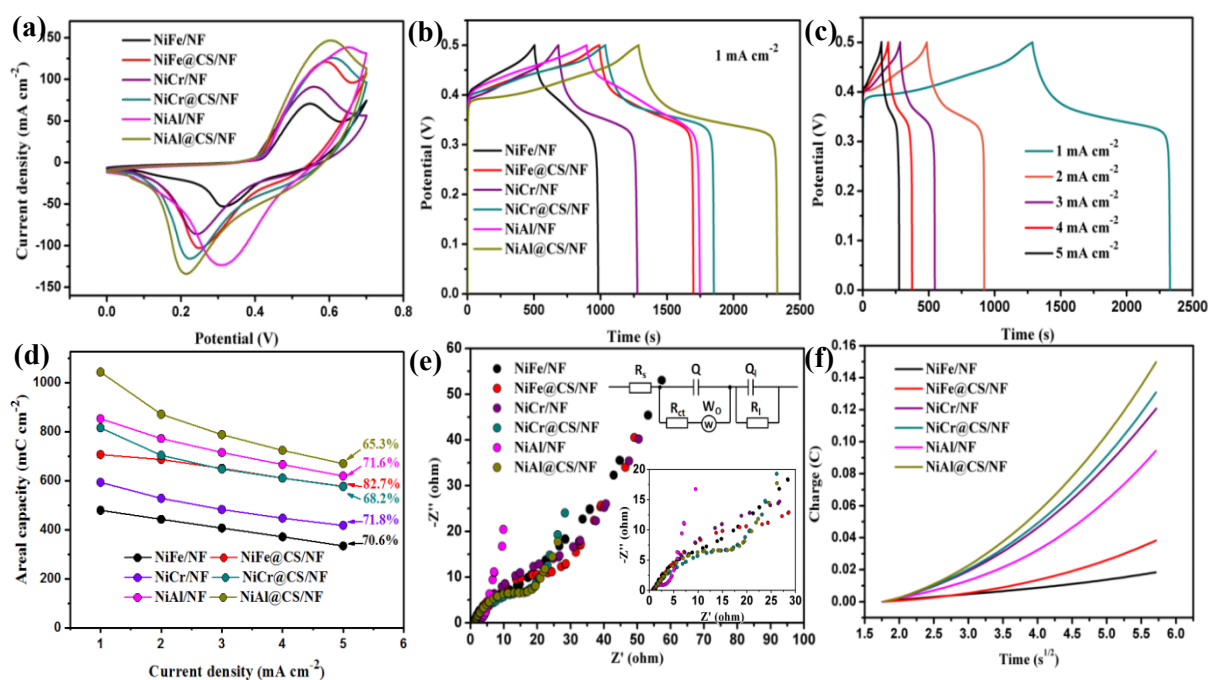

Figure 2.20: The electrochemical characteristics of the electrodes measured in a classical 3-electrode configuration cell containing 2 M KOH aqueous solution. (a) CV plots measured at 50 mV s^{-1}. (b) GCD plots acquired at 1 mA cm^{-2}. (c) GCD profiles of NiAl LDHs@CS/NF at various current densities. (d) Areal capacity at various current densities. (e) EIS acquired at open circuit potential in the 0.01 Hz to 100 kHz

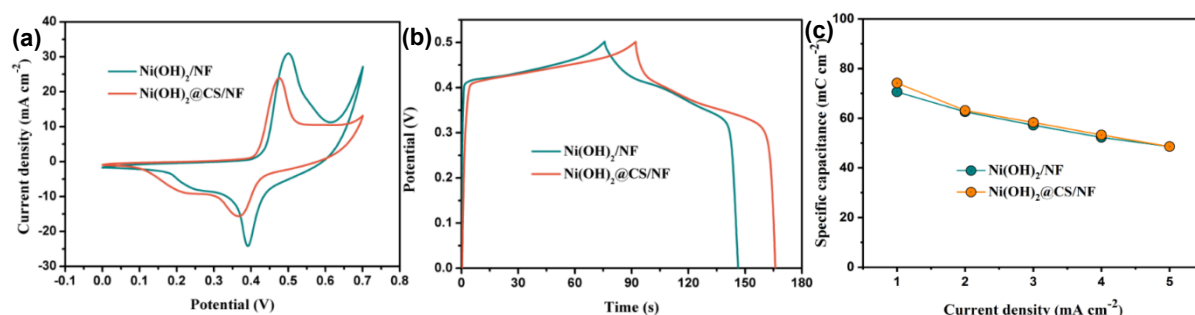frequency range. (f) Q-$t^{1/2}$ plot in 0.1 mM $K_3[Fe(CN)_6]$/0.1 M KCl aqueous solution.

Figure 2.21: The electrochemical performance of $Ni(OH)_2$/NF and $Ni(OH)_2$@CS/NF electrodes in 2 M KOH solution. (a) CV curves measured at a scan rate of 50 mV s^{-1}. (b) Galvanostatic charge-discharge (GCD) plots recorded at a current density of 20 mA cm^{-2}. (c) Specific capacity at different current densities.

Table 2.12 The areal capacity (mC cm^{-2}) of as-obtained LDH composites.

Current density (mA cm^{-2}) Composites	1	2	3	4	5
NiFe LDHs/NF	478.6	442.3	406.4	370.6	333.6
NiFe LDHs@CS/NF	705.8	685.7	649.8	610.1	576.6
NiCr LDHs/NF	592.6	527.3	482	446.4	417
NiCr LDHs@CS/NF	814.9	703	646.9	609.6	575.4
NiAl LDHs/NF	851.9	771.4	714.6	665.3	618.6
NiAl LDHs@CS/NF	1042.2	870.2	787.3	722.9	669

Notably, with the incorporation of carbon spheres, the areal capacity of NiFe LDHs@CS/NF, NiCr LDHs@CS/NF and NiAl LDHs@CS/NF were improved by 48%, 37% and 22% compared to NiFe LDHs/NF, NiCr LDHs/NF and NiAl LDHs/NF, respectively. All the samples presented excellent coulombic efficiencies (see **Table**

2.13).

Table 2.13 Coulombic efficiencies of as-prepared electrode materials.

Current density (mA cm⁻²) / Composites	1	2	3	4	5
NiFe LDHs/NF	94.9%	96.3%	96.2%	95.9%	95.2%
NiFe LDHs@CS/NF	71.1%	87.2%	91.1%	92.3%	93.2%
NiCr LDHs/NF	86.6%	92.8%	94.3%	94.8%	94.6%
NiCr LDHs@CS/NF	78.6%	86.4%	90.5%	92.3%	93.0%
NiAl LDHs/NF	95.1%	96.6%	97.1%	97.1%	96.8%
NiAl LDHs@CS/NF	81.0%	89.5%	92.4%	93.5%	94.0%

To further analyze the ion diffusion (low-frequency region) and charge transfer resistance (high-to-medium frequency region) of the samples, EIS was measured as illustrated in **Figure 2.20e**. R_s (the intersection of the plot with the X coordinate axis) and R_{ct} (the semicircle) of all the electrodes were obtained from the Nyquist plots (**Table 2.14**).

Table 2.14 Resistance values of as-prepared electrode materials.

Composites	Intrinsic resistance (R_s) / ohm cm⁻²	Charge transfer resistance (R_{ct}) / ohm cm⁻²
NiFe LDHs/NF	1.28	10.42
NiFe LDHs@CS/NF	1.30	20.78
NiCr LDHs/NF	1.08	38.78
NiCr LDHs@CS/NF	0.94	14.18
NiAl LDHs/NF	0.72	2.44
NiAl LDHs@CS/NF	1.44	22.40

R_s values of 1.28, 1.30, 0.11, 0.94, 0.72 and 1.44 ohm cm⁻² were determined for

NiFe LDHs/NF, NiFe LDHs@CS/NF, NiCr LDHs /NF, NiCr LDHs@CS/NF, NiAl LDHs/NF and NiAl LDHs@CS/NF, respectively, and the corresponding R_{ct} were 10.42, 20.78, 38.78, 14.18, 2.44 and 22.40 ohm cm^{-2}. Compared to NiFe LDHs@CS/NF and NiCr LDHs@CS/NF, NiAl LDHs@CS/NF possessed the smallest R_s but larger R_{ct}, even though it exhibited the largest areal capacity (**Figure 2.20b** and **d**). This might mainly be due to the larger electrochemical effective surface area.

Consequently, the real electrochemical effective surface area (A) of all electrodes was determined by chronocoulometry experiments using 0.1 mM K$_3$[Fe(CN)$_6$] as a probe molecule in 0.1 M KCl (**Figure 2.20f**), and the charge produced by the redox reaction at the electrodes using the Anson's **Equation 2.5**:

$$Q(t) = \frac{2nFAcD^{1/2}t^{1/2}}{\pi^{1/2}} + Q_{dl} + Q_{ads} \quad (Eq.\ 2.5)$$

where c is the substrate concentration (mol cm^{-3}), n is the number of electron transferred, F is the Faraday constant (9.6485×10^5 C mol^{-1}), A is the effective area of the electrode (cm^2), D stands for the diffusion coefficient (7.6×10^{-6} cm^2 s^{-1}), Q_{ads} is the Faradaic charge, Q_{dl} is the double layer charge, other symbols have their ordinary significance.

From the plot of Q $vs.$ t$^{1/2}$ (**Figure 2.20f**), NiAl LDHs@CS/NF displayed the largest electrochemical effective surface area of 182.8 cm^2, consistent with the above results. Notably, NiAl LDHs/NF holds a smaller electrochemical effective surface area (121.1 cm^2) than that of NiCr LDHs@CS/NF (159.5 cm^2) but larger areal capacity, which may be due to its better conductivity with smaller R_s but larger R_{ct}. As a result, the capacity of the electrode is not only related to conductivity, but also to the real electrochemical

effective surface area. Both of them encompass a great effect on the capacitance of the supercapacitors.

A hybrid supercapacitor cell was assembled in which the NiAl LDHs@CS/NF (1 cm×1 cm) was applied as the positive electrode and N-rGO/NF (1.5 cm×1.5 cm) acted as the negative electrode. The CV plots of N-rGO/NF and NiAl LDHs@CS/NF, performed in KOH (2 M) at 100 mV s^{-1} in a classical 2-electrode configuration cell, are presented in **Figure 2.22a**. Even though N-rGO/NF showed smaller CV area than that of NiAl LDHs@CS/NF, it exhibited a relatively larger operating potential window (-1 to 0.4 V), which is expected to greatly enhance the energy density of the hybrid supercapacitor.

In order to find a suitable working voltage window of the hybrid supercapacitor cell, the CV plots were performed at 100 mV s^{-1} in different cell voltage windows of 0-1.1, 0-1.2, 0-1.3, 0-1.4, 0-1.5, 0-1.6, 0-1.7 and 0-1.8 V. As can be seen in **Figure 2.22b**, the cell voltage window could be extended up to 1.8 V but with the existence of a polarization phenomenon. To protect the electrodes, the cell voltage window was limited to 0-1.6 V. Based on the results, the CV plots were acquired at various scan rates between 0 and 1.6 V (**Figure 2.22c**).
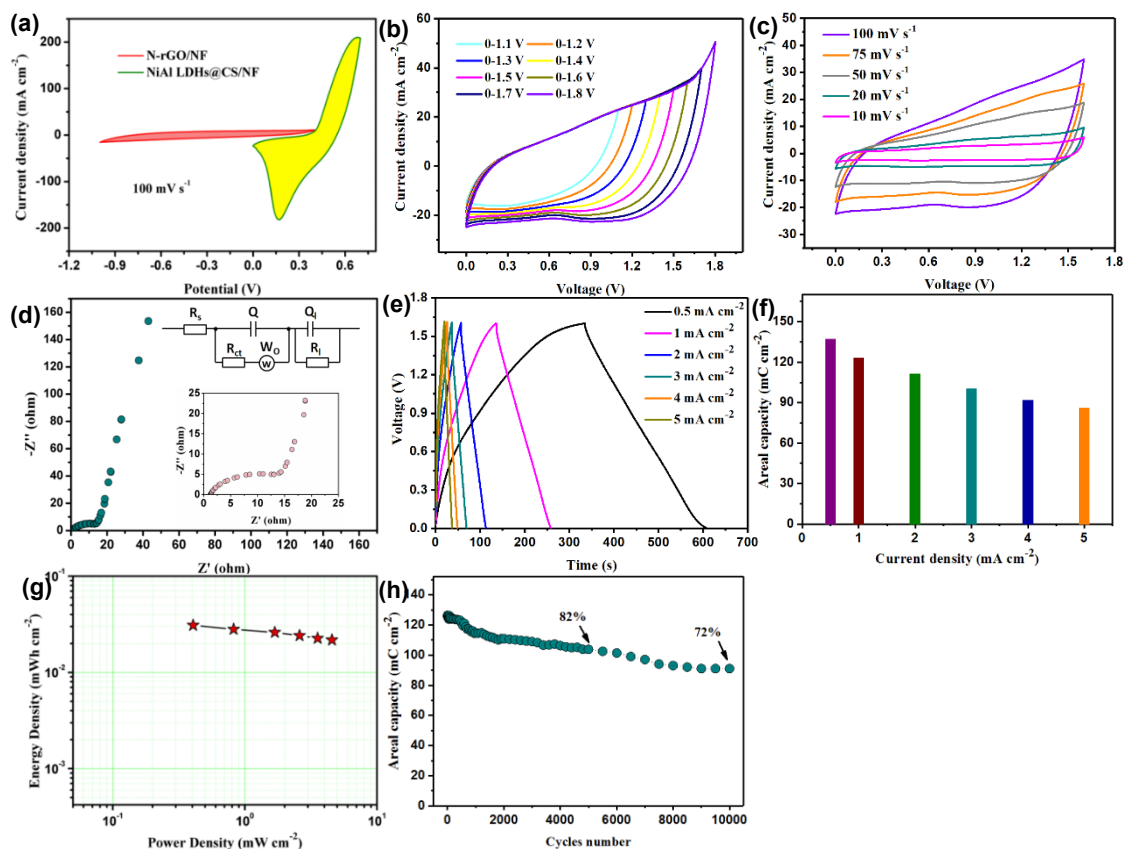
Figure 2.22: (a) CV curves of N-rGO/NF and NiAl LDHs@CS/NF performed at 100 mV s⁻¹ in a 3-electrode cell in KOH (2M) solution. (b) CV plots of the hybrid supercapacitor cell acquired at various cell voltage windows (scan rate=100 mV s⁻¹) in a classical 2-electrode configuration. (c) CV plots of the hybrid supercapacitor cell obtained at various scan rates. (d) EIS analysis of the hybrid supercapacitor cell measured in the 0.01 Hz and 100 kHz frequency range. The inset up-right in (d) is the corresponding equivalent circuit. (e) GCD profiles at various current densities. (f) Areal capacity at various current densities. (g) Ragone plot. (h) Cycling performance of the hybrid supercapacitor cell at 1 mA cm⁻².

Furthermore, EIS was recorded in the 100 kHz to 0.01 Hz frequency range; the electrochemical impedance equivalent circuit is displayed in the inset of **Figure 2.22d**.

R_s (the intersection of the plot with the X coordinate axis) and R_{ct} (the semicircle) of all the electrodes, obtained from the Nyquist plots, were 0.38 and 4.30 ohm cm^{-2}, respectively. From the GCD plots recorded at various current densities (**Figure 2.22e**) and **Equation 1.11.2**, the areal capacity of the hybrid supercapacitor cell was calculated as 137.2, 123.1, 111.4, 100.4, 91.7 and 85.8 mC cm^{-2} respectively at 0.5, 1, 2, 3, 4 and 5 mA cm^{-2} (**Figure 2.22f**). Consequently, according to **Equations 1.12** and **1.13**, the highest energy density achieved was 31 μWh cm^{-2} at a power density of 0.41 mW cm^{-2} (**Figure 2.22g**).

Furthermore, the stability of the hybrid supercapacitor cell plays an important role to evaluate its performance. Therefore, the hybrid supercapacitor was submitted to an extended charge–discharge cycling at 1 mA cm^{-2}. After 5,000 cycles, ~82% of the original capacity was retained, which slightly decreased to ~72% after 10,000 cycles (**Figure 2.22h**).

To highlight the potential of the as-fabricated supercapacitor cell for real applications, a home-designed windmill device was assembled successfully (see the schematic diagram in **Figure 2.23a**); it consists of an engine (1.5-9 V), a windmill and one as-fabricated supercapacitor cell. From **Figure 2.23a1-4**, we can see that the windmill rotated quickly, and with the consumption of energy, it stopped completely after 21 s.

Furthermore, when two hybrid supercapacitor cells were connected in parallel (insert of **Figure 2.23b**), the charge-discharge cell voltage window can reach up to 3.2

V with almost the same discharge time. Additionally, the two as-fabricated hybrid supercapacitor cells in series were applied to supply electricity to a red LED (1.8-2 V), a green LED (1.8-2 V), a yellow LED (1.8-2 V) and a blue LED (3-3.2 V) in parallel. The green, yellow and red LEDs were lightened for 37, 195, and 459 s, respectively, while the blue one was not because of the bigger operating voltage (**Figure 2.23b1-b5**). All of these findings demonstrate a promising practical energy storage application of the as-fabricated hybrid supercapacitor cells.
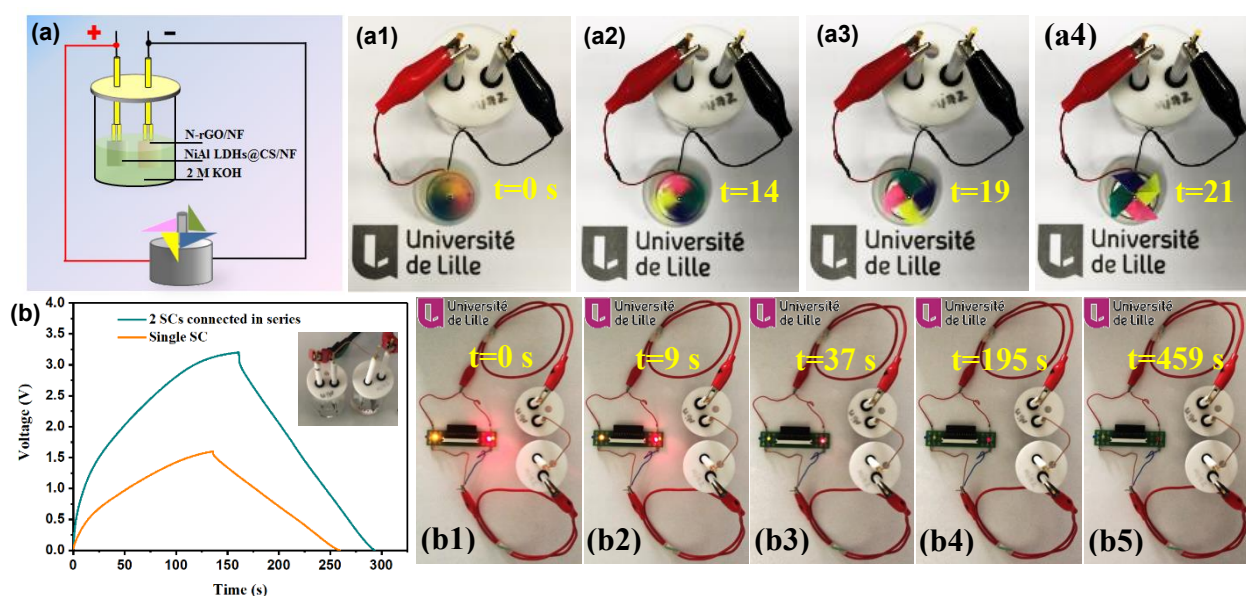

Figure 2.23: (a) Schematic of the hybrid supercapacitor cell operating a homemade windmill device. (a1 to a4) Photographs of the home-designed windmill device operation. (b) GCD curves of a single supercapacitor and two supercapacitors in series. The inset depicts the photograph of the two supercapacitors in series. (b1 to b5) A red LED, a green LED, a yellow LED and a blue LED in parallel lighten up by two supercapacitor cells in series.

Finally, a flexible hybrid supercapacitor device was assembled in which NiAl

LDHs@CS/NF (1 cm×1 cm) was applied as a positive electrode, (1.5 cm×1.5 cm) as a negative electrode, and one piece of filter paper immersed into KOH (2 M) aqueous solution for 30 min as a separator (**Figure 2.24a**). The electrochemical behavior of the device was assessed in a 2-electrode system, and the CV plots acquired at various cell voltage windows (scan rate = 100 mV s^{-1}) are displayed in **Figure 2.24b**. The results revealed that the cell voltage window could reach up to 1.8 V even though a polarization phenomenon was obvious when the cell voltage exceeds 1.7 V. In order to reduce the damage to the electrode and ensure stable operation of the device, the operating cell voltage window was chosen as 0-1.6V. **Figure 2.24c** displays the CV curves of the hybrid supercapacitor obtained at various scan rates (10 - 100 mV s^{-1}) between 0 and 1.6 V. The full device exhibited a capacitive-like characteristic with obvious deviation from ideal capacitive behavior although NiAl LDHs@CS/NF electrode performed as a battery electrode [93]. At the same time, as displayed in the Nyquist plot (**Figure 2.24d**), we can observe that the whole system reveals a smaller internal resistance (R_s=0.20 ohm cm^{-2}) and charge-transfer resistance (R_{ct}=0.84 ohm cm^{-2}) than that of the hybrid supercapacitor cell. A possible reason might be that the two integrated electrodes shorten the distance of electron transfer and ion diffusion. Consequently, the hybrid supercapacitor device exhibited a longer discharge time than that of the hybrid supercapacitor cell, signifying a larger areal capacity (**Figure 2.24e** and **f**).

According to **Equation 1.11.2**, the areal capacity of the hybrid supercapacitor device was calculated as 191.3, 166.1, 153.7, 149.8 and 145.2 mC cm^{-2} at 1, 2, 3, 4 and

5 mA cm^{-2} respectively (**Figure 2.24f**). According to **Equations 1.12** and **1.13**, the hybrid supercapacitor device attained the largest areal energy density of 43 μWh cm^{-2} at a power density of 0.805 mW cm^{-2} (**Figure 2.24g**). This value is higher than that achieved by Mg-Al LDH//rGO (24.07 μWh cm^{-2} at 81.2 μW cm^{-2}) [62], Ni-Co LDH//ketjenblack (14.4 μWh cm^{-2} at 312.5 μW cm^{-2}) [94], $Co_{0.85}Se$//AC (35.65 μWh cm^{-2} at 210 μW cm^{-2}) [95] hybrid supercapacitors, HCF fiber (27.1 μWh cm^{-2} at 66.5 μW cm^{-2}) [96], rGO/V_2O_5-rGO asymmetric flexible device (8.1 μWh cm^{-2} at 4.17 mW cm^{-2}) [97], Cu@Ni/porous Ni/$MnCo_2O_4$ symmetric supercapacitor (12.8 μWh cm^{-2} at 110 μW cm^{-2}) [98] and MnO_2/CNT//PI/CNT asymmetric supercapacitor (36.4 μWh cm^{-2} at 0.78 mW cm^{-2}) [99].

Furthermore, to test the flexibility and mechanical properties of the device and meet wearable requirements, the hybrid supercapacitor device in the middle of **Figure 2.24e** was bent at different angles (150, 90 and 60°); the CV curves, acquired at different angles, are almost overlapping together, indicating excellent flexibility and mechanical properties and providing promising potential for their application in wearable energy devices. Furthermore, the hybrid supercapacitor stability after 5,000 charging–discharging cycles was assessed (**Figure 2.24i**); the areal capacity remained ~75% and ~67% of its original value respectively after 5,000 and 10,000 cycles, suggesting a good reversibility.
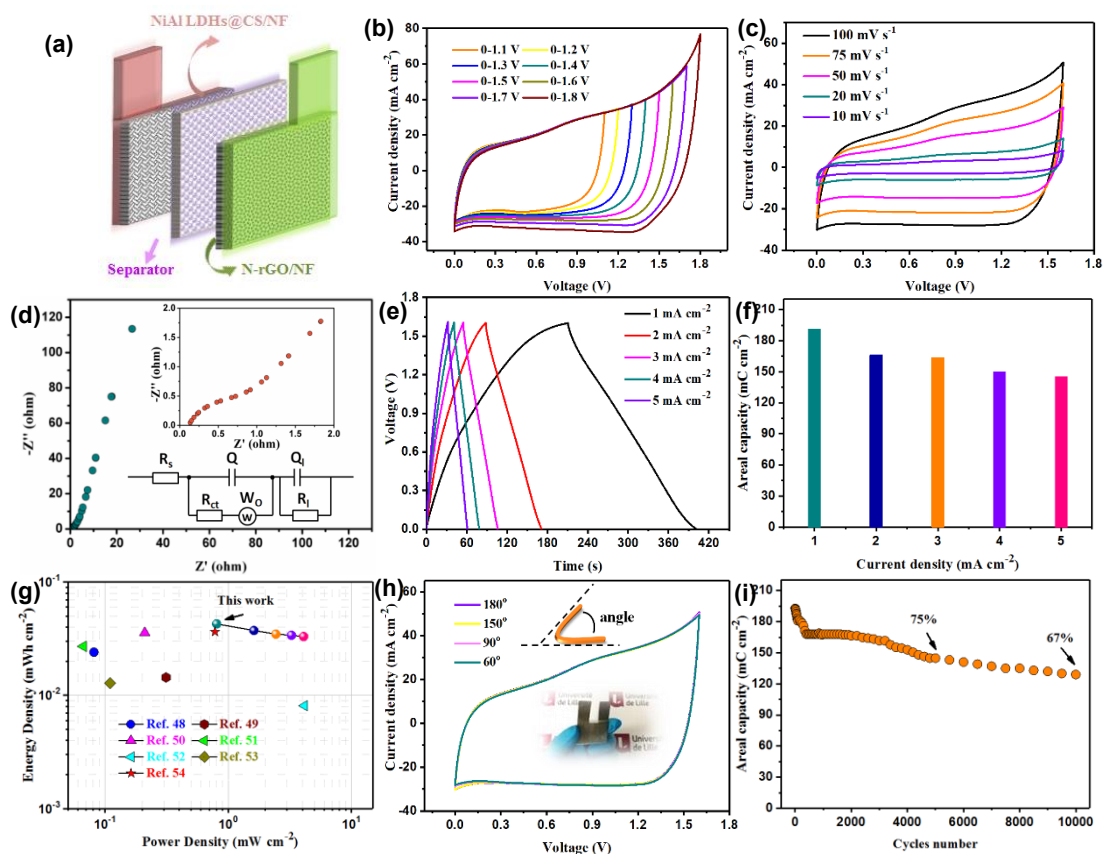
Figure 2.24: (a) Schematic of the hybrid supercapacitor. CV plots measured at (b) various cell voltage windows at 100 mV s^{-1} and (c) various scan rates between 0 and 1.6 V. (d) EIS curves acquired in the 0.01 Hz and 100 kHz frequency range. The inset up-right in (d) is the equivalent circuit. (e) GCD plots at various current densities. (f) Areal capacity at various current densities. (g) Ragone plot. (h) CV plots at acquired at 100 mV s^{-1} at different bending angles. The inset in middle of (h) is the photograph of the hybrid supercapacitor device. (i) Cycling performance at 1 mA cm^{-2}.

Furthermore, to test the practical applicability of the packed hybrid supercapacitor device, it was applied for a windmill device operation (schematic diagram in **Figure 2.25a**). Upon its connection with the hybrid supercapacitor device, the windmill rotates quickly (**Figure 2.25b-e**) and continuously for 32 s (**Figure 2.25b-e**).
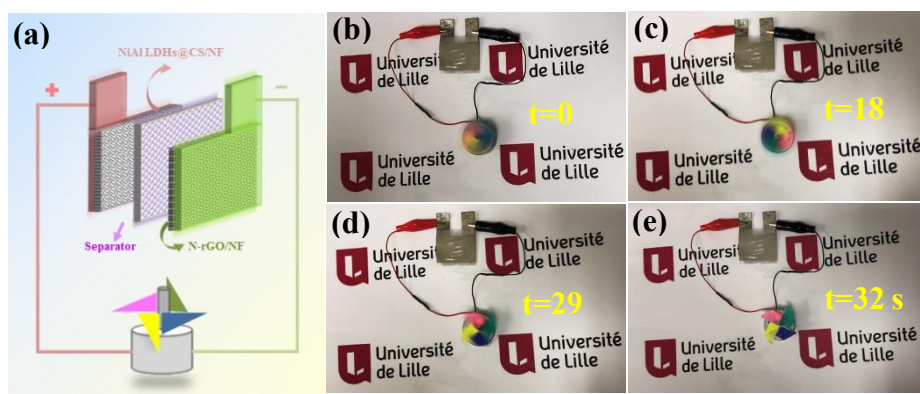
Figure 2.25: (a) Schematic diagram of the hybrid supercapacitor device for operating a homemade windmill device. (b-e) Photographs of the home-designed windmill device operation.

Finally, as shown in **Figure 2.26a-b**, when two hybrid supercapacitors were connected in series as the power source, the working cell voltage window can reach 3.2 V to supply 3 LEDs in parallel. The device can successfully light up three LEDs at the same time (**Figure 2.26c-h**). With the consumption of electricity, the light gradually dims and the green light went out after 37 s (**Figure 2.26e**), followed by the yellow one after 199 s (**Figure 2.26g**). The red LED becomes very dark but still lights up until 542 s. All the results suggest that the as-assembled hybrid supercapacitor device possess a promising potential for flexible energy storage applications.
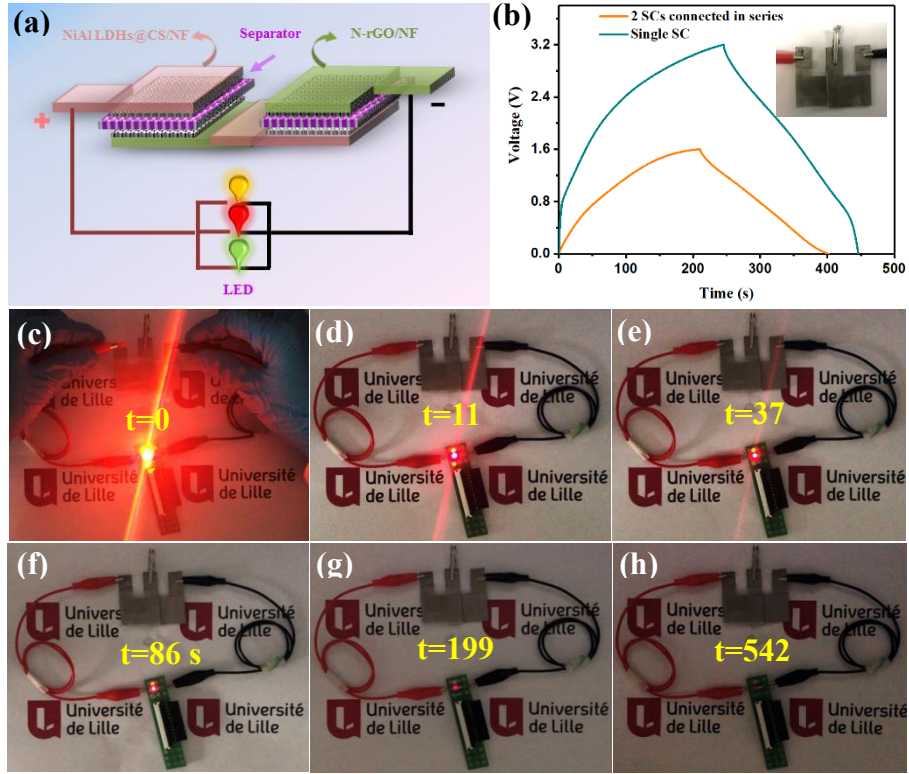
Figure 2.26: (a) Schematic diagram of the hybrid supercapacitor in series for lighting of LEDs in parallel. (b) GCD plots of a single supercapacitor and two supercapacitors in series. The inset depicts the photograph of the two supercapacitors devices in series. (c to h) A yellow LED, a red LED and a green LED in parallel lighted up by two supercapacitors in series.

2.4 NiMnCr Layered Double Hydroxides

Even though, LDHs-based supercapacitors are described in the binary structure, there are many opportunities for designing efficient electrode materials for supercapacitors based on LDHs, given the plethora of combinations of M^{2+}/M^{3+} offered by these materials. Owing to its plentiful oxidation states (from +1 to +6), Cr was chosen as the third metal in LDHs with the aim to further improve the intrinsic activity and performance of LDHs electrodes in supercapacitors.

We exploit, in this work, the capacitive properties of NiMnCr LDHs electrodes for energy storage and their improvement through hybridization with carbon spheres (CS) supported on nickel foam (NF) collector.

2.4.1 Experimental section

2.4.1.1 Synthesis of NiMnCr LDHs@CS/NF

Typically, $Mn(NO_3)_2\cdot4H_2O$ (0.45 mmol), $Cr(NO_3)_3\cdot9H_2O$ (0.075 mmol), $CO(NH_2)_2$ (4.5 mmol) and NH_4F (8 mmol) were placed in 30 mL of Milli-Q (MQ) water and stirred until formation of a homogeneous solution. The CS/NF, prepared using the same procedure as in **2.3.1.2**, was introduced into the above solution, and then transferred into a 50 mL autoclave. The mixture was placed in an oven at 120 ºC for 12 h. After being cooled to room temperature (RT), NiMnCr LDHs@CS/NF was separated by centrifugation, rinsed copiously with water and ethanol, and dried at 60 ºC for 24 h. It is noteworthy to mention that the nickel foam acts as a support, but also as a Ni source for LDHs formation during the hydrothermal reaction.

2.4.1.2　Synthesis of NiCr LDHs/NF

$Cr(NO_3)_3 \cdot 9H_2O$ (0.075 mmol), $CO(NH_2)_2$ (4.5 mmol) and NH_4F (8 mmol) were dissolved in 30 mL of Milli-Q (MQ) water and stirred to form a clear solution. A piece of nickel foam (NF) (3 cm×2 cm×0.5 cm) was dipped into the prepared solution, and transferred into a 50 mL Teflon-lined stainless-steel autoclave and heated at 120 °C for 12 h. After being cooled naturally to room temperature, the resulting NiCr LDHs/NF was washed copiously with water and ethanol, and dried at 60 °C for 24 h. It is noteworthy to mention that the nickel foam acts as a support, but also as a Ni source for LDHs formation during the hydrothermal process.

NiMn LDHs/NF was prepared with $Mn(NO_3)_2 \cdot 4H_2O$ (0.45 mmol) instead of $Cr(NO_3)_3 \cdot 9H_2O$ using the same procedure.

2.4.1.3　Synthesis of MnCr LDHs/CP

$Mn(NO_3)_2 \cdot 4H_2O$ (0.45 mmol), $Cr(NO_3)_3 \cdot 9H_2O$ (0.075 mmol), $CO(NH_2)_2$ (4.5 mmol) and NH_4F (8 mmol) were dissolved in 30 mL of MQ water and stirred to form a homogeneous solution. Carbon paper (CP) was dipped into the prepared solution, and transferred into a 50 mL Teflon-lined stainless-steel autoclave and heated at 120 °C for 12 h. After being cooled naturally to room temperature, the obtained MnCr LDHs/CP was washed copiously with water and ethanol, and dried at 60 °C for 24 h. Herein, CP acts as a support to avoid the Ni source.

2.4.1.4　Synthesis of FeOOH nanorods

In a typical synthesis, $Fe(NO_3)_3 \cdot 9H_2O$ (1 mmol), $CO(NH_2)_2$ (5 mmol) and NH_4F (1

mmol) were placed in 30 mL of deionized water. The mixture was stirred for 10 min till formation of a homogeneous solution. The resulting aqueous solution was placed in a Teflon-lined stainless-steel autoclave and heated at 120 °C for 6 h, and then cooled naturally to RT. The sample was rinsed copiously with deionized water and ethanol under ultrasonication, and dried at 60 °C for 24 h. Finally, the precursors were converted to FeOOH through annealing for 2 h at 350 °C.

2.4.1.5 Fabrication of a hybrid supercapacitor

To assemble a hybrid supercapacitor device, FeOOH/NF electrode was used as the negative electrode. The FeOOH/NF electrode consisted of FeOOH, carbon black and polyvinylidene difluoride (PVDF) in a mass ratio of 7:2:1, which was pasted on the nickel foam; the final mass of FeOOH was 3.57 mg.

Using as-prepared NiMnCr LDHs@CS/NF (1 cm×1 cm) as the positive electrode and FeOOH/NF as the negative electrode, a hybrid supercapacitor device was assembled with the separator consisting of a filter paper soaked into KOH (2 M) solution for 30 min.

To acquire the optimal performance of the hybrid supercapacitor, a charge balance Q_+ (charges stored in the positive electrode) = Q_- (charges stored in the negative electrode) between the two electrodes is necessary so that the mass balancing follows the **Equation 1.6**. The optimal mass ratio is ~0.13, but it is difficult to control the accurate mass of FeOOH when mixing and pressing FeOOH powder with auxiliary materials such as carbon black or binder onto the Ni foam. Therefore, the mass loadings

of NiMnCr LDHs@CS/NF and FeOOH on Ni foam are 1.165 and 3.57 mg, respectively, which corresponds to a mass ratio of 0.33 in our work.

Electrochemical characterization was performed in a two-electrode system at room temperature.

2.4.2 Results and discussion

The fabrication process of the NiMnCr LDHs@CS/NF electrode is illustrated in **Figure 2.27a**. Carbon spheres (CS) were first decorated on NF by a simple hydrothermal decomposition of glucose at 190°C for 4 h, followed by coating of NiMnCr LDHs at 120°C for 12 h using $Mn(NO_3)_2 \cdot 4H_2O$, $Cr(NO_3)_3 \cdot 9H_2O$, $CO(NH_2)_2$ and NH_4F precursors. The chemical process can be described using **Equations (2.6-2.8)** below:

$$NH_4F + H_2O \rightarrow NH_4^+ + OH^- + HF \qquad \text{(Eq. 2.6)}$$

$$CO(NH_2)_2 + 3H_2O \rightarrow 2NH_4^+ + 2OH^- + CO_2 \qquad \text{(Eq. 2.7)}$$

$$Ni^{2+} + Mn^{2+} + Cr^{3+} + OH^- \rightarrow NiMnCr\ LDHs \qquad \text{(Eq. 2.8)}$$

The reactions, under the hydrothermal conditions, mainly involve progressive hydrolysis of NH_4F and decomposition of $CO(NH_2)_2$, forming the NiMnCr LDHs on the NF substrate. It is noteworthy to mention that Ni^{2+} required for NiMnCr LDH formation originates from the Ni foam dissolution under our experimental conditions. Indeed, during the hydrothermal process, NH_4F dissolves nickel oxides on the Ni foam to release Ni^{2+} in the solution. As illustrated in **Figure 2.27b**, the existence of carbon

spheres (CSs) layer on the NF surface could act as the bridge between NiMnCr LDHs and NF, which could decrease the length of charge transfer and facilitate the charge transfer, further promoting the electrochemical kinetics. For comparison, a control sample consisting of NiMnCr LDHs/NF was prepared under the same experimental conditions, but in the absence of CS.
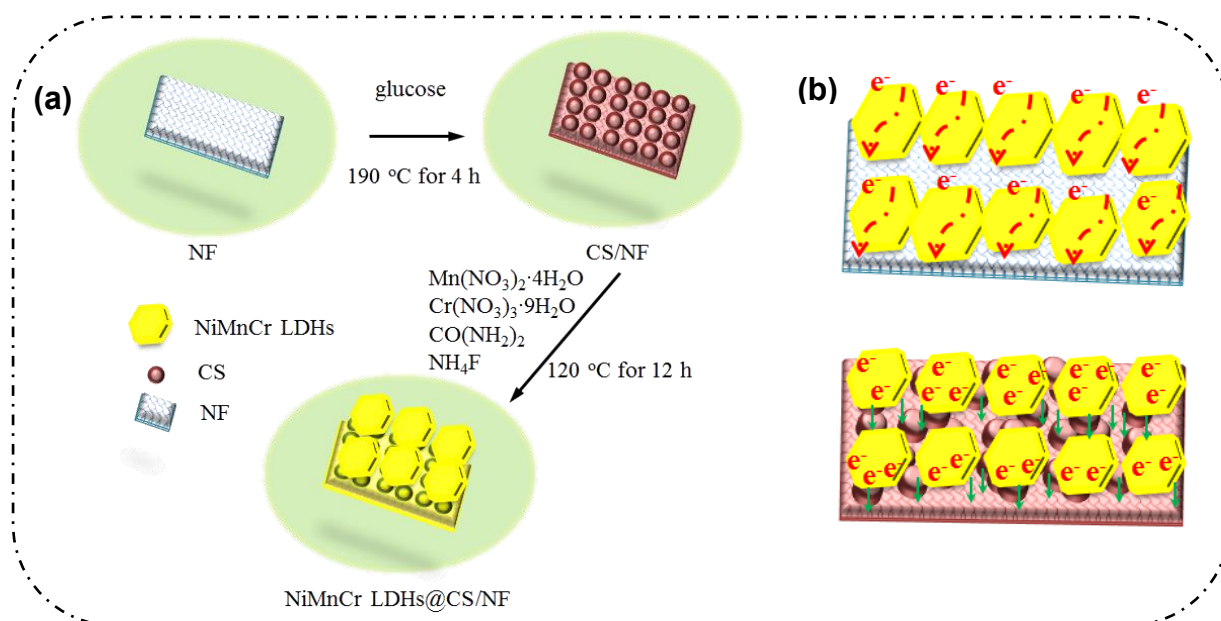

Figure 2.27: Schematic illustrations of **(a)** the synthesis of NiMnCr LDHs@CS/NF electrode using a two-step hydrothermal method, and **(b)** charge transport process in NiMnCr LDHs/NF and NiMnCr LDHs@CS/NF electrodes.

Figure 2.28a displays the XRD patterns of as-obtained materials. The patterns comprise several typical diffraction peaks of LDHs at 11.4º, 24.1º, 31.4º, 34.4º, 38.7º, 41.2 º, 59.9º and 64.6º ascribed to the (006), (009), (012), (015), (018), (110) and (113) diffraction planes, respectively.
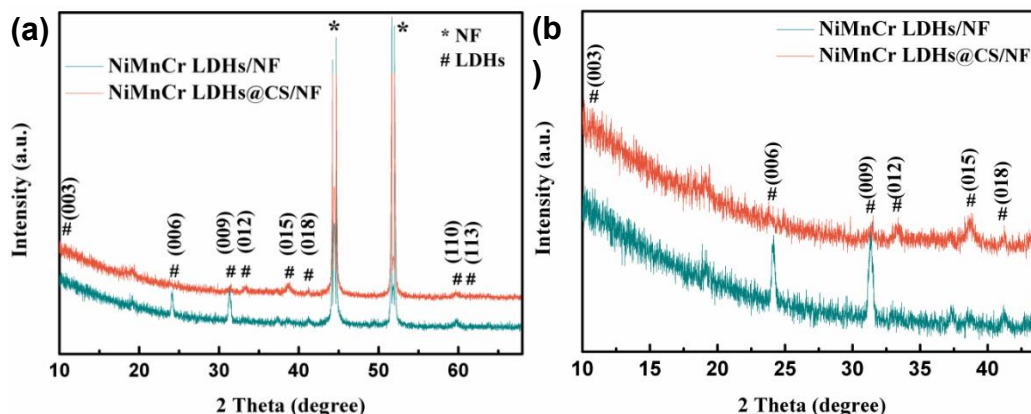
Figure 2.28：(a) XRD patterns of NiMnCr LDHs/NF and NiMnCr LDHs@CS/NF, (b) magnified patterns in the 10–44º range.

At the same time, as a negative electrode candidate for hybrid supercapacitors, the XRD pattern of FeOOH nanorods was also recorded (**Figure 2.29**) and shows diffraction peaks at 28.4 º, 34.4 º, 35.9 º, 39.5 º, 41.2 º, 46.6 º, 48.9 º, 56.3 º, 62.6 º and 64.1 º, which are indexed to the (130), (400), (211), (301), (031), (411), (141), (060), (002) and (112) diffraction planes (JCPDS card no. 18-0639), respectively. Notably, FeOOH nanorods were not completely pure with some weak peaks observed at 30.4º, 35.7º, 44.5º and 57.5º, corresponding to the (220), (311), (400) and (511) diffraction planes of Fe_3O_4 (JCPDS card no. 75-0449) [100].
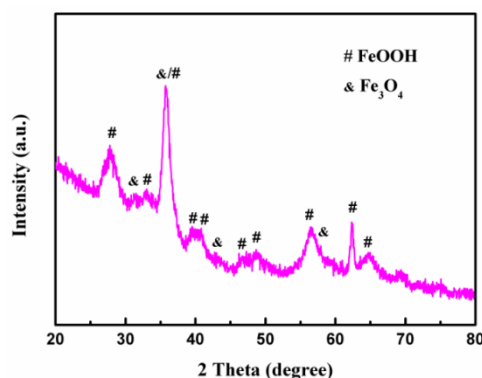

Figure 2.29: XRD pattern of FeOOH nanorods.

The morphology of CS/NF, NiMnCr LDHs/NF and NiMnCr LDHs@CS/NF was assessed by scanning electron microscopy (SEM). **Figure 2.30a** and **b** depicts the low and high magnifications SEM images of the carbon spheres used herein to improving the electrical conductivity of the material and the contact area. A dense layer of CS of ~400 nm in diameter was formed on the NF surface. All the spheres exhibit a smooth surface, suggesting the homogeneous polymerization of glucose during the hydrothermal process (**Fig. 2.30b**). **Figure 2.30c** and **d** display a NF directly coated with NiMnCr LDHs in absence of CS support. A flat lunar surface was clearly visible, which contrasts with NiMnCr LDHs supported on CS/NF where an uneven shape with rounded small protrusions (**Figure 2.30e, f**) was observed. Due to the thick NiMnCr LDHs layer (~1 μm), the CSs were not any longer visible in the SEM image even from the cross-sectional SEM image of NiMnCr LDHs@CS/NF in **Figure 2.31**, suggesting that the CSs were completely coated by NiMnCr LDHs. This could be also the reason why no diffraction peaks of CSs in the XRD pattern of NiMnCr LDHs@CS/NF were observed in **Figure 2.28**. This morphology is expected to increase the material/electrolyte contact area, which would further improve the overall performance of the electrode. As illustrated in **Figure 2.30g** and **Figure 2.31b**, the EDS elemental mapping of NiMnCr LDHs@CS/NF revealed Ni, Mn, Cr, C and O elements distributed homogeneously on the material.
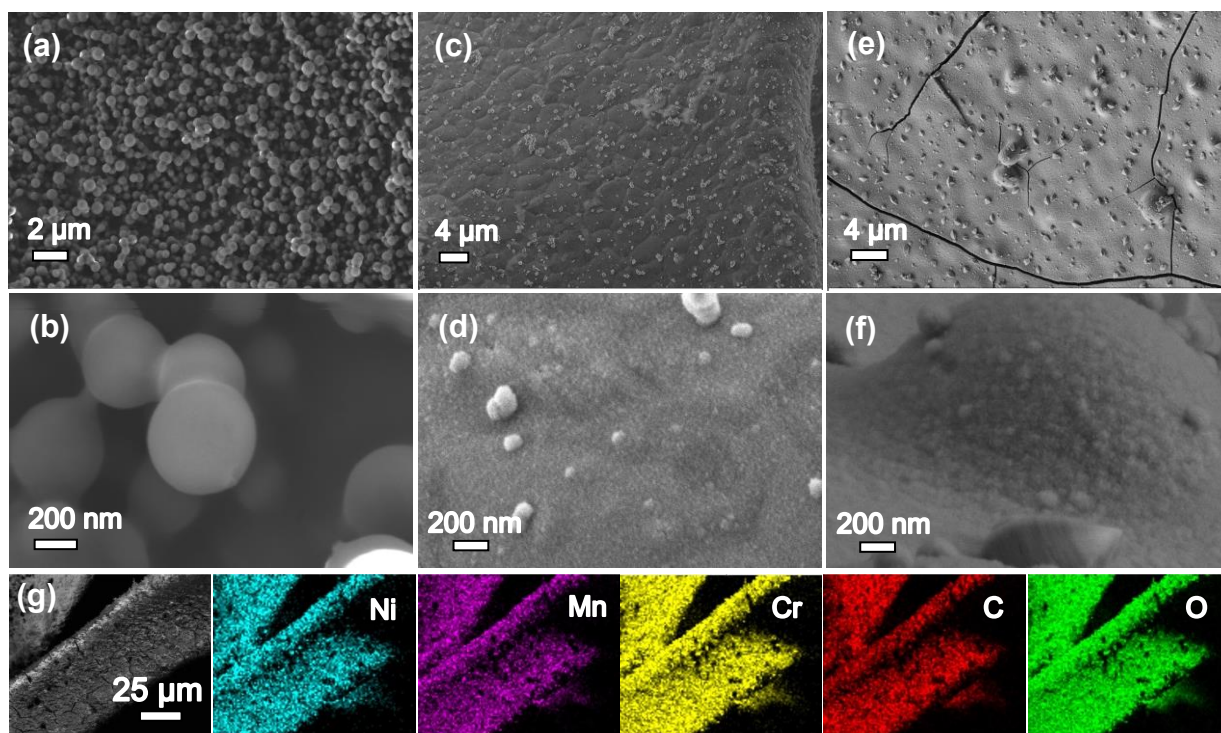
Figure 2.30: SEM images of (a, b) CS/NF, (c, d) NiMnCr LDHs/NF and (e, f)

NiMnCr LDHs@CS/NF. (g) EDS elemental mapping images of Ni, Mn, Cr, C and O
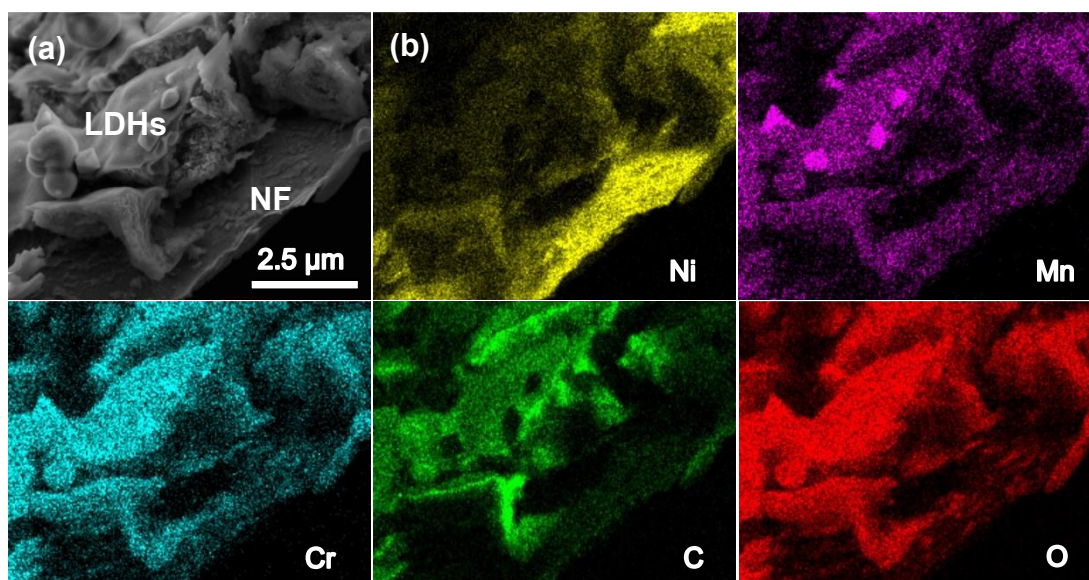
of NiMnCr LDHs@CS/NF.

Figure 2.31: (a) Cross-section SEM images of NiMnCr LDHs@CS/NF, (b) the

corresponding EDS elemental mapping images of Ni, Mn, Cr, C and O.

Furthermore, transmission electron microscopy (TEM) was performed to assess the micro-structure and morphology of NiMnCr LDHs@CS/NF (**Figure 2.32**). **Figure 2.32b, c** depicts the high high-resolution TEM (HRTEM) images of NiMnCr LDHs@CS/NF, revealing two types of lattice spacings of 0.26 and 0.38 nm, ascribed respectively to (012) and (006) planes of LDHs. These findings are in good accordance with the XRD results in **Figure 2.32**. **Figure 2.32d** exhibits the corresponding EDS elemental mapping where Ni, Mn, Cr, C and O elements are homogeneously distributed, matching the results presented in **Figure 2.30g** and **Figure 2.31b**.
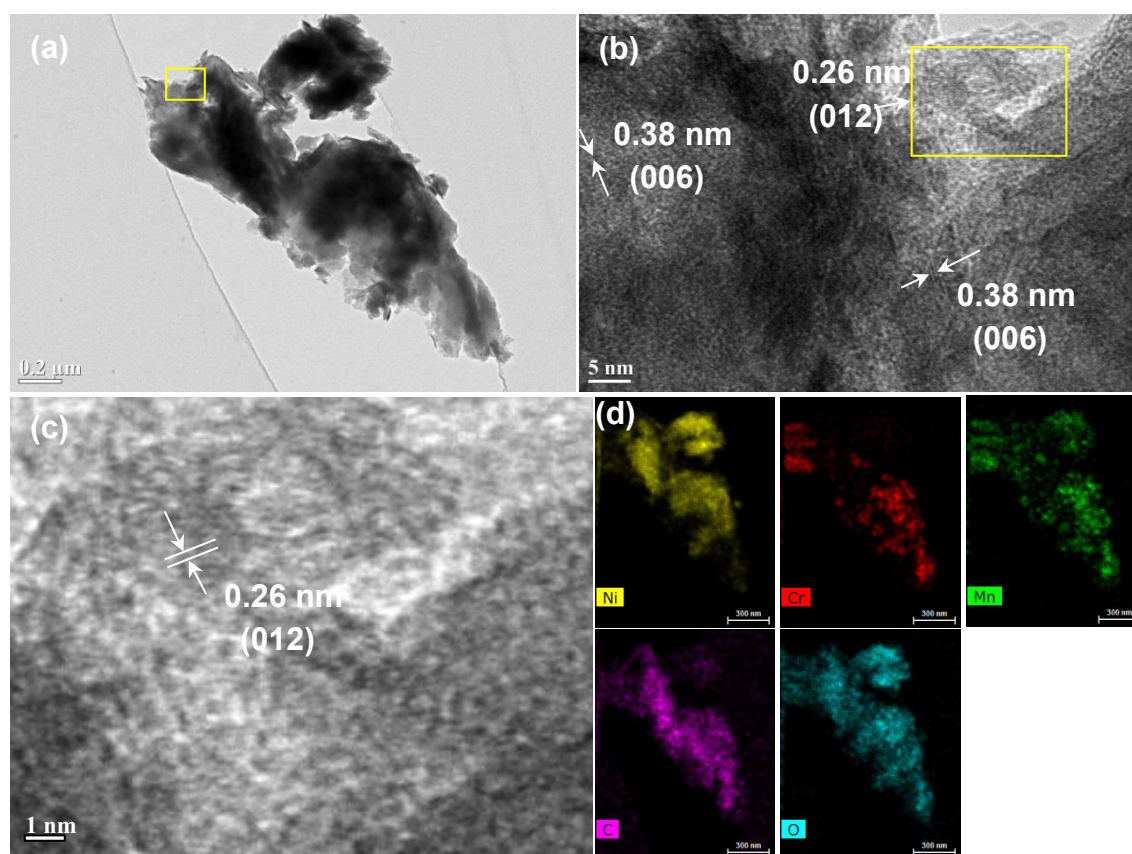

Figure 2.32: (a) TEM and (b) high-resolution TEM images of NiMnCr LDHs@CS/NF, (d) is the corresponding EDS elemental mapping of Ni, Mn, Cr, C and O elements.

X-ray photoelectron spectroscopy (XPS) was acquired to evaluate the elemental composition of NiMnCr LDHs@CS/NF (**Figure 2.33**) and NiMnCr LDHs/NF (**Figure 2.34**) composites. The wide scan XPS spectrum revealed that the electrode material consists of Ni_{2p}, Mn_{2p}, Cr_{2p}, C_{1s} and O_{1s} elements, in agreement with the elemental composition of the material. The corresponding elemental compositions are illustrated in **Table 2.15**.

The Ni_{2p} high-resolution spectrum (3.5 at%) of NiMnCr LDHs@CS/NF composite (**Figure 2.33b**) comprises two peaks due to $Ni_{2p3/2}$ and $Ni_{2p1/2}$ located respectively at 854.8 and 872.5 eV along with two satellite peaks [37]. The presence of the satellite peaks is a good indication that the nickel in the LDH is in its +2 oxidation state.

Table 2.15: Elemental composition of the samples.

Elements (at%) Composites	Ni_{2p}	Mn_{2p}	Cr_{2p}	C_{1s}	O_{1s}
NiMnCr LDHs/NF	4.6	6.0	2.4	43.3	43.7
NiMnCr LDHs@CS/NF	3.5	7.6	5.6	42.4	40.9

Figure 2.33c depicts the Mn_{2p} core level spectrum (7.6 at%) of NiMnCr LDHs@CS/NF composite, which can be fitted with two components at 652.4 and 641.1 eV assigned respectively to $Mn_{2p1/2}$ and $Mn_{2p3/2}$ peaks, indicating the presence of Mn^{3+} [101, 102]. It is easy to oxidize Mn^{2+} to Mn^{3+} due to the low redox potential under alkaline conditions. The Cr_{2p} core level spectrum (2.4 at%) of NiMnCr LDHs@CS/NF composite can be deconvoluted in two bands at 586.1 and 576.4 eV ascribed respectively to $Cr_{2p1/2}$ and $Cr_{2p3/2}$, suggesting that Cr is trivalent [4] (**Figure 2.33d**).

Figure 2.33e displays the C_{1s} core level spectrum, which can be curve-fitted with two components due to C=C (284.1 eV) and C-O (286.4 eV). The O_{1s} high resolution spectrum in **Figure 2.33f** can be curve-fitted with a single component derived from – OH groups in LDHs.
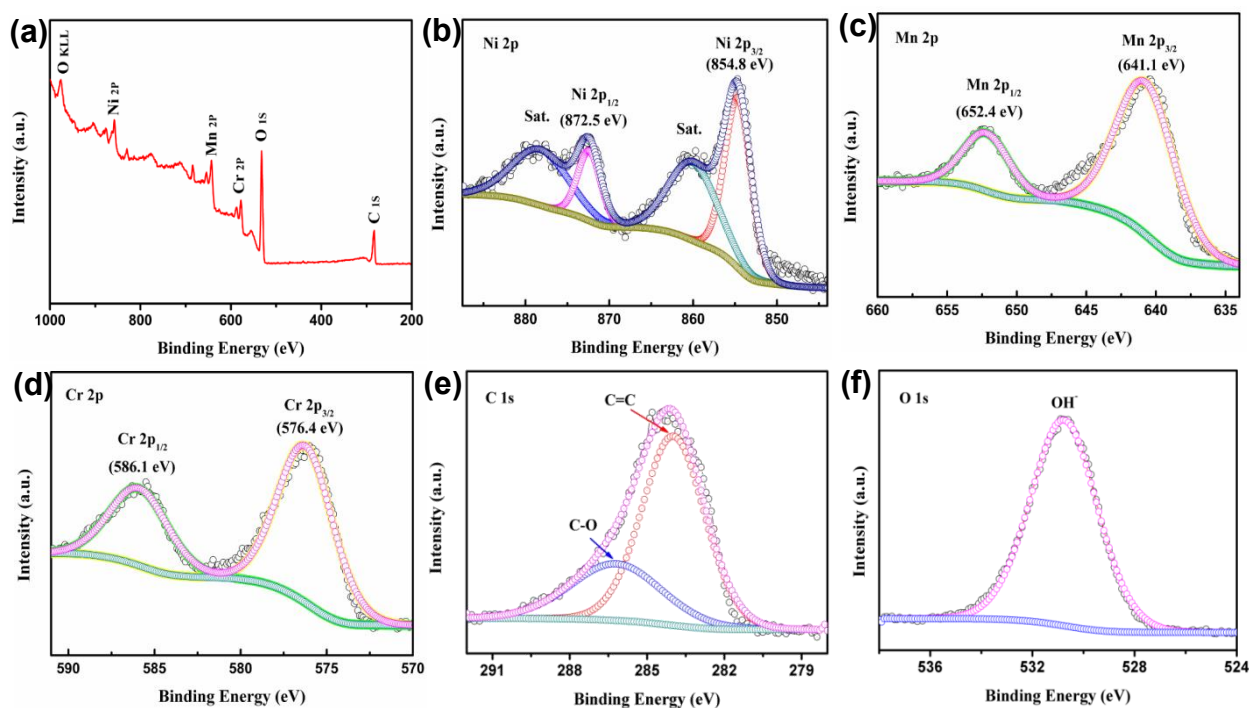

Figure 2.33: XPS analysis of NiMnCr LDHs@CS/NF: (a) Survey spectrum, and core level spectra of (b) Ni_{2p}, (c) Mn_{2p}, (d) Cr_{2p}, (e) C1s and (f) O_{1s}.

Similarly, XPS analysis of NiMnCr LDHs/NF composite revealed a comparable composition to that of NiMnCr LDHs@CS/NF composite with a slight shift of the binding energies of Ni_{2p} (4.6 at%), Mn_{2p} (6.0 at%) and Cr_{2p} (2.4 at%) (**Figure 2.34**).
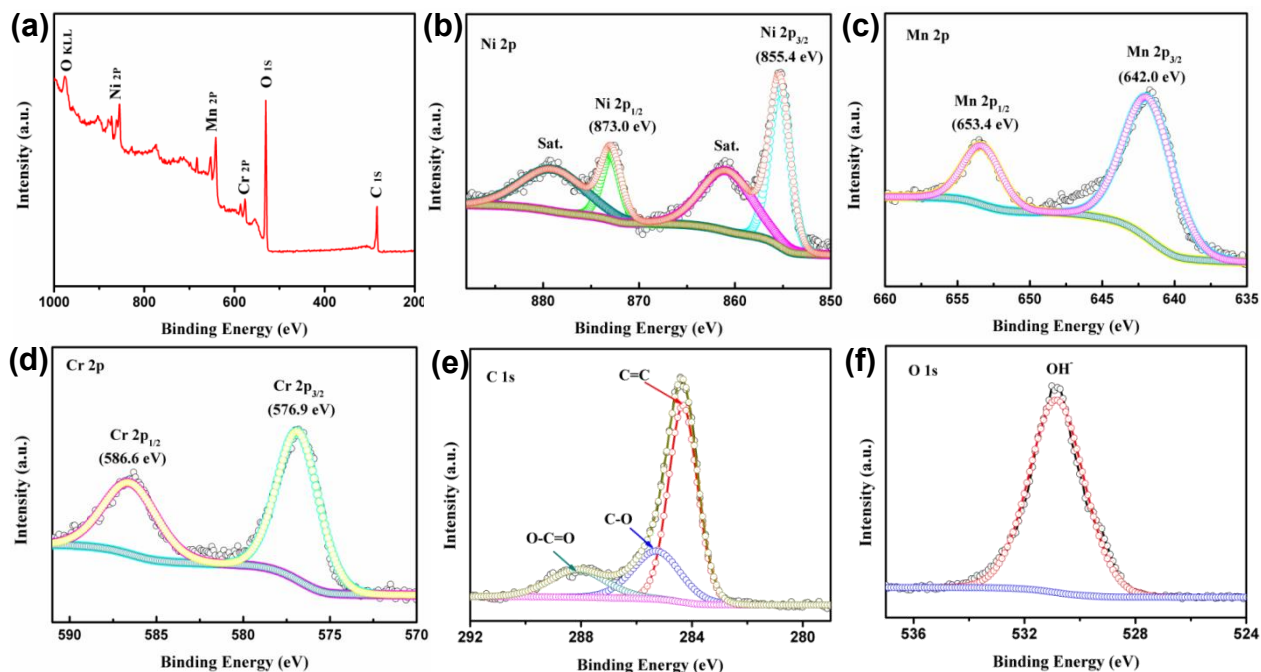
Figure 2.34: XPS analysis of NiMnCr LDHs/NF: (a) Survey spectrum, and high resolution spectra of (b) Ni_{2p}, (c) Mn_{2p}, (d) Cr_{2p}, (e) C_{1s} and (f) O_{1s}.

All electrochemical measurements were conducted in a classical three-electrode configuration cell containing 2 M KOH aqueous solution as the electrolyte using an electrochemical workstation (Autolab, Methrom) at ambient temperature. The as-obtained samples were employed as the working electrode. A platinum foil and Ag/AgCl electrodes acted as the counter and reference electrodes, respectively.

The CV curves of NiCr LDHs/NF, NiMn LDHs/NF, and NiMnCr LDHs/NF were displayed in **Figure 2.35a**. Compared with NiCr LDHs/NF and NiMn LDHs/NF, NiMnCr LDHs/NF exhibited the highest current response along with a slight shift, which could be a consequence of a synergistic effect of Ni, Mn and Cr elements. Without the Ni participation, MnCr LDHs was coated on carbon paper (MnCr LDHs/CP), and there are no apparent redox peaks observed in the CV curves (**Figure**

2.35b). In contrast, the CV curves of NiCr LDHs/NF, NiMn LDHs/NF and NiMnCr LDHs/NF presented apparent similar redox peaks, further proving that the redox peaks are due to Ni(II)/Ni(III) in the NiMnCr LDHs hydroxide sheets, which is descried in **Equation 2.1**.
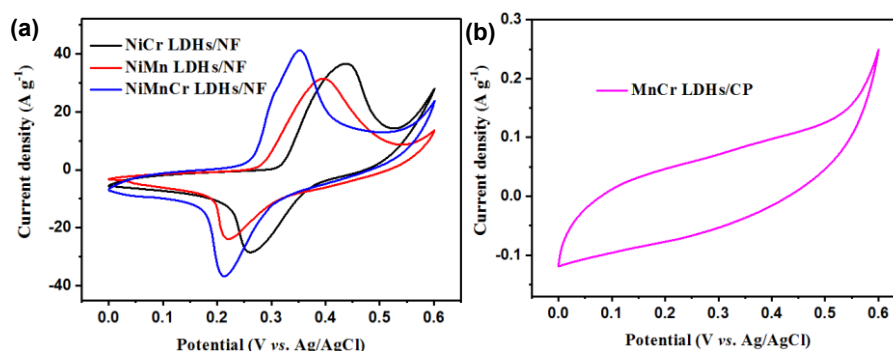

Figure 2.35: CV curves of (a) NiCr LDHs/NF, NiMn LDHs/NF, NiMnCr LDHs/NF and (b) MnCr LDHs/NF measured at a scan rate of 50 mV s^{-1} in 2 M KOH solution.

Furthermore, **Figure 2.36a** presents the CV curves of NF, CS/NF, NiMnCr LDHs/NF and NiMnCr LDHs@CS/NF (scan rate=100 mV s^{-1}). There is no apparent change of the shape of these curves; all of them exhibit obvious redox peaks, which could be attributed to Ni(II)/Ni(III) in the NiMnCr LDHs hydroxide sheets. The CV curves (**Figure 2.36b**) indicate that the peak current of NiMnCr LDHs@CS/NF electrode increases with insignificant change in the curve shape, and the peak potential shifts as the scan rate increases, due to increased internal resistance under higher scan rates.
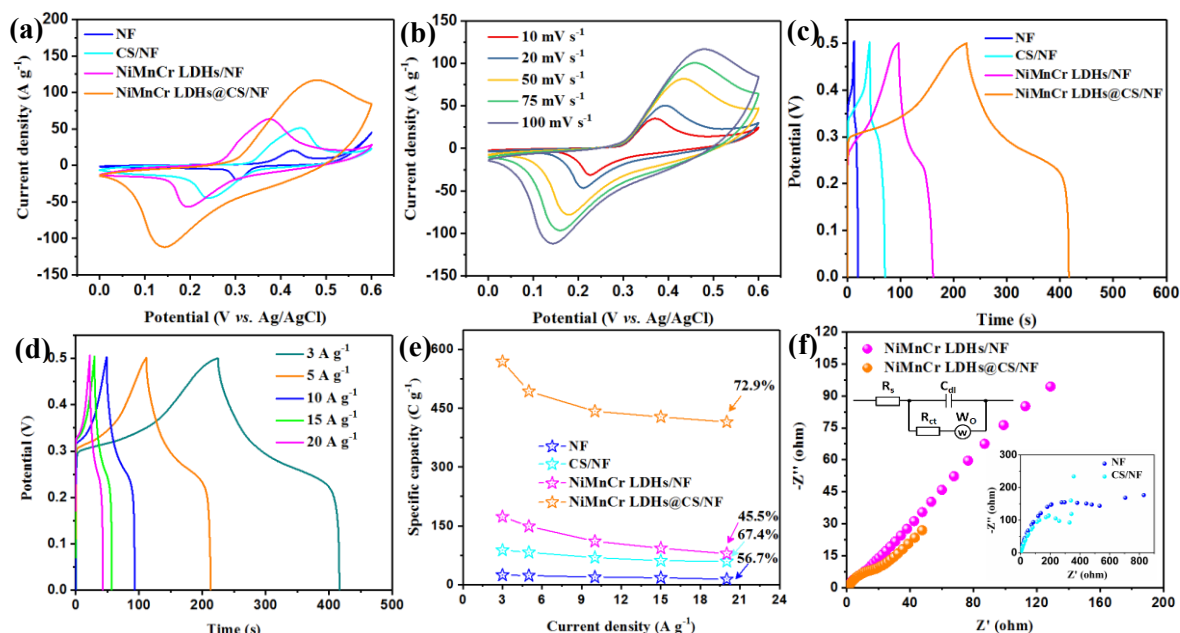
Figure 2.36 The electrochemical behavior of the electrodes measured in 2 M KOH aqueous solution. (a) CV curves acquired at 100 mV s^{-1}. (b) CV curves of NiMnCr LDHs@CS/NF recorded at different scan rates. (c) GCD curves of the electrodes at 3 A g^{-1}. (d) GCD curves of the electrodes at different current densities. (e) Specific capacity of the electrodes at different current densities. (f) Electrochemical impedance spectra of NiMnCr LDHs /NF and NiMnCr LDHs@CS/NF recorded at open circuit potential in the 0.01 Hz to 100 kHz frequency range, the inset in the top-right of (f) is the corresponding equivalent circuit and the inset in the bottom of (f) are electrochemical impedance spectra of NF and CS/NF recorded at open circuit potential in the 0.01 Hz to 100 kHz frequency range.

Figure 2.36c indicates that in the presence of CS, NiMnCr LDHs@CS/NF composite possesses larger charging/discharging time, suggesting higher specific capacity. In fact, a specific capacity of 569 C g^{-1} at 3 A g^{-1} was determined, surpassing

that of NF (24.4 C g^{-1}), CS/NF (88 C g^{-1}) and NiMnCr LDHs/NF (174.2 C g^{-1}). To establish the performance of NiMnCr LDHs@CS/NF composite, galvanostatic charge-discharge (GCD) curves were measured at various current densities (**Figure 2.36d**). **Figure 2.36e** and **Table 2.16** summarize the specific capacity values of the various electrodes at different current densities, which are determined using **Equation 1.11.2** from the values in **Figure 2.40d**.

Table 2.16: Specific capacity values (C g^{-1}) of the various electrodes investigated in this work at different current densities.

Current density (A g^{-1}) \ Samples	NF	CS/NF	NiMnCr LDHs/NF	NiMnCr LDHs@CS/NF
3	24.4	88	174.2	569
5	24.2	82.3	148.8	494.2
10	19.2	69.1	110.7	442.2
15	17.6	61.1	92.9	427.9
20	14.9	59.3	78.9	414.7

The results clearly revealed that NiMnCr LDHs/NF and NiMnCr LDHs@CS/NF exhibit higher specific capacity values than NF and CS/NF with NiMnCr LDHs@CS/NF featuring a better rate performance and specific capacity of 569, 494.2, 442.2, 427.9 and 414.7 C g^{-1} at 3, 5, 10, 15 and 20 A g^{-1}, respectively. The specific capacity value remained high (73% of the specific capacity recorded at 3 A g^{-1}) even at 20 A g^{-1}. At the same time, the IR drop of NiMnCr LDHs@CS/NF composite was lower (8 mV) than that of NiMnCr LDHs/NF (12 mV), indicating a relatively lower charge-

transfer resistance; this property contributes for the better rate performance of NiMnCr LDHs@CS/NF electrode.

EIS measurements, performed in the frequency range from 100 kHz to 0.01 Hz in 2 M KOH (Figure **2.36f**), revealed that the Nyquist plots are similar in shape and comprise a small semicircle at high frequency region and a slope line (Warburg curve) in the low frequency region. The equivalent circuit for impedance analysis is illustrated in the inset of **Figure 2.36f** (R_{ct}, R_s, C_{dl}, and W_o stand respectively for the charge-transfer resistance, internal resistance, double-layer capacitance, and Warburg element). From these measurements, we can see that compared to pure NF (622.7 Ohm cm^{-2}), CS/NF exhibits a smaller charge-transfer resistance (379.6 Ohm cm^{-2}). Even though NiMnCr LDHs@CS/NF composite possesses a relatively higher internal resistance (1.167 Ohm cm^{-2}), it displays a smallest semicircle in the high frequency region related to the electrochemical reaction process, which means a lowest charge-transfer resistance of 15.03 Ohm cm^{-2}, smaller than that NiMnCr LDHs/NF (18.28 Ohm cm^{-2}) (**Table 2.17**), consistent with the low IR drop. The results indicate that the existence of CS could facilitate the charge transfer and promote the electrochemical kinetics, as illustrated in **Figure 2.27b**.

Table 2.17 Resistance values of the various electrodes investigated in this work.

Composites	R_s *(Ohm cm^{-2})*	R_{ct} *(Ohm cm^{-2})*
NF	0.703	622.7
CS/NF	1.078	379.6
NiMnCr LDHs/NF	0.911	18.28

NiMnCr LDHs@CS/NF	1.167	15.03

As observed in **Figure 2.37,** NiMnCr LDHs@CS/NF electrode displays good stability after 10,000 cycles at 20 A g^{-1}; the electrode maintained ~76% of its initial value, which is better than ~54% achieved by NiMnCr LDHs/NF under the same cycling conditions.
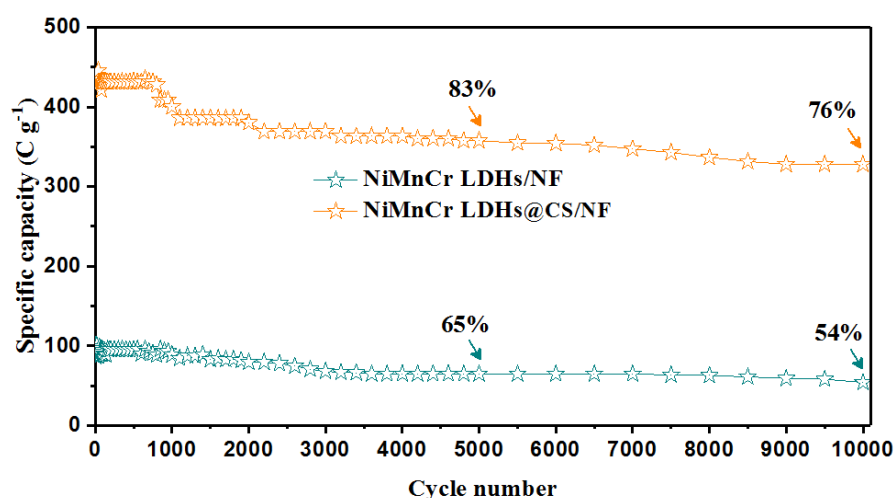

Figure 2.37: Cycling performance of NiMnCr LDHs@CS/NF and NiMnCr LDHs/NF at a constant current density of 20 A g^{-1}.

Figure 2.38 depicts the SEM images and the corresponding EDS elemental mapping images of NiMnCr LDHs/NF and NiMnCr LDHs@CS/NF after cycling. After 10,000 cycles, most of the NiMnCr LDHs on NF disappeared in NiMnCr LDHs/NF composites (**Figure 2.38a**), but there are still Ni, Mn, Cr, C and O elements distributed homogeneously on the material, with the existence of K element from the KOH electrolyte. For the NiMnCr LDHs@CS/NF composite, cracks appeared in the SEM image of the electrode material and the presence CSs becomes evident. Similarly, EDX

mapping revealed the existence of Ni, Mn, Cr, C, O and K elements (**Figure 2.38b**).

NiMnCr LDHs@CS/NF composite exhibited a more stable morphology compared to

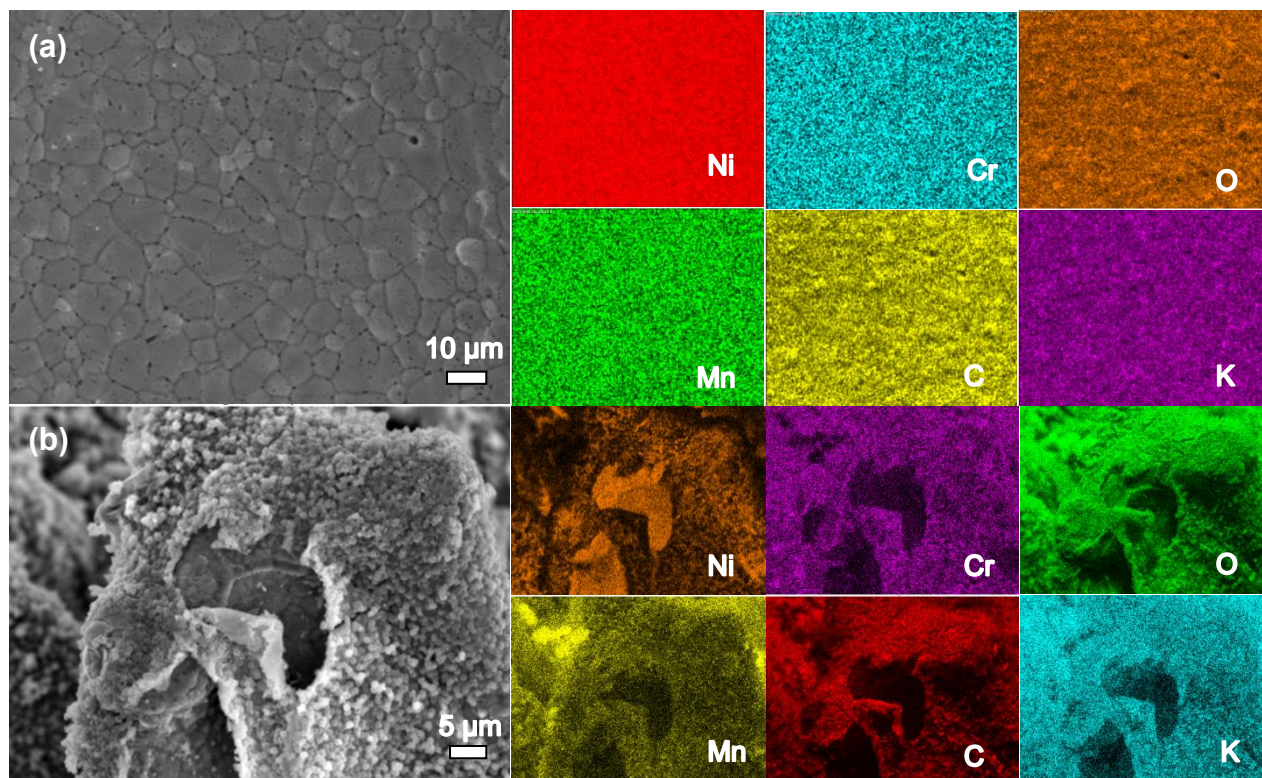NiMnCr LDHs/NF owing to the presence of CSs.

Figure 2.38: SEM images of (a) NiMnCr LDHs/NF and (b) NiMnCr LDHs@CS/NF

after 10,000 cycles and the corresponding EDS elemental mapping of Ni, Mn, Cr, C,

O and K elements.

XPS analysis of the NiMnCr LDHs/NF and NiMnCr LDHs@CS/NF electrode

materials after cycling was further acquired (**Figure 2.39** and **2.40**). From the XPS

survey spectra in **Figure 2.39** and **2.40**, we can see that both NiMnCr LDHs/NF and

NiMnCr LDHs@CS/NF still comprise Ni_{2p}, Mn_{2p}, C_{1s} and O_{1s} elements, while Cr_{2p} was

absent. An additional peak due to K_{2p}, originating from the KOH electrolyte, appeared.

Furthermore, by analyzing the elements composition changes (**Table 2.18**), one clearly sees that NiMnCr LDHs/NF experienced a significant loss as compared to NiMnCr LDHs@CS/NF, which is consistent with the cycling performance results in **Figure 2.37**. The existence of CS could help release the deformation and stress during the charging/discharging cycles to immobilize the NiMnCr LDHs layer, further improving the mechanical stability [103].
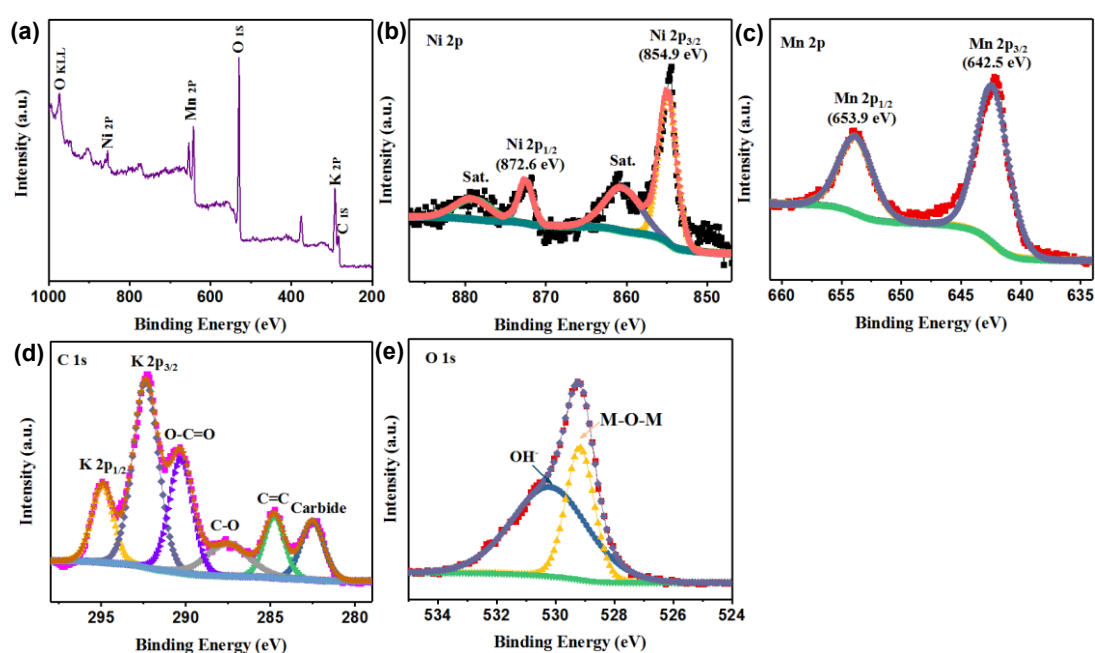

Figure 2.39: XPS analysis of NiMnCr LDHs/NF after 10,000 cycles test: (a) Survey spectrum, and high resolution spectra of (b) Ni$_{2p}$, (c) Mn$_{2p}$, (d) C$_{1s}$ and (e) O$_{1s}$.
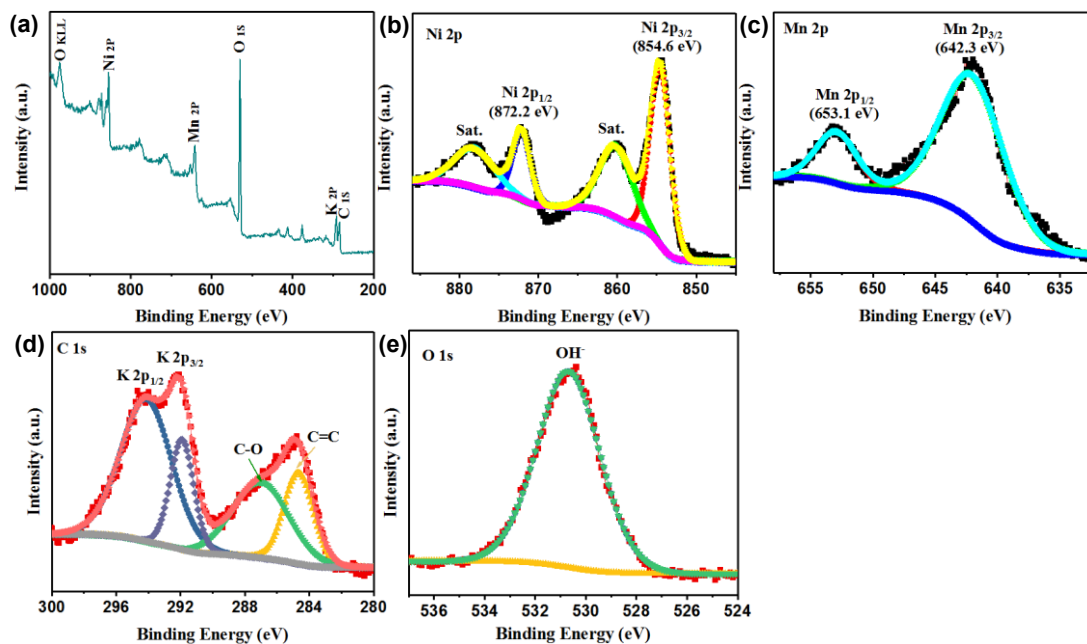
Figure 2.40: XPS analysis of NiMnCr LDHs@CS/NF after 10,000 cycles test: (a) Survey spectrum, and high resolution spectra of (b) Ni_{2p}, (c) Mn_{2p}, (d) C_{1s} and (e) O_{1s}.

Table 2.18: Elemental composition of the samples after 10,000 cycles.

Elements (at%) Composites	Ni_{2p}	Mn_{2p}	Cr_{2p}	C_{1s}	O_{1s}
NiMnCr LDHs/NF	0.3	2.7	0	69.3	27.7
NiMnCr LDHs@CS/NF	5.2	6.1	0	52.1	36.5

Finally, a hybrid supercapacitor was assembled using NiMnCr LDHs@CS/NF as a positive electrode and FeOOH/NF as a negative electrode. The morphology of FeOOH consists of nanorods (see SEM image in **Figure 2.41**).
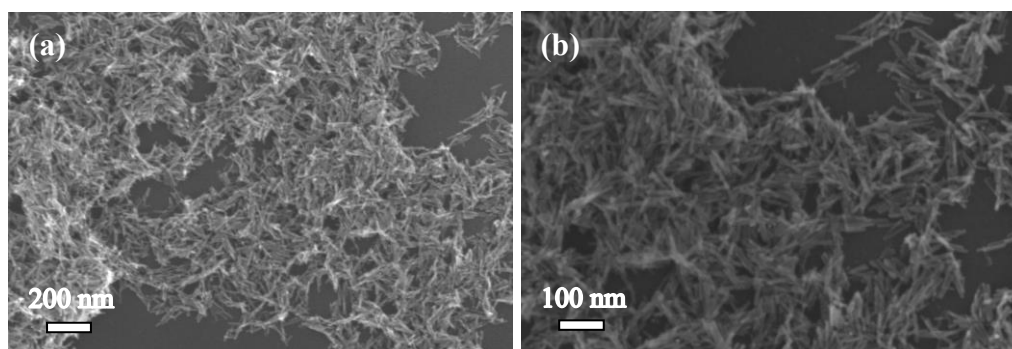
Figure 2.41: SEM images of FeOOH nanorods.

The electrochemical behavior of the FeOOH/NF electrode was examined in 2 M KOH aqueous solution. **Figure 2.42** depicts the CV curves of FeOOH/NF electrode between -1 V and -0.5 V at various scan rates, which implies its potential use as a negative electrode. Using **Equation 1.11.2**, the specific capacity of FeOOH/NF was calculated to be 126, 88.8, 72.8, 59.9, 51.6 and 49.1 C g^{-1} respectively at 1, 2, 3, 5, 10 and 15 A g^{-1}, as illustrated in **Figure 2.42b** and **c**, which proves that FeOOH could be a promising negative material.
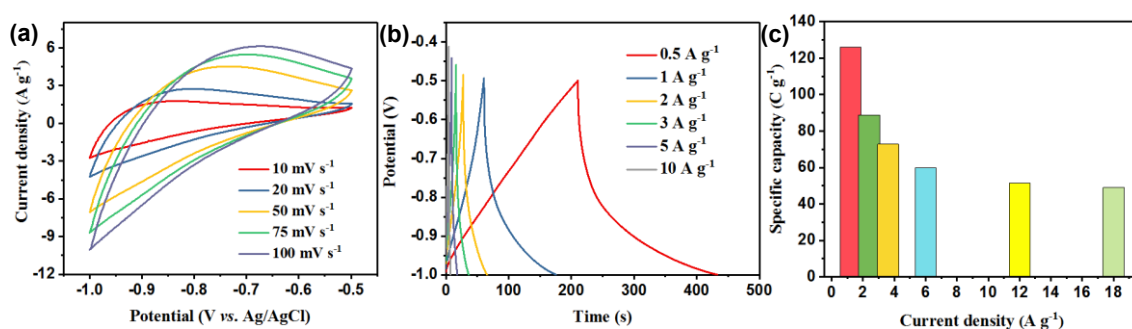

Figure 2.42: The electrochemical performance of the FeOOH electrode measured in 2 M KOH aqueous solution. (a) CV curves at various scan rates, (b) Galvanostatic charge-discharge curves at various current densities, (c) Specific capacity at different current densities.

The NiMnCr LDHs@CS/NF//FeOOH/NF hybrid supercapacitor possesses a great cell voltage window, which could be extended to 1.8 V (**Figure 2.43a**). Interestingly, the CV curves display a similar shape, suggesting an excellent capacitive performance. Obviously, there exists a polarization phenomenon when the cell voltage was higher

than 1.7 V, so the cell voltage window was chosen as 0-1.7 V to reduce the damage to the electrode. **Figure 2.43b** depicts the CV curves of the hybrid supercapacitor in the cell voltage window between 0 and +1.7 V acquired at different scan rates. Upon increasing the scan rate, one sees a shift of the redox peak potential; this may be ascribed to increased internal resistance at higher scan rates.

Figure 2.43c displays the GCD curves of the hybrid supercapacitor device at various current densities, demonstrating high coulombic efficiency (**Table 2.19**). The specific capacity values, deduced from the discharging curves in **Figure 2.43c**, are displayed in **Figure 2.43d**. The NiMnCr LDHs@CS/NF//FeOOH/NF hybrid supercapacitor achieved specific capacity values of 167.4, 154.4, 137.5, 127.5, 129.6, 104.6, 99.6, 74.7 and 59.8 C g^{-1} respectively at 1.5, 2, 3, 4, 5, 8, 10, 15 and 20 A g^{-1}, which shows a good rate performance (60% of initial areal capacity was maintained at a current density of 10 A g^{-1} and 36% of areal capacity was retained even at a current density of 20 A g^{-1}).

Additionally, the hybrid supercapacitor was characterized by electrochemical impedance spectroscopy (EIS) in the 0.01 Hz and 100 kHz frequency range; the equivalent circuit for impedance analysis was illustrated in the inset of **Figure 2.43e** (R_{ct}, R_s, C_{dl}, W_o, C_l and R_l are respectively the charge-transfer resistance, internal resistance, double-layer capacitance, Warburg element, limit capacitance and limit resistance). From the Nyquist plot, one clearly sees a semicircle at the high-frequency range associated with the charge transfer resistance, and a straight line at the low-

frequency region. The R_s and R_{ct} values are determined to be about ~0.45 and ~0.49 ohm cm^{-2}, respectively.
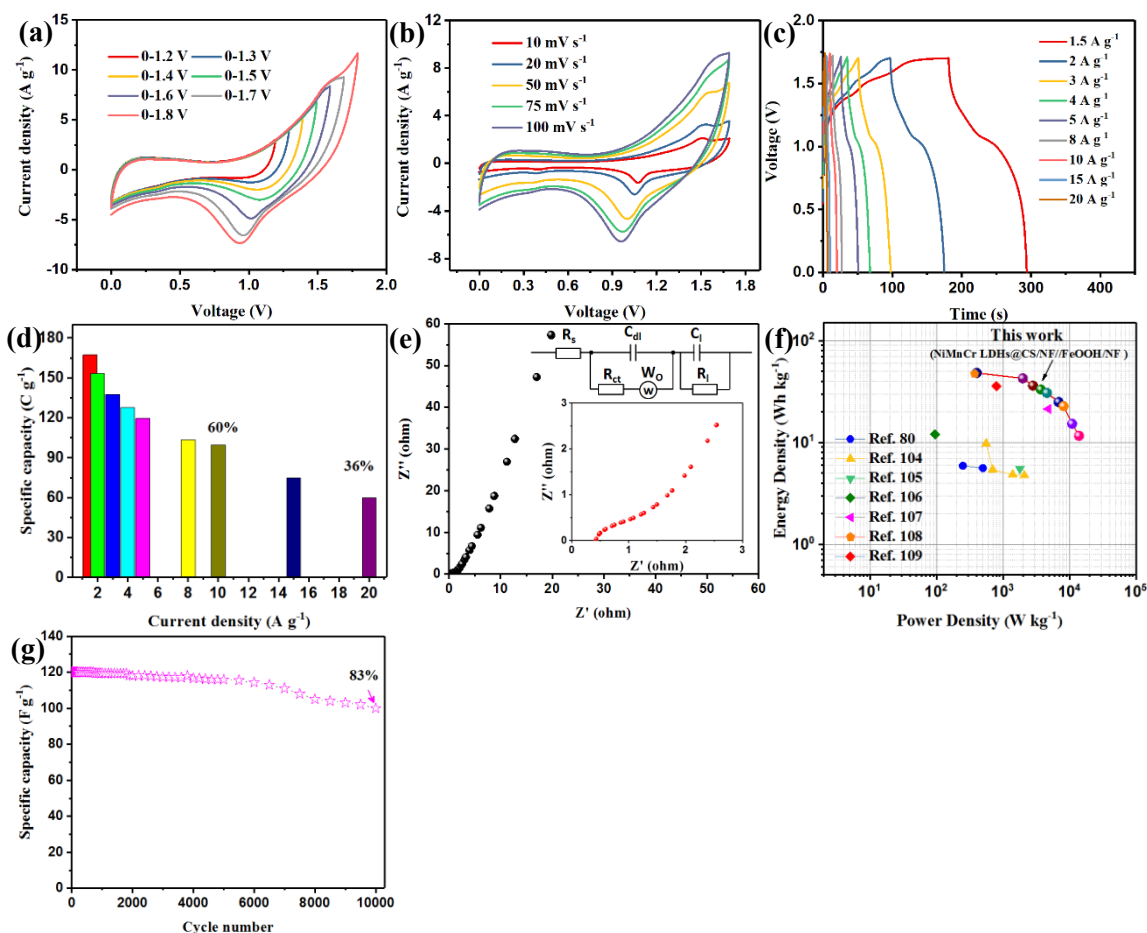

Figure 2.43: Electrochemical characterization of the NiMnCr LDHs@CS/NF//FeOOH/NF hybrid supercapacitor. (a) CV curves acquired in different cell voltage windows at 100 mV s^{-1}. (b) CV curves of the NiMnCr LDHs@CS/NF//FeOOH/NF asymmetric supercapacitor obtained at different scan rates between 0 and +1.7 V. (c) GCD curves acquired at different current densities. (d) Specific capacity at different current densities. (e) EIS curves recorded in the 0.01 Hz and 100 kHz frequency range. The inset up-right in (d) is the corresponding equivalent circuit. (f) Ragone plots related to the energy and power densities of the hybrid

supercapacitor. (g) Cycling performance of NiMnCr LDHs@CS/NF//FeOOH hybrid

supercapacitor at a constant current density of 5 A g^{-1}.

Table 2.19: Coulomb efficiency (%) of the hybrid supercapacitor device at various

current densities (A g^{-1}).

1.5	2	3	4	5	8	10	15	20
62%	79%	90%	91%	92%	93%	100%	100%	100%

To achieve a full characterization of the electrochemical performance of the as-

prepared hybrid supercapacitor, the Ragone plot is provided in **Figure 2.43f**. The hybrid

supercapacitor device attained a great energy density of 48 Wh kg^{-1} at a power density

of 402.7 W kg^{-1}, which is larger than that of CoMn-LDH/AC hybrid supercapacitor (4.4

Wh kg^{-1} at 2500 W kg^{-1}) [80], NiFe LDH/rGO/NF//MC/NF hybrid supercapacitor (9.8

Wh kg^{-1} at 560 W kg^{-1}) [104], $MnFe_2O_4/LiMn_2O_4$ hybrid supercapacitor (5.5 Wh kg^{-1}

at 1800 W kg^{-1}) [105], Ni-Co oxide/AC hybrid supercapacitor (12 Wh kg^{-1} at 95.2 W

kg^{-1}) [106], MnO_2@Co-Ni LDH (21.3 Wh Kg^{-1} at 4.8 kW kg^{-1}) [107] Co_3O_4@NiMn-

LDH/Ni (47.15 Wh kg^{-1} at 376 W kg^{-1}) [108]   and CoS_x/Ni-Co LDH nanocages (35.8

Wh kg^{-1} at 800 W kg^{-1}) [109]. Even though the developed NiMnCr

LDHs@CS/NF//FeOOH/NF hybrid supercapacitor achieved good performance, there

is room for improvement by applying suitable negative materials. **Figure 2.43g** depicts

the charging/discharging cycles at 5 A g^{-1}. The hybrid supercapacitor retained ~83% of

its initial specific capacity after 10,000 cycles, signifying a good stability of the energy

storage device.

To highlight the practical use of the as-fabricated supercapacitor device, it was applied for operating a home-designed windmill device (**Figure 2.44a** and **c**). The device comprises an engine (1.5-9 V), windmill and one as-fabricated supercapacitor device. The windmill can be rotated for about 25 s using the home-made device upon charging the supercapacitor at 1.7 V (**Figure 2.44b**). Additionally, as is shown in **Figure 2.44d**, two as-fabricated hybrid supercapacitor cells (SC) in series whose working cell voltage window can reach 3.4 V (**Figure 2.44b**) were used to supply electricity to a red LED and a yellow LED in parallel; the red LED was lighted for ~343 s and the yellow one for ~111 s at the same time.
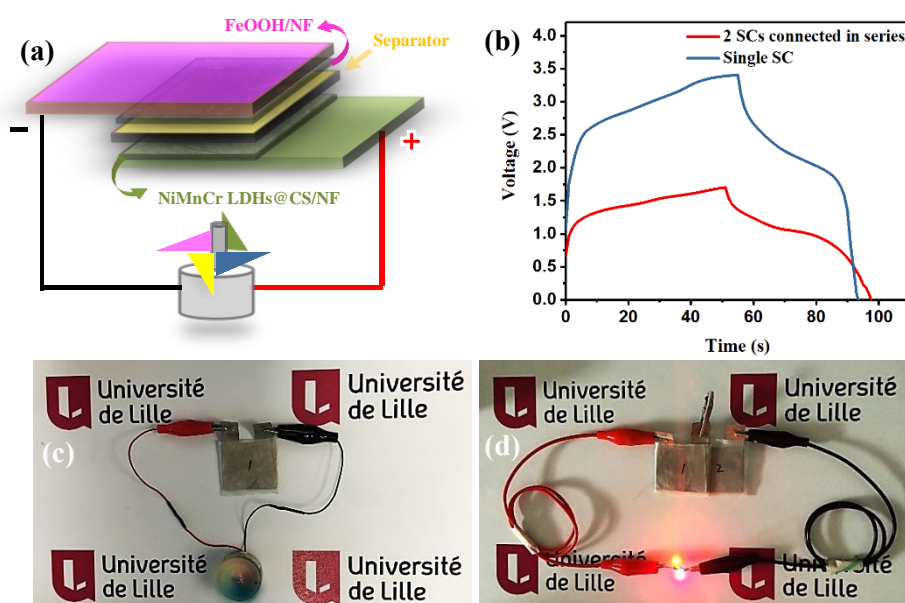

Figure 2.44: (a) Schematic diagram of the packed hybrid supercapacitor for windmill device. (b) Galvanostatic charge-discharge curves of a single supercapacitor and two supercapacitors connected in series at 3 A g^{-1}. (c) Photograph of the home-designed windmill device. (d) Lightening of a red LED and a yellow LED in parallel by two supercapacitor cells in series.

2.5 Conclusion

Firstly, NiFe LDHs/rGO/NF composites were synthesized using a two-step electrodeposition method, exhibiting improved performance with a specific capacity of 585 C g^{-1} at a current density of 5 A g^{-1}. Additionally, the capacity retention of 64.7% after 2,000 cycles was recorded, suggesting a reasonable stability of the material. Moreover, a flexible hybrid supercapacitor was assembled using NiFe LDHs/rGO/NF as positive electrode and mesoporous carbon coated on NF as negative electrode; the device displayed an energy density of 17.71 Wh kg^{-1} at a power density of 348.49 W kg^{-1}, suggesting a promising potential in supercapacitor applications.

Secondly, NiFe LDHs, NiCr LDHs and NiAl LDHs on nickel foam (NF) were synthesized by a simple hydrothermal process. With the assistance of carbon spheres (CS), NiFe LDHs@CS/NF, NiCr LDHs@CS/NF and NiAl LDHs@CS/NF were further obtained. Among all the samples, NiAl LDHs@CS/NF exhibited the best electrochemical performance as a binder-free electrode and the largest areal capacity of 1042.2 mC cm^{-2} at 1 mA cm^{-2}. Consequently, NiAl LDHs@CS/NF//N-rGO/NF hybrid supercapacitor cell in KOH solution and flexible NiAl LDHs@CS/NF//N-rGO/NF hybrid supercapacitor devices were successfully assembled, and further applied for windmill device operation, lasting for 21 and 32 s, respectively. Moreover, two NiAl LDHs@CS/NF//N-rGO/NF hybrid supercapacitor cells connected in series were able to supply electricity to LEDs in parallel and the red one was lighted up for the longest time of ~459 s. The flexible NiAl LDHs@CS/NF//N-rGO/NF hybrid supercapacitor

device displayed favorable flexibility, mechanical properties and stability; two devices in series could light a yellow LED (199 s), a red LED (542 s) and a green LED (37 s) in parallel simultaneously.

Finally, NiMnCr LDHs@CS/NF composites were prepared by the hydrothermal method, and successfully applied as efficient electrode material for supercapacitors. NiMnCr LDHs@CS/NF features a better rate performance and a specific capacity of 569 C g^{-1} at a current density of 3 A g^{-1}. Furthermore, NiMnCr LDHs@CS/NF electrode revealed good reversibility and stability. The electrode retained ~76% of the initial specific capacity after 10,000 discharge cycles. Furthermore, a hybrid supercapacitor was prepared using NiMnCr LDHs@CS/NF as the positive electrode and FeOOH coated on NF as the negative electrode. The device exhibited an energy density of 48 Wh kg^{-1} at a power density of 402.7 W kg^{-1} with good stability. A home-designed windmill device was successfully driven for 25 s by the as-fabricated supercapacitor device and two as-fabricated hybrid supercapacitor cells in series were used to light up a yellow LED and a red LED for ~111 s and ~343 s, respectively.

All the findings suggest that the developed electrodes hold a promising potential for energy storage applications, especially for hybrid supercapacitor devices.

2.6 References

[1] X. Gao, P. Wang, Z. Pan, J.P. Claverie, J. Wang, Recent Progress in Two-Dimensional Layered Double Hydroxides and Their Derivatives for Supercapacitors, ChemSusChem, 13 (2020) 1226-1254.

[2] M. Zhao, Q. Zhao, B. Li, H. Xue, H. Pang, C. Chen, Recent progress in layered double hydroxide based materials for electrochemical capacitors: design, synthesis and performance, Nanoscale, 9 (2017) 15206-15225.

[3] M. Sarfraz, I. Shakir, Recent advances in layered double hydroxides as electrode materials for high-performance electrochemical energy storage devices, Journal of Energy Storage, 13 (2017) 103-122.

[4] Y. Yang, L. Dang, M.J. Shearer, H. Sheng, W. Li, J. Chen, P. Xiao, Y. Zhang, R.J. Hamers, S. Jin, Highly Active Trimetallic NiFeCr Layered Double Hydroxide Electrocatalysts for Oxygen Evolution Reaction, Advanced Energy Materials, 8 (2018) 1703189.

[5] K.N. Dinh, P. Zheng, Z. Dai, Y. Zhang, R. Dangol, Y. Zheng, B. Li, Y. Zong, Q. Yan, Ultrathin Porous NiFeV Ternary Layer Hydroxide Nanosheets as a Highly Efficient Bifunctional Electrocatalyst for Overall Water Splitting, Small, 14 (2018) 1703257.

[6] M.M. Rao, B.R. Reddy, M. Jayalakshmi, V.S. Jaya, B. Sridhar, Hydrothermal synthesis of Mg-Al hydrotalcites by urea hydrolysis, Materials Research Bulletin, 40 (2005) 347-359.

[7] H. Chen, L. Hu, M. Chen, Y. Yan, L. Wu, Nickel-Cobalt Layered Double Hydroxide

Nanosheets for High-performance Supercapacitor Electrode Materials, Advanced Functional Materials, 24 (2014) 934-942.

[8] Z. Lu, W. Xu, W. Zhu, Q. Yang, X. Lei, J. Liu, Y. Li, X. Sun, X. Duan, Three-dimensional NiFe layered double hydroxide film for high-efficiency oxygen evolution reaction, Chemical Communications, 50 (2014) 6479-6482.

[9] L. Tan, Y. Wang, Q. Liu, J. Wang, X. Jing, L. Liu, J. Liu, D. Song, Enhanced adsorption of uranium (VI) using a three-dimensional layered double hydroxide/graphene hybrid material, Chemical Engineering Journal, 259 (2015) 752-760.

[10] G. Yilmaz, K.M. Yam, C. Zhang, H.J. Fan, G.W. Ho, In Situ Transformation of MOFs into Layered Double Hydroxide Embedded Metal Sulfides for Improved Electrocatalytic and Supercapacitive Performance, Advanced Materials, 29 (2017) 1606814.

[11] A. Tyagi, M.C. Joshi, A. Shah, V.K. Thakur, R.K. Gupta, Hydrothermally Tailored Three-Dimensional Ni-V Layered Double Hydroxide Nanosheets as High-Performance Hybrid Supercapacitor Applications, ACS Omega, 4 (2019) 3257-3267.

[12] P. Guoxiang, X. Xinhui, L. Jingshan, C. Feng, Y. Zhihong, F. Hongjin, Preparation of CoAl layered double hydroxide nanoflake arrays and their high supercapacitance performance, Applied Clay Science, 102 (2014) 28-32.

[13] L. Ai, C. Zhang, L. Meng, Adsorption of Methyl Orange from Aqueous Solution on Hydrothermal Synthesized Mg-Al Layered Double Hydroxide, Journal of Chemical

& Engineering Data, 56 (2011) 4217-4225.

[14] P. Gholami, L. Dinpazhoh, A. Khataee, A. Hassani, A. Bhatnagar, Facile hydrothermal synthesis of novel Fe-Cu layered double hydroxide/biochar nanocomposite with enhanced sonocatalytic activity for degradation of cefazolin sodium, Journal of Hazardous Materials, 381 (2020) 120742.

[15] D. Scarpellini, C. Falconi, P. Gaudio, A. Mattoccia, P.G. Medaglia, A. Orsini, R. Pizzoferrato, M. Richetta, Morphology of Zn/Al layered double hydroxide nanosheets grown onto aluminum thin films, Microelectronic Engineering, 126 (2014) 129-133.

[16] M. Gong, Y. Li, H. Zhang, B. Zhang, W. Zhou, J. Feng, H. Wang, Y. Liang, Z. Fan, J. Liu, H. Dai, Ultrafast high-capacity NiZn battery with NiAlCo-layered double hydroxide, Energy & Environmental Science, 7 (2014) 2025.

[17] X. Wang, S. Zhou, W. Xing, B. Yu, X. Feng, L. Song, Y. Hu, Self-assembly of Ni–Fe layered double hydroxide/graphene hybrids for reducing fire hazard in epoxy composites, Journal of Materials Chemistry A, 1 (2013) 4383.

[18] J. Wei, Z. Gao, Y. Song, W. Yang, J. Wang, Z. Li, T. Mann, M. Zhang, L. Liu, Solvothermal synthesis of Li-Al layered double hydroxides and their electrochemical performance, Materials Chemistry and Physics, 139 (2013) 395-402.

[19] Z. Li, M. Shao, L. Zhou, R. Zhang, C. Zhang, J. Han, M. Wei, D.G. Evans, X. Duan, A flexible all-solid-state micro-supercapacitor based on hierarchical CuO@layered double hydroxide core-shell nanoarrays, Nano Energy, 20 (2016) 294-304.

[20] M. Shao, F. Ning, M. Wei, D.G. Evans, X. Duan, Hierarchical Nanowire Arrays Based on ZnO Core-Layered Double Hydroxide Shell for Largely Enhanced Photoelectrochemical Water Splitting, Advanced Functional Materials, 24 (2014) 580-586.

[21] E. Scavetta, B. Ballarin, C. Corticelli, I. Gualandi, D. Tonelli, V. Prevot, C. Forano, C. Mousty, An insight into the electrochemical behavior of Co/Al layered double hydroxide thin films prepared by electrodeposition, Journal of Power Sources, 201 (2012) 360-367.

[22] G. Luo, K. Siong Teh, Y. Xia, Y. Luo, Z. Li, S. Wang, L. Zhao, Z. Jiang, A novel three-dimensional spiral CoNi LDHs on Au@ErGO wire for high performance fiber supercapacitor electrodes, Materials Letters, 236 (2019) 728-731.

[23] H. Li, L. Zhang, S. Wang, J. Yu, Accelerated oxygen evolution kinetics on NiFeAl-layered double hydroxide electrocatalysts with defect sites prepared by electrodeposition, International Journal of Hydrogen Energy, 44 (2019) 28556-28565.

[24] M. Li, F. Ni, Y. Wang, S. Xu, D. Zhang, S. Chen, L. Wang, Sensitive and Facile Determination of Catechol and Hydroquinone Simultaneously Under Coexistence of Resorcinol with a Zn/Al Layered Double Hydroxide Film Modified Glassy Carbon Electrode, Electroanalysis, 21 (2009) 1521-1526.

[25] Y. Li, L. Zhang, X. Xiang, D. Yan, F. Li, Engineering of ZnCo-layered double hydroxide nanowalls toward high-efficiency electrochemical water oxidation, Journal of Materials Chemistry A, 2 (2014) 13250.

[26] J. Zhao, J. Chen, S. Xu, M. Shao, Q. Zhang, F. Wei, J. Ma, M. Wei, D.G. Evans, X. Duan, Hierarchical NiMn Layered Double Hydroxide/Carbon Nanotubes Architecture with Superb Energy Density for Flexible Supercapacitors, Advanced Functional Materials, 24 (2014) 2938-2946.

[27] D. Zhao, G. Sheng, J. Hu, C. Chen, X. Wang, The adsorption of Pb(II) on Mg_2Al layered double hydroxide, Chemical Engineering Journal, 171 (2011) 167-174.

[28] J. Zhao, J. Chen, S. Xu, M. Shao, D. Yan, M. Wei, D.G. Evans, X. Duan, CoMn-layered double hydroxide nanowalls supported on carbon fibers for high-performance flexible energy storage devices, Journal of Materials Chemistry A, 1 (2013) 8836.

[29] L. Zhang, X. Zhang, L. Shen, B. Gao, L. Hao, X. Lu, F. Zhang, B. Ding, C. Yuan, Enhanced high-current capacitive behavior of graphene/CoAl-layered double hydroxide composites as electrode material for supercapacitors, Journal of Power Sources, 199 (2012) 395-401.

[30] F. Zhang, M. Sun, S. Xu, L. Zhao, B. Zhang, Fabrication of oriented layered double hydroxide films by spin coating and their use in corrosion protection, Chemical Engineering Journal, 141 (2008) 362-367.

[31] N. Hong, L. Song, B. Wang, A.A. Stec, T.R. Hull, J. Zhan, Y. Hu, Co-precipitation synthesis of reduced graphene oxide/NiAl-layered double hydroxide hybrid and its application in flame retarding poly(methyl methacrylate), Materials Research Bulletin, 49 (2014) 657-664.

[32] M. Shao, J. Han, M. Wei, D.G. Evans, X. Duan, The synthesis of hierarchical Zn–

Ti layered double hydroxide for efficient visible-light photocatalysis, Chemical Engineering Journal, 168 (2011) 519-524.

[33] M. Li, J.P. Cheng, J. Wang, F. Liu, X.B. Zhang, The growth of nickel-manganese and cobalt-manganese layered double hydroxides on reduced graphene oxide for supercapacitor, Electrochimica Acta, 206 (2016) 108-115.

[34] Y. Zhong, Q. Yang, K. Luo, X. Wu, X. Li, Y. Liu, W. Tang, G. Zeng, B. Peng, Fe(II)-Al(III) layered double hydroxides prepared by ultrasound-assisted co-precipitation method for the reduction of bromate, Journal of Hazardous Materials, 250-251 (2013) 345-353.

[35] S. Zeng, X. Xu, S. Wang, Q. Gong, R. Liu, Y. Yu, Sand flower layered double hydroxides synthesized by co-precipitation for CO_2 capture: Morphology evolution mechanism, agitation effect and stability, Materials Chemistry and Physics, 140 (2013) 159-167.

[36] X. Liu, L. Zhang, X. Gao, C. Guan, Y. Hu, J. Wang, Enlarged Interlayer Spacing in Cobalt-Manganese Layered Double Hydroxide Guiding Transformation to Layered Structure for High Supercapacitance, ACS Applied Materials & Interfaces, 11 (2019) 23236-23243.

[37] A. Tyagi, M. Chandra Joshi, K. Agarwal, B. Balasubramaniam, R.K. Gupta, Three-dimensional nickel vanadium layered double hydroxide nanostructures grown on carbon cloth for high-performance flexible supercapacitor applications, Nanoscale Advances, 1 (2019) 2400-2407.

[38] M. Du, X. Yin, C. Tang, T.J. Huang, H. Gong, Takovite-derived 2-D Ni/Al double hydroxide monolayer and graphene hybrid electrodes for electrochemical energy storage applications with high volumetric capacitance, Electrochimica Acta, 190 (2016) 521-530.

[39] X.L. Guo, X.Y. Liu, X.D. Hao, S.J. Zhu, F. Dong, Z.Q. Wen, Y.X. Zhang, Nickel-Manganese Layered Double Hydroxide Nanosheets Supported on Nickel Foam for High-performance Supercapacitor Electrode Materials, Electrochimica Acta, 194 (2016) 179-186.

[40] G. Luo, K.S. Teh, Y. Xia, Z. Li, Y. Luo, L. Zhao, Z. Jiang, Construction of $NiCo_2O_4$@NiFe LDHs core/shell nanowires array on carbon cloth for flexible, high-performance pseudocapacitor electrodes, Journal of Alloys and Compounds, 767 (2018) 1126-1132.

[41] A. Elgendy, N.M. El Basiony, F. El-Taib Heakal, A.E. Elkholy, Mesoporous Ni-Zn-Fe layered double hydroxide as an efficient binder-free electrode active material for high-performance supercapacitors, Journal of Power Sources, 466 (2020) 228294.

[42] L. Sun, Y. Zhang, Y. Zhang, H. Si, W. Qin, Y. Zhang, Reduced graphene oxide nanosheet modified NiMn-LDH nanoflake arrays for high-performance supercapacitors, Chemical Communications, 54 (2018) 10172-10175.

[43] D. Guo, X. Song, L. Tan, H. Ma, W. Sun, H. Pang, L. Zhang, X. Wang, A facile dissolved and reassembled strategy towards sandwich-like rGO@NiCoAl-LDHs with excellent supercapacitor performance, Chemical Engineering Journal, 356 (2019) 955-

963.

[44] P.F. Liu, J.J. Zhou, G.C. Li, M.K. Wu, K. Tao, F.Y. Yi, W.N. Zhao, L. Han, A hierarchical NiO/NiMn-layered double hydroxide nanosheet array on Ni foam for high performance supercapacitors, Dalton Transactions, 46 (2017) 7388-7391.

[45] W. Wang, N. Zhang, Z. Shi, Z. Ye, Q. Gao, M. Zhi, Z. Hong, Preparation of Ni-Al layered double hydroxide hollow microspheres for supercapacitor electrode, Chemical Engineering Journal, 338 (2018) 55-61.

[46] X. Gao, H. Lv, Z. Li, Q. Xu, H. Liu, Y. Wang, Y. Xia, Low-cost and high-performance of a vertically grown 3D Ni-Fe layered double hydroxide/graphene aerogel supercapacitor electrode material, RSC Advances, 6 (2016) 107278-107285.

[47] P. Bandyopadhyay, X. Li, N.H. Kim, J.H. Lee, Graphitic carbon nitride modified graphene/Ni Al layered double hydroxide and 3D functionalized graphene for solid-state asymmetric supercapacitors, Chemical Engineering Journal, 353 (2018) 824-838.

[48] Y. Gu, Z. Lu, Z. Chang, J. Liu, X. Lei, Y. Li, X. Sun, NiTi layered double hydroxide thin films for advanced pseudocapacitor electrodes, Journal of Materials Chemistry A, 1 (2013) 10655.

[49] C. Jing, Y. Huang, L. Xia, Y. Chen, X. Wang, X. Liu, B. Dong, F. Dong, S. Li, Y. Zhang, Growth of cobalt-aluminum layered double hydroxide nanosheets on graphene oxide towards high performance supercapacitors: The important role of layer structure, Applied Surface Science, 496 (2019) 143700.

[50] S.K. Kiran, M. Padmini, H.T. Das, P. Elumalai, Performance of asymmetric

supercapacitor using CoCr-layered double hydroxide and reduced graphene-oxide, Journal of Solid State Electrochemistry, 21 (2016) 927-938.

[51] D. Chen, H. Chen, X. Chang, P. Liu, Z. Zhao, J. Zhou, G. Xu, H. Lin, S. Han, Hierarchical CoMn-layered double hydroxide nanowires on nickel foam as electrode material for high-capacitance supercapacitor, Journal of Alloys and Compounds, 729 (2017) 866-873.

[52] H. Chen, H. Zhang, Y. Zhang, Y. Wang, X. Su, L. Zhang, Z. Lin, General strategy toward hexagonal ring-like layered double hydroxides and their application for asymmetric supercapacitors, Chemical Engineering Journal, 375 (2019) 121926.

[53] J.J. Zhou, Q. Li, C. Chen, Y.L. Li, K. Tao, L. Han, Co_3O_4@CoNi-LDH core/shell nanosheet arrays for high-performance battery-type supercapacitors, Chemical Engineering Journal, 350 (2018) 551-558.

[54] J. Xu, K. Liao, K. Song, J. Wu, X. Hu, H. Gao, F. Hu, J.P. Cheng, Fast in situ synthesis of CoFe layered double hydroxide onto multi-layer graphene for electrochemical capacitors, Journal of Solid State Electrochemistry, 22 (2017) 1037-1045.

[55] P. Vialat, C. Mousty, C. Taviot-Gueho, G. Renaudin, H. Martinez, J.C. Dupin, E. Elkaim, F. Leroux, High-Performing Monometallic Cobalt Layered Double Hydroxide Supercapacitor with Defined Local Structure, Advanced Functional Materials, 24 (2014) 4831-4842.

[56] W. Chen, J. Wang, K.Y. Ma, M. Li, S.H. Guo, F. Liu, J.P. Cheng, Hierarchical

NiCo$_2$O$_4$@Co-Fe LDH core-shell nanowire arrays for high-performance supercapacitor, Applied Surface Science, 451 (2018) 280-288.

[57] N. Wu, J. Low, T. Liu, J. Yu, S. Cao, Hierarchical hollow cages of Mn-Co layered double hydroxide as supercapacitor electrode materials, Applied Surface Science, 413 (2017) 35-40.

[58] X. Chu, T. Deng, W. Zhang, D. Wang, X. Liu, C. Zhang, T. Qin, L. Zhang, B. Zhang, C. Chen, W. Zheng, Architecture of Co-layered double hydroxide nanocages/graphene composite electrode with high electrochemical performance for supercapacitor, Journal of Energy Chemistry, 27 (2018) 507-512.

[59] A.A. Lobinsky, V.P. Tolstoy, Synthesis of 2D Zn-Co LDH nanosheets by a successive ionic layer deposition method as a material for electrodes of high-performance alkaline battery-supercapacitor hybrid devices, RSC Advances, 8 (2018) 29607-29612.

[60] J. Gao, H. Xuan, Y. Xu, T. Liang, X. Han, J. Yang, P. Han, D. Wang, Y. Du, Interconnected network of zinc-cobalt layered double hydroxide stick onto rGO/nickel foam for high performance asymmetric supercapacitors, Electrochimica Acta, 286 (2018) 92-102.

[61] Y. Zhang, S. Wei, Mg-Co-Al-LDH nanoparticles with attractive electrochemical performance for supercapacitor, Journal of Nanoparticle Research, 21 (2019) 14.

[62] G. Hatui, G.C. Nayak, G. Udayabhanu, One Pot Solvothermal Synthesis of Sandwich-like Mg Al Layered Double Hydroxide anchored Reduced Graphene Oxide:

An excellent electrode material for Supercapacitor, Electrochimica Acta, 219 (2016) 214-226.

[63] S.P. Adhikari, G.P. Awasthi, K.S. Kim, C.H. Park, C.S. Kim, Synthesis of three-dimensional mesoporous Cu-Al layered double hydroxide/g-C$_3$N$_4$ nanocomposites on Ni-foam for enhanced supercapacitors with excellent long-term cycling stability, Dalton Transactions, 47 (2018) 4455-4466.

[64] S. Sanati, Z. Rezvani, R. Abazari, Z. Hou, H. Dai, Hierarchical CuAl-layered double hydroxide/CoWO$_4$ nanocomposites with enhanced efficiency for use in supercapacitors with long cycling stability, New Journal of Chemistry, 43 (2019) 15240-15248.

[65] D.C. Marcano, D.V. Kosynkin, J.M. Berlin, A. Sinitskii, Z. Sun, A. Slesarev, L.B. Alemany, W. Lu, J.M. Tour, Improved Synthesis of Graphene Oxide, ACS Nano, 4 (2010) 4806-4814.

[66] W. Guo, C. Yu, S. Li, J. Yang, Z. Liu, C. Zhao, H. Huang, M. Zhang, X. Han, Y. Niu, J. Qiu, High-Stacking-Density, Superior-Roughness LDH Bridged with Vertically Aligned Graphene for High-Performance Asymmetric Supercapacitors, Small, 13 (2017) 1701288.

[67] W. Su, T. Lin, W. Chu, Y. Zhu, J. Li, X. Zhao, Novel synthesis of RGO/NiCoAl-LDH nanosheets on nickel foam for supercapacitors with high capacitance, RSC Advances, 6 (2016) 113123-113131.

[68] X. Wang, X. Li, X. Du, X. Ma, X. Hao, C. Xue, H. Zhu, S. Li, Controllable

Synthesis of NiCo LDH Nanosheets for Fabrication of High-Performance Supercapacitor Electrodes, Electroanalysis, 29 (2017) 1286-1293.

[69] G. Nagaraju, G.S. Raju, Y.H. Ko, J.S. Yu, Hierarchical Ni-Co layered double hydroxide nanosheets entrapped on conductive textile fibers: a cost-effective and flexible electrode for high-performance pseudocapacitors, Nanoscale, 8 (2016) 812-825.

[70] X. Ma, X. Li, A.D. Jagadale, X. Hao, A. Abudula, G. Guan, Fabrication of $Cu(OH)_2$@NiFe-layered double hydroxide catalyst array for electrochemical water splitting, International Journal of Hydrogen Energy, 41 (2016) 14553-14561.

[71] X. Yu, M. Zhang, W. Yuan, G. Shi, A high-performance three-dimensional Ni-Fe layered double hydroxide/graphene electrode for water oxidation, Journal of Materials Chemistry A, 3 (2015) 6921-6928.

[72] L. Yu, H. Zhou, J. Sun, F. Qin, F. Yu, J. Bao, Y. Yu, S. Chen, Z. Ren, Cu nanowires shelled with NiFe layered double hydroxide nanosheets as bifunctional electrocatalysts for overall water splitting, Energy & Environmental Science, 10 (2017) 1820-1827.

[73] X. Jiao, X. Xia, P. Liu, W. Lei, Y. Ouyang, Q. Hao, Nickel cobaltite nanosheets strongly anchored on boron and nitrogen co-doped graphene for high-performance asymmetric supercapacitors, Nanotechnology, 28 (2017) 315403.

[74] K. Kakaei, E. Alidoust, G. Ghadimi, Synthesis of N- doped graphene nanosheets and its composite with urea choline chloride ionic liquid as a novel electrode for supercapacitor, Journal of Alloys and Compounds, 735 (2018) 1799-1806.

[75] S.K. Singh, V.M. Dhavale, R. Boukherroub, S. Kurungot, S. Szunerits, N-doped

porous reduced graphene oxide as an efficient electrode material for high performance flexible solid-state supercapacitor, Applied Materials Today, 8 (2017) 141-149.

[76] N. Han, F. Zhao, Y. Li, Ultrathin nickel-iron layered double hydroxide nanosheets intercalated with molybdate anions for electrocatalytic water oxidation, Journal of Materials Chemistry A, 3 (2015) 16348-16353.

[77] C. Andronescu, S. Seisel, P. Wilde, S. Barwe, J. Masa, Y.T. Chen, E. Ventosa, W. Schuhmann, Influence of Temperature and Electrolyte Concentration on the Structure and Catalytic Oxygen Evolution Activity of Nickel-Iron Layered Double Hydroxide, Chemistry, 24 (2018) 13773-13777.

[78] K. Kakaei, M. Hamidi, S. Husseindoost, Chlorine-doped reduced graphene oxide nanosheets as an efficient and stable electrode for supercapacitor in acidic medium, Journal of Colloid and Interface Science, 479 (2016) 121-126.

[79] P. Iamprasertkun, A. Krittayavathananon, M. Sawangphruk, N-doped reduced graphene oxide aerogel coated on carboxyl-modified carbon fiber paper for high-performance ionic-liquid supercapacitors, Carbon, 102 (2016) 455-461.

[80] A.D. Jagadale, G. Guan, X. Li, X. Du, X. Ma, X. Hao, A. Abudula, Ultrathin nanoflakes of cobalt-manganese layered double hydroxide with high reversibility for asymmetric supercapacitor, Journal of Power Sources, 306 (2016) 526-534.

[81] J. Zhu, T. Feng, X. Du, J. Wang, J. Hu, L. Wei, High performance asymmetric supercapacitor based on polypyrrole/graphene composite and its derived nitrogen-doped carbon nano-sheets, Journal of Power Sources, 346 (2017) 120-127.

[82] Z. Yu, M. McInnis, J. Calderon, S. Seal, L. Zhai, J. Thomas, Functionalized graphene aerogel composites for high-performance asymmetric supercapacitors, Nano Energy, 11 (2015) 611-620.

[83] Y.T. Wang, A.H. Lu, H.L. Zhang, W.C. Li, Synthesis of Nanostructured Mesoporous Manganese Oxides with Three-Dimensional Frameworks and Their Application in Supercapacitors, The Journal of Physical Chemistry C, 115 (2011) 5413-5421.

[84] C. Tang, Z. Tang, H. Gong, Hierarchically Porous Ni-Co Oxide for High Reversibility Asymmetric Full-Cell Supercapacitors, Journal of The Electrochemical Society, 159 (2012) A651-A656.

[85] M. Kuang, T.T. Li, H. Chen, S.M. Zhang, L.L. Zhang, Y.X. Zhang, Hierarchical $Cu_2O/CuO/Co_3O_4$ core-shell nanowires: synthesis and electrochemical properties, Nanotechnology, 26 (2015) 304002.

[86] Y.P. Lin, N.L. Wu, Characterization of $MnFe_2O_4/LiMn_2O_4$ aqueous asymmetric supercapacitor, Journal of Power Sources, 196 (2011) 851-854.

[87] Y. Zhang, M. Dong, S. Zhu, C. Liu, Z. Wen, MnO_2@Colloid Carbon Spheres Nanocomposites with Tunable Interior Architecture for Supercapacitors, Materials Research Bulletin, 49 (2014) 448-453.

[88] N.M. Latiff, C.C. Mayorga-Martinez, L. Wang, Z. Sofer, A.C. Fisher, M. Pumera, Microwave irradiated N- and B,Cl-doped graphene: Oxidation method has strong influence on capacitive behavior, Applied Materials Today, 9 (2017) 204-211.

[89] J. Liu, J. Wang, B. Zhang, Y. Ruan, L. Lv, X. Ji, K. Xu, L. Miao, J. Jiang, Hierarchical $NiCo_2S_4$@NiFe LDH Heterostructures Supported on Nickel Foam for Enhanced Overall-Water-Splitting Activity, ACS Applied Materials & Interfaces, 9 (2017) 15364-15372.

[90] J. Zhao, L. Cai, H. Li, X. Shi, X. Zheng, Stabilizing Silicon Photocathodes by Solution-Deposited Ni-Fe Layered Double Hydroxide for Efficient Hydrogen Evolution in Alkaline Media, ACS Energy Letters, 2 (2017) 1939-1946.

[91] M. Jarosz, R.P. Socha, P. Jóźwik, G.D. Sulka, Amperometric glucose sensor based on the $Ni(OH)_2$/$Al(OH)_4$-electrode obtained from a thin Ni_3Al foil, Applied Surface Science, 408 (2017) 96-102.

[92] L. Wang, X. Huang, S. Jiang, M. Li, K. Zhang, Y. Yan, H. Zhang, J.M. Xue, Increasing Gas Bubble Escape Rate for Water Splitting with Nonwoven Stainless Steel Fabrics, ACS Applied Materials & Interfaces, 9 (2017) 40281-40289.

[93] Y. Shao, M.F. El-Kady, J. Sun, Y. Li, Q. Zhang, M. Zhu, H. Wang, B. Dunn, R.B. Kaner, Design and Mechanisms of Asymmetric Supercapacitors, Chemical Reviews, 118 (2018) 9233-9280.

[94] M. Yang, H. Cheng, Y. Gu, Z. Sun, J. Hu, L. Cao, F. Lv, M. Li, W. Wang, Z. Wang, S. Wu, H. Liu, Z. Lu, Facile electrodeposition of 3D concentration-gradient Ni-Co hydroxide nanostructures on nickel foam as high performance electrodes for asymmetric supercapacitors, Nano Research, 8 (2015) 2744-2754.

[95] J. Yang, Y. Yuan, W. Wang, H. Tang, Z. Ye, J. Lu, Interconnected $Co_{0.85}Se$

nanosheets as cathode materials for asymmetric supercapacitors, Journal of Power Sources, 340 (2017) 6-13.

[96] G. Qu, J. Cheng, X. Li, D. Yuan, P. Chen, X. Chen, B. Wang, H. Peng, A Fiber Supercapacitor with High Energy Density Based on Hollow Graphene/Conducting Polymer Fiber Electrode, Advanced Materials, 28 (2016) 3646-3652.

[97] C.Y. Foo, A. Sumboja, D.J.H. Tan, J. Wang, P.S. Lee, Flexible and Highly Scalable V_2O_5-rGO Electrodes in an Organic Electrolyte for Supercapacitor Devices, Advanced Energy Materials, 4 (2014) 1400236.

[98] Y. Ji, J. Xie, J. Wu, Y. Yang, X.Z. Fu, R. Sun, C.P. Wong, Hierarchical nanothorns $MnCo_2O_4$ grown on porous/dense Ni bi-layers coated Cu wire current collectors for high performance flexible solid-state fiber supercapacitors, Journal of Power Sources, 393 (2018) 54-61.

[99] G. Huang, Y. Zhang, L. Wang, P. Sheng, H. Peng, Fiber-based MnO_2/carbon nanotube/polyimide asymmetric supercapacitor, Carbon, 125 (2017) 595-604.

[100] F. Li, H. Chen, X.Y. Liu, S.J. Zhu, J.Q. Jia, C.H. Xu, F. Dong, Z.Q. Wen, Y.X. Zhang, Low-cost high-performance asymmetric supercapacitors based on Co_2AlO_4@MnO_2 nanosheets and Fe_3O_4 nanoflakes, Journal of Materials Chemistry A, 4 (2016) 2096-2104.

[101] A. D. Jagadale, G. Guan, X. Li, X. Du, X. Ma, X. Hao, A. Abudula, Ultrathin Nanoflakes of Cobalt-Manganese Layered Double Hydroxide with High Reversibility for Asymmetric Supercapacitor, Journal of Power Sources, 306 (2016) 526-534.

[102] S. Liu, S.C. Lee, U. Patil, I. Shackery, S. Kang, K. Zhang, J.H. Park, K.Y. Chung, S. Chan Jun, Hierarchical MnCo-layered double hydroxides@Ni(OH)$_2$ core–shell heterostructures as advanced electrodes for supercapacitors, Journal of Materials Chemistry A, 5 (2017) 1043-1049.

[103] X. Zang, C. Shen, E. Kao, R. Warren, R. Zhang, K. S. Teh, J. Zhong, M. Wei, B. Li, Y. Chu, M. Sanghadasa, A. Schwartzberg, L. Lin, Titanium Disulfide Coated Carbon Nanotube Hybrid Electrodes Enable High Energy Density Symmetric Pseudocapacitors, Advanced Materials, 30 (2018) 1704754.

[104] M. Li, R. Jijie, A. Barras, P. Roussel, S. Szunerits, R. Boukherroub, NiFe layered double hydroxide electrodeposited on Ni foam coated with reduced graphene oxide for high-performance supercapacitors, Electrochimica Acta, 302 (2019) 1-9.

[105] Y.P. Lin, N.L. Wu, Characterization of MnFe$_2$O$_4$/LiMn$_2$O$_4$ Aqueous Asymmetric Supercapacitor, Journal of Power Sources, 196 (2011) 851-854.

[106] C. Tang, Z. Tang, H. Gong, Hierarchically Porous Ni-Co Oxide for High Reversibility Asymmetric Full-Cell Supercapacitors, Journal of the Electrochemical Society, 159 (2012) A651-A656.

[107] H. Luo, B. Wang, T. Liu, F. Jin, R. Liu, C. Xu, C. Wang, K. Ji, Y. Zhou, D. Wang, S. Dou, Hierarchical design of hollow Co-Ni LDH nanocages strung by MnO$_2$ nanowire with enhanced pseudocapacitive properties, Energy Storage Materials, 19 (2019) 370-378.

[108] W. Huang, A. Zhang, X. Li, J. Tian, L. Yue, L. Cui, R. Zheng, D. Wei, J. Liu,

Multilayer NiMn layered double hydroxide nanosheets covered porous Co_3O_4 nanowire arrays with hierarchical structure for high-performance supercapacitors, Journal of Power Sources, 440 (2019) 227123.

[109] X. Guan, M. Huang, L. Yang, G. Wang, X. Guan, Facial design and synthesis of CoSx/Ni-Co LDH nanocages with rhombic dodecahedral structure for high-performance asymmetric supercapacitors, Chemical Engineering Journal, 372 (2019) 151-162.

CHAPTER 3

High Performance Flexible Hybrid Supercapacitors Based on Ni(OH)₂@CuO@Cu Foam Composites for a Sunlight-Powered Rechargeable Energy Storage System

3.1 Introduction

Typically, transition metal hydroxides/oxides (Co_3O_4 [1], NiO [2], $Ni(OH)_2$ [3], Ni-Al layered double hydroxides [4] etc.) are commonly employed for pseudocapacitors, owing to their fast reversible redox behavior. Among the battery-like electrode materials, $Ni(OH)_2$ with large theoretical specific capacitance (2082 F g^{-1}) has drawn plenty of interest. For example, Jiang *et al*. fabricated 3D porous $Ni(OH)_2$/Ni electrode and achieved a specific capacity of 414 mC cm^{-2} at 10 mA cm^{-2} [5]. Xiong *et al*. reported the formation of ultrathin $Ni(OH)_2$ nanosheets on nickel foam (NF), demonstrating an areal capacity of 2160 mC cm^{-2} at 2 mA cm^{-2} [3]. Zou *et al*. synthesized $Ni(OH)_2$ nanosheets on electrochemically activated carbon cloth, exhibiting a specific capacity of 918 mC cm^{-2} at 2 mA cm^{-2} [6]. Shi *et al*. prepared $Ni(OH)_2$–Cu electrode, which delivered 3464 mC cm^{-2} at 1 mA cm^{-2} [7]. Even though the electrode materials achieved a good performance, the capacity was far below the theoretical value. Therefore, there is enough room for alternative methods to improve the properties of Ni-based electrodes.

In this chapter, we synthesized $Ni(OH)_2$ through electrochemical deposition on Cu foam as current collector due to its three-dimensional (3D) structure and good conductivity. Before $Ni(OH)_2$ electrochemical deposition, CuO was formed on Cu foam (CuO@Cu foam) by chemical oxidation, followed by thermal annealing at 190 °C for 3 h. The electrodeposition of $Ni(OH)_2$ was investigated for various time spans (30, 50, 90, 150 and 200 s) to gain some insights on the effect

of deposition time on the electrochemical properties of the resulting Ni(OH)$_2$@CuO@Cu foam electrode materials. Among them, Ni(OH)$_2$@CuO@Cu-150 composite exhibited the largest areal capacity of ~7063 mC cm^{-2} at 20 mA cm^{-2}. Hence, Ni(OH)$_2$@CuO@Cu-150 was investigated as a positive electrode to assemble a hybrid supercapacitor device, while N-doped reduced graphene oxide on nickel foam (N-rGO/NF) was applied as a negative electrode. The device displayed a large areal energy density of 130.4 μWh cm^{-2} at a power density of 1.6 mW cm^{-2}. For practical applications, two hybrid supercapacitor devices were assembled in series to successfully lighten up a red LED for 12 min 39 s. In addition, a three-digit digital display was powered for 1 min 28 s using three devices in series. Finally, a sunlight-powered integration system based on the hybrid supercapacitor device, solar cells, and a homemade windmill device was constructed. The hybrid supercapacitor was charged by the solar cell, which further powered the windmill device and ensured its continuous operation for 59 s, indicating the successful practical application of the hybrid supercapacitors based on Ni(OH)$_2$@CuO@Cu foam composites as energy storage devices.

3.2 Experimental section

3.2.1 Synthesis of CuO@Cu foam

CuO@Cu foam was prepared by chemical oxidation at room temperature (RT). Cu foam (1×3 cm^2) was washed sequentially before use with HCl (2M), acetone and MQ water under sonication for 10 min each. Then, an aqueous solution (40 mL) of 8 mM (NH$_4$)$_2$S$_2$O$_8$ and 60 mM NaOH was prepared to serve as the alkaline oxidative etchant solution. The clean Cu foam was placed in the above solution for 20 min to produce Cu(OH)$_2$@Cu foam with a blue color. Furthermore, the Cu(OH)$_2$@Cu sample was annealed at 190 $^{\circ}$C for 3 h to produce CuO@Cu foam.

3.2.2 Synthesis of Ni(OH)$_2$@CuO@Cu foam

Ni(OH)$_2$@CuO@Cu foam was synthesized through electrochemical deposition by applying

CuO@Cu foam, platinum foil and Ag/AgCl respectively as the working, counter, and reference electrodes. The electrolyte was $Ni(NO_3)_2 \cdot 6H_2O$ (0.3 M, 40 mL). The potentiostatic deposition was carried out at -1 V *vs.* Ag/AgCl for 30, 50, 90, 150 and 200 s to afford respectively $Ni(OH)_2$@CuO@Cu-30, $Ni(OH)_2$@CuO@Cu-50, $Ni(OH)_2$@CuO@Cu-90, $Ni(OH)_2$@CuO@Cu-150 and $Ni(OH)_2$@CuO@Cu-200. The resulting $Ni(OH)_2$@CuO@Cu samples were rinsed with MQ water, and dried in ambient air.

3.2.3 Assembly of a hybrid supercapacitor device

A hybrid supercapacitor was assembled using $Ni(OH)_2$@CuO@Cu-150 (positive electrode), N-rGO (negative electrode) and a filter paper (separator), immersed into 2 M KOH aqueous solution overnight. The current collector (nickel foam) was coated with N-rGO and polyvinylidene difluoride (PVDF) in a mass proportion of 8:2.

3.2.4 Construction of a sunlight-powered energy storage system

A sunlight-powered energy storage system was constructed by combining the as-prepared hybrid supercapacitor device with two solar cells (SC-3012-2A) obtained from abandoned solar-powered toys. Furthermore, a home-designed windmill device including an engine (1.5-9 V) and a windmill was prepared, and was powered by the hybrid supercapacitor device.

3.3 Results and discussion

The main target of the present work was to prepare high performance positive electrode for hybrid supercapacitors. Ni-based electrodes display high theoretical capacitance values. Therefore, we investigated $Ni(OH)_2$ modified CuO@Cu foam [$Ni(OH)_2$@CuO@Cu] as a binder-free electrode for supercapacitors. As illustrated in Figure 3.1, Cu foam with gold color (Figure 3.2a) was partially oxidized at ambient temperature to produce $Cu(OH)_2$@Cu sample with a blue-grey

color (Figure 3.2b). The chemical oxidation reaction could be described using Equation 3.1. The Cu(OH)$_2$@Cu sample was further calcined at 190 °C for 3 h to form CuO@Cu foam (Equation 3.2) (Figure 3.2c) with improved electrochemical characteristics (Figure 3.3). Ni(OH)$_2$ was deposited on CuO@Cu at -1 V *vs.* Ag/AgCl for 30, 50, 90, 150 and 200 s to form Ni(OH)$_2$@CuO@Cu-30, Ni(OH)$_2$@CuO@Cu-50, Ni(OH)$_2$@CuO@Cu-90, Ni(OH)$_2$@CuO@Cu-150 and Ni(OH)$_2$@CuO@Cu-200, respectively. Ni(NO$_3$)$_2$·6H$_2$O (0.3 M, 40 mL) was the electrolyte, which provided Ni^{2+} and OH$^-$ (Equation 3.3) during the whole deposition process.
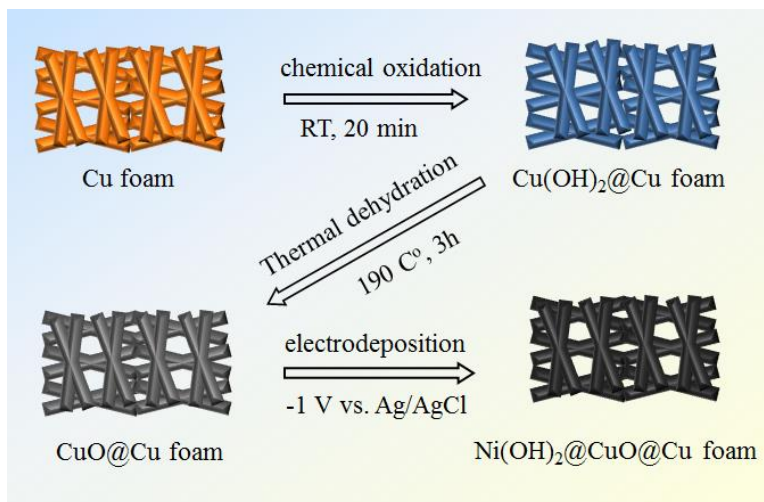
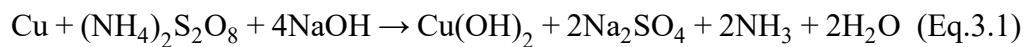**Figure 3.1:** Illustration of the synthesis of Ni(OH)$_2$@CuO@Cu foam electrode.

$$Cu + (NH_4)_2S_2O_8 + 4NaOH \rightarrow Cu(OH)_2 + 2Na_2SO_4 + 2NH_3 + 2H_2O \ (Eq.3.1)$$

$$Cu(OH)_2 \xrightarrow{190\ ^oC} CuO + H_2O \ (Eq.3.2)$$

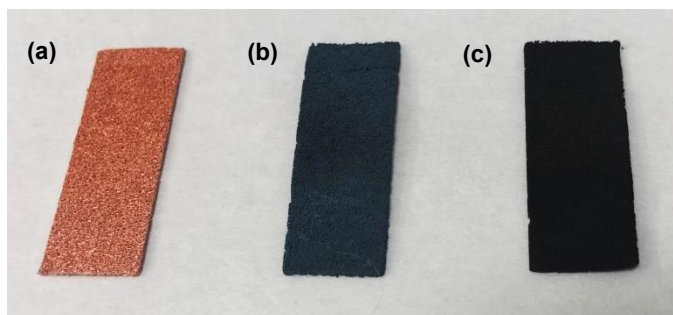$$NO_3^- + H_2O + 2e^- = NO_2^- + 2OH^- \ (Eq.\ 3.3)$$
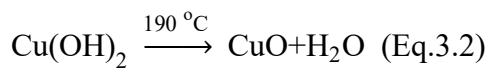
Figure 3.2: Photographs of (a) Cu foam, (b) Cu(OH)₂/Cu foam and (c) CuO/Cu foam.
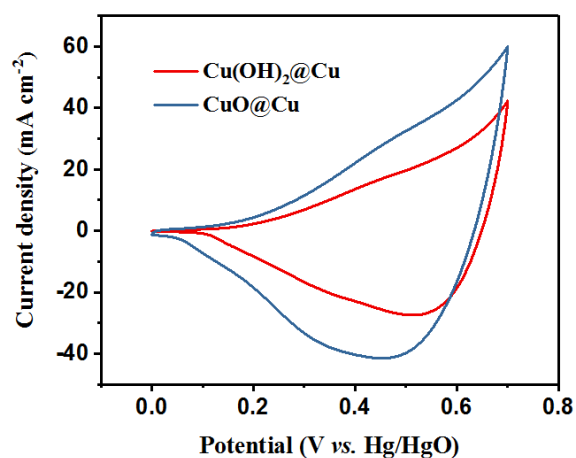

Figure 3.3: CV curves of Cu(OH)₂@Cu and CuO@Cu measured at a scan rate of 20 mV s⁻¹.

To investigate the crystallinity of the samples, X-ray diffraction (XRD) patterns were acquired. All the results are displayed in **Figure 3.4**, from which we can see peaks due to CuO at 35.5°, 38.7°, 38.9°, 48.7°, 61.5° and 67.9° assigned to the (-111), (111), (200), (-202), (-113), (-311) and (113) planes, respectively (JCPDS No. 41-0254). However, there are no obvious peaks of Ni(OH)₂, suggesting poor crystallinity of the material.
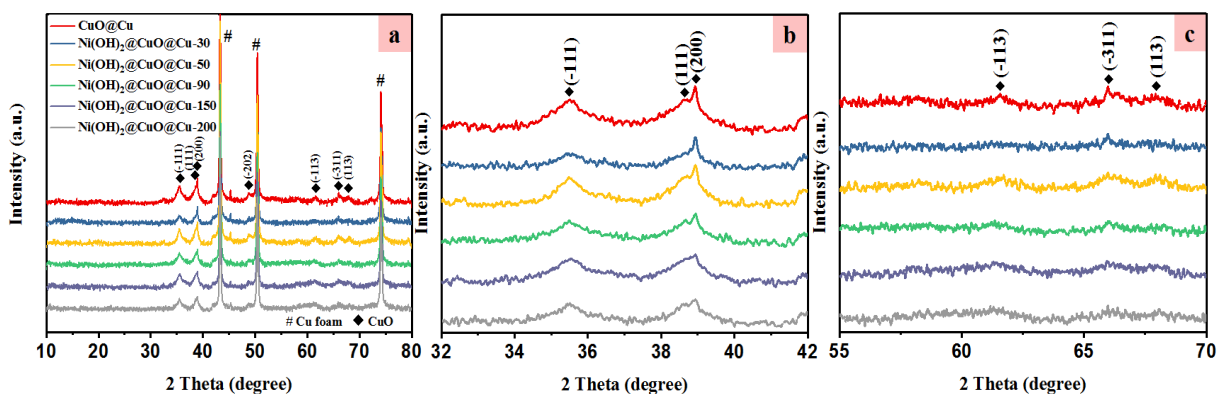
Figure 3.4: (a) XRD patterns of the prepared samples, (b) magnified patterns in the 30°-42° and 55°-70° *2θ* ranges.

Scanning electron microscopy (SEM) was further recorded to gain insight on the morphology of the composites. **Figure 3.5a** and **b** displays the SEM images of CuO@Cu foam where 1-dimensinal (1D) CuO nanowires decorated with nanoflowers were observed. This structure was expected to be beneficial for electron and ion transfer.
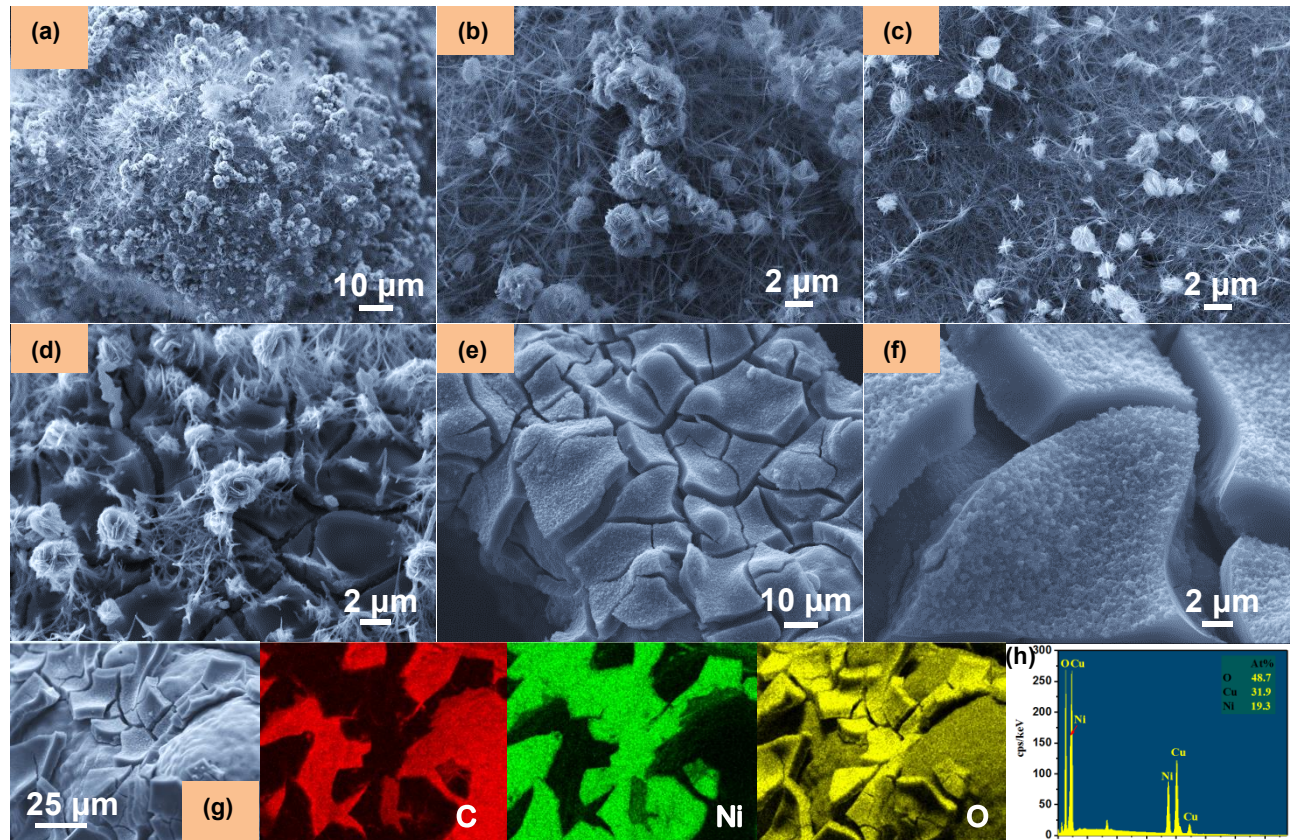
Figure 3.5: SEM images of (a,b) CuO@Cu foam, (c) Ni(OH)$_2$@CuO@Cu-30, (d) Ni(OH)$_2$@CuO@Cu-90 and (e,f) Ni(OH)$_2$@CuO@Cu-150. (g) EDS elemental mapping images and EDS spectrum of Ni(OH)$_2$@CuO@Cu-150.

The EDS elemental mapping images of CuO@Cu foam (**Figure 3.6**) revealed the homogeneous distribution of Cu and O elements. The SEM images of Ni(OH)$_2$@CuO@Cu-30 and Ni(OH)$_2$@CuO@Cu-50 are exhibited in **Figure 3.5c** and **Figure 3.7a**, respectively, showing no obvious difference with the morphology of the CuO@Cu support. This is most likely due to the short deposition time of Ni(OH)$_2$, even though EDS elemental mapping images shown in **Figure 3.8a** and **b** provided a proof of the existence of Ni element in these composites.

At the same time, the EDS spectra in **Figure 3.9** and elemental composition (**Table 3.1**) also demonstrated differences between CuO@Cu foam, Ni(OH)$_2$@CuO@Cu-30 and Ni(OH)$_2$@CuO@Cu-50, revealing 1.2 and 4.3 at.% of Ni element in Ni(OH)$_2$@CuO@Cu-30 and Ni(OH)$_2$@CuO@Cu-50, respectively, confirming Ni(OH)$_2$ successful deposition on CuO@Cu foam.
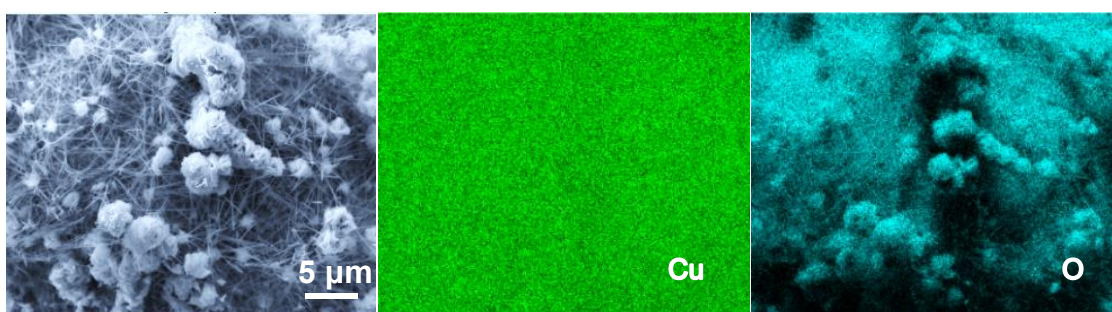

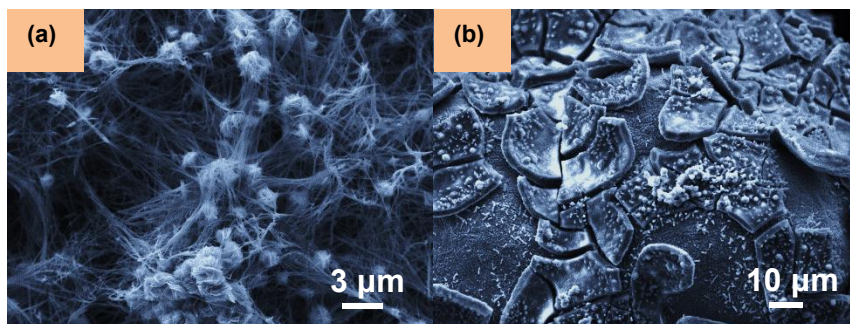**Figure 3.6**: EDS elemental mapping images of CuO@Cu foam.

Figure 3.7: SEM images of Ni(OH)$_2$@CuO@Cu-50 and Ni(OH)$_2$@CuO@Cu-200 electrodes.
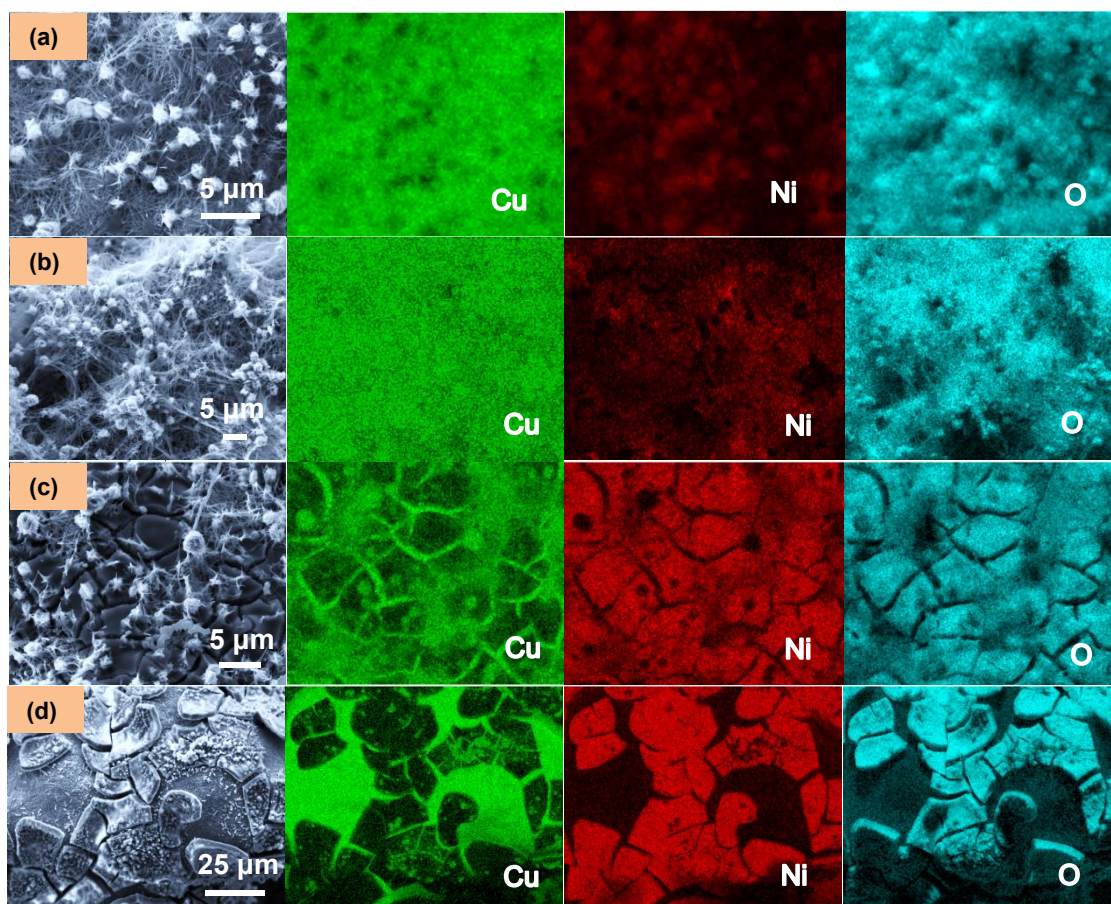
Figure 3.8: EDS elemental mapping images of (a) Ni(OH)$_2$@CuO@Cu-30, (b)

Ni(OH)$_2$@CuO@Cu-50, (c) Ni(OH)$_2$@CuO@Cu-90 and (d) Ni(OH)$_2$@CuO@Cu-200.
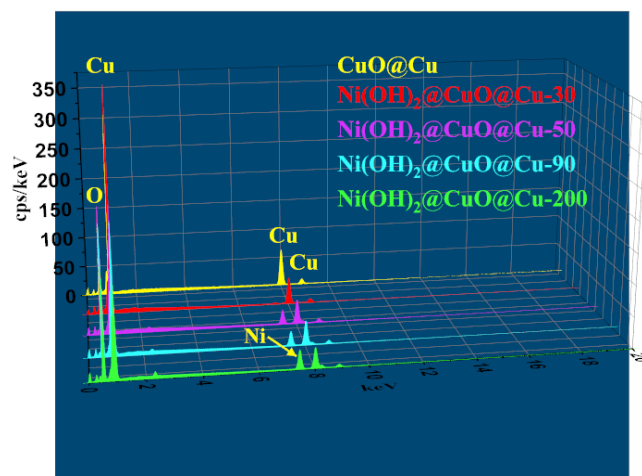
Figure 3.9: EDS spectra of CuO@Cu, Ni(OH)$_2$@CuO@Cu-30, Ni(OH)$_2$@CuO@Cu-50, Ni(OH)$_2$@CuO@Cu-90 and Ni(OH)$_2$@CuO@Cu-200.

Table 3.1. Elemental composition of the different samples.

Elements (At%) Composites	Ni	Cu	O
CuO@Cu		44.6	55.4
Ni(OH)$_2$@CuO@Cu-30	1.2	44.0	54.7
Ni(OH)$_2$@CuO@Cu-50	4.3	41.7	53.9
Ni(OH)$_2$@CuO@Cu-90	13.7	31.1	55.2
Ni(OH)$_2$@CuO@Cu-150	19.3	31.9	48.7
Ni(OH)$_2$@CuO@Cu-200	20.2	27.7	52.0

With increasing the deposition time to 90 s, apparent changes appeared on the sample morphology. Ni(OH)$_2$ exists obviously and covers the CuO nanowires partly, with the nanoflowers on the surface much like the muddy flowers (**Figure 3.5d**). The elemental mapping results showed the presence of Ni, Cu and O elements (**Figure 3.8**). There was an increase of Ni element content, which accounted for 13.7 at.%. Moreover, **Figure 3.5e** and **f** illustrate the SEM images of Ni(OH)$_2$@CuO@Cu-150, in which a thick Ni(OH)$_2$ film covers all the CuO on Cu foam, forming a "dry land"-type architecture, paved on the Cu foam surface. The thick Ni(OH)$_2$@CuO film presents cracks and is partially scratched, which can offer channels for electrolyte diffusion during

electrochemical measurements. Notably, some thick Ni(OH)$_2$@CuO pieces fall off on the surface of Cu foam. EDS elemental mapping images and EDS spectrum in **Figure 3.5g** and **h** revealed that the Ni, Cu and O elements are dispersed on the material and the Ni content increased to 19.3 at.%. However, the Ni element in Ni(OH)$_2$@CuO@Cu-200 (20.2 at.%) did not increase much, as compared to Ni(OH)$_2$@CuO@Cu-150; this was most likely due to falling off of the thick Ni(OH)$_2$@CuO piece on Cu foam, as seen in the SEM image in **Figure 3.7b** and EDS elemental mapping images in **Figure 3.8d**.

Furthermore, X-ray photoelectron spectroscopy (XPS) analysis was acquired to evaluate the chemical composition of the samples. From the survey spectra of Ni(OH)$_2$@CuO@Cu-150 (**Figure 3.10**) and CuO@Cu foam (**Figure 3.11**), we can see obviously that there are Cu$_{2p}$ and O$_{1s}$ elements for both samples, along with Ni$_{2p}$ element in Ni(OH)$_2$@CuO@Cu-150 composite, consistent with the EDS elemental mapping results in **Figures 3.6**, **3.8** and **3.5g**.

The high resolution spectrum of the Cu$_{2p}$ in Ni(OH)$_2$@CuO@Cu-150 (**Figure 3.10b**) comprises Cu$_{2p3/2}$ and Cu$_{2p1/2}$ peaks respectively at 934.5 and 954.6 eV, and two satellite peaks at ~942.4, and 963.0 eV. Similarly, from **Figure 3.11b**, we can see that the Cu$_{2p}$ high-resolution spectrum in CuO@Cu can be deconvoluted in two peaks ascribed to Cu$_{2p3/2}$ and Cu$_{2p1/2}$ at respectively 933.7 and 953.7 eV along with two satellite peaks at 943.5 and 962.1 eV, indicating the existence of CuO [8]. There is a small apparent shift in the binding energy compared with Ni(OH)$_2$@CuO@Cu-150, which can be assigned to the interaction between Ni(OH)$_2$ and CuO. Figure 3.10c depicts the core-level spectrum of Ni$_{2p}$. It consists of two typical peaks corresponding to Ni$_{2p3/2}$ and Ni$_{2p1/2}$ at respectively 856.1 and 873.6 eV, and two satellite peaks at 861.6 and 879.8 eV, suggesting the existence of Ni^{2+} oxidation state [5].

Furthermore, the core-level spectrum of the O$_{1s}$ of Ni(OH)$_2$@CuO@Cu-150 (**Figure 3.10d**)

can be curve-fitted with three components at 530.2, 531.6 and 533.1 eV, ascribed to M-O binding, M-OH binding and physi- and/or chemisorbed molecular water [5, 9], further proving the successful synthesis of Ni(OH)$_2$@CuO@Cu-150 composite. In contrast, the core-level spectrum of the O$_{1s}$ of CuO@Cu (**Figure 3.11c**) displays a pair of peaks at ~529.6 and 531.1 eV corresponding to Cu=O and intrinsic oxygen defects in the crystal lattice, respectively [10].
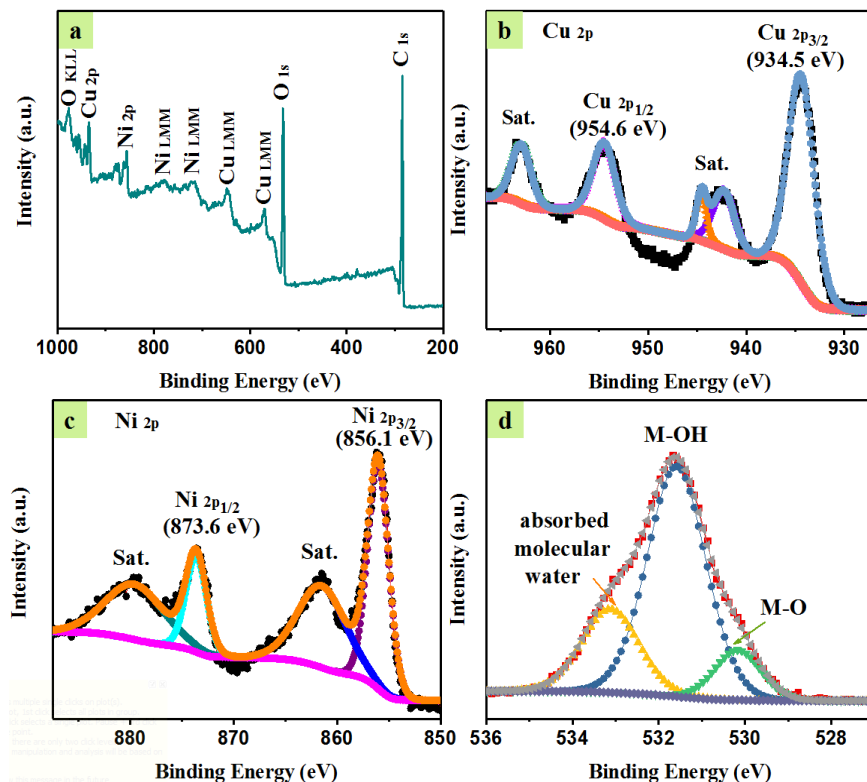

Figure 3.10: XPS analysis of Ni(OH)$_2$@CuO@Cu-150: (a) Survey spectrum, and core-level spectra of (b) Cu$_{2p}$, (c) Ni$_{2p}$ and (d) O$_{1s}$.
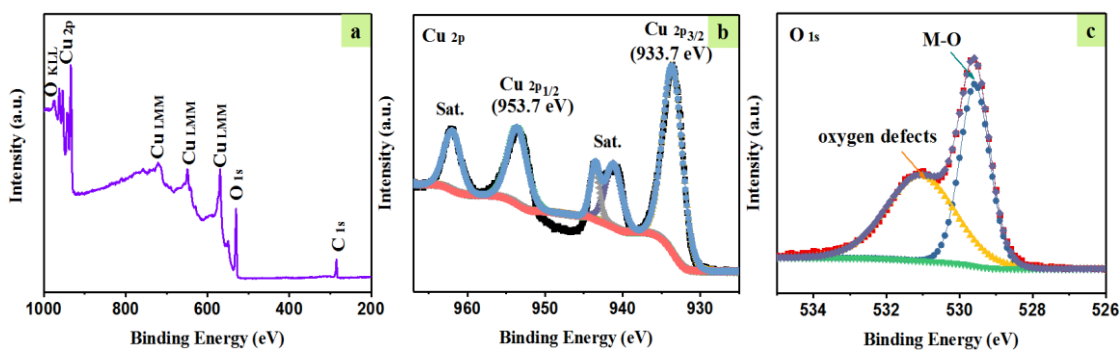
Figure 3.11: XPS analysis of CuO@Cu: (a) survey spectrum, and high resolution spectra of (b) Cu_{2p} and (f) O_{1s}.

All samples obtained in this work were investigated by electrochemical measurements in aqueous KOH (2 M) electrolyte in a classical 3-electrode cell (Figure 3.12). Figure 3.12a depicts the CV curves of all the samples in the potential range of -0.2 to +0.9 V recorded at 20 mV s^{-1}. The presence of redox active peaks for Ni(OH)$_2$@CuO@Cu foam composites is consistent with the redox process shown in **Equation 2.1**.

By varying the deposition time, Ni(OH)$_2$@CuO@Cu foam composites exhibited different electrochemical performances. Among all samples, Ni(OH)$_2$@CuO@Cu-150 attained the largest current density at 20 mV s^{-1}. The areal capacity values were determined by integrating the area under the CV curves using the following **Equation 1.15.2**, where *m* (the mass loading of SC electrodes) is replaced by *A* (cm^{-2}) (the area of active material). The results are summarized in **Table 3.2**, which revealed that Ni(OH)$_2$@CuO@Cu-150 possessed the largest areal capacity of 7742 mC cm^{-2} at 20 mV s^{-1}.

Table 3.2. The areal capacitance of as-obtained composites at a scan rate of 20 mV s^{-1}.

Composites	Areal capacitance (mC cm^{-2})
CuO@Cu	1683.4
Ni(OH)$_2$@CuO@Cu-30	3430.9
Ni(OH)$_2$@CuO@Cu-50	4495.5
Ni(OH)$_2$@CuO@Cu-90	5711.9
Ni(OH)$_2$@CuO@Cu-150	7742.2
Ni(OH)$_2$@CuO@Cu-200	6820.9

Figure 3.12b depicts the CV plots of Ni(OH)$_2$@CuO@Cu-150 measured at various scan rates; as the scan rate increases the redox peak potential shifts positively, suggesting good conductivity of the electrode and facile ion transport kinetics.
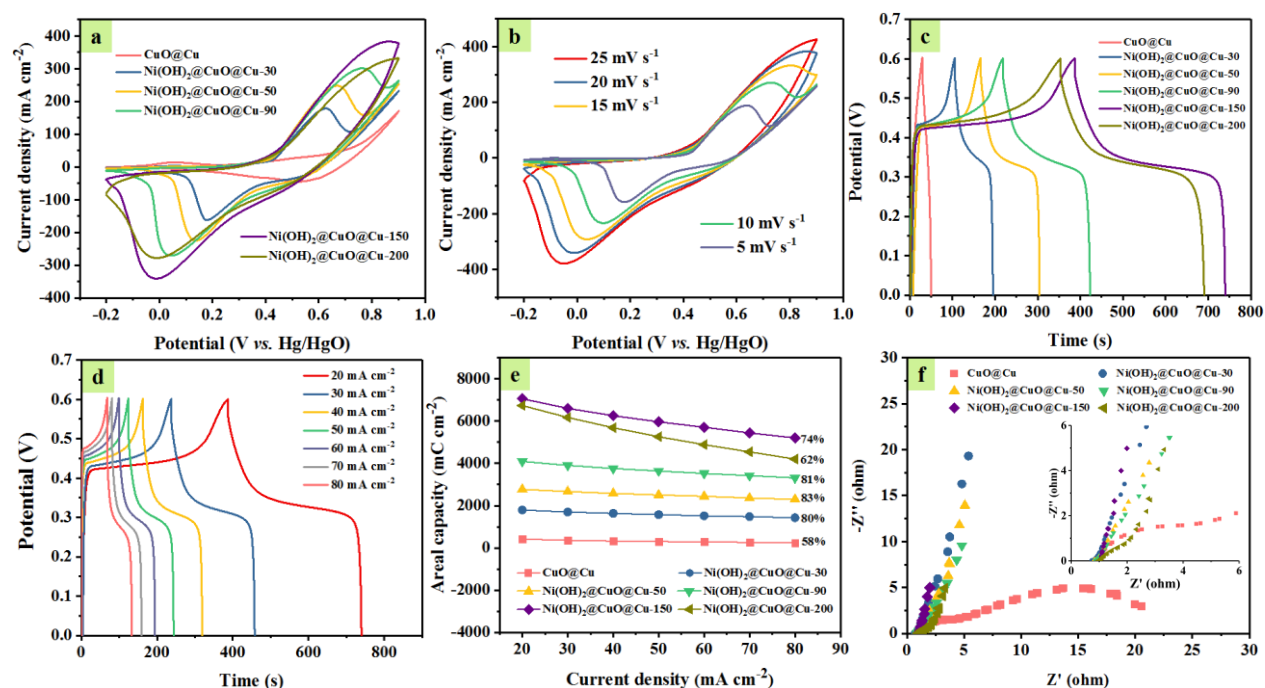

Figure 3.12: The electrochemical behavior of the different electrodes measured in KOH (2 M) aqueous solution. (a) CV plots acquired at 20 mV s^{-1}. (b) CV curves of Ni(OH)$_2$@CuO@Cu-150 recorded at different scan rates. (c) GCD plots of the different electrodes acquired at 20 mA cm^{-2}. (d) GCD profiles of Ni(OH)$_2$@CuO@Cu-150 measured at various current densities. (e) Areal capacity of the electrodes at various current densities. (f) Electrochemical impedance spectra in the 0.01 Hz to 100 kHz frequency range recorded at open circuit potential.

GCD plots of all the samples were carried out to assess their performance. As seen in **Figure 3.12c**, the Ni(OH)$_2$@CuO@Cu-150 composite exhibited the longest discharge time, signifying the largest areal capacity compared with other samples, in accordance with the results of CV curves

in **Figure 3.12a**. Furthermore, the GCD profiles of the electrodes at various current densities were acquired and the corresponding coulombic efficiencies are depicted in **Table 3.3**. All Ni(OH)$_2$@CuO@Cu foam composites revealed higher coulombic efficiencies than CuO@Cu foam.

Table 3.3 Coulombic efficiencies of as-prepared electrode materials.

Current density (mA cm^{-2}) / Composites	20	30	40	50	60	70	80
CuO@Cu	77.8%	78.7%	72.8%	67.6	60%	63.3%	56.8%
Ni(OH)$_2$@CuO@Cu-30	88.8%	90.6%	90.4%	89.4%	83.4%	85.9%	79.3%
Ni(OH)$_2$@CuO@Cu-50	87.4%	90.9%	91.2%	90.5%	90.4%	89.2%	87.8%
Ni(OH)$_2$@CuO@Cu-90	94%	95.8%	96.1%	95.6%	95.1%	94.7%	94.3%
Ni(OH)$_2$@CuO@Cu-150	91.5%	94.2%	96.2%	96.3%	96.1%	96%	95.6%
Ni(OH)$_2$@CuO@Cu-200	95.5%	96.8%	97.5%	96.4%	96.4%	94.9%	95%

Figure 3.12d displays the areal capacity values of Ni(OH)$_2$@CuO@Cu-150, determined using Equation 1.11.2. The composite attained areal capacities of ~7063, 6606, 6259, 5970, 5709, 5443 and 5203 mC cm^{-2} at 20, 30, 40, 50, 50, 60, 70 and 80 mA cm^{-2}, respectively (see **Figure 3.12e** and **Table 3.4**). One sees that the areal capacity is deposition time dependent. At the initial stage, the areal capacity increases with increasing the deposition time, but saturates when the deposition times exceeds 200 s. This is might be attributed to partial removal of the active materials on Cu foam (**Figure 3.7b**). Moreover, compared with CuO@Cu foam, all Ni(OH)$_2$@CuO@Cu composites exhibited improved rate performance (**Figure 3.12e**).

Table 3.4. The areal capacity (mC cm^{-2}) of as-obtained composites at various current densities.

Current density (mA cm^{-2}) Composites	20	30	40	50	60	70	80
CuO@Cu	412.8	360	321.6	300	280.8	260.4	240
Ni(OH)$_2$@CuO@Cu-30	1792	1699	1632	1572	1519	1478	1430
Ni(OH)$_2$@CuO@Cu-50	2770	2664	2578	2502	2441	2360	2298
Ni(OH)$_2$@CuO@Cu-90	4092	3906	3758	3642	3521	2360	2298
Ni(OH)$_2$@CuO@Cu-150	7063	6606	6259	5970	5710	5443	5203
Ni(OH)$_2$@CuO@Cu-200	6737	6174	5688	5262	4889	4544	4205

Electrochemical impedance spectroscopy (EIS) analysis in the frequency range of 100 kHz to 0.01 Hz was recorded to gain further insight into the electrochemical processes at different time constants (**Figure 3.12f**). For all the Ni(OH)$_2$@CuO@Cu composites, the Nyquist plots revealed a very small depressed semicircle (high-to-medium frequency region) related to the electrochemical reaction process, and a straight line (low-frequency region) arising from ion diffusion in the electrode material. **Figure 3.13a** illustrates the corresponding equivalent circuit, where R_s is the internal resistance, R_{ct} represents the charge-transfer resistance related to the depressed semicircle in the curves, Q is the pseudocapacitance, W_o is the ion transport resistance.
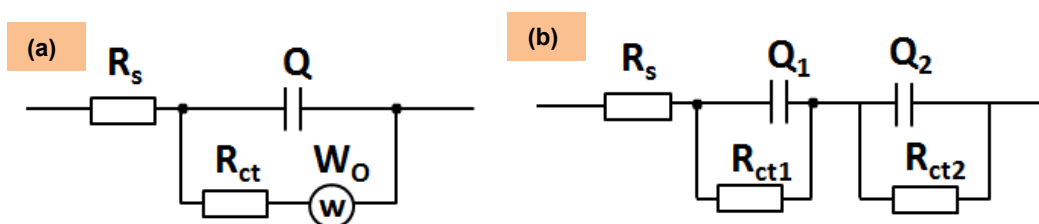

Figure 3.13: The equivalent circuit of (a) Ni(OH)$_2$@CuO@Cu foam and (b) CuO@Cu composites.

Among all Ni(OH)$_2$@CuO@Cu composites, Ni(OH)$_2$@CuO@Cu-150 displayed the smallest R_{ct} (0.34 ohm cm^{-2}) (**Table 3.5**) and the biggest slope for the straight line, suggesting favorable access for the charge transfer and ion diffusion. However, for CuO@Cu foam, there is no ion diffusion process in the 100 kHz to 0.01 Hz frequency range. Two charge transfer processes were observed instead, which take place at the CuO/electrolyte and Cu foam/CuO interfaces. Using the equivalent circuit in **Figure 3.13b**, R_s = 0.94 ohm cm^{-2}, R_{ct1} = 3.22 ohm cm^{-2} and R_{ct2}=22.05 ohm cm^{-2} were determined. These values are larger than those recorded for Ni(OH)$_2$@CuO@Cu foam composites (**Table 3.5**).

Table 3.5. Resistance values of as-prepared electrode materials.

Composites	Intrinsic resistance (R_s) / ohm cm^{-2}	Charge transfer resistance (R_{ct}) / ohm cm^{-2}
CuO@Cu	0.94	R_{ct1}=3.22, R_{ct2}=22.08
Ni(OH)$_2$@CuO@Cu-30	0.80	1.01
Ni(OH)$_2$@CuO@Cu-50	0.88	0.82
Ni(OH)$_2$@CuO@Cu-90	0.91	0.67
Ni(OH)$_2$@CuO@Cu-150	1.04	0.34
Ni(OH)$_2$@CuO@Cu-200	0.97	1.69

Furthermore, to investigate the kinetics during the electrochemical reaction, the relationship between log(i) and log(v) for cathodic and anodic peak currents according to the CV curves of Ni(OH)$_2$@CuO@Cu-90 (**Figure 3.14a**) and Ni(OH)$_2$@CuO@Cu-150 (**Figure 3.12b**) was studied to determine the capacitive contribution: $i = av^b$, where i stands for the current, v represents the scan rate. When the variable b=1, the electrochemical reaction is controlled by a capacitive process, while when the variable b=0.5, the electrochemical reaction is derived from a semi-infinite diffusion process (Faradaic mode).
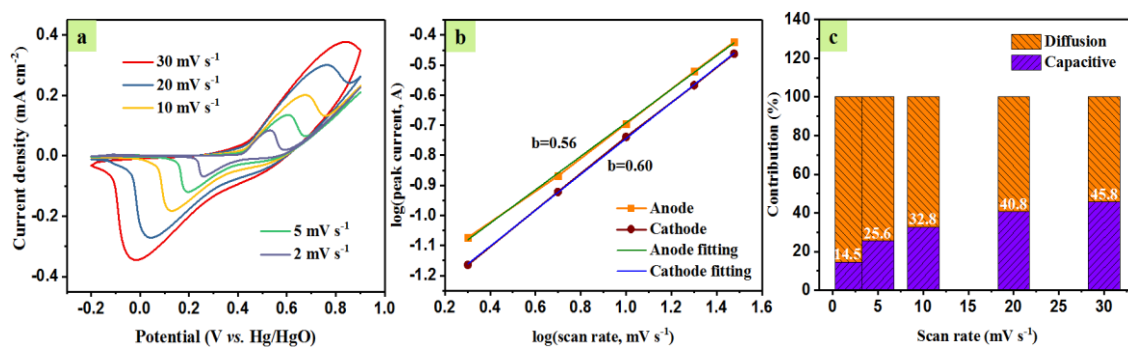
Figure 3.14: (a) CV curves of Ni(OH)$_2$@CuO@Cu-90 measured at different scan rates. (b) Relationship between logarithm peak current and logarithm scan rate of Ni(OH)$_2$@CuO@Cu-90. (c) Capacitive contribution ratio of Ni(OH)$_2$@CuO@Cu-90 at different scan rates.

As displayed in **Figure 3.14b**, the *b*-values of Ni(OH)$_2$@CuO@Cu-90 were calculated as 0.56 and 0.60 from the anode and cathode peak currents, respectively, and for Ni(OH)$_2$@CuO@Cu-150 (**Figure 3.15a**), the *b*-values were found to be as 0.51 and 0.55 at different scan rates, signifying the contribution of both capacitive and Faradaic battery behaviors in the charge storage process. The whole electrochemical process can be represented by the equation $i = k_1v + k_2v^{1/2}$, and from the relationship of $v^{1/2}$ *vs.* $1/v^{1/2}$, we can determine the slope (k_1) and the y-axis intercept (k_2). From **Figure 3.15b**, we can see that the capacitive contribution ratio for Ni(OH)$_2$@CuO@Cu-150 sample at 5 mV s^{-1} is about 24.1%, and further improves with the increasing the scan rate to attain 41.6% at 25 mV s^{-1}. For the Ni(OH)$_2$@CuO@Cu-90 composite (**Figure 3.14b**), the capacitive contribution ratio at 2 mV s^{-1} is ~14.5%, and reaches 45.8% at 30 mV s^{-1}. All the results revealed the complex charge storage mechanism based on the combination of capacitive process and diffusion controlled faradaic characteristic with the latter contributing more on the performance.
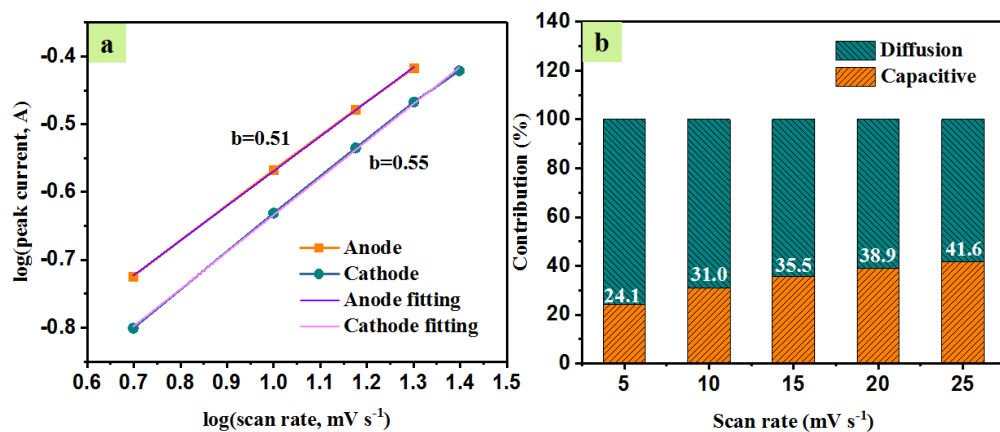
Figure 3.15: (a) Relationship between $\log(i)$ and $\log(v)$ of Ni(OH)$_2$@CuO@Cu-150. (b) Capacitive contribution ratio of Ni(OH)$_2$@CuO@Cu-150 at various scan rates.

Consequently, Ni(OH)$_2$@CuO@Cu-150 composite was chosen as the positive electrode to construct a hybrid supercapacitor, according to the schematic diagram presented in **Figure 3.16a**, while N-rGO coated on NF (N-rGO/NF) acts as the negative electrode. The electrochemical performance was investigated in a 2-electrode system. To choose the suitable operating potential window of the hybrid supercapacitor device, as illustrated in **Figure 3.16b**, the CV plots were acquired at 100 mV s^{-1} in different potential windows. The results indicated that the operating cell voltage window can be extended up to 1.8 V although there was an obvious polarization phenomenon occurring at cell voltage larger than 1.7 V. Hence, 0-1.6V was selected as the operating cell voltage window to reduce the damage to the electrode and ensure stable operation of the device.

Figure 3.16c displays the CV plots acquired between 0 and 1.6 V at various scan rates, which show a typical capacitive-like behavior of a hybrid supercapacitor device with obvious deviation from ideal capacitive characteristics [11]. Moreover, the GCD profiles at various current densities were recorded (**Figure 3.16d**) according to **Equation 1.11.2**, and the corresponding areal

capacities of the hybrid supercapacitor device were calculated and displayed in **Figure 3.16e**. Areal capacities of 587, 387, 318, 274, 209, 186 and 162 mC cm^{-2} were obtained respectively at 2, 3, 4, 5, 8, 10 and 15 mA cm^{-2}. Accordingly, the Ragone plot related to energy density and power density, calculated by **Equations 1.12** and **1.13**, is depicted in **Figure 3.16f**, achieving the largest areal energy density of 130.4 µWh cm^{-2} at a power density of 1.6 mW cm^{-2}. In comparison, this value is higher than that achieved by NiCo$_2$S$_4$//C (121 µWh cm^{-2} at 0.8 mW cm^{-2}) [12], Mn$_3$O$_4$//Ni(OH)$_2$ (12 µWh cm^{-2} at 0.04 mW cm^{-2}) [13], Ni-Co LDH//ketjenblack (14.4 µWh cm^{-2} at 312.5 µW cm^{-2}) [14], Ni(OH)$_2$-AC-based hybrid capacitor (33.6 µWh cm^{-2} at 0.46 mW cm^{-2}) [15], YP-80F//Ni$_1$Co$_1$-OH (125.6 µWh cm^{-2} at 62.16 mW cm^{-2}) [16] and RGO@CoNi-LDH//RGO@AC (8.89 µWh cm^{-2} at 0.525 mW cm^{-2}) [17] hybrid supercapacitor devices.

EIS analysis was further performed in the 100 kHz to 0.01 Hz frequency range to highlight the electrochemical processes of the hybrid supercapacitor device (**Figure 3.16g**), showing small internal resistance (R_s=0.166 ohm cm^{-2}) and charge-transfer resistance (R_{ct}=0.438 ohm cm^{-2}).

Additionally, the mechanical characteristics and flexibility of the device were assessed by bending at various angles, as illustrated in the schematic diagram in the middle of **Figure 3.16h**. We can see that there was no obvious shape change of the CV plots at various angles 0º, 30º, 60º, 90º and 150º, signifying the good mechanical stability and enhanced flexibility of the hybrid supercapacitor device. In addition, the stability was tested for 10,000 charging-discharging cycles at 2 mA cm^{-2}. The device retained about 92% and 72% of the original capacity after 2,000 and 10,000 cycles, respectively, suggesting a good cycling stability.
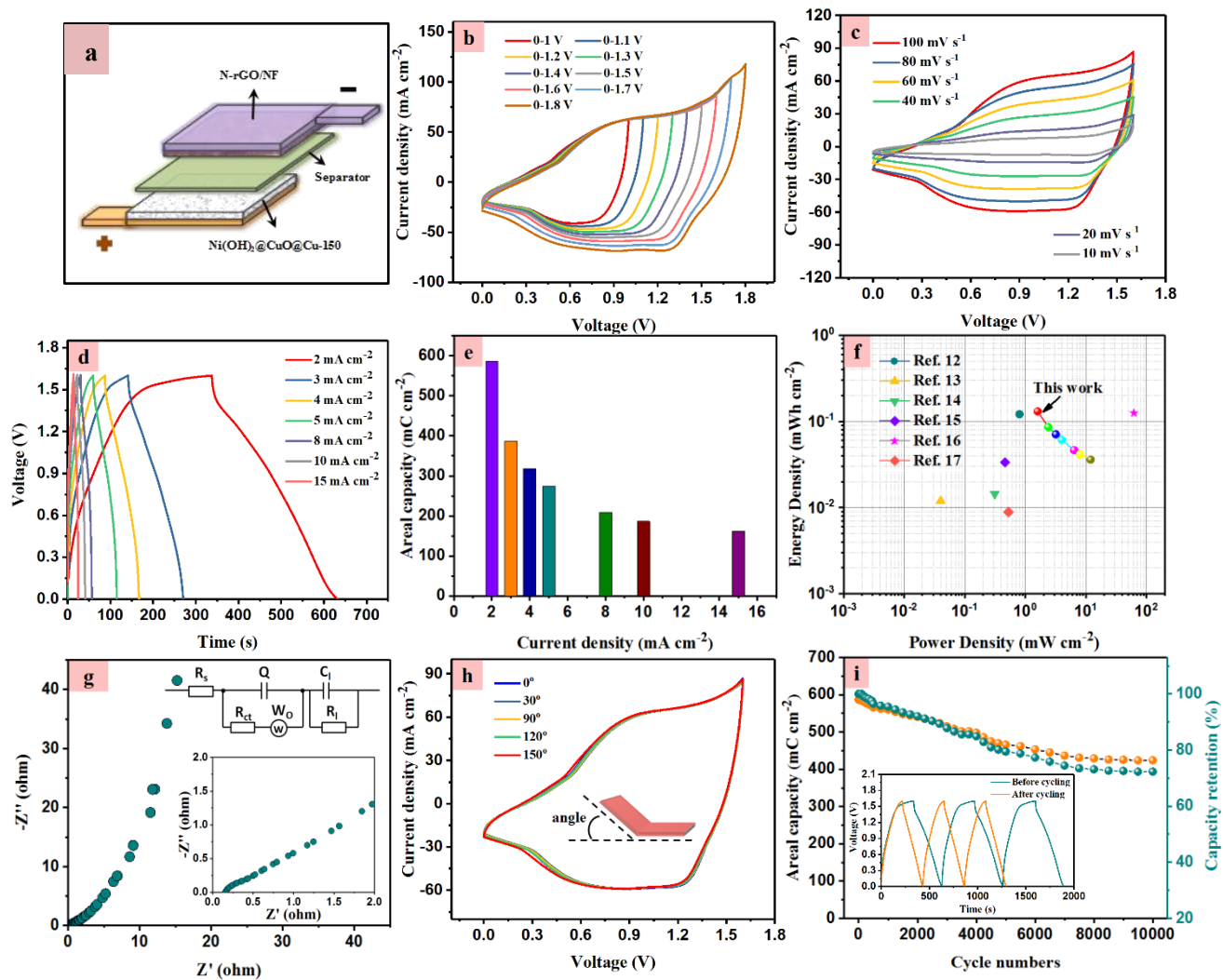
Figure 3.16: (a) Schematic of the packed hybrid supercapacitor device. CV plots measured at 100 mV s^{-1} at (b) different cell voltage windows, and (c) different scan rates between 0 and 1.6 V. (d) GCD curves recorded at various current densities. (e) Areal capacity at various current densities. (f) Ragone plot. (g) EIS curve acquired in the frequency range of 0.01 Hz and 100 kHz; the inset up-right in (g) is the corresponding equivalent circuit. (h) CV plots acquired at 100 mV s^{-1} at different bending angles. (i) Cycling performance at 2 mA cm^{-2}; the inset in (i) are the GCD plots before and after cycling.

To explore the potential of the device for practical applications, two as-prepared hybrid

Ni(OH)$_2$@CuO@Cu-150//N-rGO/NF supercapacitor devices in series were connected to provide energy for a red LED (1.8-2 V), as illustrated in **Figure 3.17a**. **Figure 3.17b** reveals the successful lighting of the red LED powered by the devices, which can last for 12 min 39 s. Additionally, we constructed a three-digit digital display (4-30 V) with three as-prepared hybrid supercapacitor devices connected in series (**Figure 3.17c**). The three-digit digital display was successfully lighted up by the supercapacitor devices for 1 min 28 s (**Figure 3.17d**). All of these results demonstrate the promising application of the hybrid supercapacitor for flexible energy storage.
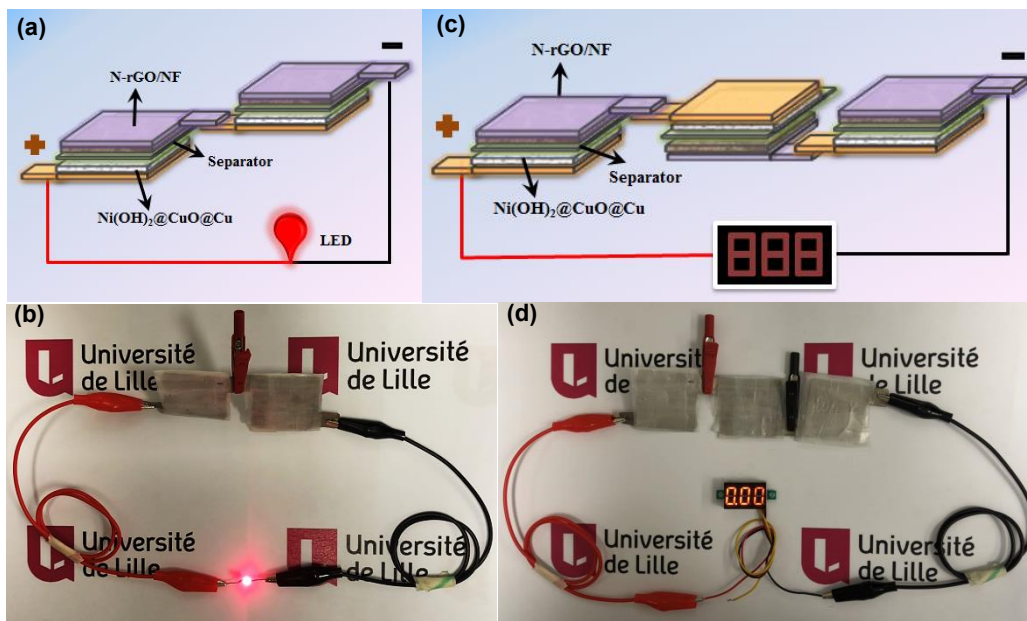

Figure 3.17. (a) Schematic diagram of two hybrid supercapacitor devices in series for lighting of a LED. (b) A red LED lighted up by two supercapacitor devices in series. (c) Schematic diagram of three hybrid supercapacitor devices in series for lighting a digital display. (d) A three-digit digital display lighted up by three supercapacitor devices in series.

Furthermore, taking benefit of the cleanest and earth abundant solar energy to power a hybrid supercapacitor device represents an appealing method. Therefore, solar cells were used to supply

energy to the $Ni(OH)_2$@CuO@Cu-150//N-rGO/NF hybrid supercapacitor (**Figure 3.18a**). From the schematic diagram, we can see that the whole system comprises two steps. In the first step: the hybrid supercapacitor device was charged by solar cells, while in the second step, the hybrid supercapacitor device was used to supply electricity for a home-designed windmill device, including an engine (1.5-9 V) and a windmill. Herein, the solar cells acted as the energy conversion system, the hybrid supercapacitor device was employed as the energy storage device and home-designed windmill device was applied as the energy utilization device, constituting the entire system. The entire operation process can be equivalent to the circuit diagram on the right. The test was performed outdoors; the two solar cells (SC-3012-2A) connected in series were powered by sunlight from 0.638 V to 1.561 V (**Figure 3.18b** and **c**), and then provided energy for the home-designed windmill device (**Figure 3.18d**), which continuously worked for 59 s. At the same time, the solar cells were obtained from abandoned solar-toy, realizing waste utilization, in line with the concept of sustainable development. All the results provided a proof for the combination of solar cells and a hybrid supercapacitor device, signifying the promising potential and direction for the energy storage devices for the future applications.
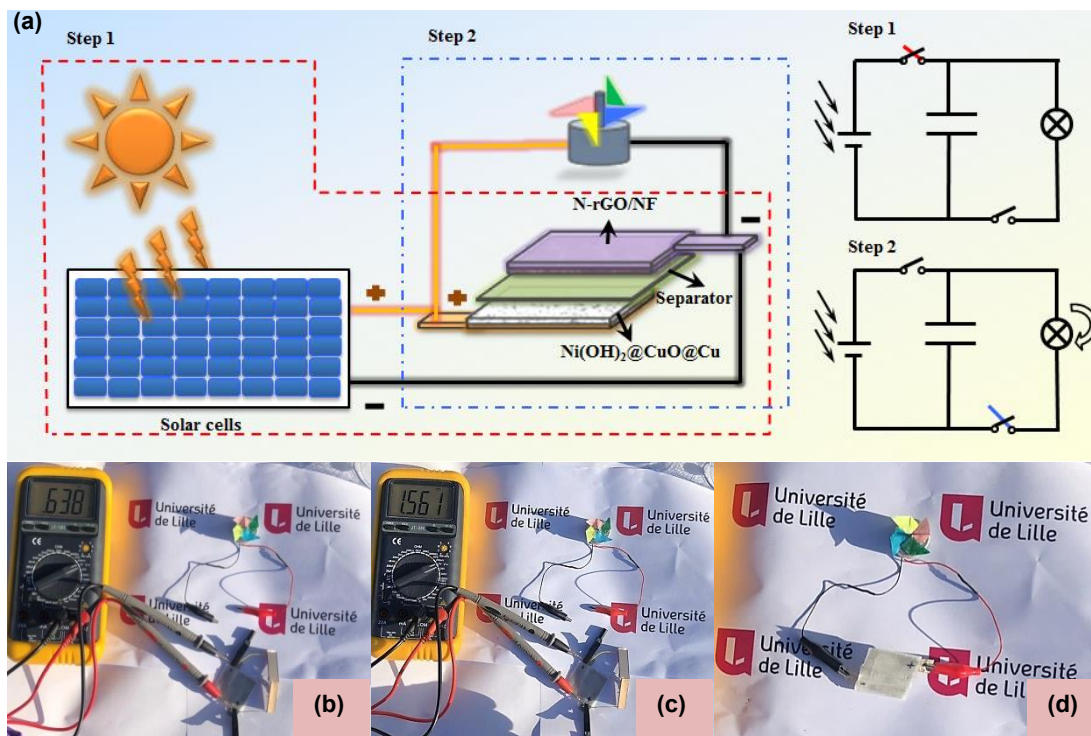
Figure 3.18. Schematic diagram and equivalent circuit of integrated system combining solar cells with the hybrid supercapacitor device for operating a homemade windmill device. (b-c) Photographs of the solar cells charging of the hybrid supercapacitor device. (d) Photograph of the home-designed windmill device operation.

3.4 Conclusion

In conclusion, $Ni(OH)_2$@CuO@Cu foam composites were prepared by electrochemical deposition at different times (30, 50, 90, 150 and 200 s) of $Ni(OH)_2$ on CuO@Cu foam. Among all the samples, $Ni(OH)_2$@CuO@Cu-150 achieved the highest performance with an areal capacity of 7063.2 mC cm^{-2} at 20 mA cm^{-2}. Therefore, this composite was further investigated as a positive electrode to assemble a hybrid supercapacitor device. As an energy storage device, the as-assembled hybrid supercapacitor attained a high areal energy density of 130.4 µWh cm^{-2} at a power

density of 1.6 mW cm^{-2}. Two hybrid supercapacitor devices in series were able to power a red LED for 12 min 39 s and three devices in series successfully supplied electricity for a three-digit digital display for 1 min 28 s. Finally, an integrated system combining solar cells with the hybrid supercapacitor device for operating a homemade windmill device was constructed. After charging by solar cells, the hybrid supercapacitor device stored energy and further powered a homemade windmill device for 59 s. All of the findings suggested that Ni(OH)$_2$@CuO@Cu foam composites have potential for hybrid supercapacitor devices application, and the combination of solar cells with the supercapacitor device described a promising future for sunlight-powered energy storage device applications.

3.5 References

[1] W. Wang, Y. Liu, M. Wang, G. Ren, S. Wu, J. Shen, Facilely prepared oxidized carbon Fiber@Co_3O_4@RGO as negative electrode for a novel asymmetric supercapacitor with high areal energy and power density, Applied Surface Science, 450 (2018) 66-76.

[2] S. Yin, Y. Wu, Q. Xiong, H. Qin, H.Z. Chi, Flower-like NiO with a Hierarchical and Mesoporous Structure for Supercapacitors, ChemElectroChem, 4 (2017) 2563-2570.

[3] X. Xiong, D. Ding, D. Chen, G. Waller, Y. Bu, Z. Wang, M. Liu, Three-dimensional ultrathin $Ni(OH)_2$ nanosheets grown on nickel foam for high-performance supercapacitors, Nano Energy, 11 (2015) 154-161.

[4] W. Wang, N. Zhang, Z. Shi, Z. Ye, Q. Gao, M. Zhi, Z. Hong, Preparation of Ni-Al layered double hydroxide hollow microspheres for supercapacitor electrode, Chemical Engineering Journal, 338 (2018) 55-61.

[5] H. Jiang, Y. Guo, T. Wang, P.L. Zhu, S. Yu, Y. Yu, X.Z. Fu, R. Sun, C.P. Wong, Electrochemical fabrication of $Ni(OH)_2$/Ni 3D porous composite films as integrated capacitive electrodes, RSC Advances, 5 (2015) 12931.

[6] Q. Zou, D. Khalafallah, Z. Wu, J. Chen, M. Zhi, Z. Hong, Supercritical ethanol deposition of $Ni(OH)_2$ nanosheets on carbon cloth for flexible solid-state asymmetric supercapacitor electrode, The Journal of Supercritical Fluids, 159 (2020) 104774.

[7] D. Shi, L. Zhang, X. Yin, T.J. Huang, H. Gong, A one step processed advanced interwoven architecture of $Ni(OH)_2$ and Cu nanosheets with ultrahigh supercapacitor performance, Journal of Materials Chemistry A, 4 (2016) 12144-12151.

[8] J. Yuan, J.J. Zhang, M.P. Yang, W.J. Meng, H. Wang, J.X. Lu, CuO Nanoparticles Supported on TiO_2 with High Efficiency for CO_2 Electrochemical Reduction to Ethanol, Catalysts, 8 (2018)

171.

[9] T. Zhou, Z. Cao, P. Zhang, H. Ma, Z. Gao, H. Wang, Y. Lu, J. He, Y. Zhao, Transition metal ions regulated oxygen evolution reaction performance of Ni-based hydroxides hierarchical nanoarrays, Scientific Reports, 7 (2017) 46154.

[10] A. Devadoss, P. Sudhagar, C. Ravidhas, R. Hishinuma, C. Terashima, K. Nakata, T. Kondo, I. Shitanda, M. Yuasa, A. Fujishima, Simultaneous glucose sensing and biohydrogen evolution from direct photoelectrocatalytic glucose oxidation on robust Cu_2O-TiO_2 electrodes, Physical Chemistry Chemical Physics, 16 (2014) 21237-21242.

[11] Y. Shao, M.F. El-Kady, J. Sun, Y. Li, Q. Zhang, M. Zhu, H. Wang, B. Dunn, R.B. Kaner, Design and Mechanisms of Asymmetric Supercapacitors, Chemical Reviews, 118 (2018) 9233-9280.

[12] W. Kong, C. Lu, W. Zhang, J. Pu, Z. Wang, Homogeneous core–shell $NiCo_2S_4$ nanostructures supported on nickel foam for supercapacitors, Journal of Materials Chemistry A, 3 (2015) 12452-12460.

[13] J.X. Feng, S.H. Ye, X.F. Lu, Y.X. Tong, G.R. Li, Asymmetric Paper Supercapacitor Based on Amorphous Porous Mn_3O_4 Negative Electrode and $Ni(OH)_2$ Positive Electrode: A Novel and High-Performance Flexible Electrochemical Energy Storage Device, ACS Applied Materials & Interfaces, 7 (2015) 11444-11451.

[14] M. Yang, H. Cheng, Y. Gu, Z. Sun, J. Hu, L. Cao, F. Lv, M. Li, W. Wang, Z. Wang, S. Wu, H. Liu, Z. Lu, Facile electrodeposition of 3D concentration-gradient Ni-Co hydroxide nanostructures on nickel foam as high performance electrodes for asymmetric supercapacitors, Nano Research, 8 (2015) 2744-2754.

[15] H.B. Li, M.H. Yu, F.X. Wang, P. Liu, Y. Liang, J. Xiao, C.X. Wang, Y.X. Tong, G.W. Yang,

Amorphous nickel hydroxide nanospheres with ultrahigh capacitance and energy density as electrochemical pseudocapacitor materials, Nature Communications, 4 (2013) 1894.

[16] Z. Li, S. He, C. Ji, H. Mi, C. Lei, Z. Li, H. Pang, Z. Fan, C. Yu, J. Qiu, Hierarchical Bimetallic Hydroxides Built by Porous Nanowire-Lapped Bundles with Ultrahigh Areal Capacity for Stable Hybrid Solid-State Supercapacitors, Advanced Materials Interfaces, 6 (2019) 1900959.

[17] Q. Yin, D. Li, J. Zhang, Y. Zhao, C. Wang, J. Han, CoNi-layered double hydroxide array on graphene-based fiber as a new electrode material for microsupercapacitor, Applied Surface Science, 487 (2019) 1-8.

Conclusion and Perspectives

As a link for energy-power difference between a traditional capacitor and fuel cells/batteries, supercapacitors (SCs) have drawn widespread interest owing to their advantages like enhanced power density, being almost maintenance-free, experiencing no memory effect, safe, short charge/discharge time, and low cost. However, the relatively low energy density hinders their wide application in daily life. Therefore, the research in the field of SCs is mainly oriented towards the development of novel high-performance electrode materials.

Among all the materials, Ni-based hydroxides have drawn great attention and interest in the field of supercapacitors. $Ni(OH)_2$ with large theoretical specific capacitance (2082 F g^{-1}) has been extensively investigated for supercapacitors. Besides, Ni-based layered double hydroxides (LDHs), due to their well-defined and high redox activity, wide tunability of the types of metal cations and environmentally friendly nature, were also greatly explored for supercapacitor applications. However, the low electrical conductivity of hydroxides hinders their potential application. To overcome this problem, composites combining Ni-based hydroxides with carbon-based (reduced graphene oxide and carbon spheres) materials were prepared with the aim to enhance their electrical conductivity. Additionally, deposition on porous supports such as nickel foam (NF) or cupper foam (Cu foam) endows the composite with high surface area and certain flexibility.

In this thesis, NiFe LDHs/rGO/NF, NiAl LDHs@CS/NF and NiMnCr LDHs@CS/NF composites were first synthesized, and showed improved specific/areal capacity than that of the same composites without carbon-based materials. NiFe LDHs/rGO/NF achieved a specific capacity (585 C g^{-1} at 5 A g^{-1}) higher than that of NiFe LDHs/NF (530 C g^{-1} at 5 A g^{-1}). NiAl LDHs@CS/NF electrode material attained an areal capacity (1042.2 mC cm^{-2} at 1 mA cm^{-2}) greater than that of NiAl LDHs/NF (851.9 mC cm^{-2} at 1 mA cm^{-2}). NiMnCr LDHs@CS/NF composite

exhibited a much larger specific capacity (569 C g^{-1} at 3 A g^{-1}) than that of NiMnCr LDHs/NF (173.2 C g^{-1} at 3 A g^{-1}).

To further improve the energy density, hybrid supercapacitor devices with wide working potential window were fabricated. A hybrid supercapacitor device was assembled based on as-prepared NiFe LDHs/rGO/NF as the positive electrode and mesoporous carbon (MC)/NF as the negative electrode, exhibiting an energy density of 17.71 Wh kg^{-1} and a power density of 348.49 W kg^{-1}. Besides, a hybrid supercapacitor device comprising NiAl LDHs@CS/NF as the positive electrode and N-doped reduced graphene/NF as the negative electrode attained an energy density of 43 μWh cm^{-2} at a power density of 0.805 mW cm^{-2} and was applied successfully to operate a windmill device continuously for 32 s. Moreover, two flexible NiAl LDHs@CS/NF//N-rGO/NF hybrid supercapacitors, connected in series, were able to light up a green, a red and a yellow LED in parallel, lasting for 37 s, 542 s and 199 s, respectively. Finally, a hybrid supercapacitor was fabricated using NiMnCr LDHs@CS/NF as the positive electrode and FeOOH coated on NF (FeOOH/NF) as the negative electrode, reaching an energy density of 48 Wh kg^{-1} at a power density of 402.7 W kg^{-1}. For practical applications, the as-fabricated NiMnCr LDHs@CS/NF//FeOOH/NF supercapacitor device was successfully used to operate a home-designed windmill device and two as-fabricated hybrid supercapacitor cells in series were used to light up a yellow LED and a red LED in parallel for ~111 s and ~343 s, respectively, indicating their potential application for flexible energy storage devices.

At the same time, Ni(OH)$_2$@CuO@Cu foam binder-free electrodes were fabricated by a two-step process at room temperature with different deposition times. Ni(OH)$_2$@CuO@Cu-150 exhibited large areal capacity of 7063 mC cm^{-2} at 20 mA cm^{-2}, and was therefore chosen as the positive electrode in a hybrid supercapacitor. Using N-doped reduced graphene oxide on nickel

foam (N-rGO/NF) as the negative electrode, a hybrid supercapacitor was assembled. It displayed good flexibility, cycling stability and high areal energy density of 130.4 μWh.cm^{-2} at a power density of 1.6 mW.cm^{-2}. Two hybrid supercapacitor devices were connected in series to successfully lighten up a red LED for 12min 39s, while three devices assembled in series were able to successfully power a three-digit digital display for 1min 28s. Interestingly, the hybrid supercapacitor device, charged by solar cells, further supplied a homemade windmill device for 59s, achieving sunlight-powered integration system.

Even though the high energy density of the hybrid supercapacitor devices were achieved and were successfully applied for practical applications, they are still far from real commercialization. There is plenty of room to explore new electrode composites for supercapacitors. At the same time, in this thesis, we only investigated the electrochemical performance of the as-prepared composites in aqueous electrolytes, which limited the working potential window, further reducing the energy density. In future works, it will be of interest to investigate low-cost high-performance electrode materials, and explore their electrochemical performance in different electrolytes such as organic and ionic liquids electrolytes with the aim to construct hybrid supercapacitor devices with higher energy and power densities, which can potentially replace batteries for practical applications.

S1 APPENDIX

S1.1 Chemicals

Nickel(II) nitrate hexahydrate (Ni(NO$_3$)$_2$·6H$_2$O), Iron(III) nitrate nonahydrate (Fe(NO$_3$)$_3$·9H$_2$O), Manganese(II) nitrate tetrahydrate [Mn(NO$_3$)$_2$·4H$_2$O], chromium(III) nonahydrate [Cr(NO$_3$)$_3$·9H$_2$O], aluminum(III) nitrate nonahydrate [Al(NO$_3$)$_3$·9H$_2$O], urea [CO(NH$_2$)$_2$], ammonium fluoride (NH$_4$F), hydrazine monohydrate (NH$_2$NH$_2$·H$_2$O), glucose, mesoporous carbon (MC) and graphite were obtained from Sigma-Aldrich (France).

Graphene oxide (GO) was purchased from Graphitene (UK).

Nickel foam (NF) was purchased from Jiayisheng Company (China).

Carbon paper (CP) was purchased from Maipengchen Electronic Technology Co., Ltd. (China).

The water used throughout the experiments was purified with a Milli-Q system from Millipore Co. (resistivity = 18 MΩ.cm).

S1.2 Characterization techniques of electrode materials

For the as-prepared electrode materials, it is necessary to assess their morphologies, and chemical compositions, which provide an evaluation method for supercapacitor applications. Various characterization techniques are commonly used and are introduced as follows.

S1.2.1 Scanning Electron Microscopy (SEM)

SEM is the most commonly used method to observe the surface morphology of the material. The principle is to collect the signals of different characteristic particles (mainly secondary electrons) generated by the high-energy electron beam irradiated on the sample surface, forming the different images to obtain the resulting topography information of the sample surface. In

addition to secondary electrons, the irradiated area can also be excited to produce characteristic X-rays, and the content and type information of elements in the sample can be obtained based on the obtained X-ray information, which is the corresponding energy dispersive spectrometer (EDS) and element scanning analysis (mapping).

SEM images in this thesis were obtained using an electron microscope ULTRA 55 (Zeiss) equipped with a thermal field emission emitter and three different detectors (EsB detector with filter grid, high-efficiency In-lens SE detector, Everhart-Thornley secondary electron detector). For EDS elemental mapping images, the k-line was used. For each point of images, a spectrum from 0 to 20 keV was recorded.

For the samples obtained on NF, SEM imaging was directly performed on the samples. For powder samples, they were first dissolved in 50 μL MQ water or ethanol, and then dropped on a clean silicon wafer, followed by drying in an oven at 80 °C to remove the solvent.

S1.2.2 Transmission Electron Microscopy (TEM)

TEM provides more detailed microscopic morphological observations on the prepared materials. The high-resolution tests on specific selection areas allow observing the lattice fringes of the materials, and the corresponding crystal plane spacing can further determine the composition of the materials. In addition, surface scan element analysis (mapping) of the material selection gives a precise image of the elements' distribution on the surface of the samples.

In this thesis, TEM analysis was performed on a TECNAI-G2 working at 200 kV, equipped with an EDS spectrometer. The samples on NF were scratched off and were dispersed on a thin carbon film of a 3 mm diameter copper grid to perform the measurement.

S1.2.3 X-ray diffraction (XRD)

XRD is widely used for phase and crystal structure analysis of materials. The working principle

is to use monochromatic X-rays incident on the surface of the material to obtain X-ray diffraction in different directions and intensities. According to its diffraction direction and intensity, different diffraction patterns are obtained, depending on different phase components and crystal structure.

In this thesis, the crystal structure of the synthesized nanomaterials was investigated by powder X-ray diffraction analysis. XRD patterns were recorded using a Bruker D8 Advance equipped with 1D LynxeEye detector at a scanning rate of 3° min^{-1} and 2θ value ranging from 10 to 80° using Cu Kα (α= 1.54056Å) as the X-ray source and operates at a generator voltage of 40 kV and a current of 40 mA.

S1.2.4 X-ray photoelectron spectroscopy (XPS)

XPS can be used to analyze the elemental composition, content and chemical valence of the material surface. By fitting the individual high-resolution spectra of a certain element to the peak, the valence bond form and the content of different valence bonds can be analyzed.

In this thesis, XPS experiments were performed on a PHI 5000 VersaProbe-Scanning ESCA Microprobe (ULVAC-PHI, Japan/USA) instrument at a base pressure below 5×10^{-9} mbar. Monochromatic AlK$_\alpha$ radiation was used and the X-ray beam, focused to a diameter of 100 μm, was scanned on a 250 × 250 μm surface, at an operating power of 25 W (15 kV). Photoelectron survey spectra were acquired using a hemispherical analyzer at pass energy of 117.4 eV with a 0.4 eV energy step. Core-level spectra were recorded at pass energy of 23.5 eV with a 0.1 eV energy step. All spectra were obtained with 90° between X-ray source and analyzer and with the use of low energy electrons and low energy argon ions for charge neutralization. After subtraction of the linear-type background, the core-level spectra were decomposed into their components with mixed Gaussian-Lorentzian (30:70) shape lines using the CasaXPS software. Quantification calculations were performed using sensitivity factors supplied by PHI.

S1.2.5 Raman spectroscopy

Raman spectroscopy is a commonly used tool for characterizing the degree of defects and graphitization of carbon-based materials. The principle is that the excitation light irradiates the sample surface, and collision with the sample will exchange energy, causing the frequency of the scattered light to change. The difference between the frequency of the incident light and the frequency of the scattered light is defined as the Raman shift. The number of waves is the reciprocal of the wavelength (in cm^{-1}) to indicate the amount of shift.

Raman spectroscopy measurements in this thesis were performed on a LabRam HR Micro-Raman system (Horiba Jobin Yvon) using a 473-nm laser diode as excitation source. Visible light is focused by a 100× objective. The scattered light is collected by the same objective in backscattering configuration, dispersed by a 1800 mm focal length monochromator and detected by a CCD camera.

PUBLICATIONS

1. **Min Li**, Ahmed Addad, Mathias Dolci, Pascal Roussel, Mu. Naushad, Sabine Szunerits and Rabah Boukherroub*, NiMnCr Layered Double Hydroxide-Carbon Spheres Modified Ni Foam: An Efficient Positive Electrode for Hybrid Supercapacitors, **Chemical Engineering Journal**, 2020, 396: 125370.

2. **Min Li**, Ahmed Addad, Pascal Roussel, Sabine Szunerits and Rabah Boukherroub*, High Performance Flexible Hybrid Supercapacitors based on Nickel Hydroxide Deposited on Cupper oxide supported by Cupper Foam for a Sunlight-Powered Rechargeable Energy Storage System, **Journal of Colloid and Interface Science**, 2020, 579: 520-530.

3. **Min Li**, Mathias Dolci, Pascal Roussel, Alexandre Barras, Sabine Szunerits and Rabah Boukherroub*, High-performance Flexible Hybrid Supercapacitor Based on NiAl Layered Double Hydroxide as a Positive Electrode and Nitrogen-Doped Reduced Graphene Oxide as a Negative electrode, **Electrochimica Acta**, 2020, 354: 136664.

4. **Min Li**, Roxana Jijie, Alexandre Barras, Pascal Roussel, Sabine Szunerits, Rabah Boukherroub*, NiFe Layered Double Hydroxide Electrodeposited on Ni Foam Coated with Reduced Graphene Oxide for High-Performance Supercapacitors, **Electrochimica Acta**, 2019, 302: 1-9.

5. Yuan Zhang[1], Ning Cao[1], **Min Li**, Sabine Szunerits, Ahmed Addad, Pascal Roussel, Rabah Boukherroub*, Self-template Synthesis of ZnS/Ni_3S_2 as Advanced Electrode Material for Hybrid Supercapacitors, **Electrochimica Acta**, 2019, 328: 135065.